

University of Nottingham
UK | CHINA | MALAYSIA

Inkjet Printing Heterostructures for Optoelectronic Device Applications

Jonathan Steven Austin

Thesis submitted to the University of Nottingham for the degree of Doctor of Philosophy

December 2023

Abstract

Devices that combine the tuneable optical properties of 0-dimensional (0D) materials, such as perovskite nanocrystals (NCs), with the unique electrical properties of 2-dimensional (2D) layers, such as graphene, are promising candidates for the next generation of optoelectronics. However, these high-performance devices typically require bespoke fabrication techniques and are yet to reach commercial viability. Inkjet printing can offer a promising route for scalable manufacturing of devices on various substrates from Si/SiO_2 to flexible polymers. However, many functional nanomaterials have not yet been formulated or optimised for deposition via inkjet printing and the fully printed heterostructures needed for many optoelectronic devices have proven challenging to fabricate.

This work reports on the formulation of inks for inkjet deposition of all-inorganic $CsPbX_3$ (X = Br or Br/I) perovskite NCs, graphene quantum dots (GQD), poly-TPD and TPBI, thereby increasing the availability of optically active and charge transport materials for additive manufacturing technologies. Using these inks, heterostructures were printed and their interfaces investigated to optimise printing strategies so as to improve uniformity and reduce intermixing between printed layers.

With this knowledge, a variety of optoelectronic devices were printed. The perovskite and GQD inks were printed onto pristine graphene devices, which achieved photodetection in the ultraviolet to visible (UV-Vis) range with photoresponsivity up to $R \sim 10^6$ A/W. Fully printed photodetectors were also fabricated for applications on flexible substrates, by decorating inkjet printed graphene with perovskite NCs, which achieved photoresponsivity of $R > 10$ A/W. A fully printed perovskite light emitting diode (LED) was also fabricated, with six different materials, including the charge injection layers poly-TPD and TPBI, and while no emission was recorded, promising results were measured, indicating the viability of the fabrication method. This work expands the library of functional material inks and demonstrates the great potential of inkjet printing for the manufacturing of optoelectronic devices.

PUBLICATIONS, CONFERENCES, AND AWARDS

Publications:

- Photosensitisation of inkjet printed graphene with stable all-inorganic perovskite nanocrystals, **J. S. Austin**, N. D. Cottam, C. Zhang, F. Wang, J. H. Gosling, O. Nelson-Dummet, G. F. Trindade, Y. Zhou, T. S. S. James, P. H. Beton, C. Tuck, R.Hague, O. Makarovsky, L. Turyanska, *Nanoscale*, 2023, 15, 2134.

- Stable large area drop-on-demand deposition of a conductive polymer ink for 3D-printed electronics, enabled by bio-renewable co-solvents, Geoffery Rivers, **J. S. Austin**, Y. He, A. Thompson, N. Gilani, N. Roberts, P. Zhao, C. J. Tuck, R. Hague, R. D. Wildman, L. Turyanska, *Addit. Manuf.*, 2023, 66, 103452.

- Magnetic and electric field dependent charge transfer in perovskite/graphene field effect transistors, N. D. Cottam, **J. S. Austin**, C. Zhang, A. Patanè, W. Escoffier, M. Goiran, M. Pierre, C. Coletti, V. Mišeikis, L. Turyanska and O. Makarovsky, *Adv. Electron. Mater.*, 2023, 9, 2200995.

- Formulation of Functional Materials for Inkjet Printing: a Pathway Towards 3D electronics, A. Bastola, Y. He, J. Im, F. Wang, R. Worsley, **J. S. Austin**, O. Nelson-Dummett, R. D. Wildman, R. Hague, C. J. Tuck, L. Turyanska, *Mater. Today Electron*, 2023, 6, 100058.

- Functionalized Gold Nanoparticles with a Cohesion Enhancer for Robust Flexible Electrodes, J. Im, G.F. Trindade, T.T. Quach, A. Sohaib, F. Wang, **J. S. Austin**, L. Turyanska, C.J. Roberts, R. Wildman, R. Hague, C. Tuck, , *ACS Appl. Nano Mater.*, 2022, 5, 6708.

Conference Presentations:

- European Materials Research Society Fall Meeting, Warsaw (18-21 September 2023). Oral presentation. Inkjet printing Graphene: from Transport Nature to Photodetectors and Multifunctional Sensors.

- Materials Research Society Spring Meeting and Exhibit, San Francisco (10-14 April 2023). Poster presentation. Photosensitisation of Inkjet Printed Graphene with Stable All-Inorganic Perovskite Nanocrystals.

- Advanced Electronic and Photonic Materials conference, Manchester (7-8 September 2022). Poster presentation. Inkjet Printed Graphene Photodetector Decorated with All-Inorganic Perovskite Nanocrystals.

- Engineering Research Showcase, Nottingham (28 April 2022). Poster presentation. Additive Manufacturing Low-Dimensional Optoelectronic Devices.

Awards:

- Second place poster prize at Advanced Electronic and Photonic Materials conference, Manchester 2022.

- Winner of best poster prize for research quality at Engineering Research Showcase, Nottingham 2022.

ACKNOWLEDGMENTS

First and foremost, I'd like to express my deepest gratitude to my supervisor, Dr. Lyudmila Turyanska. Her knowledge and guidance have been paramount to all the successful research that I have carried out during my PhD. Her work ethic inspires me and I am deeply thankful for her unwavering support, her brilliant feedback, and for all the time she has spent developing my skills. It has been an absolute pleasure working with her over these past three years, despite her frustrating habit of always being right.

My sincere thanks go to my co-supervisor Dr. Oleg Makarovsky who first made me aware of this PhD position and inspired me to apply. His wealth of knowledge astounds me and his support and guidance during my experiments in the Wendy House were hugely important to my work.

I am highly grateful to my co-supervisors Prof. Richard Hague and Prof. Chris Tuck for their continued support and guidance. The breadth of their experience and knowledge has been very helpful throughout my studies, and their relentless work ethic is inspirational.

I am thankful for all my friends and colleagues in the Centre for Additive Manufacturing (CfAM) and in the School of Physics: Dr. Feiran Wang, Dr. Nathan Cottam, and Dr. Geoffrey Rivers taught me almost every experimental technique I know and were all excellent friends and mentors at every step of the way through my PhD. Jisun Im, Negar Gilani, Oliver Nelson-Dummett, Weitong Xiao, Tyler James, Jonathan Gosling, Yinfeng He, Robyn Worsley, Anil Bastola, Charles Heaton, Ellie Ward, Chris Strong, Thomas Girerd, I appreciate all the help that each of you gave me and I thoroughly enjoyed working with everyone.

I would like to thank Mark East, Mark Hardy, and Adam Whitbread for their constant technical support in the lab and thanks to Mirela Axinte and Flavia Guzman Villarroel for their excellent organisation and administrative support.

I acknowledge the support and collaboration of Dr. Mike Fay and Dr. Graham Rance from the Nanoscale and Microscale Research Centre (nmRC); Dr. Gustavo Trindade, Dr. Yundong Zhou, and Dr. Ian Gilmore from the National Physics Laboratory (NPL); and Dr. Peter Beton from the School of Physics for access to his laboratory. I also acknowledge the support and funding of the University of Nottingham, Engineering and Physical Research Council (ESPRC).

Finally, I would like to thank my family and friends, particularly my parents and my little sister Katy. I am forever grateful to my parents for their eternal support and encouragement. Without their sacrifices I could not be where I am today. Lastly, I want to thank Emily. Her support, patience and tea-making skills carried me to the end of this PhD.

Contents

1 Introduction 1

1.1 Thesis Overview 2

2 Literature Review 4

2.1 Additive Manufacturing of Electronics 4

2.2 Inkjet Printing Process 5

2.3 Novel Materials for Inkjet Printed Electronics 9

2.3.1 2D Van der Waal Materials 9

2.3.2 0D Materials 13

2.3.3 Organic Materials 21

2.4 Formulation of Materials for Inkjet Deposition and Properties of Printed Materials 26

2.4.1 2D Material Inks 26

2.4.2 0D Material Inks 30

2.4.3 Organic Material Inks 36

2.5 Inkjet Printed Heterostructures and Devices 39

2.5.1 Heterostructures 40

2.5.2 Electronic Devices 44

2.5.3 Optoelectronic Devices 48

2.6 Challenges For Inkjet Printing of Electronics 57

2.7 Summary 58

3 Aims and Objectives 62

4 Materials and Experimental Methods 64

4.1 Materials and Substrates 64

4.2 Ink Formulations 65

4.3 Rheology Measurements 67

4.4 Inkjet Printing Process and Printing Parameters 68

4.4.1 Inkjet Printing Process 68
4.4.2 Post-Processing Treatments 71
4.4.3 Printing Parameters 72
4.5 Morphological and Optical Characterisation 77
4.5.1 Optical Microscopy 77
4.5.2 Electron Microscopy 78
4.5.3 Atomic Force Microscopy 79
4.5.4 Time-of-Flight Secondary Ion Mass Spectroscopy 81
4.5.5 Raman Spectroscopy 82
4.5.6 Photoluminescence Spectroscopy 83
4.5.7 Absorption Spectroscopy 84
4.6 Electrical Measurements 86
4.6.1 Sample Preparation for Electrical Measurements 86
4.6.2 Sheet Resistance Measurements 90
4.6.3 Electrical Measurements under Applied Gate Voltage 92
4.6.4 Photocurrent Measurements 93
4.6.5 Electrical Performance under Mechanical Bending 95
5 Formulation and Characterisation of AM Materials 97
5.1 Optimisation of Graphene Ink and Development on Flexible Substrates 97
5.2 Formulation of Perovskite Nanocrystals Inks 99
5.2.1 All-Inorganic $CsPbX_3$ NC Inks 99
5.2.2 $CsPbX_3$-PVP Ink 104
5.2.3 iGr-$CsPbX_3$ Hybrid Inks 105
5.3 Graphene Quantum Dots 109
5.4 PEDOT:PSS 115
5.5 Poly-TPD and TPBI 119
5.6 Summary 122

6 Inkjet Printing Heterostructures 125

6.1 Introduction 125

6.2 Wetting Phenomena Observed on Printed Heterostructures 126

6.3 Probing Cross-Sectional Heterostructures 129

6.4 Summary 139

7 Printed Optoelectronic Devices 141

7.1 Introduction 141

7.2 Printed $CsPbBr_3$ and $CsPb(Br/I)_3$ Perovskite Photodetectors 143

7.3 Fully printed $CsPbBr_3$ and $CsPb(Br/I)_3$ Perovskite Photodetectors 152

7.4 GQD Photodetectors 160

7.5 Fully-Printed Perovskite LED 166

7.6 Summary 171

8 Conclusions 173

9 Outlook and Future Work 177

References 180

LIST OF ACRONYMS AND VARIABLES

Acronyms:

0D /2D /3D – 0- /2- /3-dimensional

AFM – Atomic force microscopy

AM – Additive manufacturing

BP – Black phosphorus

CB – Conduction band

CNT – Carbon nanotubes

CVD – Chemical vapour deposition

DMF – N,N-Dimethylmethanamide

DMSO – Dimethylsulfoxide

DoD – Drop-on-demand

EC – Ethyl cellulose

EDX – Energy dispersive x-ray

EELS – Electron energy loss spectroscopy

FET – Field effect transistor

FIB – Focussed ion beam

FWHM – Full width at half maximum

GC – Glycerol carbonate

GO – Graphene oxide

GOPS – Glycidoxypropyltrimethoxysilane

GQD– Graphene quantum dot

hBN – Hexagonal boron nitride

iGr – Inkjet printed graphene

IPA – Isopropyl alcohol

IPL – Intense pulsed light

IR – Infrared

LED – Light emitting diode

LPE – Liquid phase exfoliation

MBE – Molecular beam epitaxy

NC – Nanocrystal

NMP – N-nethylpyrrolidone

NP – Nanoparticle

NPB – N,N'-bis(I)naphthyl)-N,N'-diphenyl-1,1'-biphenyl-4,4'-diamine

OFET – Organic field effect transistor

Oh – Ohnesorge number

P3HT – Poly(3-hexylthiophene-2,5-diyl)

PANI – Polyaniline

PBA – Phenyl boric acid

PBTTT – Poly(2,5-bis(3-alkylthiophen-2-yl)thieno[3,2-b]-thiophene

PCB – Printed circuit board

PCE – Power conversion efficiency

PEDOTL:PSS – Poly(3,4-ethylenedioxythiophene) polystyrene sulfonate

PEG – Poly(ethylene glycol)

PEN – Polyethylene naphthalate

PEO – Polyethylene oxide

PET – Polyethylene terephthalate

PFP-3 – 1,1-(9,9-bis(4-(hexyloxy)phenyl)-9H-fluorene2,7-diyl)dipyrene

PL – Photoluminescence

PMMA – Poly(methyl methacrylate)

Poly-TPD – Poly(N,N′diphenylbenzidine diphenylether)

Ppy – Polypyrrole

PVP – Polyvinylpyrrolidone

QD – Quantum dot

QY – Quantum yield

rGO – Reduced graphene oxide

SLG – Single layer graphene

TAPC – 1,1-bis[(di-4-tolylamino)phenyl]cyclohexane

TEM /SEM– Transmission electron microscopy /scanning electron microscopy

TMDC – Transition metal dichalcogenides

ToF-SIMS – Time-of-flight secondary ion mass spectroscopy

TPBI – 2,2',2"-(1,3,5-benzinetriyl)-tris(1-phenyl-1-H-benzimidazole)

TPGDA – Tripropylene glycol diacrylate

UV/ UV-VIS – Ultraviolet /ultraviolet to visible

VB – Valence band

VdP – Van der Pauw

VdW – Van der Waals

Variables:

a – Nozzle diameter/apeture

d – Dielectric thickness

E_{em} – Energy of photon emitted by sample

E_{ex} – Energy of photon absorbed sample

E_g – Band gap energy

I_{dark} – Dark current

I_{pc} – Photocurrent

I_{sd} – Source-drain current

l – Length of sample

l_{2t} – Length between 2-terminal contacts

m^* – Charge carrier effective mass

P – Power density

P_{sample} – Power incident on sample

q – Electron charge

R – Photoresponsivity

R_{2t} – Electrical resistance measured in 2-terminal configuration

R_{4t} – Electrical resistance measured in 4-terminal configuration

R_A – Vertical component of sheet resistance measured in VdP configuration

R_B – Horizontal component of sheet resistance measured in VdP configuration

R_s – Sheet resistance

t – Time

T_{anneal} – Annealing temperature

$T_{substrate}$ – Substrate temperature

$V(x,y,z)$ – Potential energy

V_{4t} – Votlage change recorded across 4-terminal contacts

V_g – Gate voltage

V_{sd} – Source-drain voltage

$\boldsymbol{V_{VdP}}$ – Votlage change recorded across VdP contacts

$\boldsymbol{w}$ – Width of sample

$\boldsymbol{Z}$ – Inverse of the Ohnesorge number

$\boldsymbol{\gamma}$ – Surface tension

$\boldsymbol{\varepsilon}$ – Relative permittivity

$\boldsymbol{\varepsilon_0}$ – Permittivity of free space

$\boldsymbol{\eta}$ – Viscosity

$\boldsymbol{\lambda}$ – Wavelength

$\boldsymbol{\lambda_{ex}}$ – Excitation wavelength

$\boldsymbol{\mu}$ – Carrier mobility

$\boldsymbol{\rho_d}$ – Density

$\boldsymbol{\rho_{sd}}$ – Resistivity

$\boldsymbol{\sigma_{sd}}$ – Conductivity

$\boldsymbol{\tau_{rise}}$ – Excitation response time

$\boldsymbol{\tau_{fall}}$ – Relaxation response time

$\boldsymbol{\mu}$ – Carrier mobility

$\boldsymbol{\Psi(x,y,z)}$ – Wavefunction

1 INTRODUCTION

Traditional optoelectronic devices based on three dimensional (3D) semiconductors, such as Si, have limited size scalability due to carrier scattering from surface defects [1], and poor compatibility with the expanding market of flexible and wearable devices [2]. In recent years, optoelectronic devices based on low dimensional materials have been developed to address these challenges, and they are considered promising candidates for the next generation of optoelectronics [3–5]. These devices have risen to prominence in the last decade following the synthesis of new 0-dimensional (0D) materials, such as all-inorganic lead halide perovskite nanocrystals (NC), which display high photoluminescent quantum yields (PL QY) of near unity across the UV to visible (UV-Vis) spectral range, along with superior stability compared to organic or organic/inorganic perovskite materials [6,7]. These novel materials have enabled the fabrication of photodetectors that combine the tuneable optical properties of 0D materials with the unique electrical properties of 2-dimensional (2D) conductive layers, such as graphene, which have achieved photon detectors with high photoresponsivity up to $R \sim 10^9$ A/W [4,8].

However, these high-performance nanomaterial-based devices typically require bespoke fabrication techniques, limiting their reproducibility and scalability [4,9]. Additive manufacturing (AM), specifically inkjet printing, has the significance of offering a promising route for large scale, industrial style fabrication of devices incorporating nanomaterials, such as graphene [10,11], perovskites [12–16], and quantum dots. [17–19]. But there are still major challenges in developing these materials into inks, and printing the multi-layered and multi-material heterostructures required for many optoelectronic devices.

1.1 THESIS OVERVIEW

In this thesis, the development of inkjet printing formulations and techniques for deposition of functional materials is presented, including all-inorganic lead halide perovskite NCs and graphene quantum dots (GQD), alongside an exploration of the fabrication of printed heterostructures for photon detection and emission applications.

Chapter 1 is the introduction and overview of the chapters contained in this thesis.

Chapter 2 provides a literature review on additive manufacturing of electronics, specifically using inkjet printing, how the process works, and how inks are formulated for inkjet deposition. This is followed by a literature review of the materials used for inkjet printed electronics. Then, a literature review on the methods used to formulate these materials into inks for inkjet printing is presented. Finally, a literature review is presented on inkjet printed heterostructures and electronic and optoelectronic devices.

Chapter 3 outlines the main aims and objectives of this PhD thesis.

Chapter 4 describes the materials and experimental methods involved in inkjet printing and characterising optoelectronic devices based on low-dimensional materials. This includes, details on rheological measurements, ink formulations, and inkjet printing parameters used for each material, the morphological measurements used to characterise materials, and the electrical and optical measurements performed on devices throughout this thesis.

Chapter 5 reports on the experiments performed towards the formulation and optimisation of materials for inkjet deposition and the characterisation of inks and printed films.

Chapter 6 presents and investigation on inkjet printed heterostructures for optoelectronic devices, including wetting phenomena that can occur when printing heterostructures and a study of how printing parameters affect the quality of heterostructure interfaces.

Chapter 7 investigates the properties and performances of partially and fully-printed graphene-based photodetectors decorated with photoactive materials, such as perovskites and graphene quantum dots. Progress towards a fully printed perovskite LED is also presented.

Chapter 8 concludes the thesis, providing an overview of the key findings

Chapter 9 remarks on the future prospects for work beyond this thesis.

2 LITERATURE REVIEW

2.1 ADDITIVE MANUFACTURING OF ELECTRONICS

Additive manufacturing (AM) technology is based on layer by layer deposition of materials and has attracted interest for applications in many sectors including the aerospace [20,21], biomedical [22], and electronics industries [23]. This technological approach enables digital information to be transformed into physical forms and is increasingly being used for the production of end use parts [21,23]. AM offers unique benefits, such as the ability to produce complex designs, minimizing waste, enabling affordable manufacturing, and reducing lead time [24]. Structural parts fabricated using AM are typically based on a single material [25], however, the next generation of AM technologies requires the production of multi-material structures. Moreover, the AM deposition of functional materials, required for advanced electronic components, is still under development [11,26–29] but could provide an important step to achieving the fabrication of fully printed electronic components [30].

Among the AM processes, ink- and material-jetting techniques are considered the most promising for multi-material electronics. This is because multiple printheads can be used to facilitate the deposition of multiple different materials with relative simplicity. Jetting techniques also allow for a high resolution of patterns and are highly adaptable to different fabrication processes [31–33]. In these processes, an ink is ejected through a nozzle and structures are produced by moving the stage or printhead in a pre-determined pattern. No physical contact is made with the substrate during deposition so the risk of damaging the sample is minimal and a wide range of substrates are suitable for these methods including rigid, flexible, and curved substrates [30].

2.2 INKJET PRINTING PROCESS

Inkjet printing enables the deposition of inks with a resolution of ~ 20 μm [34]. Inkjet printing can be operated continuously or in a drop-on-demand (DoD) mode. In continuous inkjet printers, drops are selectively charged by an electrode after they are formed. They then pass through a high voltage deflection plate where charged drops are allowed to fly directly through and onto the substrate, while the uncharged drops are deflected into a gutter for recirculation [35]. DoD inkjet printers produce a droplet only when one is required, hence providing a more sustainable manufacturing option. There are four categories of DoD depending on the mechanism used for drop formation: thermal, piezoelectric, electrostatic, and acoustic [35].

Piezo-driven DoD inkjet printheads are usually employed due to low power consumption, long lifetime, and because they enable the use of inks with a wide range of viscosities and solvents [36]. A piezoelectric transducer is used in a piezo-driven DoD printhead. When a drop is required an excitation pulse distorts the piezoelectric material in the printhead, creating pressure waves in the fluid. A drop is ejected when the kinetic energy transferred from the piezo transducer to the fluid is sufficient to overcome the surface tension of the ink at the nozzle [37]. A schematic diagram of a piezo-driven DoD inkjet printhead is shown in **Figure 2.1a**. The process of droplet formation from the printhead can be controlled by adjusting the voltage waveform to manipulate the electronic pulses to the piezo jetting device. This can then be optimised for a particular ink by using a drop-watcher system. The size of the ejected droplet is dependent on the diameter of the nozzle, however, the resolution of the print itself is dependent on many other variables, such as substrate wettability and the precision of the positioning system [36].

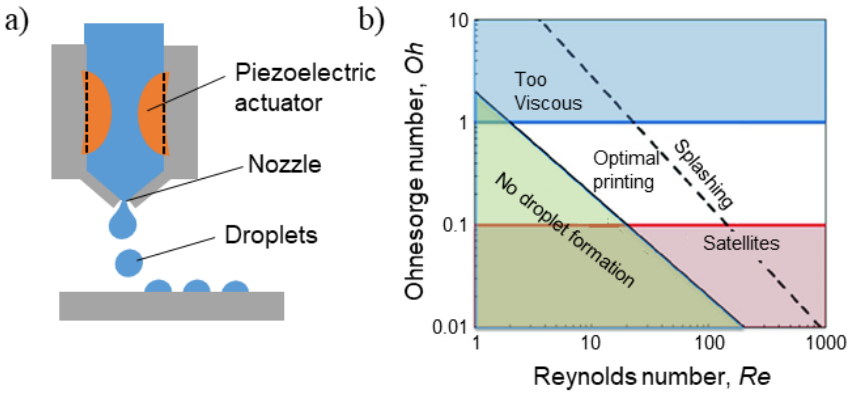


Figure 2.1. a) Schematic diagram of piezo-driven DoD printhead. When a drop is required, an electric pulse deforms the piezo-ceramic plate to eject ink through the nozzle. The ink is replenished after the removal of this electronic pulse. **b)** Relationship between Ohnesorge number and Reynolds number, for a given printhead which shows the regime of fluid properties require for DoD inkjet printing.(reproduced from reference [36]).

High resolution patterns can only be printed when the formation of droplets is reliable and stable, which requires ink formulations with particular rheological properties (**Figure 2.1b**) [36]. The printability of an ink formulation can be quantified by the Ohnesorge number, Oh, which can calculated using **Equation 1**, where ρ_{d} is the density, γ is the surface tension, and η is the viscosity of the ink for a given nozzle diameter a.

$$Oh = \frac{\eta}{\sqrt{\rho_{\mathrm{d}}\gamma a}} = \frac{\sqrt{We}}{Re} \tag{1}$$

These parameters can be visualised using the Reynolds number Re, and Weber number We, derived from the Navier–Stokes flow equation [38]:

$$Re = \frac{\rho_d v a}{\eta}, \tag{2}$$

where v is the velocity of ejected droplets. Derby et al. showed that optimal printing is achieved when the inverse of the Ohnesorge number, $Z = 1/Oh$, has a value between 1 and 10 [39]. For a standard printer with a nozzle diameter of 20 μm, this means optimal printing is achieved using an ink with viscosity between 1 and 25 mPa.s and surface tension between 25 and 50 mN/m [36]. Printhead heating can be used to adjust ink viscosity during printing, however, only over a small range (20 – 40 °C) to avoid ink drying in the nozzle. High boiling point solvents are often added to ink formulations to avoid nozzle clogging. For nanoparticle-based inks, the size of particles that can be printed is limited by nozzle size. Typically, particles with size > 1% of the orifice diameter can cause the nozzles to clog and stop droplets from forming [36].

The smallest feature size that can be achieved during printing is highly dependent on the wettability of the ink on the substrate. The wettability of a specific solvent on a substrate can be quantified by the contact angle formed between a drop of solvent and the solid surface. A larger contact angle tends to lead to smaller feature size (greater resolution) and greater film thickness. This contact angle, θ, is dependent on the free solid surface energy, γ_s, the interfacial energy, γ_{sl}, and the solvent surface tension, γ_l. These values are visualised in **Figure 2.2a**. and can be expressed by Youngs equation:

$$\gamma_{sl} = \gamma_s - \gamma_l . cos\theta \tag{3}$$

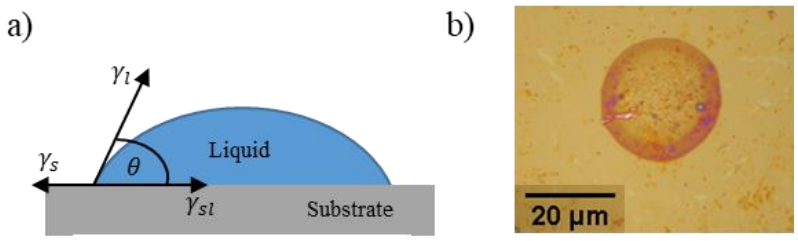


Figure 2.2. a) Diagram expressing a liquid droplet on a substrate to visualise the contact angle θ, the free solid surface energy γ_s, the solvent surface tension γ_l, and the interfacial energy γ_{sl}. **b)** Optical image of a single printed drop of $CsPbBr_3$ perovskite nanocrystals with a coffee ring drying pattern.

The drying behaviour of the ink after deposition on the substrate is also an important factor that must be controlled to achieve uniform films. Evaporation of the solvent can lead to unfavourable and inhomogeneous distributions of the dispersed material due to the 'coffee ring effect'. This phenomenon is where dispersed material in a droplet is carried to the edges of the drop during drying, leaving a ring shape of the dispersed material, with more material at the edge and less at the centre of the droplet when the solvent has completely evaporated (**Figure 2.2b**). This effect occurs because liquid at the edges of the droplet evaporates more readily than liquid at the centre [40]. To compensate for this loss in solvent at the edges of the droplet, the solution is carried by capillary flow from the centre to the edges, where solute is deposited over time forming the aforementioned ring shape [40].

Marangoni flow also occurs in these droplets, where liquid flows from areas of low surface tension to areas of high surface tension and is driven by the gradient of the surface tension, $\Delta\gamma$, on the surface of the droplet [40]. This effect redistributes the solute back from the edges of the droplet to the centre. The strength of the Marangoni flow, $M_{strength}$, is dependent on $\Delta\gamma$ and the viscosity of the liquid, η, as follows [40]:

$$M_{strength} \propto \frac{\Delta\gamma}{\eta} \quad (4)$$

To eliminate the coffee ring effect and achieve homogeneous films, an equilibrium between capillary flow and Marangoni flow rates must be achieved. This can be done by carefully selecting an inks solvents with appropriate viscosities, surface tensions, and boiling points [40]. Heating the printing stage/substrate can also benefit the drying behaviour of the ink by increasing evaporation speed and thus changing the rates of capillary and Marangoni flow [41].

To fulfil the requirements for inkjet printing, ink formulations are developed with suitable ink rheology for stable and reliable droplet formation during jetting. The formulation must also enable the printing of uniform films with well-defined edges after drying [42]. Finally post-processing techniques must be carried out on the printed film to remove the solvents and additives present in the ink. It is important that during all these steps, the functional properties of the material being printed are maintained.

2.3 NOVEL MATERIALS FOR INKJET PRINTED ELECTRONICS

A growing number of materials are available for inkjet printing electronics; of particular importance are materials with useful electronic and optical properties. In this section, these materials and their properties are outlined.

2.3.1 2D Van der Waal Materials

Van der Waals (VdW) materials are a class of material with strong in-plane covalently bonded 2D sheets that are held together by weak VdW forces [43]. These 2D sheets can be isolated via mechanical exfoliation or by other means and have a variety of

useful properties for electronics [43]. Examples of 2D VdW materials include: graphene, hexagonal boron nitride (hBN), InSe, In_2Se_3, MoS_2, WSe_2, and black phosphorus (BP).

Since its isolation and characterisation [44], single layer graphene (SLG) has been extensively investigated for applications in many scientific fields [45]. SLG consists of a flat monolayer of carbon atoms in a 2D honeycomb lattice with aromatic π-bonds above and below the SLG's plane (**Figure 2.3a,b**). SLG is described as a zero-gap material [46]. Due to the high crystal symmetry of SLG, the charge carriers can be described by theories of massless relativistic particles [46]. Furthermore, the energy of charge carriers in SLG displays a linear (rather than quadratic) dependence on momentum and a pronounced ambipolar electric field effect, meaning charge carriers can be tuned between holes and electrons with very high densities up to 10^{13} cm^{-2} by applying an external electric field (**Figure 2.3c**) [46]. The combination of easily tuneable electrical conductivity, flexibility, and mechanical strength displayed by this material, could offer benefits for electronics.

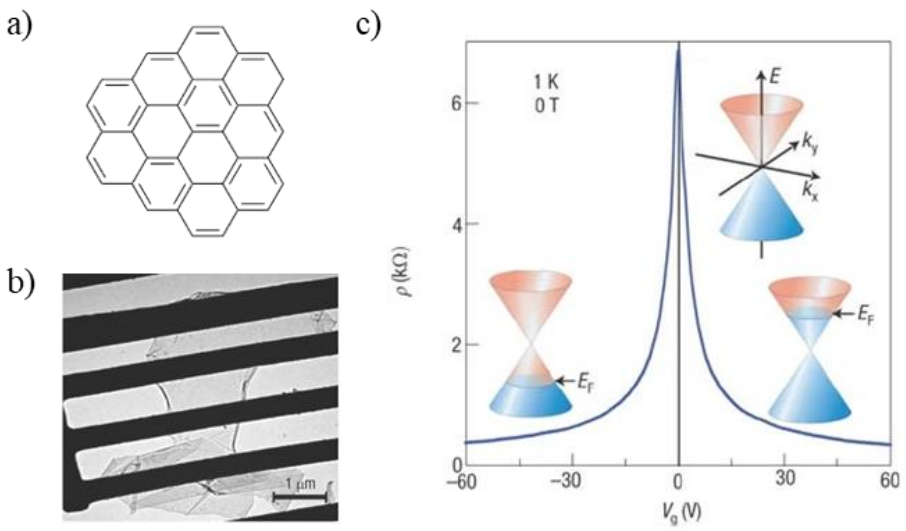


Figure 2.3. a) Chemical structure of single layer graphene. **b)** Transmission electron microscopy image of graphene sheet suspended on metallic scaffold (reproduced from reference [47]) **c)** Ambipolar field effect of SLG: shows the effect of gate voltage on the resistivity of the material. The inset shows the energy spectrum of SLG and how the Fermi energy E_F changes with gate voltage. The sharp decrease in resistivity following the introduction of charge carriers indicates their high mobility (reproduced from reference [46]).

SLG has been integrated into a variety of different architectures for electronic devices [48], however, upscaling device processing and co-depositing large-area graphene with other materials remain challenging [11]. Relatively large area SLG ($\gtrsim$ 10 µm [49]) has been produced via chemical vapour deposition (CVD) (carrier mobility μ ~ 8800 $cm^2/V{\cdot}s$ [50]) and molecular beam epitaxy (MBE) (μ ~ 1000 $cm^2/V{\cdot}s$ [51]). However, the electronic properties of these materials are inferior to high quality SLG produced via mechanical exfoliation (μ ~ 200,000 $cm^2/V{\cdot}s$ [52]).

Graphene inks have been formulated for solution processing techniques using graphene fabricated via more scalable liquid phase exfoliation (LPE) [11,53]. This technique involves the dispersion of graphite in a solvent (often n-methylpyrrolidone

(NMP)) and using ultasonication or shear mixing to overcome the weak VdW forces in the graphite to remove 2D flakes [54]. While LPE offers limited control over the size and thickness of flakes [55], researchers have aimed to improve the yield and efficiency of LPE for more efficient and upscaled manufacturing of graphene [56,57]. For example, the addition of α-functionalised alkanes as dispersion-stabilising agents during LPE increased the yield of single and few-layer graphene [56]. Similarly, 4-(decyloxy)acobenzene was included during LPE of graphite to improve the efficiency of the process by undergoing a large conformational change (due to photochemical isomerisation) under irradiation at λ = 365 nm to act as a dispersion-stabilising agent [57]. LPE graphene is compatible with solution processing techniques such as spin-coating and inkjet printing and thus enables graphene fabrication over much larger areas (10s of cms) than CVD or MBE [11,53].

Other forms of SLG include graphene oxide (GO), which is a highly oxidised form of SLG containing various oxygen containing functionalities [58]. When GO is reduced, a material known as reduced graphene oxide (rGO) is formed. rGO is similar in structure to SLG but contains structural defects and residual oxygen which leads to lower conductivity [45]. GO is often used in AM due to compatibility with polar solvents, such as water, and ease of functionalisation [59].

Insulating and semiconducting VdW materials were also isolated [60–62]. hBN is a wide bandgap (~5.9 eV) insulating material that displays high thermal conductivity and inertness [60]. hBN exhibits excellent chemical stability and is often used as an encapsulant and as a gate dielectric material in 2D field effect transistors (FET) [60]. When used to encapsulate SLG for example, hBN has been reported to improve the electrical properties of SLG, such as carrier mobility [63]. hBN also displays interesting optical properties such as high internal quantum efficiency of ~ 40% for

deep UV emissions [60]. Metal chalcogenides such as InSe and In_2Se_3 and the transition metal dichalcogenides (TMDCs) such as MoS_2 and WSe_2 are also commonly used 2D VdW materials for optoelectronics. The band gap of TMDCs can be tuned from ~ 1 eV in the near infrared (IR) to > 2.5 eV in the visible wavelength range of the electromagnetic spectrum [61] and they have high mobilities up to μ ~ 1000 $cm^2/V{\cdot}s$ [64] making them attractive for spectrally selective photodetection [65] and light emission applications [66].

2.3.2 0D Materials

2.3.2.1 Metal Nanoparticles

Metal nanoparticles (NPs) have been studied for many years and are widely used in various different fields from medicine to electronics [67,68]. Metal NPs can be produced with different sizes using colloidal synthesis to tune the absorption of the NPs due to surface plasmon resonance (**Figure 2.4**) [69]. Reduced NP size can also lead to lower sintering temperatures [70]. Metal NPs can also be modified with functional groups to further tune the NPs properties such as preventing NP aggregation [71], preventing crack formation in films [27], and improving NP uptake in cells [72]. Colloidal metal NPs are highly suited to solution processing techniques, which has provided new avenues for additive manufacturing [73].

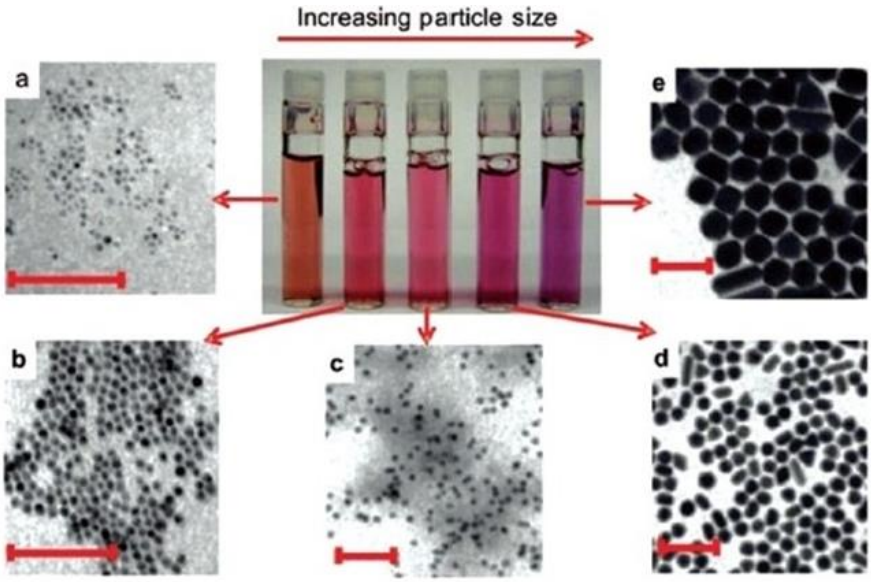


Figure 2.4. (middle) Optical image of aqueous solutions of AuNPs with particle diameter increasing from 4 to 40 nm from left to right and **a-d)** corresponding transmission electron microscopy (TEM) images for each solution. All scale bars are 100 nm (reproduced from reference [69]).

AuNP have received significant interest as they offer benefits of surface functionalization, high chemical stability, and low toxicity [74,75]. AuNPs are often used as an electrode material in optoelectronic devices [76,77] due to their high electrical conductivity and their size and shape dependent electrical and optical properties (**Figure 2.4**)[69,78]. Moreover, a much lower sintering temperature is required for AuNPs (~200 °C) compared to bulk gold (~1000 °C) (as is the case with Cu and Ag NPs), due to their increased surface area. This enables cheaper manufacturing and the possibility of deposition on a wide variety of heterostructures and substrates such as flexible Kapton [27,79]. Ag and Cu NPs are also widely studied 0D materials [80,81]. AgNPs and CuNPs have high conductivity, low cost (compared to AuNPs and SLG), and low melting point which enables the formation of thin conductive films using low temperature annealing [82]. CuNPs are particularly low

cost, however, they are highly prone to oxidation under ambient conditions so require protective coatings for use in electronic applications [83].

2.3.2.2 Semiconductor Nanocrystals

Colloidal quantum dots (QDs) are semiconducting NCs synthesised in solution. Their charge carriers experience quantum confinement, which occurs when the exciton Bohr radius is smaller than the NC size [84–86]. Since the charge carriers in colloidal QDs are confined in all three spatial directions, the system no longer has a continuous conduction band (CB) and valence band (VB), as observed in bulk semiconductors. Instead, the energy levels are discrete (**Figure 2.5a**) [84,85]. By solving the Schrödinger equation (**Equation 5**):

$$\varepsilon\psi(x,y,z) = \frac{-\hbar^2}{2m^*}\left(\frac{\partial^2}{\partial x^2}+\frac{\partial^2}{\partial y^2}+\frac{\partial^2}{\partial z^2}\right)\psi(x,y,z) + V\psi(x,y,z), \qquad (5)$$

the ground state energy , $\varepsilon_{\text{ground state}}$, for charge carrier motion in a QD can be expressed as **Equation 6**.

$$\varepsilon = \varepsilon_{xn} + \varepsilon_{ym} + \varepsilon_{zl} = \frac{\hbar^2}{2m^*}\left(\frac{n\pi}{L}\right)^2 + \frac{\hbar^2}{2m^*}\left(\frac{m\pi}{L}\right)^2 + \frac{\hbar^2}{2m^*}\left(\frac{l\pi}{L}\right)^2$$

$$\varepsilon_{\text{ground state}} = \varepsilon_{x1} + \varepsilon_{y1} + \varepsilon_{z1} = \frac{3\,\hbar^2}{2m^*}\left(\frac{\pi}{L}\right)^2 \propto \frac{1}{L^2}, \qquad (6)$$

where ε is the total energy of the charge carriers, ε_{x1}, ε_{y1}, and ε_{z1}, are the lowest energy eigenvalues of the 3D Schrodinger equation, and m^* is the effective mass of the charge carriers [86]. Hence, charge carrier motion in a QD is found to be proportional to $1/L^2$, where L is the diameter of the QD [86]. Thus quantum confinement also makes the band gap energy, E_g, of QDs highly tuneable by size over a large spectral range (**Figure**

2.5b) [85] and the size-dependent band gap energy of QDs can be calculated using the Brus equation [87]:

$$\Delta E_{\mathrm{g}} = E_{\mathrm{g}}^{bulk} + \frac{h^2}{2L^2}\left(\frac{1}{m_{\mathrm{e}}{}^*} + \frac{1}{m_{\mathrm{h}}{}^*}\right), \quad (7)$$

where E_g^{bulk} is the bulk semiconductor band gap energy, and $m_{\mathrm{e}}{}^*$ and $m_{\mathrm{h}}{}^*$ are effective electron and hole mass, respectively.

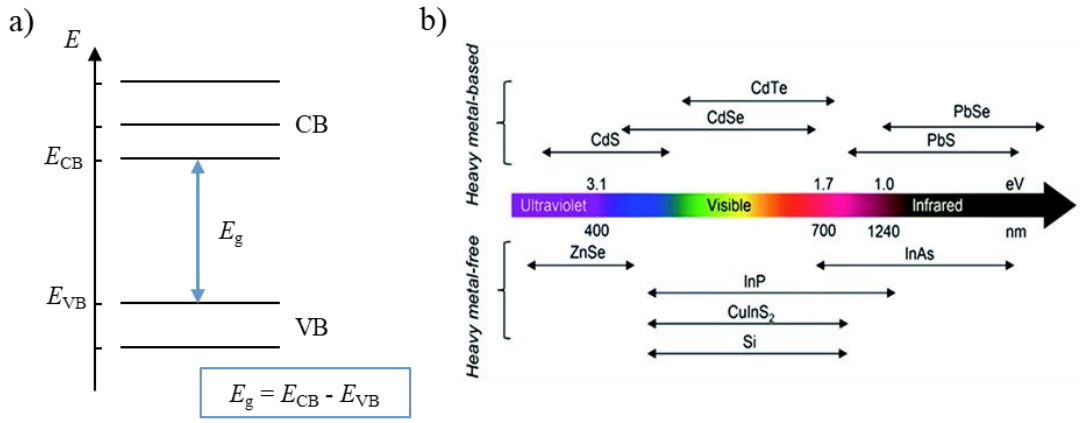


Figure 2.5. a) Diagram of the band structure of a colloidal QD. **b)** Diagram showing the spectral range over which the band gap energy of colloidal QDs with different sizes can be tuned (reproduced from reference [88]) .

Colloidal QDs can also be adopted for deposition via solution processing techniques [18,19]. CdS, CdSe, and PbS QDs are among the most commonly used QDs for optoelectronics due to their narrow emission lines, high PL QY, and colloidal stability [88,89]. Less toxic, heavy metal free QD materials have also been explored including ZnSe, ZnO, InP, and InAs QDs (**Figure 2.5b**) with improved biocompatibility [89].

More recently, perovskite NCs were synthesised in colloidal solution [90]. Perovskites encompass a wide range of materials that have a crystalline structure in the form of ABX_3 (**Figure 2.6a**), where A^+ is a monovalent cation, usually Cs^+, Rb^+, MA^+ ($CH_3NH_3^+$), FA^+ ($HC(NH_2)_2^+$), or a mixture. B^{2+} is a divalent cation, typically divalent

metals such as Pb^{2+}, Sn^{2+}, Ge^{2+}, or a mixture, and X_3 are monovalent anions, normally halides such as I^-, Br^-, Cl^-, or a mixture [91]. Perovskite nanoparticles were produced with different compositions and sizes. 2D and 3D perovskites were also grown to for larger band gap energies and enhanced stability [92].

Hybrid organic-inorganic metal halide perovskite NPs, such as $MAPbX_3$ (where X = Cl, Br, I, or mixed) have optical emission between 530 and 460 nm, depending on NP size [93] with narrow emission linewidths of ~ 20 nm [94]. However, poor stability under ambient conditions limits their shelf life to a few days [12,95]. All-inorganic lead halide perovskite NCs, $CsPbX_3$ (where X = Cl, Br, I, or mixed) are a promising alternative with greater stability and shelf-life up to months [96]. $CsPbX_3$ NCs have tuneable optical properties, near-unity PL QY of over 90%, and narrow emission line widths (15-50 nm) (**Figure 2.6b**) [6,97]. The optical properties of these NCs are tuneable across the UV-Vis wavelength range by changing their size, shape, or composition, which can be achieved by substituting their halide atoms between Cl, Br, I, and mixtures of the three (**Figure 2.6c**) [98]. $CsPbX_3$ NCs also display a high tolerance to defects, meaning defect states in the NCs usually have a low density and are localised outside of the band gap; hence the optical properties of the NCs are largely unaffected. This is because the size of these NCs is larger than their exciton Bohr radius, making their band structure more 'bulk-like' [99,100]. Surface states on the NCs are passivated with organic capping ligands to make the NCs soluble, as shown in **Figure 2.6a** [96].

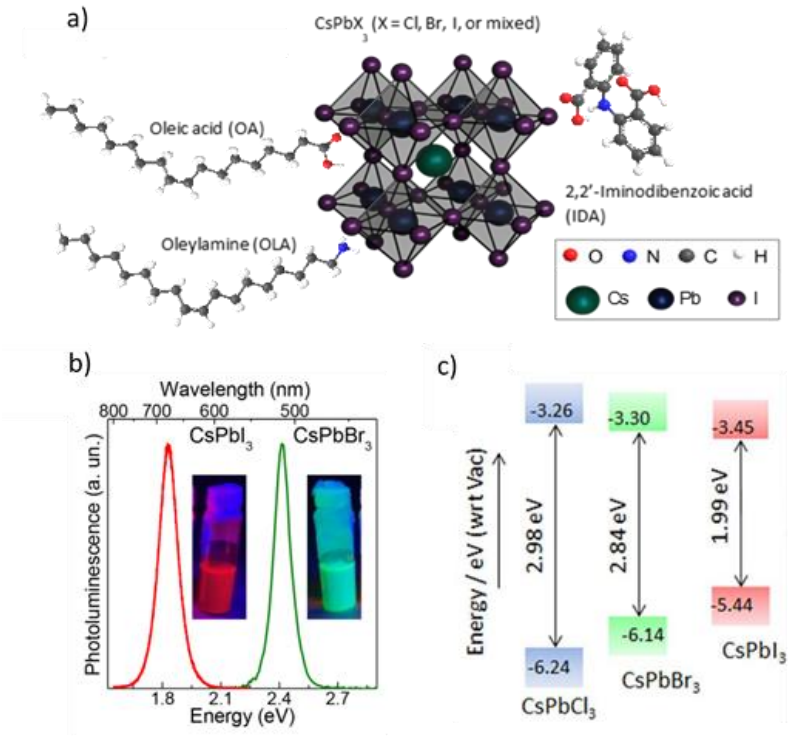


Figure 2.6. a) Composition of a single $CsPbI_3$ perovskite NC capped with organic capping ligands and **b)** photoluminescence (PL) spectra of $CsPbI_3$ and $CsPbBr_3$. Inset: optical images of the NCs under excitation with an excitation wavelength of λ_{ex} = 365 nm light (a and b reproduced from reference [96]). **c)** Band energy diagrams of $CsPbCl_3$, $CsPbBr_3$, and $CsPbI_3$ demonstrating the band gap tunability of perovskite NCs by changing composition. (Reproduced from reference [98]).

Despite their promising properties, the integration of all-inorganic lead halide NCs into devices so far has been slowed by limited stability and shelf-life [101]. For example, cubic phase $CsPbI_3$ NCs tend to spontaneously convert to their orthorhombic yellow phase when exposed to light, oxygen, humidity, or high temperatures which leads to a loss of the desired optoelectronic properties such as reduced PL QY [101].

To improve perovskite NC stability, the NCs were capped with long chain polymer polyvinylpyrrolidone (PVP) [102], carnauba wax [103], and $PbBr_2$-adlayers [104], which provide stronger binding to the NC surface, hence improving stability. Another

approach to enhance NC stability is the formation of core/shell structures. Synthesis of $MAPbBr_3/SiO_2$ [105] and $FAPbBr_3/CsPbBr_3$ [106] were reported and the shell-capped NCs had enhanced shelf life and environmental stability. Post synthesis ligand replacement of oleic acid ligands with iminodibenzoic acid was also shown to improve shelf life by up to 2 months [96] and in-situ growth of $CsPbI_3$ NCs on the surface of rGO improved stability and charge transfer properties of the NCs [101]. Another method for improved perovskite NC stability is via doping [107] which improved the photoactive and optical phase stability of $CsPbX_3$ NCs using Mn^{2+} [108] and Sn^{2+} [109] cations.

Researchers have reported a variety of different approaches for improving perovskite stability and shelf life. Because of this, perovskite optoelectronic devices have rapidly improved in recent years and are emerging as a competitor to traditional Si-based devices [110].

Colloidal graphene quantum dots (GQDs) have been considered as an alternative QD material due to their excellent environmental stability of > 6 months [111]. They consist of single to few layer graphene sheets with a size of < 10 nm, which is achieved through the introduction of defects and functional groups to cap the small graphene sheets (**Figure 2.7a**) [112,113]. Not only do the GQDs maintain many of the properties derived from SLG, such as excellent biocompatibility but also display new properties, for example, they have a band gap and relatively high PL QY (up to 28% [114]). The band gap of GQDs is highly tuneable by changing their size and surface chemistry [115] (**Figure 2.7b**); fluorescence has been demonstrated in the IR [116], visible [117], and UV [118] regions of the electromagnetic spectrum.

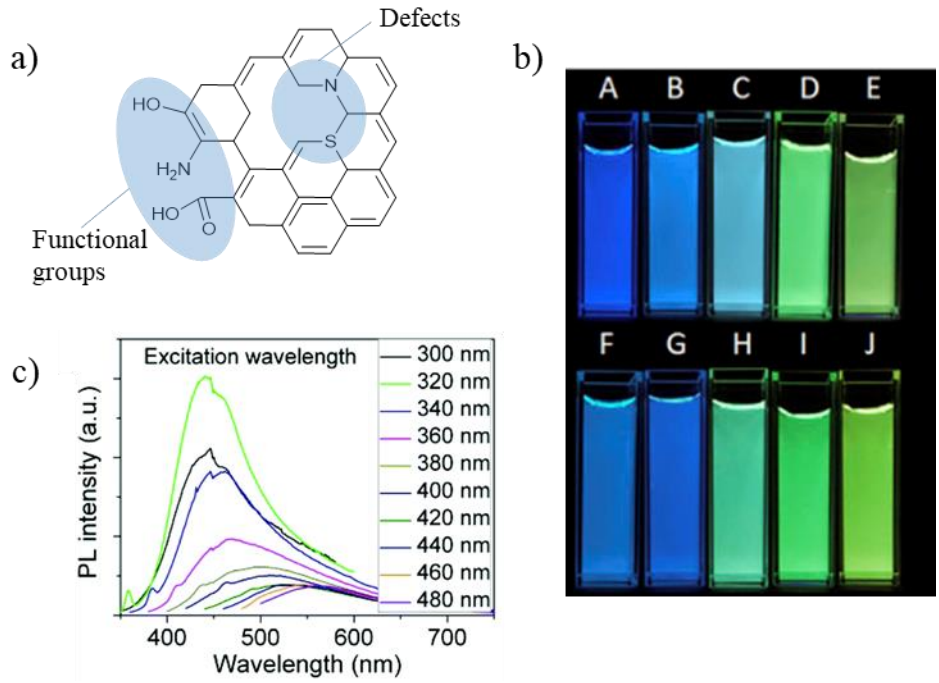


Figure 2.7. a) Example composition of GQD with defects/dopants and functional groups highlighted**. b)** Optical images of different n-doped GQDs suspensions, with bright fluorescence under λ_{ex} = 360 nm excitation (reproduced from reference [117]). **c)** Representative PL spectra of rGO under different excitation wavelengths (reproduced from reference [119]).

Interestingly, the excitation wavelength λ_{ex} affects the PL of GQDs (**Figure 2.7c**) [119,120]. As the excitation wavelength is increased from 300 to 500 nm, the PL emission peak increases from 400 to 600 nm. The excitation dependent PL in GQDs makes them an attractive material for applications that require fluorescence emission tuneable by external triggers. Different models were proposed to explain this phenomenon considering effects of quantum confinement [121], surface traps [122], edge states [123], and electronegativity of heteroatoms [124]. However, so far, no comprehensive model exists to explain this phenomenon [120].

Stability of GQDs in solution is important, as their aggregation can lead to PL quenching due to photon reabsorption and non-radiative energy transfer [125].

Aggregation can be prevented by suspending the GQDs in polymeric matrices, such as poly(vinyl alcohol) [126], epoxy resin [127], and silica [128]. Also, the PL intensity of GQDs is sensitive to the presence of metal ions due to changes in GQD surface states [129], making them useful for a variety of chemical sensing applications [129].

GQDs have a much lower PL QY compared to $CsPbX_3$ NCs [6,97,130], however, GQD are generally made from more abundant materials and have lower toxicity [131], which makes them a promising material in bioelectronic and bioimaging applications [132]. Furthermore, GQDs have potential to extend the detection/emission range of low-dimensional optoelectronic devices deeper into the UV range due to their highly tuneable band gap.

2.3.3 Organic Materials

2.3.3.1 Conductive Polymers

Conductive polymers tend to have poorer conductivity than metallic conductors [133]. Instead, conductive polymers offer greater flexibility and stretchability, enhanced biocompatibility, and are highly suitable for solution processing techniques, such as inkjet printing [133]. Various semiconducting and near-metallic polymers have received interest in recent years including poly(3,4-ethylenedioxythiophene) polystyrene sulfonate (PEDOT:PSS) [26], polypyrrole (PPy) [134], polyaniline (PANI) [135] poly(3-hexylthiophene-2,5-diyl) (P3HT) [136], and poly(2,5-bis(3-alkylthiophen-2-yl)thieno[3,2-b]-thiophene) (PBTTT) [137]. Among these, PEDOT:PSS is the most promising due to its high conductivity (up to 1700 S/cm [138]), stability, and its ability to form aqueous suspensions [139].

PEDOT:PSS incorporates two ionomers: the conducting conjugated poly(3,4-ethylene dioxythiophene) (PEDOT) with positive charges and the soluble insulating polystyrene sulfonate (PSS) with negative charges (**Figure 2.8**) [139]. PSS facilitates the dispersion of PEDOT in water and allows the PEDOT to maintain a stable configuration via Coulomb attractions [140,141]. When PEDOT:PSS is dispersed in water it forms micelles due to Coulomb interactions which consist of a PEDOT-rich core and a PSS shell. Each grain is composed of tangled PSS chains with many PEDOT segments attached [141]. π-orbital interactions between PEDOT chains in the core region ensure the polymer chains are relatively well-stacked. Charge transport is fast along the PEDOT chains and moderate between the chains where π-stacking occurs [140].

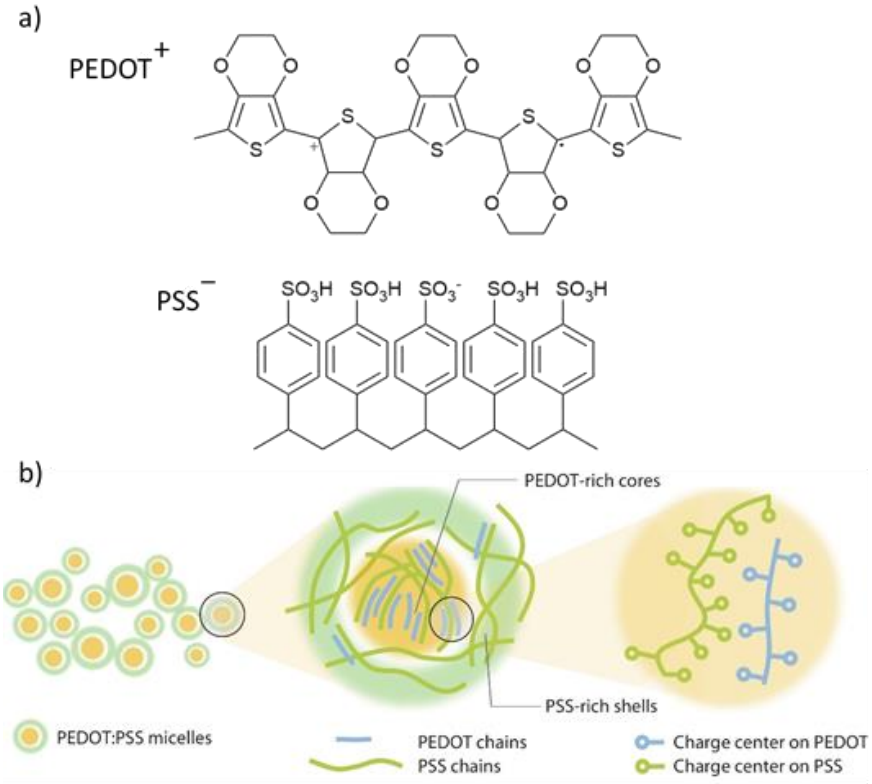


Figure 2.8. a) Chemical structure of $PEDOT^+$ and PSS^-. **b)** The hypothesised morphology of individual PEDOT:PSS micelles consisting of a PEDOT rich core and a PSS shell (Reproduced from reference [142]).

Various processing methods have been shown to improve the electrical conductivity of PEDOT:PSS by removing excess PSS to induce conformational changes in the PEDOT chain, hence optimising the conduction pathways [140,141]. Pristine PEDOT:PSS films displayed an electrical conductivity of 1 S/cm [140]. The addition of acids, such as perfluorooctane sulfonic acid, increased the conductivity up to 1700 S/cm [138]. Similarly, treatment with salts [143] and polar solvents (typically dimethylsulfoxide (DMSO)) [144] have increased PEDOT:PSS conductivity up to 1400 S/cm [144]. The electrical conductivity of PEDOT:PSS inks can therefore be precisely tuned by ink formulation and post processing conditions. Owing to this tuneable electrical conductivity, as well as optical transparency over the visible range and high flexibility [139], PEDOT:PSS is commonly used in LEDs and other optoelectronic devices, as a hole transport material [139,145,146].

2.3.3.2 Organic Dielectric Materials

Organic dielectric materials are also important for electronic devices, they are often used as a gate material or as a capping agent to protect other materials from ambient conditions and possess improved flexibility and biocompatibility compared to inorganic dielectrics [147,148]. Materials with a high dielectric constant are known to improve the energy density of capacitors and reduce the driving voltage of transistors, hence, researchers search for high dielectric polymers for improved performances in flexible electronic devices [148]. Among the most commonly used dielectric polymers are poly-4-vinylphenol [147], tripropylene glycol diacrylate (TPGDA) [149], poly(methyl methacrylate) (PMMA) [150], and polyimide [151], all of which have been deposited by solution processing techniques. Researchers have also combined

dielectric polymers with ceramics, such as $BaTiO_3$ [152] or $Ba_{0.6}Sr_{0.4}TiO_3$ [153], to create composite materials with improved dielectric properties.

2.3.3.3 Organic Charge Injection Materials

Organic charge injection materials are commonly used in many optoelectronic devices, such as LEDs, where their role is to inject either holes or electrons into the optically active material, where they recombine and emit a photon [154]. A good charge injection material must have favourable band alignment with the optically active material and also have a high mobility for the charge carrier type that requires injection and a low mobility for the other carrier type. This enables efficient injection of one carrier type into the optically active layer while blocking the other carrier type from escaping, which increases the chance of recombination and thus increases device efficiency [154].

Commonly used organic hole injection layers for LEDs include 1,1-bis[(di-4-tolylamino)phenyl]cyclohexane (TAPC) [155], N,N'-bis(I)naphthyl)-N,N'-diphenyl-1,1'-biphenyl-4,4'-diamine (NPB) [156], 4,4',4''-tris((3-methylphenyl)phenyl amino)triphenylamine (m-MTDATA) [157], and Poly(*N*,*N*′-diphenylbenzidine diphenylether) (poly-TPD) [158]. Poly-TPD (**Figure 2.9a**) offers favourable band alignment for perovskite LEDs [159,160] and also displays a hole mobility of $1x10^{-4}$ $cm^2/V{\cdot}s$ [161] and hydrophobicity which can provide protection from moisture to neighbouring perovskite layers [162]. Poly-TPD is also solution processable; layers have been deposited in LEDs and solar cells by spin coating using chlorobenzene as a solvent and it require relatively low post-processing temperatures between 100 °C and 140 °C [106,158,163].

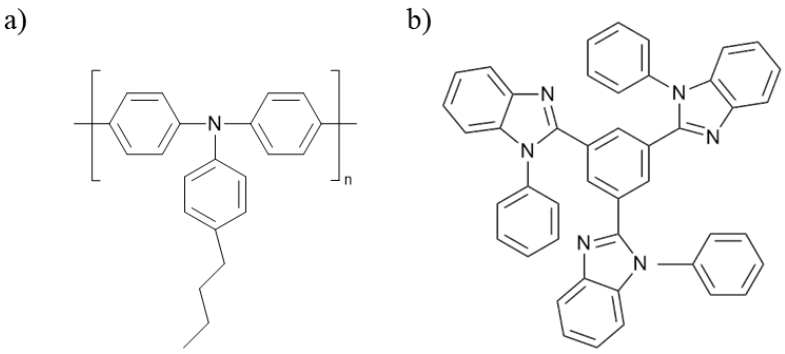


Figure 2.9. Chemical structures of **a)** poly-TPD and **b)** TPBI

Commonly used organic electron injection layers for LEDs include 4-biphenyloxolate aluminium(III) bis(2-methyl-8-quinolinato)-4-phenylphenolate (BAlq) [164], tris(8-quinolinolato) aluminum (Alq3) [165], 2,9-dimethyl-4,7-diphenyl-1,10-phenanthroline (BCP) [166], and 2,2',2''-(1,3,5-benzinetriyl)-tris(1-phenyl-1-H-benzimidazole) (TPBI) [146,167] (**Figure 2.9b**). TPBI is used in perovskite LEDs due to its favourable band alignment, high optical transmittance and thermal stability [168], and electron mobility of up to $8x10^{-5}$ $cm^2V{\cdot}s$ [169]. Furthermore, it has been shown to have excellent hole blocking capabilities and reduce contact-based issues when used as an electron transport layer in LED devices [168]. Other applications of TPBI have also been explored in optoelectronic devices, for example as a buffer layer in organic solar cells [170] and as a host for emissive layers in LEDs [171]. TPBI films are most often deposited by thermal evaporation [146,172], but spin coated films have been demonstrated using solutions of chloroform and chlorobenzene [167,173].

2.4 FORMULATION OF MATERIALS FOR INKJET DEPOSITION AND PROPERTIES OF PRINTED MATERIALS

For inkjet printing of electronics, the availability of ink formulations for different materials presents challenges. To deposit a uniform film of a material via inkjet printing, there are several criteria that an ink formulation must meet, including suitable rheology, concentration, and drying behaviour (**Chapter 2.2**). A number of different strategies have been established for developing formulations of functional materials, a few key examples of which are discussed below.

Typically to formulate a functional material ink, material is dispersed or dissolved in a solvent or mixture of solvents. The rheology of the solvents is optimised to achieve a *Z* value between 1 and 10, for desirable jetting, and the solvent boiling points are optimised for favourable drying behaviour to achieve uniform films. An ink may also contain stabilising agents to prevent particle aggregation and improve solubility. Viscosity or surface tension modifiers can be added to further improve an inks *Z* number, and additives which may have a desirable effect on the printed material can be added, such as an encapsulation agent to improve stability. Finally, printed films are often treated or annealed to remove solvents and additive, and modify the properties of the printed material as required.

2.4.1 2D Material Inks

Graphene and other 2D material inks, consist of a suspension of 2D flakes ($\lesssim 1\ \mu m^2$) produced using LPE method [11,29,174]. A commercially available graphene ink was formulated with a mixture of terpineol and cyclohexanone, as solvents, and contains graphene flakes with an average lateral size of ~ 50 nm [11,63,175]. Ethyl cellulose

(EC) was added to the ink to increase viscosity and improve sheet resistance, R_s of inkjet printed graphene (iGr) films after thermal annealing at 250 °C, where R_s ~ 100 Ω/sq for 10 printed layers [11,63,175]. Graphene inks have also been formulated by dispersing graphene flakes in a single solvent such as NMP [53] or ethanol [63].

Recently, water-based graphene inks have been formulated for improved biocompatibility and with larger flake sizes to preserve the unique properties of the SLG [176,177]. Graphene flakes with a lateral size of ~ 200 nm were formulated into water-based inks for inkjet printing using propylene glycol as a co-solvent, pyrene sulfonic acid derivatives as stabilising agents, and Triton x-100, as a surface tension modifier (**Figure 2.10a**) [176]. The sheet resistance of printed films was improved by up to 100× after thermal annealing at 300 °C, achieving sheet resistance R_s < 1 kΩ/sq for films with 40 printed layers. Majee et al. also formulated a water-based graphene ink, mostly consisting of 4-layer graphene flakes with a lateral size of ~ 160 nm made by LPE using starch as a stabilisation agent and propylene glycol as viscosity modifier (**Figure 2.10b**) [177]. Rapid photonic annealing was used to achieve flexible graphene films with R_s ~ 200 Ω/sq for 4 printed layers [177]. Water-based graphene inks with average flake thickness of 8 nm and a diameter of 490 nm with high concentrations up to ~ 10 mg/ml were formulated with sodium deoxycholate (SDC) stabilising agent [178]. After annealing at 400 °C to combust the stabilising agent in the ink, films with R_s ~ 3 Ω/sq at a thickness of 4 µm were demonstrated [178]. High performance graphene inks have been demonstrated using a variety of different approaches, however, understanding of the charge transfer between individual graphene flakes in printed films is still limited. Moreover, many of these printed graphene films require high annealing temperatures of > 200 C to achieve high conductivity [11,177,178], which limits the number of substrates and materials that the graphene can be printed

on. Further work is needed to uncover how these annealing processes work, and find alternative methods such as photonic annealing so that graphene can be printed on a wider range of materials.

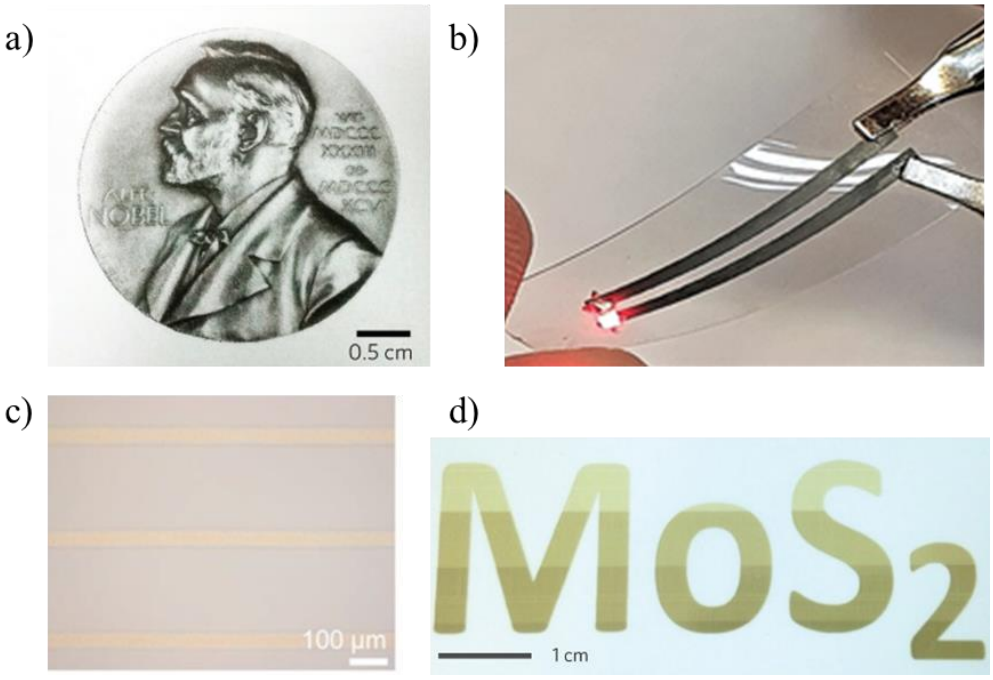


Figure 2.10. Water-based graphene inks printed **a)** on paper, in the shape of a Nobel medal (reproduced from reference [176]) and **b)** on flexible polyethylene terephthalate (PET) in a simple circuit configuration used to light an LED (reproduced from reference [177]). **c)** Printed hBN lines on glass (from reference [179]) and **d)** printed MoS_2 pattern on paper with water-based formulation (reproduced from reference [176]).

rGO films can be deposited via inkjet printing by using inks based on GO and reducing the printed films via thermal or chemical post-processing [59]. Since GO is polar, these inks can be formulated in aqueous solutions using water and other polar solvents without surfactants. He et al. demonstrated an aqueous GO ink containing ultra-large GO flakes with a mean diameter of 36 µm (produced via LPE) [59]. Despite the size being more than 50% larger than the nozzle diameter, no nozzle blocking was observed due to the highly flexible nature of the material. To achieve conductive films, GO inks

were printed on Si/SiO_2 substrates and were then reduced by heat treatment of 80 °C for 30 minutes [59]. The resulting rGO film of 30 printed layer displayed a sheet resistance of 150 Ω/sq [59]. Another method for the deposition of rGO films involves formulating inks containing rGO powder. rGO films can then be deposited via inkjet printing without the need for reduction as a post-processing step [180]. Martínez-Flores et al. prepared a rGO dispersion in isopropyl alcohol (IPA) with the use of PVP as a stabiliser [180]. The average lateral size of the dispersed rGO flakes was ~ 340 nm. It was reported that after annealing at 400 °C, rGO films with 10 printed layers on fluorine-doped tin oxide displayed optical transmittance of over 90% [180]. Printed GO and rGO films, tend to have poorer conductivity than printed graphene due to introduction of defects [181], however, the advantages of easier ink formulation (without surfactants) and less harsh post-processing condition make them a promising alternative to graphene for many applications.

Other 2D materials were also formulated for jetting including dielectric hBN and semiconducting metal chalcogenides [53,63,179,182]. hBN (**Figure 2.10c**) [179] and MoS_2 [182] inks were formulated with terpineol and cyclohexanone solvents with EC additive, as was shown for the graphene formulation in [11,63,175]. Similarly, water-based hBN, WS_2, and MoS_2 (**Figure 2.10d**) inks were demonstrated using the same graphene formulation described in [182], with propylene glycol as a co-solvent, pyrene sulfonic acid derivatives as stabilising agents, and Triton x-100 as a surface tension modifier. A water-based hBN ink was formulated for jetting which consisted of hBN powder with flakes of < 10 µm in size and carboxymethylcellulose sodium salt which acted a biocompatible stabilisation agent and rheology modifier [63]. For deposition by inkjet printing, liquid exfoliated flakes of WSe_2 were dispersed in NMP [53], WS_2

flakes were dispersed in N,N-dimethylmethanamide (DMF) [183] and MoS_2 flakes were dispersed in isopropanol (IPA) with PVP additive for optimised rheology [184].

Due to the wide range of 2D materials that have been formulated into inks and printed, 2D materials are a promising class of material for many applications in printed electronics. Moreover, the prevalence of water-based 2D inks enables their use in electronic devices for biological applications. However, there are still major challenges in understanding the charge transport systems in these materials and exploring new post-processing techniques to achieve high conductivity films without the use of high temperature annealing.

2.4.2 0D Material Inks

2.4.2.1 Conductive Nanoparticles

AgNP inks for inkjet printing are commercially available and well optimised, displaying resistivity as low as 3.3 μΩ.cm [185]. The AgNP ink from Advanced Nano Products (SilverJet DGP-40LT-15C) consists of 38.85 wt% of AgNPs dispersed in triethylene glycol monomethyl ether and other additives which modify viscosity and surface tension [186]. The ink also contains PVP, which is a commonly used stabiliser and reducing agent in the synthesis of AgNP. The ink was printed on a substrate heated to 90 °C for fast solvent evaporation and post-processing was performed by thermal annealing at 150 °C or UV sintering, to achieve a resistivity of 11 μΩ·cm [186]. Further research is ongoing and aims to formulate inks with greater AgNP content to enable the printing of films with greater conductivity [82,187]. Moreover, researchers are developing photonic sintering post-processing techniques that remove the need for high thermal annealing temperatures [188].

Commercially available CuO NP inks (Novacentrix, ICI002HV) are also well optimised, consisting of 16 % (by weight) CuO NPs, which achieved printed films with sheet resistance R_s = 335 mΩ/sq after reduction by photonic sintering [188]. CuNP inks have proved more challenging to develop as they experience oxidation under ambient conditions. To reduce oxidation and thus improve conductivity, researchers used core/shell structures consisting of copper/silver to print patterns with resistivity as low as 30 mΩ.cm [189]. Also, PVP was used to protect CuNPs from oxidation in an ink formulation consisting of ethylene glycol (EG), 2-methoxyethanol, and methyl alcohol solvent mixture; printed Cu films displayed a resistivity of ~ 11 μΩ.cm after annealing at 275 °C [190].

More recently AuNPs were adopted for inkjet printing. Researchers demonstrated a reactive inkjet printing method for deposition of AuNPs whereby the size AuNPs could be precisely controlled by changing the concentration of a gold precursor solution [79]. AuNP inks with NPs with diameter of ~ 2.5 nm were also developed for use in flexible applications by including a multifunctional thiol cohesion enhancer in the ink formulation which prevented the formation of microcracks and pores in printed films during bending [27]. The printed AuNP films displayed an electrical conductivity of ~ 10^6 S/m after sintering at 150 °C, with stable electrical properties after undergoing 1000 bending cycles and in a salt-rich phosphate-buffered saline solution, demonstrating it's potential in flexible and bioelectronics [27]. An eco-friendly AuNP ink formulation was realised using 5 – 10 nm AuNPs functionalised by poly(ethylene glycol) (PEG) ligands in a solvent mixture of water and ethanol [191]. Printed films with 4 layers displayed a conductivity of 1 x 10^7 S/m and high surface reactivity, close to polycrystalline bulk-gold [191].

Metal NPs are the most developed low-D material for inkjet printing and are already being used in commercial applications [73,192]. However, research is still ongoing to improve flexibility, biocompatibility, stability, and post-processing to improve performance and further expand their applications.

2.4.2.2 Semiconducting Nanoparticles

Several colloidal semiconducting QDs have been formulated for printing, with its inks typically only consisting of an optimised mixture of organic solvents [193–198]. For example, PbS QDs were printed in a solvent mixture of hexane and terpineol (**Figure 2.11a**) [193], ZnO NCs were printed in a solvent mixture of ethanol, ethylene glycol, and glycerol [194], HgTe QDs were printed in tetradecane [19], and Si QDs were printed in mestilylene [195]. CdSe/ZnS core/shell QDs were printed using dichlorobenzene and toluene solvents with an organic monolayer included to enhance the QDs ability to form a solution (**Figure 2.11b**) [196]. While jetting of these colloidal QDs has proven relatively simple, there is still further work required to optimise formulations to achieve the very thin uniform films that are required for many optoelectronic device applications, and also to ensure the QD optical properties are maintained after deposition.

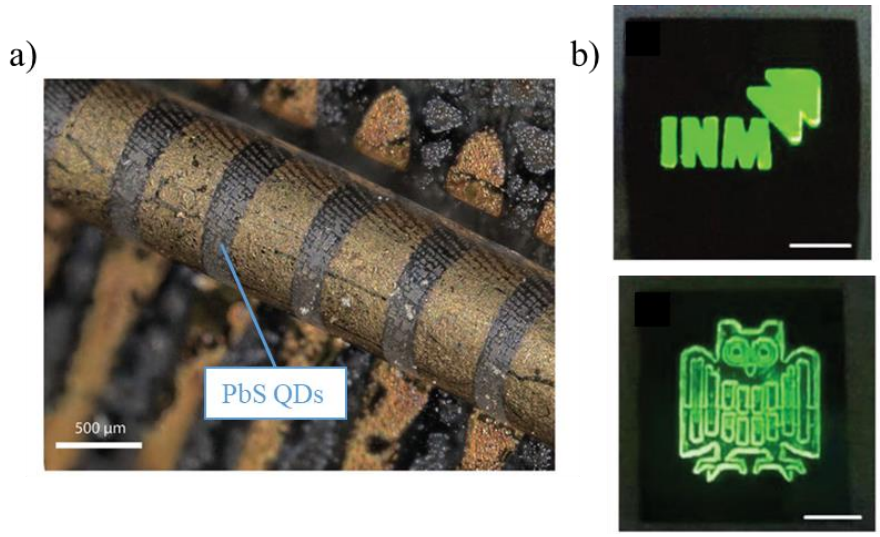


Figure 2.11. a) An optical image of a PbS QD film printed onto Au on a curved surface (reproduced from reference [193]). **b)** Optical images of inkjet printed patterns of CdSe-ZnS core-shell QDs under illumination (reproduced from reference [196]).

Researchers have printed perovskite materials by depositing perovskite pre-cursor solutions and forming the perovskite NCs in-situ [12,197,199]. Gu et al. developed inkjet printing of $MAPbI_3$, $MA_3Sb_2I_9$, and $(BA)_2PbBr_4$ perovskites by printing perovskite precursors in DMSO solvent and introducing a polyethylene oxide (PEO) layer during printing to help control nucleation and crystal growth [12]. $MAPbI_3$ perovskites were also printed using an ink consisting of perovskite precursors and the solvents DMSO and γ-butyrolactone (GBL) with a vacuum assisted thermal annealing step to improve film uniformity [200]. $Cs_{0.05}MA_{0.14}FA_{0.81}PbI_{2.55}Br_{0.45}$ perovskites films were printed using the solvents DMF and NMP which slows the crystallisation rate of the printed liquid film to form high quality perovskite layers after annealing [197]. Shi et al. developed an in-situ printing strategy for $CsPbBr_3$ perovskite NCs whereby perovskite precursor inks were deposited onto various polymers such as poly(methyl methacrylate) (PMMA) and polyvinyl chloride that were partially

dissolved during the inks drying process [198]. This caused perovskite NCs to form inside the polymeric matrix, hence improving the NCs stability. The printed films displayed PL quantum yields up to 80 % and were composed of micro disk arrays that formed during the drying process (**Figure 2.12**). Similarly, Liu et al. demonstrated in-situ printing of perovskite NCs and used the long chain polymer additive PVP which increased ink viscosity and controlled the morphology and size distribution of the synthesised NCs, with films achieving PL QY up to 64.3% [102].

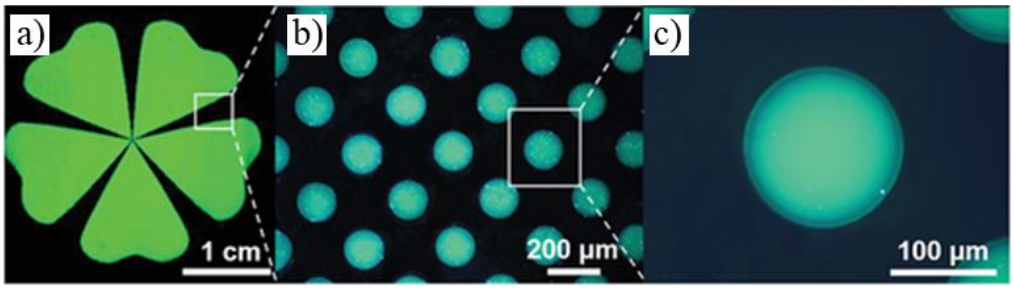


Figure 2.12. $CsPbBr_3$ NCs formed by inkjet printed precursor solution onto polymeric substrate showing **a)** printed pattern and **b)**,**c)** individual micro disks formed during printing (reproduced from reference [198]).

Printing a solution containing a dispersion of all-inorganic $CsPbX_3$ (X = I, Br, Cl, or mixed) perovskite NCs is a simpler deposition strategy, which can generally be performed on a wider range of substrates. The formulation of all-inorganic perovskite NC inks is still in its infancy; they have only been inkjet printed a handful of times [40,101,201]. Gao et al. developed a printable $CsPbBr_3$ ink by using a mixture of high boiling dodecane with low-boiling point toluene as a solvent (60:40 Vol%) to eliminate the coffee ring effect [40]. Zhang et al. grew $CsPbI_3$ NCs in-situ onto rGO and then printed these 0D/2D heterostructures using a mixture of organic solvents and the rGO was shown to improve charge transport properties [106]. Researchers also printed a $CsPbBr_3$ ink which used oleyamine and hexylphosphonic acid ligands in combination

with a liquid crystal monomer to achieve thick printed films which are required for colour conversion applications [199].

All-inorganic lead halide perovskite NCs have also been printed using other additive manufacturing methods such as stereolithography for large scale 3D perovskite structures with the inclusion of α-tocopherol (α-TCP, vitamin E) for improved perovskite photophysical properties and stability [28].

While printing of perovskites has seen significant progress in recent years, there is still need for all-inorganic $CsPbX_3$ (X = I, Br, Cl, or mixed) perovskite NC ink formulations that are optimised to achieve the thin films required for optoelectronic devices, such as LEDs, rather than the thick colour converter films developed previously [199]. Moreover, the ink formulation should be printable on Si and compatible with Si-based electronics, rather than only being printable on particular polymers [198], and the performance of the NCs should be maintained after the formulation and inkjet deposition processes, such that high performance optoelectronic devices can be printed

GQDs are a new material, and their deposition via inkjet printing has only been achieved a couple of times [202,203]. Researchers formulated GQD inks for inkjet printing by dispersing them in a single solvent: dimethylformamide ($HCON(CH_3)_2$) [202] or tris(hydroxymethyl)aminomethane hydrochloride (Tris-HCl, pH 7.4) [203]. However, in both cases the solvents used were toxic which is not ideal for biocompatibility, and the GQD inks do not contain polymers to suspend the GQDs in a polymeric matrix to prevent aggregation and PL quenching.

Despite a body of work, the formulation of 0D materials into printable inks remains challenging, with limited strategies that are transferable across different 0D materials or onto different substrates.

2.4.3 Organic Material Inks

A wide variety of conductive polymers have been formulated for inkjet printing [26,134–137]. PPy was printed with water and ethanol solvents with the addition of gemini acid and a mixed $FeCl_3$/FepTS oxidant to improve polymer dispersion. Also, a novel gemini surfactant 9BA-4-9BA was employed which improved conductivity of the printed films up to 0.69 S/cm [134]. Ppy films were also printed on fabrics using a reactive inkjet printing technique with direct freeze drying of inks, whereby, the PPy was synthetized in situ by oxidative polymerization of pyrrole using ammonium peroxydisulfate (APS) in partially frozen state [204]. Printed PPy films with R_s = 790 Ω/sq were achieved on polypropylene fabric (**Figure 2.13a**) [204]. Researchers have also printed PANI with the addition of graphene nanoplatlets which enabled the deposition of thin and homogeneous films with high conductivity up to 3.67 S/cm for 5 printed layers [205]. The ink was water-based but viscosity and surface tension were controlled by the PANI and a sodium dodecylbenzenesulfonate surfactant, respectively [205]. Inkjet printing has also been achieved with conductive polymer P3HT [136], PBTTT [137], and PEDOT:PSS. [26].

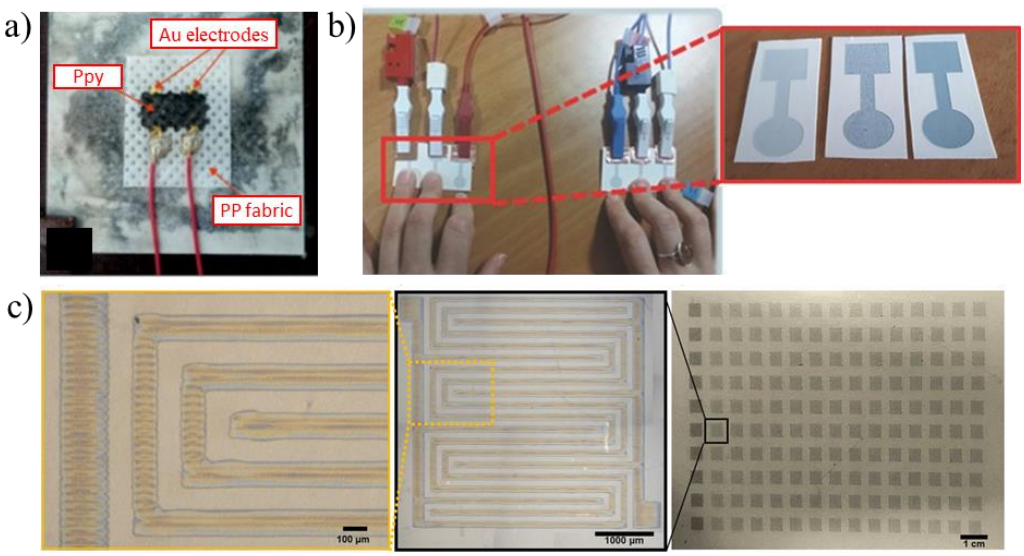


Figure 2.13. a) Inkjet printed Ppy on fabric (reproduced from reference [204]). **b)** Printed PEDOT:PSS electrode pads on paper (reproduced from reference [206]) **c)** Printed array of serpentine electrodes on flexible PEN substrate (reproduced from reference [26]).

PEDOT:PSS inks have been widely studied and developed for deposition via inkjet printing [26,207–209]. PEDOT:PSS inks that include DMSO as a co-solvent were shown to effectively eliminate the coffee ring effect to achieve more uniform films [207]. Researchers have also optimised the printing temperature and drop spacing to fabricate homogeneous printed PEDOT:PSS films with a conductivity of 219 S/cm [145]. For lightweight electrode applications Bihar et al. [206,208] developed PEDOT:PSS inks with the cross-linking agent glycidoxypropyltrimethoxysilane (GOPS) which prevented shunts in the printed films to ensure precise patterning of subsequently printed layer and printed films showed good biocompatibility and a high conductivity of 295 S/cm (**Figure 2.13b**) [208]. Researchers have also formulated highly optimised PEDOT:PSS inks for deposition over large areas (> 30 cm) using the green solvents dihydrolevoglucosenone (cyrene) and glycerol carbonate (GC) [26]. The printed PEDOT:PSS films displayed high conductivity up to 218 S/cm and

excellent uniformity, which was achieved using an 'offset' inkjet printing deposition method (**Figure 2.13c**) [26]. Conductive polymers, especially PEDOT:PSS, have been highly optimised for inkjet printing. With tuneable work functions and high biocompatibility, they play an important role in printed electronics as an alternative to metal NPs, despite their much lower conductivities. Further research is required, however, to reduce their solvent toxicity, improve environmental stability, and reduce film thickness while maintaining high uniformity.

Dielectric polymers were also printed [147,149–151], however a major challenge for these materials is the formation of pin-holes during the printing process which can ruin device performance [147]. One strategy for printing dielectric polymers is by formulating and jetting inks based on photo-initiated reactive monomers such as TPGDA, followed by a UV curing post-processing step to initiate polymerisation and form the dielectric layer [149]. Other dielectric polymers can be diluted in solvents and printed normally such as poly-4-vinylphenol [147]. Researchers optimised the printing parameters of poly-4-vinylphenol inks to enhance the coffee ring effect to achieve very thin films (< 200 nm) for capacitor applications [147]. High uniformity PMMA films were printed using a mixture of DMSO and anisole solvents and pin-holes were avoided by drying at 120 °C for 40 minutes immediately after printing [150]. The performance of PMMA as a dielectric layer was improved by the addition of the ceramic material $Ba_{0.6}Sr_{0.4}TiO_3$ [150]. This composite material was printed using butyldiglycol as the solvent and printed films demonstrated dielectric constant up to 55. Printing of dielectric polymers is a mature area of study and they are a promising alternative to 2D dielectric materials such as hBN, especially for flexible and bioelectronics applications. However, further optimisation of inks and the printing

process is required to eliminate the formation of pin-holes and improve uniformity in printed dielectric films.

Charge injection polymers have also been formulated for inkjet printing. Giuri et al. achieved a printable poly-TPD ink by dissolving the polymer in chlorobenzene [210]. After printing the film was treated with UV and annealed in air at 140 °C. Similarly, the hole injection layer NPB was printed on top of a PEDOT:PSS layer using a solvent mixture of tetralin and indane [211]. These solvents were chosen as they do not dissolve the PEDOT:PSS layer below and therefore reduces intermixing. Intermixing of layers is one of the main challenges of printed heterostructures (see **Chapter 2.5.1**), and this is especially true for charge injection layers which generally need to be very thin (~ 50 nm) for device operation [212,213]. These challenges are why many of the most common charge injection materials, such a TPBI, have not yet formulated for inkjet printing.

Overall there is a large body of work developing conducting and dielectric polymers for inkjet printing, however, the formulation of charge injection polymers and their integration into heterostructures remains challenging.

2.5 INKJET PRINTED HETEROSTRUCTURES AND DEVICES

Inkjet printing has been used in a variety of fields, from tissue engineering [22] to drug delivery [214]. Importantly for this project, inkjet printing offers a cost-efficient and accurate solution for material deposition for electronic components and has thus been used to manufacture a large range of electronic and optoelectronic devices, such as transistors [11,215], sensors [216–219], capacitors [220–222], photodetectors [201,223], LEDs [224–226], and solar cells [208,227].

2.5.1 Heterostructures

Heterostructures are important components of many electronic and optoelectronic devices, including those made via inkjet printing. A printed vertical heterostructure is fabricated by deposition of two or more different materials directly on top of one another (**Figure 2.14a**), and with a wide range of conducting, semiconducting, and dielectric materials available, printed heterostructure designs can be tailored for particular device applications such as transistors [53] or LEDs [228]. Compared to other manufacturing techniques, deposition of heterostructures via inkjet printing provides unique challenges and opportunities.

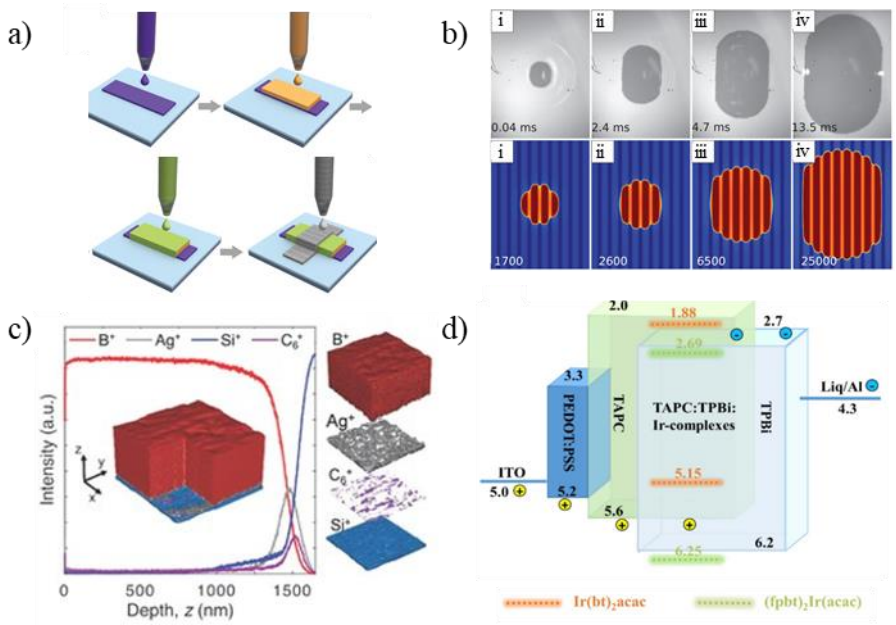


Figure 2.14. a) Diagram representing the inkjet printing process of an exemplar heterostructure (reproduced from reference [228]). **b)** Optical images (top row) and simulations (bottom row) showing the spreading of a water droplet over time across bands of hydrophilic (light blue) and hydrophobic (dark blue) materials (reproduced from reference [229]). **c)** 3D mapping and chemical composition of fully printed graphene/hBN FET displaying inhomogeneity in printed layers (reproduced from reference [11]). **d)** Device structure and energy level diagram of printed organic LED with blurred interfaces (reproduced from reference [230]).

Heterostructures for electronic/optoelectronic applications usually require high uniformity in each layer. Roughness and non-uniformity in just a single layer can reduce device performance [231]. Achieving high control of uniformity and film thickness in inkjet printing remains challenging, especially for the very thin layers (< 50 nm), which are required in devices such as LEDs [212,213]. To address this challenge, inks are formulated specifically for printing onto the previous material in the heterostructures, to ensure favourable wetting and reduction of the coffee ring effect. Zhao et al. achieved this by adding the polymer PEO to adjacent perovskite and PEDOT:PSS layers in an LED heterostructure [228]. However, this is a time-

consuming approach as it requires the development of many inks for a single material in different heterostructures. Different printing strategies have also been shown to reduce surface roughness. Printing each subsequent layer of a material with an offset equal to half the drop spacing was demonstrated to reduce surface roughness of PEDOT:PSS films [26].This resulted in unevenness caused by the coffee ring effect, to be filled in by subsequent layers, hence, decreasing film roughness [26]. In contrast, for device applications that require high interfacial surface areas [232], such as printed batteries [233], the large roughness that can be obtained via inkjet printing can be beneficial to device performance.

For more complex heterostructure designs, where a single layer is printed over several different materials (the bottom right panel of **Figure 2.14a** for example), wetting phenomena can lead to reduced printing resolution and further layer non-uniformity [229,234]. An example of this is shown in **Figure 2.14b**, where a water droplet atop alternating bands of hydrophobic and hydrophilic material spreads preferentially along one direction [229]. To account for such effects, the architecture and ink formulations used for inkjet printed heterostructures must be planned carefully to maintain high uniformity and resolution.

Another common challenge is intermixing between printed layers due to dissolution of previous layers. This can lead to short-circuiting or reduced device performance in vertical heterostructures [235]. Depth profiling and 3D mapping via time-of-flight secondary ion mass spectroscopy (ToF-SIMS) on a hBN/AgNP/graphene heterostructure revealed that the printed graphene layer was non-homogeneous and large intermixing of layers was present due to the inkjet printing deposition method (**Figure 2.14c**) [11]. To reduce intermixing between printed layers, orthogonal solvent systems were used, where the solvents in each layer are selected such that they are not

compatible with previous layers, thus reducing redissolution and intermixing [236]. While this is the simplest approach to reduce intermixing, again it complicates the ink formulation process, and requires a single ink to be reformulated for different applications.

Addition of cross-linking agents were also shown to make layers in a heterostructure insoluble to prevent intermixing [237]. For example, thermally cross-linkable perfluorocyclobutane [238] and vinyl benzyl [239] -based cross-linking agents were used to functionalised hole transport layers of organic LEDs. While this is a promising approach, the requirement for extra post-processing steps to initiate cross-linking can affect device performance and further complicate the fabrication process. Alternatively, some heterostructures include a buffer layer between functional layers to provide protection from intermixing [228]. Blocking layers, e.g. polyethyleneimine between a perovskite emissive layer and a Ag nanowires (AgNWs) electrode in an LED, were shown to prevent intermixing, while also lowering the barrier for electron injection [228]. However, this approaches is only applicable to devices where a blocking layer will not hinder device performance. To date, intermixing is not fully understood or controlled and there are no general solutions to prevent it, rather, it is a problem that has been tackled on a case-by-case basis. Further studies are needed to better understand how and when the process occurs with different materials, and investigate how different printing strategies effect intermixing.

There are applications where intermixing offers benefits by generating blurred interfaces, employed in printed TAPC:TPBi:Ir-complexes as both the hole transport layer and emissive layer in an organic LED [230] (**Figure 2.14d**). The inclusion of the blurred interface was shown to facilitate exciton formation and improve charge balance in the emissive layer [230].

Overall, the issues of uniformity, wetting, and intermixing are currently major challenges that hinder the performance and progress of inkjet printed heterostructures. However, ongoing research has made large strides towards controlling printed layers and interfaces in heterostructures, and exploiting the unique properties of printed heterostructures for specific applications. Future work should look to better understand inkjet printed heterostructures and develop strategies to prevent intermixing.

2.5.2 Electronic Devices

Inkjet printing of metal NPs enables huge design freedom and flexibility for printed electronic components and they have been widely used as electrodes and conductive pathways in electrical devices [11,63,240] and printed circuit boards (PCB) [241,242]. Despite this, the conductivity of printed metal NPs is far inferior to those made by traditional manufacturing techniques. Trindade et al. showed that the organic stabiliser PVP used in AgNP inks left residues that accumulated at the vertical interface between printed layers which resulted in an anisotropic conductivity decrease in the printed AgNP films [186]. This demonstrates the need for further optimisation and understanding of the formulation and post-processing of printed metal NP inks to remove such residues which can improve conductivity and adhesion strength [243]. The resolution of inkjet printed metal NPs (10s of microns) is also far inferior to the traditional manufacturing methods which are used to deposit the conductive pathways on chips and circuit boards [244]. Due to this inferior resolution, inkjet PCBs tend to be larger than traditional circuit boards, however, they can be made with complex geometries that are highly optimised for particular applications [244]. Smaller resolutions (< 1 μm) have been achieved in AM by integrating metal NPs in the two-photon polymerisation process [245]. Inkjet printing on the other hand, has achieved

free-standing vertical AgNP interconnects with heights of ~ 1 cm (**Figure 2.15a**) [192], which are very challenging to make by other manufacturing techniques and could lead to the fabrication of inkjet PCBs and antennas with more complex geometries.

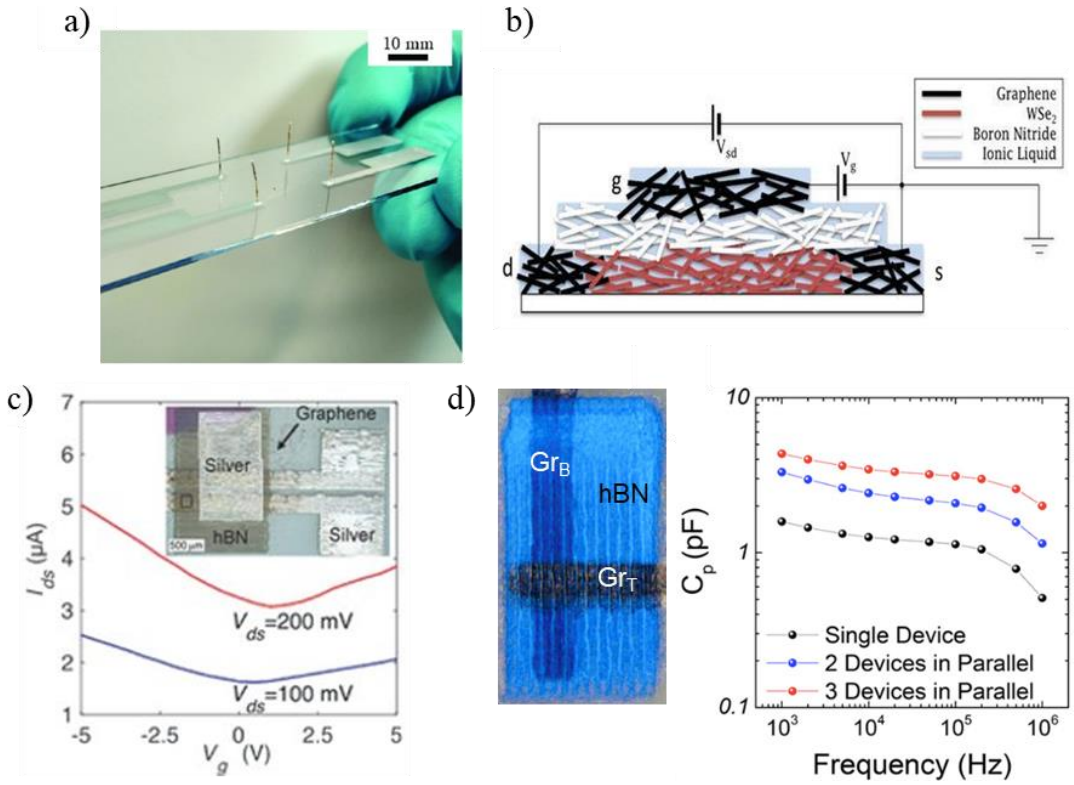


Figure 2.15. a) Optical image of inkjet printed freestanding silver pillars on glass substrate (reproduced from reference [192]). **b)** Schematic diagram of electrolytically gated thin film transistors with inkjet printed graphene electrodes and WSe_2 active channel, and a spray coated hBN dielectric layer (reproduced from reference [53]). **c)** Gate voltage dependence on source-drain current in fully printed graphene/hBN FET. Inset: photograph of graphene/hBN FET with 500 µm scale bar (reproduced from reference [11]). **d)** Photograph of fully inkjet printed capacitor consisting of graphene top (Gr_T) and bottom (Gr_B) electrodes and a hBN dielectric material (left) and graph showing the aerial capacitance of the device as a function of frequency for 1, 2, and 3 devices in parallel (reproduced from reference [222]).

More complex devices that incorporate 2D materials into printed heterostructures have also been explored and have enabled the fabrication of a number of electronic devices such as transistors [11,53] and capacitors [220,222]. Kelly et al. fabricated electrolytically gated thin film transistors with inkjet printed graphene electrodes, a WSe_2 active channel, and a spray coated hBN dielectric layer (**Figure 2.15b**) [53]. Researchers also demonstrated fully inkjet printed FETs consisting of a graphene active channel, an hBN gate dielectric, and silver electrodes, with a field effect mobility of μ = 91 $cm^2/V{\cdot}s$ [63]. In these devices, the hBN protected the graphene from the local environment and improved charge transfer in the graphene [63]. Wang et al. demonstrated a similar device with a field effect mobility of μ = 25 $cm^2/V{\cdot}s$ (**Figure 2.15c**) [11], and to explain charge transport through the graphene networks, a charge transport model was developed that included quantum tunnelling between graphene flakes and percolation dynamics [11]. This revealed that the electrical properties of the device are strongly influenced by the packing fraction of graphene flakes and by complex electron trajectories that traverse several printed layers [11], illustrating the complex transport dynamics of inkjet printed 2D materials and devices.

Capacitors have been fabricated using printed graphene electrodes and hBN dielectric layers (**Figure 2.15d**), achieving areal capacitances up to 2 nF/cm^2 and a dielectric constant of ~ 6 for printed hBN [222]. Le et al. inkjet printed graphene oxide films for supercapacitor electrodes, which displayed specific capacitances of up to 132 F/g after undergoing thermal reduction at 200 °C [246]. Inkjet printing has also been utilised to deposit pseudocapacitive additives onto graphene supercapacitor electrodes [220] and carbon nanotube (CNT) electrodes for supercapacitor applications [221].

Printed sensors have also utilised low-dimensional materials. Researchers demonstrated vapour sensors based on printed GO and printed GQDs which

experience a change in conductivity in the presence of NO_2 (**Figure 2.16a**) [219], Cl [219], or water [202,216]. This is caused by a change in GO surface charge carrier density when exposed to electron acceptor/donor vapours. Inkjet printed GO and GQDs are especially suited to this role as oxygen functional groups on their surface allows water to permeate into the materials and provides enhanced absorption to gas molecules [247]. Moreover, printed GO and GQD films which are made up of randomly ordered 2D platelets have a large surface area for vapours to interact with. Researchers also developed fluorescent aniline functionalised GQD (a-GQD) films which were modulated using phenyl boric acid (GQD-PBA) [203]. This quenched their fluorescence due to π-π stacking between a-GQDs and PBA, resulting in electron transfer between them. GQD-PBA fluorescence was drastically increased in the presence of glucose, which was ascribed to the reversible disassembly of the PBA linker from the a-GQDs, since the boronic acid groups of PBA form negatively charged boronic ester complexes with the cis-diols of glucose [203]. GQD-PBA films were then deposited via inkjet printing to produce wearable fluorescent turn-on glucose sensors with high sensitivity and selectivity (**Figure 2.16c**) [203]. Printed graphene and CNTs have been utilised in inkjet printed strain and pressure sensors for flexible and wearable applications (**Figure 2.16c**) [248–250]. Upon bending or stretching, gaps are created between the graphene flakes or CNTs; the size and number of gaps increases with further strain which gives rise to a linear increase in resistivity which is mostly reversible [251].

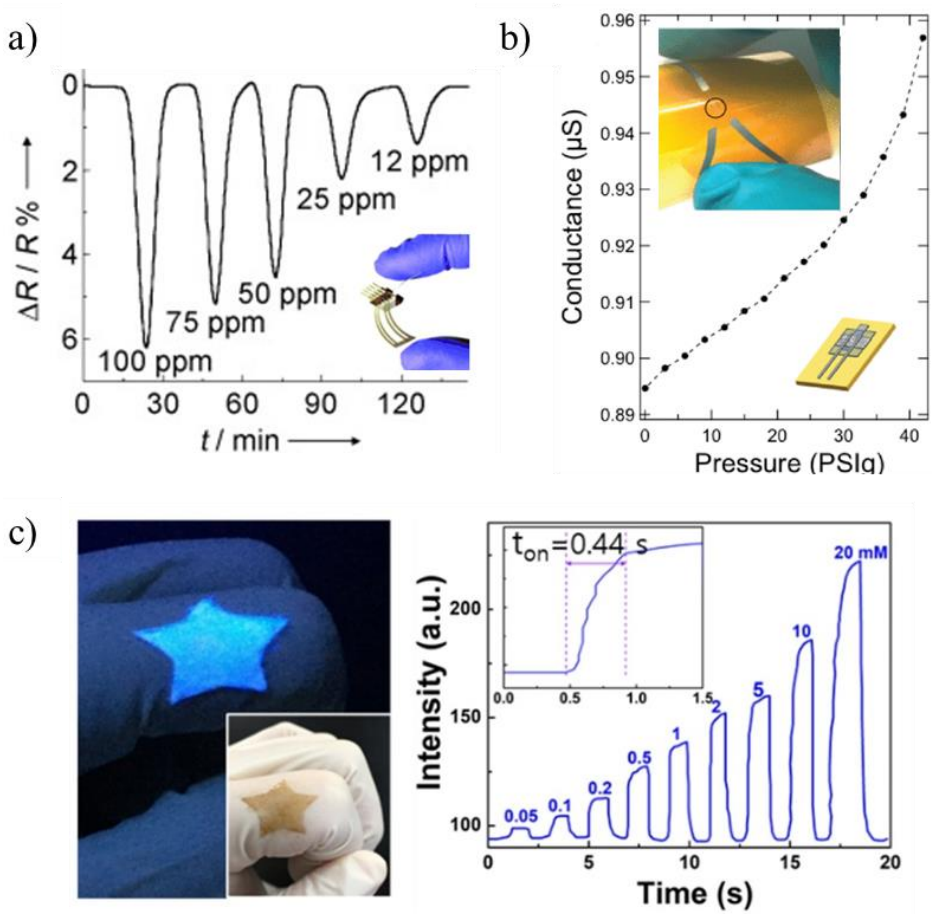


Figure 2.16. a) Change in resistance as a function of time for printed GO humidity sensor when exposed to NO_2 vapour at different concentrations. Inset: optical image of sensor on flexible substrate (reproduced from reference [219]). **b)** Conductance as a function of pressure for printed CNT pressure sensor on Kapton. Inset: optical image and diagram of pressure sensor. (reproduced from reference [250]). **c)** Optical images of aniline functionalised GQD glucose sensors printed on latex gloves with and without UV illumination (left). Graph of GQD PL intensity over time in the presence of different glucose concentrations (right) (reproduced from reference [203]).

2.5.3 Optoelectronic Devices

2.5.3.1 Photodetectors

Various approaches were explored to achieve high responsivity photodetectors via inkjet printing. For example, Pace et al. demonstrated fully-printed organic

photodetectors with semitransparent PEDOT:PSS electrodes and a photoactive layer containing small organic dyes, which achieved external quantum efficiencies up to 46% [252]. However, organic devices tend to have slower response time due to unbalanced electron and hole mobilities [253] and poor long-term stability [254].

Low-dimensional semiconductor materials could offer potential solutions as photosensitive layers due to their stable and tuneable optical properties [19,36,255]. 2D BP was deposited via inkjet printing within a graphene/silicon Schottky junction, enhancing its responsivity by 10-fold to ~ 10^{-1} A/W and enabling the device to detect in the near-IR wavelength range [255]. Wang et al. deposited AgNPs via inkjet printing atop ZnO films for UV photodetection, where surface plasmons in the AgNPs increased the photocurrent in the devices and achieved a detectivity of 1.45×10^{10} Jones [256]. HgTe [19] (**Figure 2.17a,b**) and PbS [18] QDs were printed onto graphene field-effect transistors (FETs) with high precision by electrodynamic nano-printing [18,19] to achieve infrared photodetectors with responsivity of ~ 10^3 A/W, with spectral sensitivity range tuneable by QD composition. Sliz et al. developed a colloidal QD ink based on lead halide anions (PbX_2 X = Br or I) that was deposited in photodetectors with specific detectivities over 10^{12} Jones across the IR range [257].

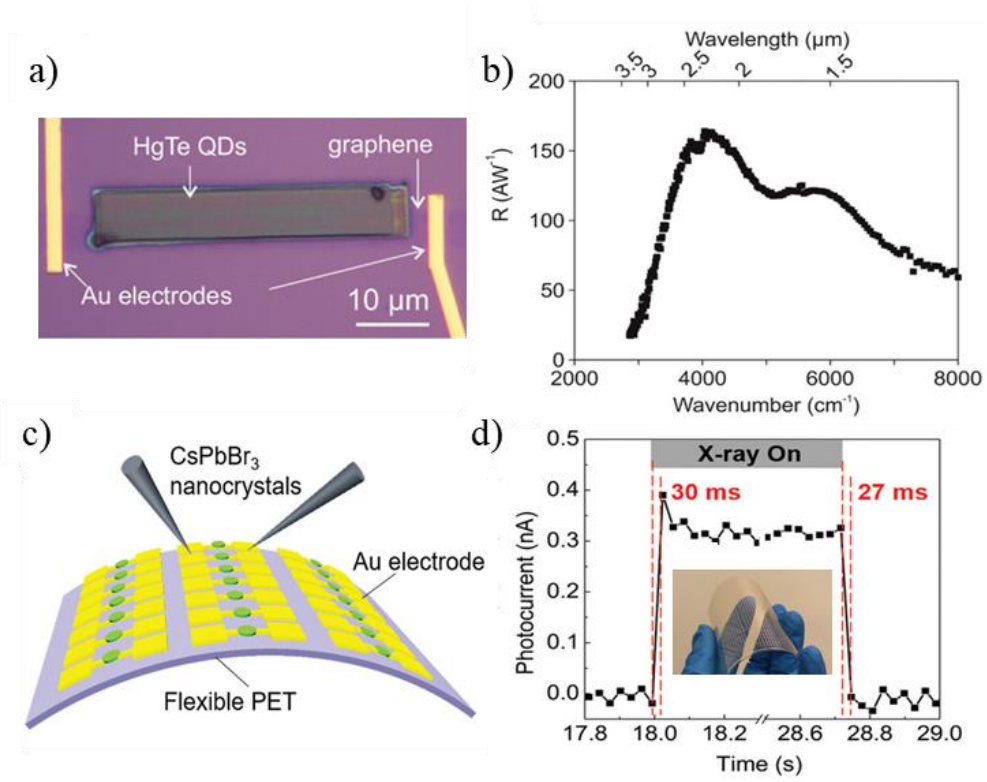


Figure 2.17. a) Optical image of printed HgTe QDs on graphene FET and **b)** responsivity of the device as a function of wavelength. (reproduced from reference [19]) **c)** Schematic diagram of an X-ray detector based on an inkjet printed perovskite QD photoactive layer and **d)** temporal dependence of the photocurrent induced in the device by incident X-rays with response times of ~ 30 ms. Inset shows a photograph of an array of these photodetectors on a flexible substrate (reproduced from reference [258]).

Perovskite NCs are a promising material for light detection applications due to their high absorption cross-sections, long carrier diffusion lengths, and band-gap tuneability [99,259]. Gu et al. introduced a soluble PEO layer during the printing of hybrid ($MAPbBr_3$) perovskites on flexible substrates and printed photodetectors which displayed responsivities up to ~ 1 A/W, which was maintained after 2000 bending cycles [12]. Hybrid $CH_3NH_3PbI_3$ perovskites were deposited on ITO, which formed perovskite microwires during printing due to ink formulation and drying conditions, resulting in the fabrication of photodetectors with a responsivity of 1.2 A/W [15]. Min

et al. deposited 2D layered organohalide $(CH_3(CH_2)_3NH_3)_2(CH_3NH_3)_{n-1}Pb_nI_{3n+1}$ (n = 2, 3, and 4) perovskites onto flexible polyimide films to produce photodetectors with a responsivity of 0.16 A/W [16]. Hybrid $MAPbX_3$ (X =Cl, Br, I, or mixed) perovskites with a variety of different halide ratios in the composition were printed, with responsivities up to 10^{-2} A/W [14]. Printed perovskites can also be used as efficient detectors of high energy photons, such as X-rays [258]. Liu et al. printed all-inorganic $CsPbBr_3$ QDs onto flexible and rigid substrates between Au electrodes for soft-x-ray detection (**Figure 2.17c,d**) [258]. At a low bias voltage of 0.1 V, these devices displayed high sensitivities up to 1450 μC Gy_{air}^{-1} cm^{-2} (70 times more sensitive than traditional α-Se devices) with a fast response time of 30 ms.

Photoexcited electron-hole pairs produced in perovskite NCs tend to recombine very quickly (~ 300 ps for $CsPbX_3$ NCs [260]) and so cannot produce significant photocurrent [261]. By utilising graphene as a carrier transportation material, with its high carrier mobility, high performance photodetectors were realised by fully printing a $CH_3NH_3PbCl_{X-3}I_3$/graphene heterostructure (**Figure 2.18**) [5]. The device displayed a responsivity of 0.53 A/W (**Figure 2.18b**) and could function without an external driving voltage [5]. Researchers have only scratched the surface of inkjet printed perovskite photodetectors, with especially limited work on graphene-based devices and all-inorganic $CsPbX_3$ NCs. With further development these devices could extend the range of commercial photodetectors which is particularly promising in the UV range below 280 nm where conventional Si-based photodetectors have poor responsivities of < 0.04 A/W [262,263].

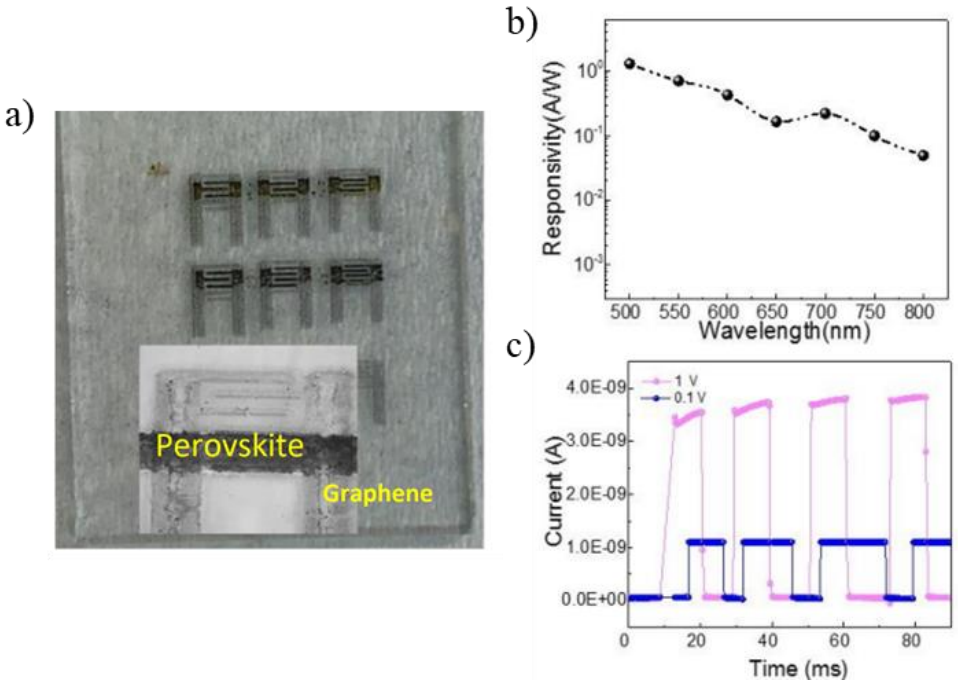


Figure 2.18. a) Optical image of $CH_3NH_3PbCl_{X-3}I_3$/graphene photodetector morphology, **b)** responsivity of the device as a function of wavelength, and **c)** temporal response of device at source-drain voltage V_{sd} = 0.1 and 1 V.

2.5.3.2 LEDs

The integration of optically active materials with the inkjet printing processes has enabled the fabrication of photoluminescent films, lasing devices, and LEDs [225,255]. The unique and random drying behaviour of each printed droplet has enabled the fabrication of unclonable security labels and full-colour converter films [264] using inks of $Zn_xCd_{1-x}Se_yS_{1-y}$ QDs encapsulated by NaCl crystals [264]. QD films with optical emission in the red, green, and blue wavelength ranges of the electromagnetic spectrum, were sequentially inkjet printed onto flexible substrates to fabricate full-colour RGB (red, green, and blue) QD@NaCl convertor films for full-colour displays with a pixel size of 3.74 ± 0.5 μm [264].

Photoactive materials have also been printed in LED structures. For example, the small-molecule organic material 1,1′-(9,9-bis(4-(hexyloxy)phenyl)-9H-fluorene2,7-diyl)dipyrene (PFP-3) (**Figure 2.19a**) was inkjet printed as an emissive layer in an LED to produce large-area light-emitting flexible patterns, with a luminance of 800 $cd \cdot m^{-2}$ at 13 V and maximum current efficiency of 0.6 $cd \cdot A^{-1}$ [265]. LEDs were also reported with an inkjet printed CdSe/ZnS QD emissive layer [266], where coffee-ring-free and low-roughness QD films were achieved using a mixture of dodecane and cyclohexylbenzene solvents. The fabricated LEDs displayed a low turn-on voltage of 2.0 V, a luminance of 12100 $cd \cdot m^{-2}$ at 12 V, and a maximum current efficiency of 4.44 $cd \cdot A^{-1}$.

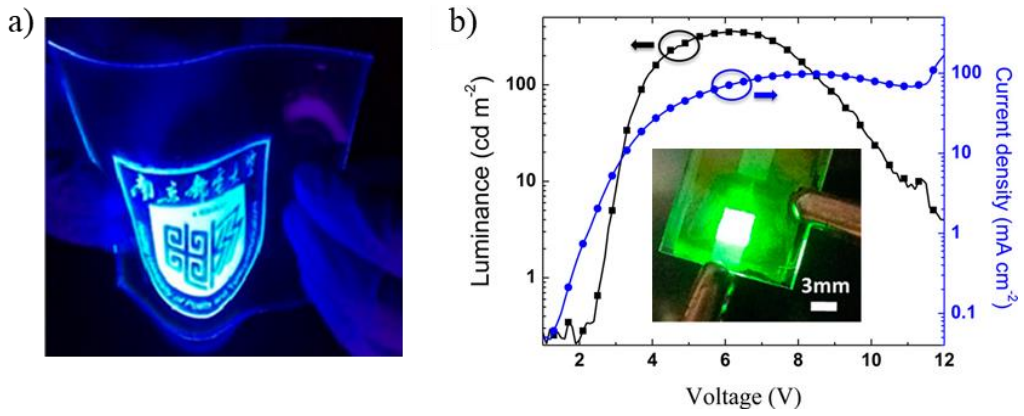


Figure 2.19. a) Optical image of printed emissive PFP-3 films (reproduced from reference [265]). **b)** Current density–voltage–luminance intensity characteristics of printed $MAPbBr_3$-PEO LED. Inset: optical image of $MAPbBr_3$-PEO LED under operation (reproduced from reference [267]).

More recently, lead halide perovskites have attracted attention for LEDs: Hammerschmidt et al. [225] developed a method to directly control the crystallisation of inkjet printed perovskite composites with polyethylene glycol ($MAPbBr_3$:PEG) and achieved the first inkjet printed perovskite emissive layer in an LED. This was performed by blending a PEDOT:PSS hole injection layer with KCl to create a seeding

template for the inkjet printed perovskite layer. The inclusion of KCl in the PEDOT:PSS increased the luminance of the device by a factor of 20, achieving a maximum luminance of 4000 $cd \cdot m^{-2}$ with a turn-on voltage of 2.5 V [225]. A $MAPbBr_3$- PEO composite was also printed as an LED emissive layer, exhibiting a low turn-on voltage of 2.6 V and a maximum luminance of 210 $cd \cdot m^{-2}$ (**Figure 2.19b**) [267].

Common charge carrier-transport materials such as ZnO [268], PEDOT:PSS [269], PVK [270], and poly-TPD [210] have also been printed previously, however, the fabrication of fully inkjet printed LED remains very challenging for several reasons. High efficiency LED devices require the deposition of several layers on top of one another, with uniform thicknesses as small as ~ 50 nm [212,213,271]; this is still challenging via inkjet printing and further work on the formulation of inks and their integration with the deposition process is needed. Also, the deposition of heterostructures for photodetectors, solar cells, or LEDs can lead to intermixing between layers [11], which further affects the ability to control the layer thickness and/or the quality of the interface (**Chapter 2.5.1**).

A fully inkjet printed perovskite LED was fabricated by Zhao et al. using $CH_3NH_3PbBr_3$ perovskites mixed with PEO as the emissive layer (**Figure 2.20a,b**) [228]. The LEDs were printed on flexible substrates and displayed a turn-on voltage, maximum luminance intensity, and maximum current efficiency of 3.46 V, 10227 $cd \cdot m^{-2}$, and 2.01 $cd \cdot A^{-1}$, respectively, which were maintained after bending (**Figure 2.20c**.More stable $CsPbBr_3$ perovskite NCs were also deposited via inkjet printing as the emissive layer for LED heterostructures [272]. These fully-printed devices incorporated a PEDOT:PSS hole transport layer, a NiO hole injection layer, and a SnO_2 electron injection layer and achieved a luminance of 324 $cd \cdot m^{-2}$. This work

has the significance of achieving the first perovskite LED with printed charge injection layers, however, inorganic charge injection materials tend to require high temperature processing which limits device applications [272,273]. Organic injection layers are typically more compatible with solution processing techniques at room temperature [273]. Moreover, they offer unique advantages for perovskite LEDs, including, tunability of their band energy alignments for compatibility with a wide variety of emissive layers, and layers with hydrophobic conjugated backbone provide the perovskites with protection from moisture [273]. It should be noted that a printed LED structures with organic hole and electron injection layers (such as poly-TPD and TPBI for example) could achieve higher efficiencies than the printed LEDs fabricated thus far, however, such devices have not yet been demonstrated.

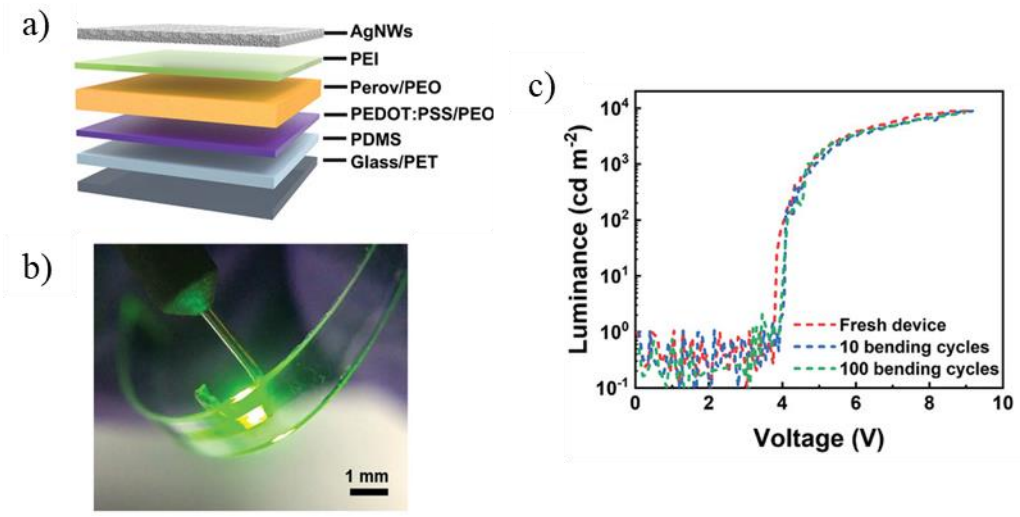


Figure 2.20. a) Fully printed perovskite LED device structure and **b)** optical image of fully printed perovskite LED on flexible substrate during operation undergoing bending. **c)** Graph of Luminance as a function of voltage before and after bending cycles (reproduced from reference [228]).

2.5.3.3 Solar cells

Inkjet printed solar cells incorporating low dimensional materials comprise a growing area of research [208,209,274]. The performance of conventional Si solar cells has been enhanced by surface decoration with an inkjet printed anti-reflective porous layer of Si QDs. Inkjet printing here enabled low-waste deposition while also allowing for control of the thickness and porosity of the QD film, resulting in a 15% increase in external quantum efficiency in the 300 - 400 nm wavelength range [195].

In recent years, a high power conversion efficiency (PCE) of 22.1% [275] was reported for solar cells with a spin-coated perovskite photoactive layer. To achieve scalability and customisation, inkjet printed perovskite ($MAPbI_3$) photoactive layers were inkjet-deposited with the layer thickness controlled by the printing strategy and crystal size tuned by a vacuum annealing step [227]. The resulting device displayed a PCE of ~ 11%, comparable to that achieved in spin-coated devices. Solar cells incorporating inkjet printed triple cation $Cs_{0.1}(FA_{0.83}MA_{0.17})_{0.9}Pb(Br_{0.17}I_{0.83})_3$) perovskites with improved temperature and moisture stability [274] displayed PCEs up to 12.9 % and were shown to withstand temperatures of 80 °C for 120 minutes, with a small decrease in PCE of ~ 10%. To further enhance device performance, greater control over the NP crystallisation process is required [274].

Despite demonstrating lower PCE than perovskite solar cells, organic devices offer the benefits of being fully inkjet printed and are well-suited for applications in wearable and healthcare electronics [208,209]. In these devices, semi-transparent electrodes were achieved with PEDOT:PSS and a silver NP grid [209], and the solar cells were fabricated in an ambient atmosphere with an area > 1 cm^2 and PCE = 4.1 %. Fully inkjet printed indium tin oxide (ITO)-free, ultrathin, lightweight organic solar cells on biocompatible parylene substrates was demonstrated with PCE = 3.6 %.

In summary, optoelectronic devices have been fabricated via inkjet printing using a wide variety of materials and techniques. However, many novel functional materials have not yet been formulated for inkjet deposition, and major challenges must still be addressed to enable the co-deposition of multi-materials required for vertical heterostructure devices.

2.6 Challenges For Inkjet Printing of Electronics

Inkjet printing is a highly promising method for upscaled manufacturing of electronic components and devices, however, there are still major challenges that must be addressed before the technique can become more widely adopted [73]. There are four key challenges remaining: ink formulation, print resolution, layer thickness and uniformity, and intermixing of layer in printed heterostructures.

Ink formulations need to fulfil the strict requirements of ink rheology, stability, and reliable droplet formation during jetting [36,40,276]. The formulation must also enable the printing of uniform films with well-defined edges on the desired substrates, and post-processing techniques must be investigated to remove solvents and additives present in the ink, all while maintaining the functional properties of the material being printed [36,40,276]. Currently, development of an ink formulation is highly time consuming and demanding process. Further work is needed to find formulations strategies that can be used for a wide range of different materials. Moreover, new methods to improve and streamline the process of ink formulation are required.

The resolution of inkjet printing is limited by the volume of the drops produced by the printer (tens of microns), along with surface tension, contact angle, and suitability of the substrate. Hence, the resolution of inkjet printing is far inferior to lithography-

based technologies commonly used for manufacturing electronics [277]. It is also challenging to produce the very thin and uniform films often required for optoelectronic devices via inkjet printing [231], as the coffee-ring effect and other wetting phenomena often lead to loss of film uniformity and print resolution [229]. Moreover, printed film thickness is dependent on the drop contact angle, with very thin films requiring very small contact angles. However, small contact angles can lead to uncontrollable droplet spreading on the substrate, thus there is a minimum thickness that can be achieved while still maintaining a reasonable printing resolution [278]. Highly optimised ink formulations can inhibit the coffee-ring effect, however, other deposition techniques such as spin coating tend to achieve thin films with greater uniformity and smaller thicknesses than is possible via inkjet printing [279] .

Intermixing between printed layers in heterostructure devices is another major challenge for inkjet printed electronics [11], often leading to short-circuiting and loss in device performances [235]. Researchers have used several methods to reduce intermixing on a case by case basis [228,236], however, further understanding of the intermixing process and further tools to prevent intermixing are needed. Due to these challenges, many complex devices that require many printed layers, such as a fully printed LED, with charge injection layers for improved efficiency, has not yet been realised.

2.7 SUMMARY

Inkjet printing is low waste process that allows for highly customisable designs and is highly upscalable. A plethora of different material have been deposited via printing, including 0D, 2D, and organic materials, with conducting, semiconducting, and

insulating electrical properties. Printed 2D materials comprise of many 2D flakes, which form a network with complex charge transport dynamics. Inks of 2D materials typically include additives and encapsulants that can affect their electrical properties after post-deposition treatments, such as high temperature annealing [11,177,178]. Researchers have also explored photonic annealing [177] as a viable alternative for applications on flexible substrates, but further understanding and optimisation of these processes is needed.

Metal NPs inks are commercially available, but more recent research has developed inks with greater NP content [82,187] and reduced anisotropy [186] in printed layers for improved performances. Many of the 0D materials required for optical emission/absorption applications suffer from poor environmental stability, such as colloidal QDs. This makes printing challenging, as the properties of the NCs must be maintained following formulation, printing, and post-processing. Thus a number of techniques were proposed to improve stability and enable the printing of such materials including surface capping [102], ligand replacement [96], and core/shell structures [106]. All-inorganic metal halide perovskite NCs are of particular interest for printed optoelectronics owing to their increased stability, but as of yet, the inks formulated in the literature can only be printed on certain polymers [102] and are optimised for thick colour converter film applications [199]. No ink has been formulated to produce the thin films required for some optoelectronic devices

Organic materials have been widely printed with improved flexibility and biocompatibility compared to inorganics. Conducting and insulating polymers are well optimised, with many formulations using different solvents and additives to tune the properties of the polymers [26,147,208]. Charge injection materials on the other hand, such as poly-TPD and TPBI, are much more challenging to print, as very thin (~

50 nm) and uniform layers are required for high efficiency devices [212,213], thus further work on the formulation of inks and their integration with the deposition process is needed.

For similar reasons, printing heterostructures remains a key challenge. The very thin uniform layers required for high efficiency devices [231] are challenging to print in complex heterostructures, as the coffee-ring effect and other wetting phenomena can lead to loss of film uniformity and print resolution [229]. Intermixing is another key challenge for printed heterostructures [11], often leading to short-circuiting and loss in device performances [235]. Researchers reduced intermixing on a case by case basis, using approaches such as orthogonal solvent systems [236] and the introduction of blocking layers [228], however, further understanding of the intermixing process and further tools to prevent intermixing are needed. Due to these challenges, a fully printed LED, with the inclusion of charge injection materials for improved efficiency, has not yet been realised.

The wide variety of materials available for printing, has enabled the inkjet deposition of many different devices. Electronic devices such as transistors [11,215], sensors [216–219], and capacitors [220–222] have all been printed; they utilise the unique properties of printed materials such as high surface areas to achieve high performances, and the inkjet deposition enables new device geometries and applications on flexible substrates. Inkjet deposition also enables the precise patterning of nanomaterials onto pristine graphene to produce photodetectors [19,255]. With the ability to co-deposit multiple dissimilar materials on flexible substrates, this technology enables the fabrication of detector arrays with highly selective sensitivity over a broad spectral range [5,19,280,281]. However, more printable materials are required to fabricate broadband detectors across the entire UV-Vis-IR spectral range.

There is also limited work on devices incorporating all-inorganic $CsPbX_3$ NCs [258] and fully printed devices incorporating inkjet printed graphene [5], which could enable the fabrication of wearable and flexible detectors.

3 AIMS AND OBJECTIVES

The primary aim of this PhD project is to formulate inks and develop the inkjet deposition of functional materials, towards fabricating and investigating printed heterostructures for photodetector and LED applications. To achieve this aim, the following objectives are set:

(**i**) Formulate inks and develop inkjet printing deposition methods for different functional materials to expand the number of optically active and charge transport materials available for additive manufacturing technologies. Specifically, ink formulations will be prepared, and printing will be performed for $CsPbX_3$ (X = Cl, Br, I or mixed) perovskite NCs and GQDs, as optically active materials, and poly-TPD and TPBI as charge injection materials for LED applications.

(**ii**) Characterise and optimise commercially available and previously developed inks, such as graphene and PEDOT:PSS. For graphene inks, different post-processing methods will be explored to enable its deposition on a wider range of substrates and heterostructures. For PEDOT:PSS inks, its stability will be tested under different post-processing methods and in different heterostructure configurations to determine its viability in heterostructures for applications in optoelectronic devices.

(**iii**) Investigate the properties of fully printed heterostructures made using functional material inks for their use in optoelectronic device applications. This includes: ensuring the electronic and morphological properties of films are maintained after deposition of printed layers on top, investigating how ink wetting on heterostructures can affect film morphology; and investigating how different printing parameters can be used to control intermixing at printed heterostructure interfaces for improved device performance.

(**iv**) Fabricate photodetectors sensitive in the UV-Vis range by decorating conventional single layer graphene (e.g. CVD graphene on Si/SiO_2 substrate) with printed perovskite NCs and (for the first time) GQDs, to upscale the manufacturing of these devices and expand the spectral sensitivity range of printed detectors. The use of inkjet printed graphene, instead of single layer graphene, in these devices will also explored towards the goal of fabricating fully printed detectors on flexible substrates.

(**v**) Develop a fully inkjet printed perovskite LED using the inks formulated in this work and explore how different printing parameters affects the properties of the LED.

4 MATERIALS AND EXPERIMENTAL METHODS

4.1 MATERIALS AND SUBSTRATES

All chemicals used for formulation were purchased from Sigma Aldrich without further purification. This includes, hexane, terpineol, cyclohexanone, n-butanol, isopropyl alcohol (IPA), chlorobenzene, dimethyl sulfoxide (DMSO), tetraethylene glycol dimethyl ether (Tetraglyme), 3-glycidyloxypropyl trimethoxysilane (GOPS), cyrene, glycerol carbonate (GC), Triton X-100 (Tx), polysorbate 80 (Tween-80), polyethylene glycol (PEG) (molecular weight M_w = 1000), and polyvinylpyrrolidone (PVP) (molecular weight M_w = 40,000).

All-inorganic lead halide perovskite nanocrystals (NC) (green $CsPbBr_3$ and red $CsPb(Br/I)_3$ with Br:I = 2:3) were provided for this work by the supervisory team and were synthesised as described in [96]. Octanethiol-functionalized gold nanoparticles (AuNPs) were provided by Dr. Im [27]. Silver nanoparticle (AgNP) ink was purchased from Advanced Nano Products (SilverJet DGP-40LT-15C) and contain 38.85 wt% AgNPs dispersed in triethylene glycol monomethyl ether. Three developmental PEDOT:PSS inks (see **Chapter 4.4.3.6**) were provided by Dr. Rivers [26], which were formulated using PEDOT:PSS (1.1 wt%, PH 1000) purchased from Clevios. Graphene ink (product number: 793663) was purchased from Sigma Aldrich which consisted of liquid exfoliated graphene flakes (average size of 2590 nm^2 and average thickness of 3 nm) encapsulated in ethyl cellulose (EC) dispersed into an 85:15 mixture of cyclohexanone/terpineol. hBN ink encapsulated by EC (product number: 901410) was also purchased from Sigma-Aldrich with 5.4 wt% EC-hBN composite solids dispersed in the same solvents as the graphene ink. Graphene quantum dots (GQD) were also purchased from Sigma Aldrich (product number: 793663) (1 mg/ml in water) with blue fluorescence and reported diameter of < 5 nm.

A variety of substrate materials were used for inkjet deposition. Prime grade silicon wafers were purchased from PI-KEM with a 200 nm SiO_2 thickness. Single layer CVD graphene/SiO_2/Si FET devices were provided by the Centre for nanotechnology innovation at NEST, Italy [282] with a 285 nm SiO_2 thickness. Borosilicate glass microscope slides with 1 mm thickness were purchased from Fisher Scientific, Quartz coverslips with 0.5 mm thickness were purchased from Agar Scientific, and Sapphire substrates with 0.8 mm thickness were purchased from PI-KEM. Polyimide (Kapton® HN general purpose polyimide film) thermal insulating films were purchased from DUPONT. Polyethylene naphthalate (PEN) with 75 μm thickness and polyethylene terephthalate (PET) with 12 μm thickness were supplied by GTS Flexible Materials Ltd.

Before printing, all substrates were cleaned by sonicating (RS Pro Ultrasonic cleaning tank, 100W, 3L, cleaning mode: full) in acetone for 20 minutes at room temperature followed by washing with IPA and then drying with N_2

4.2 INK FORMULATIONS

$CsPbX_3$ (X = Br or Br/I mixture) perovskite NC inks were formulated for inkjet printing by dispersing 5 mg/mL of $CsPbBr_3$ or $CsPb(Br/I)_3$ NCs in a mixture of hexane, cyclohexanone, and terpineol (1:3:1 v/v) and sonicating for 30 minutes at room temperature. The ink was usually made in batches of 1 mL. The perovskite NC ink had a viscosity of 1.53 mPa s, a surface tension 37.8 mN/m, and a density 1.33 g/cm^3. By adding 5 mg/ml of PVP to the $CsPbBr_3$ or $CsPb(Br/I)_3$ perovskite NC inks and sonicating for 30 minutes at room temperature, a perovskite-PVP mixed ink ($CsPbX_3$-PVP) was formulated. The $CsPbX_3$-PVP ink had a viscosity of 1.65 mPa s,

surface tension of 29.1 mN/m, and density of 1.36 g/cm^3. To ensure the PVP was fully dissolved, it was stirred overnight in cyclohexanone at a temperature of 40 °C before the ink was formulated. The iGr-$CsPbX_3$ hybrid ink was formulated by dispersing 5 mg/ml of $CsPbX_3$ NCs in a mixture of the graphene ink and hexane (2:1 v/v) and sonicating for 30 minutes at room temperature. The hybrid ink had a viscosity of 2.96 mPa s, a surface tension of 27.4 mN/m, and density of 0.93 g/ml. All inks containing perovskite NCs were stored in Dimatix inkjet printing containers (**Figure 4.1c**) under inert N_2 atmosphere which were sealed using the containers lid and Parafilm.

GQD inks were formulated as follows: 1 mg/ml GQD solution in water was mixed (0.86 mL) with butanol (25.8 mg) and IPA (85.9 mg), and sonicated at room temperature for 30 minutes. By adding 0.86 mg/ml of PEG (M_w = 1000), or by adding 0.86 mg/ml PVP (M_w = 40,000) to the GQD ink and sonicating for 30 minutes at room temperature, GQD-PEG and GQD-PVP inks were formulated, respectively. The GQD ink had a viscosity of 1.23 mPa s, a surface tension of 30.9 mN/m, and density of 1.04 g/ml. The GQD-PEG ink had a viscosity of 0.75 mPa s, a surface tension of 71.2 mN/m, and density of 1.06 g/ml. The GQD-PVP ink had a viscosity of 1.18 mPa s, a surface tension of 32.6 mN/m, and density of 1.06 g/ml. All GQD inks were stored in a sealed Dimatix inkjet printing container in ambient conditions.

Poly-TPD ink was formulated by dispersing 1.5 mg/ml of poly-TPD in chlorobenzene and stirring at 40 °C for 2 hours, as described previously in reference [210]. The poly-TPD ink was stored in a sealed Dimatix inkjet printing container in air in a refrigerator at ~5 °C. The poly-TPD ink had a viscosity of 0.61 mPa s, a surface tension of 28.5 mN/m, and density of 1.28 g/ml.

TPBI ink was formulated by dispersing 4 mg/ml of TPBI in a mixture of hexane, n-butanol, and terpineol (1:3:1 v/v) and sonicating for 30 minutes at room temperature. The TPBI ink was stored in a sealed Dimatix inkjet printing container in air in a refrigerator at ~5 °C. The TPBI ink had a viscosity of 2.62 mPa s, a surface tension of 26.4 mN/m, and density of 0.90 g/ml.

4.3 RHEOLOGY MEASUREMENTS

Rheology measurements were carried out to find the viscosity, surface tension, and density of inks to determine their printability. A Malvern Kinexus rotational rheometer was used to measure the viscosity of inks as a function of shear rate. These measurements were performed at room temperature in a plate-plate geometry with a working distance of 0.2 mm. The top plate rotates at a set shear rate, γ_{sr} in contact with the ink and measures the shear stress, τ_{ss} exerted by the ink. The viscosity, η, of the ink is then calculated by [283]:

$$\eta = \frac{\tau_{ss}}{\gamma_{sr}} \tag{8}$$

Viscosity was measured as a function of shear rate from 0.1 - 1000 s^{-1}. The shear rate experienced by inks during printing is ~ 1000 s^{-1}, however, the viscosity of inks usually reached a constant minimum value, between 100 s^{-1} and 1000 s^{-1} and this value was taken as the ink viscosity.

Surface tension measurements were performed on a Kruss DSA100 drop-shape analyser using the pendant drop method at room temperature. Here, a camera continuously took images of the silhouette of a droplet formed at the end of a 1 mL syringe with a 1.25 mm diameter metal needle or a 0.69 mm diameter plastic needle.

The needle type was chosen depending of the wettability of the ink, to avoid the droplet climbing the sides of the needle during measurements. 20 μL dosing was applied until the droplet was ejected and fell from the syringe. The interfacial surface tension, γ, was then calculated using the Young-Laplace model, which relates γ to the curvature of the interface between two fluids (the droplet and the air) at the moments before the droplet is ejected [284]. For each test, measurements were made for five separate droplets and the surface tension was calculated from the average. Finally, the density of inks was calculated by transferring 1.00 ± 0.01 mL of ink via syringe to an analytical balance to measure its mass.

4.4 INKJET PRINTING PROCESS AND PRINTING PARAMETERS

4.4.1 Inkjet Printing Process

In this work, a Fujifilm Diamatix DMP-2800 drop-on-demand (DoD) piezo driven inkjet printer was used for material deposition (**Figure 4.1a**). Cartridges, which house and eject the ink, are installed onto the printer (**Figure 4.1b**). Cartridges consist of two components, the container where the ink is stored, and the printhead, where the ink is ejected during printing (**Figure 4.1c**). In this work two different models of printhead were used: either the Dimatix DMC printhead with a 10 pL drop volume and a nozzle diameter of a = 21.5 μm (**Figure 4.1d**) or the Dimatix Samba printhead with a 2.4 pL drop volume and a nozzle diameter of a = 17 μm (**Figure 4.1e**). Note that the Dimatix DMC printheads were discontinued by the manufacturer in 2021 which is why Samba printheads were predominantly used after this point.

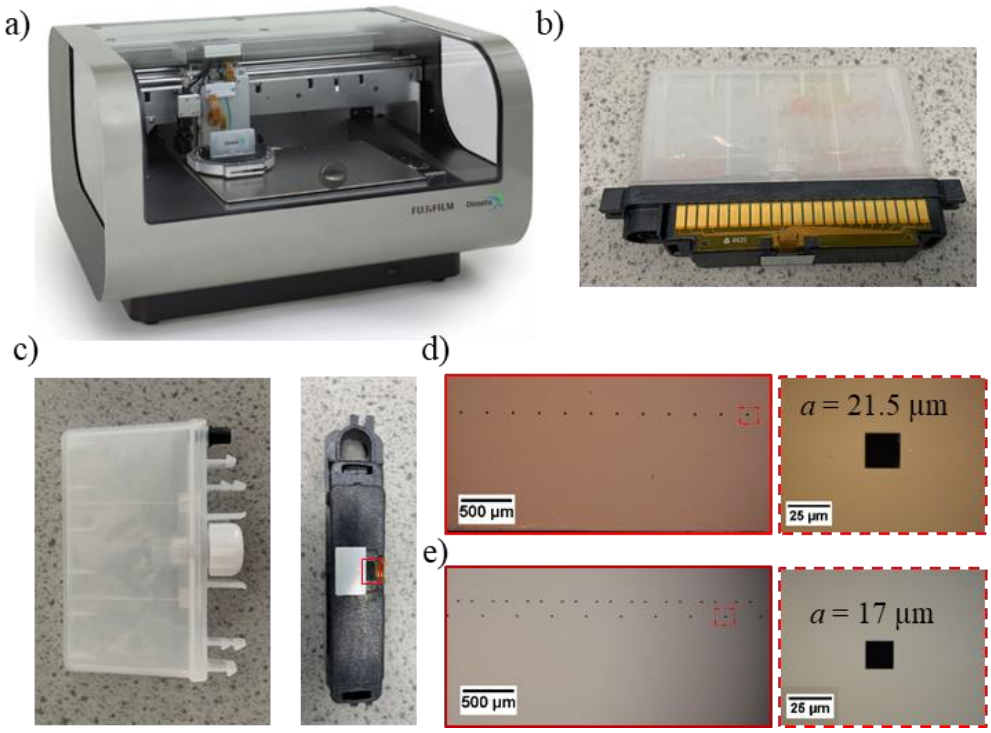


Figure 4.1. Images of **a)** Fujifilm Diamatix DMP-2800 inkjet printer**, b)** Dimatix inkjet printing cartridge, **c)** sealed Dimatix inkjet printing container (left) and Dimatix Samba printhead with nozzles highlighted in red square (right) (note that DMC and Samba printheads are visually identical apart from the nozzles) Optical images of the nozzles from **d)** Dimatix DMC printhead with nozzle diameter a = 21.5 µm and **e)** Dimatix Samba printhead with nozzle diameter a = 17 µm.

Once an ink formulation was prepared with suitable rheology for jetting, it was loaded into a Dimatix inkjet printing container. Before printing, ink was purged through the printhead nozzles to expel air pockets from the ink reservoir and remove any nozzle blockages. Next, the formation of droplets ejected from the nozzles was optimised. For high quality printing, all droplets must be formed with a consistent shape and size. To achieve this, a drop-watcher system was used to observe the nozzles during printing, while custom voltage waveforms, which control the piezo plate used to push droplets out of the nozzles, were created and modified. Small incremental changes were then

made to the shape and intensity of the waveforms until the formation of consistent spherical droplets was observed, travelling between 6 and 8 m/s and falling vertically without producing any satellite droplets, as shown in **Figure 4.2**. The optimal waveform for droplet formation was different for each material that was printed, so this process was repeated for each ink formulated. Before, during, and after printing, cleaning cycles were employed to stop nozzle blockage and ensure consistent drop formation. During a cleaning cycle, the nozzles were first purged and then blotted against a cleaning pad, different cleaning cycle durations and frequencies were selected for each material, as was deemed necessary to achieve consistent jetting and drop formation.

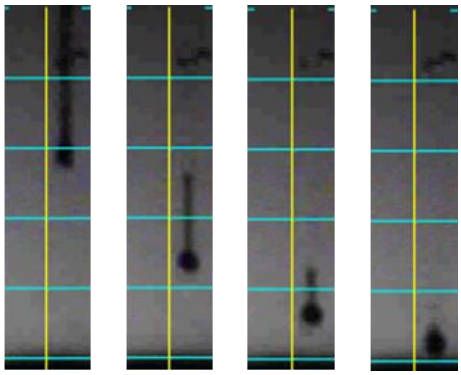


Figure 4.2. Representative optical images of droplet formation during printing taken by Fujifilm Dimatix drop watcher using graphene ink. The droplets fall vertically and the long tail contacts during flight to form a single spherical shape. The blue lines are 100 µm apart.

Once the drop formation was optimised for a particular ink, it could be printed. During printing, drops were deposited using a single nozzle from a height of ~ 0.5 mm above the substrate. Patterns were deposited in individual rows from left to right, starting at the top of a pattern. Each printed row of droplets deposited from left to right is referred to as a printed swath. For multiple printed layer this process is repeated, with

subsequent layers printing directly on top of the previous layers. All patterns for printing were made and edited using the software GIMP [285] (version 2.10.14) in bitmap form. For all the patterns printed in this work, leader bars were employed. These are small redundant bars placed to the left of a printed pattern that ensures the first droplets of each printed swath are deposited in the leader bar and not in the pattern. This improved the quality of printed patterns as the first droplets ejected in each swath are usually the least stable and are prone to being slightly misshapen/misplaced.

The drop spacing is the distance between the centres of neighbouring droplets deposited by the printer and is a parameter that significantly affects the film morphology. For each material, the drop spacing was optimised to form uniform films. To find the appropriate drop spacing for a given material, single swaths were printed using different drop spacings until one was found that gave printed lines with straight edges, as observed with optical microscopy, without any gaps or bulges [41]. Substrate temperature during printing ($T_{substrate}$) also affects printed film morphology (see **Chapter 2.2**) and was optimised for each printed material. The Dimatix print-bed provides heating between 0 - 60 °C, and a custom heating plate built in-house was also inserted on top of the print-bed to achieve temperatures up to 120 °C. Similarly, the post-processing annealing temperature (T_{anneal}) was optimised for each ink to remove solvents from the printed film.

4.4.2 Post-Processing Treatments

Several different post-processing techniques were used in this work. Post-deposition thermal annealing in air was performed in a natural convection oven (Carbolite Gero PN). Post-deposition thermal annealing in vacuum with a pressure of 1 mbar was

performed in a Thermo Scientific™ Vacutherm Vacuum Heating and Drying Oven. Infrared sintering was performed with a λ = 1300 nm twin tube lamp (600 W, Heraeus Noblelight Ltd., P = 60 mW/mm^2). A custom-built intense pulsed light (IPL) sintering setup was also used for photonic annealing. The IPL had a broad spectral range of 550-900 nm with maximum intensity at 600 nm, and several peaks between 800 and 950 nm (**Figure 4.3a**). The pulse duration was ~ 4 s (**Figure 4.3b**) with a flash power of 5.4 J/cm^2. Samples were annealed by the IPL system at a distance of 10 mm away from the light source using a single flash. UV light exposure tests were performed with a FireFly 25x10AC395-4W lamp (λ = 395 nm, P = 3.7 mW/mm^2).

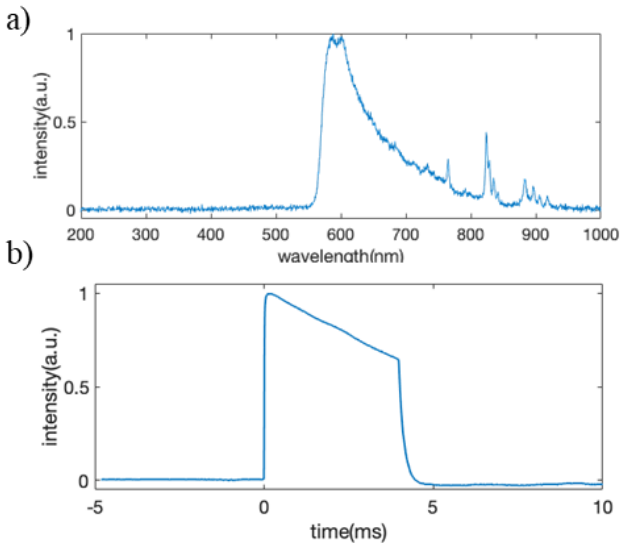


Figure 4.3. a) Spectra of light emitted by IPL annealing system and **b)** graph of intensity as a function of time during IPL flash.

4.4.3 Printing Parameters

For each material used in this work, the ink formulation was optimised and specific printing parameters such as drop spacing, $T_{substrate}$, and T_{anneal} were used to achieve uniform films. The printing parameters and post-processing methods developed for each material are outlined below.

4.4.3.1 Deposition of Graphene

Inkjet graphene ink was printed as purchased without further purification. At room temperature and at a concentration of 2.4 wt% solids, the graphene ink had a viscosity of 11.3 mPa s, a surface tension of 33 mN/m, and a density of 9.665 g/cm^3. The ink was stored in a Dimatix inkjet printing container (**Figure 4.1**c) under ambient conditions which were sealed using the container's lid and Parafilm. Graphene printing was performed using a 10 pL drop volume Dimatix DMC printhead. The ink was deposited with a drop spacing of 20 µm, the printer was paused for 30 seconds between printing each layer to allow for drying, and nozzles were purged before printing each layer and periodically during printing (for 0.1 s every 100 printed swaths) to achieve consistent jetting. Inkjet printed graphene (iGr) films were thermally annealed from T_{anneal} = 150 - 250 °C for periods between t = 30 minutes and t = 24 hour in air or under 1 mbar vacuum and photonic annealing using intense pulsed light (IPL) was also investigated.

4.4.3.2 Deposition of Hexagonal Boron-Nitride

Hexagonal boron-nitride (hBN) ink was printed using exactly the same protocol and printing parameters as those developed for the graphene ink, which are descried in **Chapter 4.4.3.1**. Printed hBN films were then annealed at T_{anneal} = 250 °C, t =30 minutes under ~ 1 mbar vacuum.

4.4.3.3 Deposition of Perovskite Nanocrystals

All perovskite containing inks were stored in Dimatix inkjet printing containers under inert N_2 atmosphere at room temperature. $CsPbX_3$ (X = Br or Br/I) perovskite NC inks were printed using 2.4 pL drop volume Dimatix Samba printheads, which formed spots with a diameter of ~ 40 µm on Si/SiO_2. Perovskite NCs were deposited with a drop-spacing of 20 µm and with $T_{substrate}$ = 60 °C in a N_2 atmosphere. The printer was paused for 60 seconds between printing each layer to allow for drying and to prevent excessive cartridge heating by the high temperature substrate, and nozzles were purged before printing each layer for 0.2 s. After printing, films were left to dry for 1 hour on the printbed at 60 °C under N_2 or were annealed at T_{anneal} = 100 °C, t =30 minutes in vacuum. The $CsPbX_3$-PVP ink was printed and annealed using the exact same parameters optimised for the $CsPbX_3$ ink.

The iGr-$CsPbX_3$ hybrid ink was printed using 10 pL drop volume Dimatix DMC printheads with nozzles with a diameter of 21.5 µm. The printing parameters optimised for the iGr ink (**Chapter 4.4.3.1**) were also used for the iGr-$CsPbX_3$ hybrid ink, which formed spots with a diameter of ~ 50 µm on Si/SiO_2. After printing, the hybrid iGr-$CsPbX_3$ films were annealed at 250 °C, t = 1 hour or at 150 °C, t = 24 hours under ~ 1 mbar vacuum and photonic annealing using intense pulsed light (IPL) was also investigated.

4.4.3.4 Deposition of Graphene Quantum Dots

GQD inks were stored in a sealed Dimatix inkjet printing container in air in a refrigerator at ~ 5 °C. Printing of GQD inks was performed with 2.4 pL drop volume Dimatix Samba printheads using a 30 µm drop spacing and $T_{substrate}$ = 60 °C for all

three inks (GQD, GQD-PEG, and GQD-PVP - described in **Chapter 4.2**). No cleaning cycles were employed for these inks, but a 60 s pause was used between printed layers to prevent excessive cartridge heating by the high temperature substrate. Printed films were annealed at T_{anneal} = 100 °C, t = 30 minutes in air.

4.4.3.5 Deposition of AuNPs and AgNP

The AuNP and AgNP inks were stored in a sealed Dimatix inkjet printing container in air in a refrigerator at ~5 °C. AuNP printing was performed with 2.4 pL drop volume Dimatix Samba printheads with nozzle temperature set to 35 °C to reduce viscosity, $T_{substrate}$ = 90 °C, and a drop spacing of 30 µm, as described in reference [27]. AuNP films were then annealed with T_{anneal} = 150 °C from 30 to 90 minutes in air or using infrared sintering in air for 30 minutes. AgNP printing was performed using a 10 pL drop volume Dimatix DMC printheads with a drop spacing of 30 µm and $T_{substrate}$ = 90 °C, as described in reference [186]. AgNP films were then annealed at T_{anneal} = 150 °C for t = 30 minutes in air.

4.4.3.6 Deposition of PEDOT:PSS

Three PEDOT:PSS inks were provided by Dr. Rivers and their composition is shown in **Table 4.1**, as described in reference [26]. Ink_{DMSO} had a viscosity of 10.1 mPa.s and a surface tension of 35.6 mN/m; Ink_{CG} had a viscosity of 8.6 mPa.s and a surface tension of 31.5 mN/m, $Ink_{CG\text{-}Samba}$ had a viscosity of 7.5 mPa.s and a surface tension of 35.4 mN/m. The PEDOT:PSS inks were stored glass vials in a refrigerator at ~ 5 °C.

Table 4.1: Compositions of investigated PEDOT:PSS inks by weight percentage.

Composition (wt%)	*Ink_{DMSO}*	*Ink_{CG}*	*$Ink_{CG\text{-}Samba}$*
PEDOT:PSS dispersion	46.2	38.4	31.8
Water	46.7	55.2	58.3
DMSO	5.1		
Tetraglyme	0.5		
Tx	0.5		
GOPS	1	0.45	0.34
Cyrene		4.3	5.1
GC		0.85	0.71
Tween-80		0.8	0.67
n-butanol			3.0

Printing of Ink_{DMSO} and Ink_{CG} was performed with 10 pL drop volume Samba printheads using a drop spacing of 34 µm. $Ink_{CG\text{-}Samba}$ printing was performed with 2.4 pL drop volume Samba printheads with a drop spacing of 20 µm. All PEDOT:PSS inks were deposited at $T_{substrate}$ = 45 °C, 0.2 s cleaning cycles were employed before each layer, and the printer was paused for 30 s between printed layer. After printing, films were annealed in air at T_{anneal} = 150 °C for t = 30 minutes.

4.4.3.7 Deposition of Poly-TPD and TPBI

Poly-TPD printing was performed with 2.4 pL drop volume Samba printheads, which formed spots with a diameter of ~ 75 µm on Si/SiO_2. Poly-TPD ink was stored in a sealed Dimatix inkjet printing container in air in a refrigerator at ~ 5 °C. Poly-TPD films were deposited with a drop-spacing of 40 µm at room temperature in air. Nozzles were cleaned for 0.3 s before printing and during printing (every 40 printed swaths)

for consistent jetting. After printing, films were annealed in air at T_{anneal} = 140 °C for t = 30 minutes.

TPBI printing was performed with 2.4 pL drop volume Samba printheads. Films were deposited with a drop spacing of 40 µm and $T_{substrate}$ = 40 °C. TPBI ink was stored in a sealed Dimatix inkjet printing container in air in a refrigerator at ~ 5 °C. No cleaning cycles were employed as jetting was very reliable, but a 30 s delay was set between layers to prevent nozzle heating. Printed spots were formed a diameter of ~ 50 µm on Si/SiO_2. Printed films were annealed in air at T_{anneal} = 140 °C for t = 30 minutes.

4.4.3.8 Deposition of TPGDA

TPGDA ink was formulated and printed as described in reference [149] and was stored in a sealed Dimatix inkjet printing containers in air in a refrigerator at ~ 5 °C. The containers were also sealed from ambient light by covering the transparent parts with electrical tape. TPGDA printing was performed using a 10 pL drop volume Dimatix DMC printheads in an inert N_2 environment with $T_{substrate}$ = 40 °C, and a drop spacing of 30 µm. The TPGDA was UV-cured during printing with the built-in UV lamp in the Dimatix printer (λ = 365 nm, P = 1245 W/m^2).

4.5 MORPHOLOGICAL AND OPTICAL CHARACTERISATION

4.5.1 Optical Microscopy

Optical microscopy uses visible light and a series of objectives to magnify images of small samples, for inspection and imaging. This was performed on a Nikon Eclipse LV100ND optical microscope with Nikon NIS-Elements microscope imaging software.

4.5.2 Electron Microscopy

Electron microscopy (EM) utilises electron beams to probe samples [286]. EM can image significantly higher resolutions than optical microscopy due to the much smaller de Broglie wavelength of electrons compared to visible light [287].

Transmission electron microscopy (TEM) uses a high voltage electron beam focused onto a thin sample with an electromagnetic lens. The electron beam either passes through the sample onto a screen or is scattered, depending on the electron density of the material. TEM can achieve resolutions up to ~ 0.2 nm [287] and thus is suitable for imaging the structures of individual nanoparticles. Samples were prepared for TEM imaging by drop casting highly diluted solutions onto graphene oxide support grids with thickness of < 1 nm. TEM images were acquired on a JEM-2100F, JEOL operated at 200 kV and on a JEOL- 2100Plus – equipped with a Gatan Ultrascan1000XP CCD camera for imaging. TEM was operated, and images were recorded by Dr Michael W. Fay at the Nanoscale and Microscale Research Centre, University of Nottingham. The sizes of nanoparticles captured by TEM were analysed independently using ImageJ software [288].

Scanning electron microscopy (SEM) is a technique where a focussed electron beam is rastered across the surface of a sample and an image of the surface is formed by detecting backscattered or secondary electron signals. Focussed ion beam (FIB)-SEM employs a second beam of ions which are used to cut the sample while SEM imaging is carried out. This can be used to image the cross-sections of 3D structures or to obtain a thin lamella from a sample which can then be analysed by other techniques such as TEM. SEM imaging was performed at 5 kV using a FEI Quanta 3D FIB scanning

electron microscope. To protect samples from the FIB, platinum was selectively deposited on top of samples using electron beam induced deposition at 1 kV. Samples were milled using a 30 kV accelerating voltage for the FIB. FIB-SEM was performed at the Nanoscale and Microscale Research Centre, University of Nottingham by Dr. Negar Gilani.

Energy dispersive X-ray (EDX) spectroscopy is a technique used for the elemental analysis and thus the chemical characterisation of samples [289] and is often used in conjunction with TEM or SEM. This works by firing a focussed electron beam at a sample to excite ground state electrons into excited states. The relaxation of these electrons to their ground state causes the emission of X-rays which are detected by an energy dispersive spectrometer. Since every atom has a unique emission spectrum, determined by their atomic structure energy, the elemental composition of the sample can be found [289]. EDX spectroscopy was performed Dr. Negar Gilani using the Oxford Instruments XMax 100 TLE spectrometer at the Nanoscale and Microscale Research Centre, University of Nottingham. Analysis and interpretation of FIB-SEM and EDX results were performed independently.

4.5.3 Atomic Force Microscopy

Atomic force microscopy (AFM) was used to access the nanoscale topology of both electrically conducting and insulating samples [290]. AFM was performed in peak force tapping mode, where the tip is raised above the sample, and ‘taps’ the sample at discrete points in space. When the tip is close to the surface, short range forces (caused by tip and sample orbital overlap) over fractions of nm, and long range forces (like Van der Walls, electrostatic, and magnetic) up to 100 nm, both act on the tip [290].

These forces are measured by a laser deflection system, whereby a laser is reflected from the back of the cantilever (which houses the AFM tip) onto a photodetector (**Figure 4.4**). The laser position on the photodetector is then used to calculate the force acting on the AFM tip. As the tip is lowered towards the sample, the force-distance relationship between sample and tip is measured, which is then used to calculate the height of the sample. By periodically tapping an area of the samples surface, its topology can be found. AFM measurements were performed using a Bruker's Dimension Icon® using silicon probes (Bruker, model RTESPA-150) with a tip radius of 8 nm and spring constant of 6 N/m in air. For each measurement, 256 points were taken in the *X* and *Y* directions and scans were taken with sizes from 100 × 100 nm to 20 × 20 µm. The speed of the tip varied with scan size and other parameters varied with material but generally the following parameters were used during measurements: peak force amplitude = 150 nm, noise threshold = 2 nm, lift height = 50 nm, peak force setpoint = 15 nN, and feedback gain = 13.

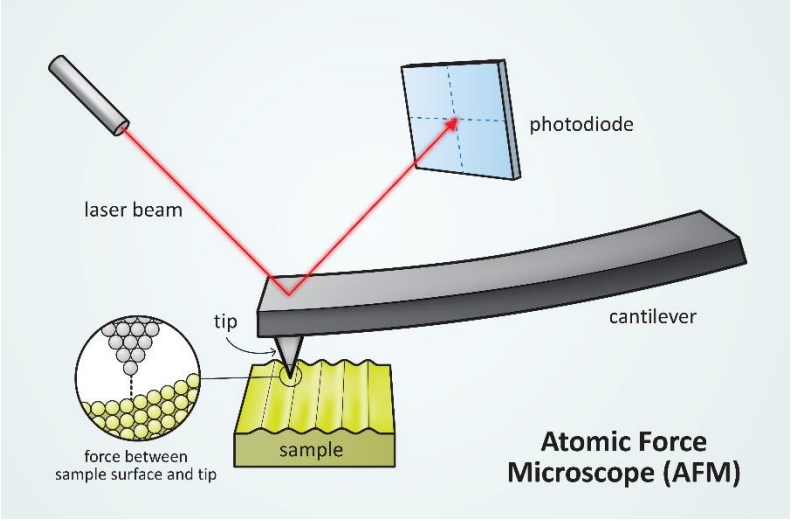


Figure 4.4. Schematic diagram of atomic force microscopy tip and laser deflection system. Reproduced from reference [291].

4.5.4 Time-of-Flight Secondary Ion Mass Spectroscopy

Time-of-flight secondary ion mass spectroscopy (ToF-SIMS) uses a primary ion beam which is focused onto the surface of a sample to produce secondary ions in a sputtering process. These secondary sputtered ions are then analysed via mass spectroscopy to identify the molecules present on the sample. The primary ion beam can rastered across a surface to produce mass spectral information in the *X*-*Y* dimension and can be continuously operated to etch deep into a sample for mass spectral information in the *Z* dimension. With this information, ToF-SIMS can be used to produce 3D maps of the distribution of molecules within a sample with nanoscale resolution.

ToF-SIMS 3D mapping was carried out by Dr. Trindade and Dr. Zhou at the National Physics Laboratory, using a TOF.SIMS 5 instrument from IONTOF GmbH in a dual-beam fashion. ToF-SIMS data was acquired in positive or negative ion polarity modes, depending on the sample, by raster scanning a 30 keV Bi_3^+ primary ion beam and delivering 0.08-0.2 pA. For negative ion polarity mode, an argon gas cluster ion beam (GCIB) operated with energies between 5 and 10 keV with up to 4 nA beam current was used for sputtering, and for positive ion polarity mode, an O_2 beam with current up to 20 nA was used for sputtering. A field of view between 32 × 32 µm and 200 × 200 µm was measured with raster size up to 400 × 400 μm^2. A low-energy (20 eV) electron flood gun was employed to neutralise charge build up. Prior to profiling a heterostructure, profiles of each of the individual materials were acquired to establish characteristic signals for each material. Analysis and interpretation of ToF-SIMS data was performed independently.

4.5.5 Raman Spectroscopy

In Raman spectroscopy, a monochromatic light source excites electrons in a molecule to an excited state and some photons undergo Raman scattering [292], where the energy of the photon emitted during radiative recombination is less than that of the photon absorbed by the sample (as is the case in **Figure 4.5**). The Raman scattered light is collected by a detector and can be used to determine the vibrational modes of motion of a molecule [292].

Micro Raman spectroscopy was performed by Dr Graham Rance at the Nanoscale and Microscale Research Centre, University of Nottingham using a Horiba Jobin Yvon LabRAM HR Raman spectrometer equipped with an automated *x*-*y*-*z* stage (Märzhäuser). For single point Raman measurements, spectra were acquired using a 785 nm laser (at a power of 0.2 mW μm^2, 100× objective) and a confocal pinhole of 200 µm over the range of 65 - 3000 cm^{-1} with an acquisition time of 120 s and 2 accumulations to improve the signal-to-noise ratio and automatically remove the spikes due to cosmic rays. Spectra were detected by a Synapse CCD detector (1024 pixels) thermoelectrically cooled to −60 °C. Before measurements, the instrument was calibrated using the Rayleigh line at 0 cm^{-1} and a standard Si (100) reference band at 520.7 cm^{-1}. Raman spectroscopic maps were acquired using a 785 nm laser (at a power of 3.2 µW μm^2 conferred using the DuoScan function, 100× objective) and a confocal pinhole of 200 µm over the range 65-3000 cm^{-1} at 1 µm steps within a 10 × 10 µm square and at 10 µm steps within a 100 × 100 µm square (a total of 100 spectra per map). Analysis and interpretation of Raman data was performed independently.

4.5.6 Photoluminescence Spectroscopy

Photoluminescence (PL) spectroscopy is a technique used to investigate the band structure of materials by measuring the energy of light emitted by a material (E_{em}) following photoexcitation [293]. For a semiconductor with band gap energy, E_g, a photoexcitation laser with photon energy $E_{ex} > E_g$ is focused onto the semiconductors surface. The semiconductor absorbs the photon which causes the excitation of an electron from the valence band (VB) to the conduction band (CB) (**Figure 4.5**). When an excited electron in the CB recombines with a hole in the VB, PL emission occurs, emitting a photon with $E_{em} \approx E_g$.

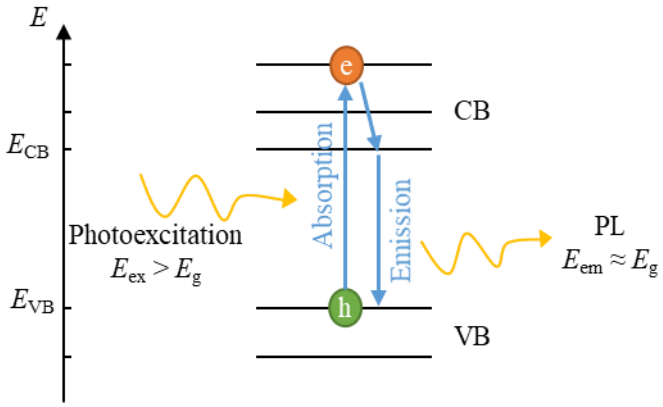


Figure 4.5. Diagram of photoexcitation and radiative emission for PL spectroscopy.

PL spectroscopy and confocal PL mapping of $CsPbBr_3$ perovskite NCs and GQDs were performed in air or under vacuum using a λ_{ex} = 405 nm pulsed diode laser as the excitation source (pulse rate of 100 MHz with a time-averaged power ~ 10 µW and a spot size of ~ 2 µm) and a Horiba MicOS optical spectrometer with Si CCD array detector and 50× objective, NA: 0.5, and 150 /mm grating. The samples were moved in steps of 20 µm using a motorised Zaber stage attached to the cryostat. $CsPb(Br/I)_3$ PL spectra was obtained in air using a frequency-doubled Nd:YVO4 laser (wavelength

λ_{ex} = 532 nm, power, P = 70 μW, and a spot size of ~ 5 μm) for optical excitation. The laser was used in continuous wave (CW) mode and PL spectra were recorded using a Horiba LabRAM system equipped with a Si CCD array detector. PL measurements were performed with assistance from Dr. Tyler James and Prof. Peter Beton and access was provided to their lab in the Physics Department at the University of Nottingham to perform these measurements.

4.5.7 Absorption Spectroscopy

Absorption spectroscopy is used to excite electrons in the VB of a material into excited energy states by passing monochromatic light through a thin film or solution. By measuring the intensity of light on the other side of the material, over a range of different wavelengths, information is gained about the energy and density of excited states in the material (**Figure 4.5**) [294]. The light was produced using a monochromator, where a white light source is first collimated and then directed onto a diffraction grating, and the angle of deflection of the grating controls the wavelength of light that is produced (**Figure 4.6**).

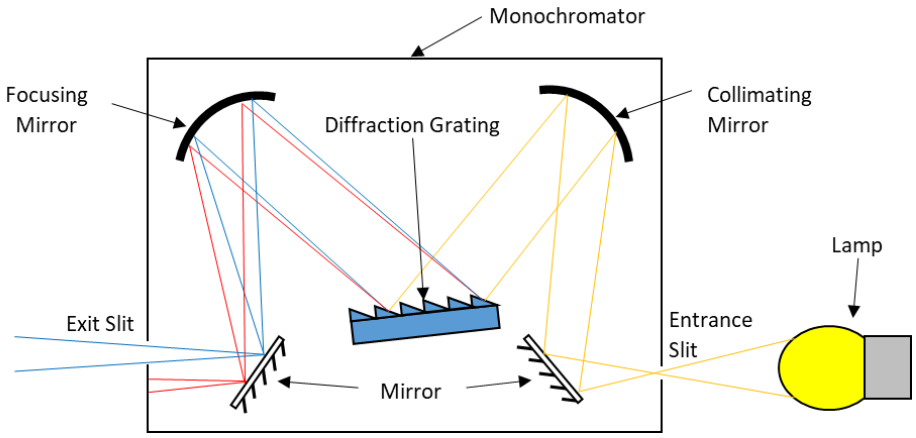


Figure 4.6. Scheme of monochromator, used to produce monochromatic light for absorption spectroscopy measurements, provided by Dr. Nathan Cottam.

For ink absorption measurements, the solvent mixture used in the ink was used as a control. For absorption measurements of printed films, the substrate was used as the control. Absorption measurements were conducted using Cary 3500 UV-Vis spectrophotometer. For the perovskite NC samples, a 1 mg/ml solution of the $CsPb(Br/I)_3$ ink and a 0.5 mg/ml solution of the $CsPbBr_3$ ink were loaded into Kartell Art. 1938" cuvettes made from PMMA. Absorption measurements were taken over a wavelength range between 800 nm and 400 nm, with steps of 0.2 nm. GQD absorption measurements were obtained by loading 0.01 mg/ml solution of GQD inks into quartz cuvettes (Hellma Analytics) and thin film absorption measurements were made by drop-casting or printing GQD inks onto quartz substrates. Absorption measurements were taken over a wavelength range between 600 nm and 200 nm with steps of 0.2 nm. Absorption measurements were conducted with assistance from Mr. Oliver Neslon-Dummett.

4.6 ELECTRICAL MEASUREMENTS

Electrical measurements were carried out on printed samples and devices to access their properties. Electrical measurements were carried out using Keithley 2401 Sourcemeters and frequency dependent AC measurements of resistance and capacitance were performed using a Rohde & Schwarz HM8118 Bench LCR Meter. The length, l, and width, w, of samples was measured by optical microscopy (**Chapter 4.5.1**). Electrical measurements were conducted with assistance from Dr. Nathan Cottam.

4.6.1 Sample Preparation for Electrical Measurements

Electrical characterisation first requires electrical contacts to be made with a sample. For large samples (up to ~ 20 cm) that could be measured in air, a four-probe micropositoner system (Micromanipulator, model 450PM) was employed, as shown in **Figure 4.7a**. This system used four tungsten probes (Micromanipulator, model 7B-5) with a tip radius of 0.5 mm that could be placed on top of a sample to make electrical contacts for measurements. The four probes were controlled by micropositioners and could be viewed through a microscope for precise placement onto a sample. The system also used a vacuum pump, which held the sample in place on the sample bed and kept the micropositioners in place on the stage. For rigid samples, like gold (**Figure 4.7b**) electrical contacts were made by placing the probes directly on top of the sample. For more delicate polymer samples, like PEDOT:PSS, small areas of the sample were manually covered in Ag paste (RS Pro Conductive Silver Paste), as shown in **Figure 4.7c**. The Ag paste was deposited using the end of a wire or a tooth pick, and given at least 20 mins to dry. The probes were then placed on top of the Ag paste without damaging the sample underneath. AgNP and AuNP inks were also used to

print contacts with greater accuracy than could be made by hand, as shown in **Figure 4.7d**. Ag/Au electrodes were deposited onto the substrate first, and the sample was printed on top, to ensure annealing of the metal NPs did not affect the properties of the sample. These printed electrodes allowed for contacts to be made in very precise locations on the sample, with printed contact pads extending away from the sample where contact could be made safely using the four-probe system. The micropositioner was then connected directly to Keithley 2400s or LCR meter via bayonet nut coupling (BNC) cables to conduct measurements.

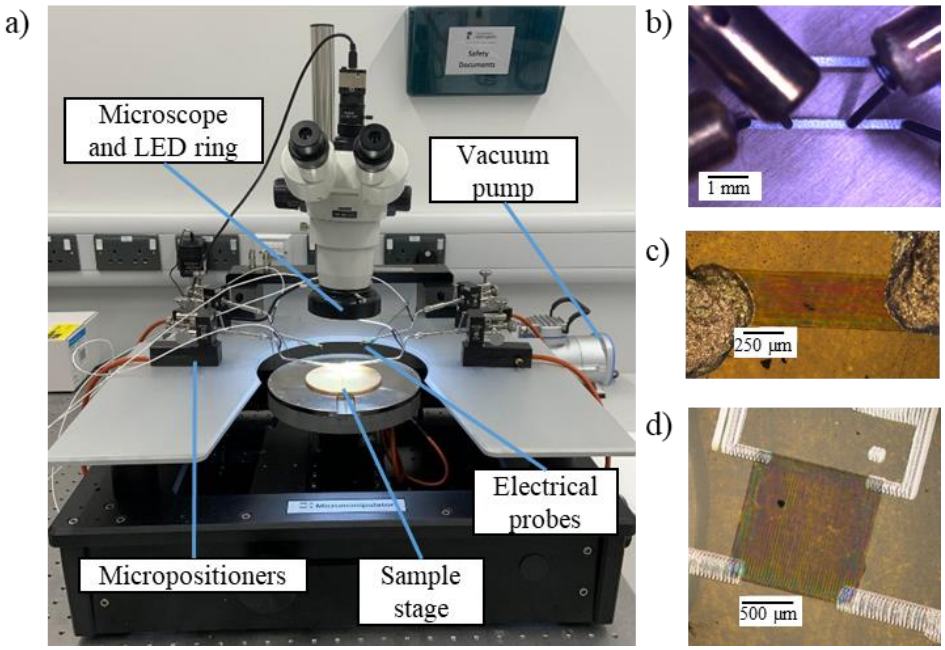


Figure 4.7. a) Labelled image of four-probe micropositioner system used for electrical measurements and **b)** optical microscope image of four probes making contact with a printed Ag line. Optical microscope images of **c)** printed PEDOT:PSS line with Ag paste manually deposited on top and **d)** printed PEDOT:PSS square with Ag contacts pre-deposited via inkjet printing.

Smaller samples (< 5 mm) could be measured by mounting them onto non-magnetic headers which were built in-house (**Figure 4.8a-d**). The headers had up to 12 pins

(**Figure 4.8b,c**) to make separate electrical contacts with the sample (**Figure 4.8d**) and some included a metallic back plate (**Figure 4.8b**). Samples deposited on Si/SiO_2 substrate were glued to the header using Ag conductive paste, which both held the sample in place and acted as conductive pathway between the Si back gate and one of the header pins. The headers with metallic plates assisted in making a conductive pathway between the pin and back gate. Samples on other substrates without a back gate such as Kapton or PEN were glued to the substrate using GE Varnish (Nanoshel). Electrical contacts were then made with the device using gold wires with 25 µm diameter (Advent, 99.99% purity), which were bonded to a header pin on one end and the sample on the other end using DuPont conductive Ag paste (4929N). Electrical contacts were made either directly on top of the sample (**Figure 4.8e**) or onto printed contact pads as before. The single layer graphene (SLG) devices provided by the Centre for nanotechnology innovation at NEST, Italy [282] included pre-patterned Au electrodes and contact pads (made using electron beam lithography) and so, electrical contacts were made on the contact pads, as shown in **Figure 4.8f,g**.

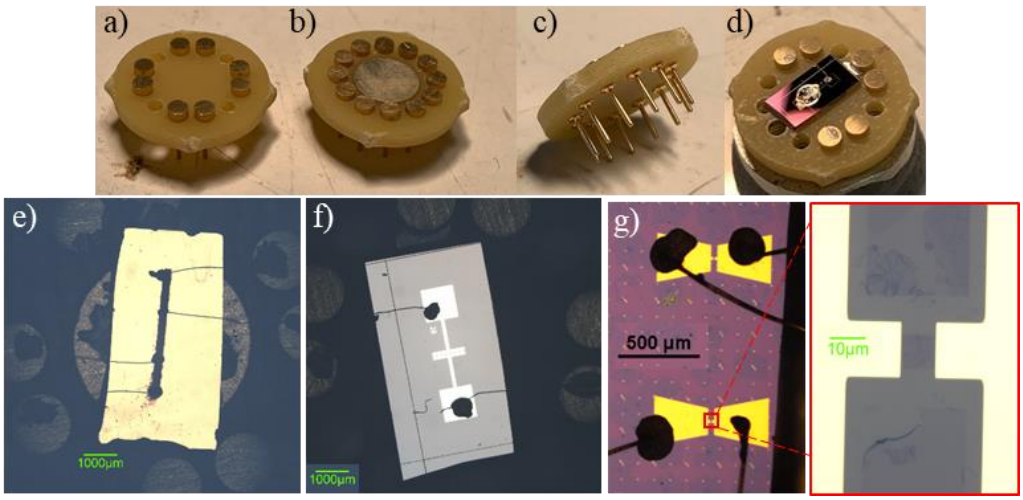


Figure 4.8. Photographs of non-magnetic headers with **a)** 8 pins, **b)** 12 pins and metallic plate, **c)** from below, and **d)** with sample bonded to it. Optical microscope images of bonded samples mounted on headers: **e)** printed iGr line with contacts made directly on the sample and **f)** 2-terminal OFET device made in Nottingham and **g)** 2-terminal SLG device made in NEST with contacts made on pre-patterned Au contact pads.

Headers were then mounted into a vacuum cryostat and connected to a vacuum pump (HiCube 80 DN40K) to achieve pressures down to ~ 10^{-6} mbar. The cryostat was then connected via BNC cables to a custom-made box, with 12 BNC connectors corresponding to the 12 pins on the header. Finally, Keithley 2400 Sourcemeters were used to conduct electrical measurements on the sample. A schematic diagram of this configuration is shown in **Figure 4.9**.

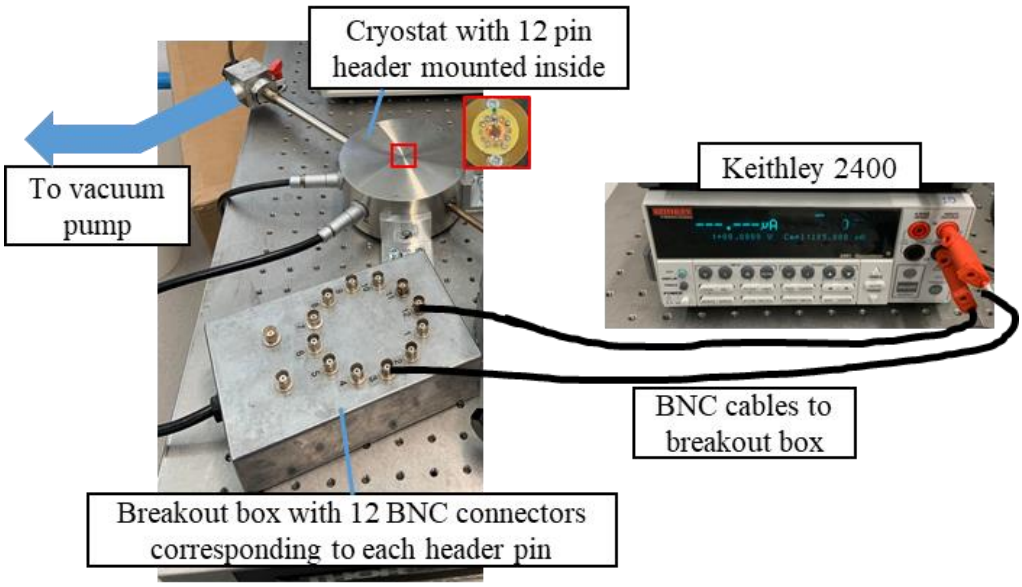


Figure 4.9. Schematic diagram of experimental setup for electrical characterisation (not to scale). A sample is mounted on a header in a cryostat and connected to Keithley 2400 sourcemeters via BNC cables and a breakout box.

4.6.2 Sheet Resistance Measurements

To calculate the sheet resistance of printed samples, 3 different methods were used. 2-terminal geometries were generally used for long and thin samples (where $w < 0.5 \cdot l$) with high resistances (> 500 Ω), where the resistance caused by the wires and contacts was negligible compared to sample resistance. Using one Keithley 2401, a voltage was applied (V_{sd}) and swept over a custom range which was selected so that a current less than ~ 3 mA was measured to avoid damaging the device. The source-drain current was also measured (I_{sd}) between the 2 contacts using the same Keithley 2401 (**Figure 4.10a**). The resistance ($R_{2\mathrm{t}}$) was then found by plotting V_{sd} against I_{sd} and finding the gradient and the sheet resistance (R_{s}) was then calculated by:

$$R_{\mathrm{s}} = R_{2\mathrm{t}} \frac{w}{l_{2\mathrm{t}}}, \tag{9}$$

where $l_{2t}$is the distance between the 2 contacts and w is the width of the sample.

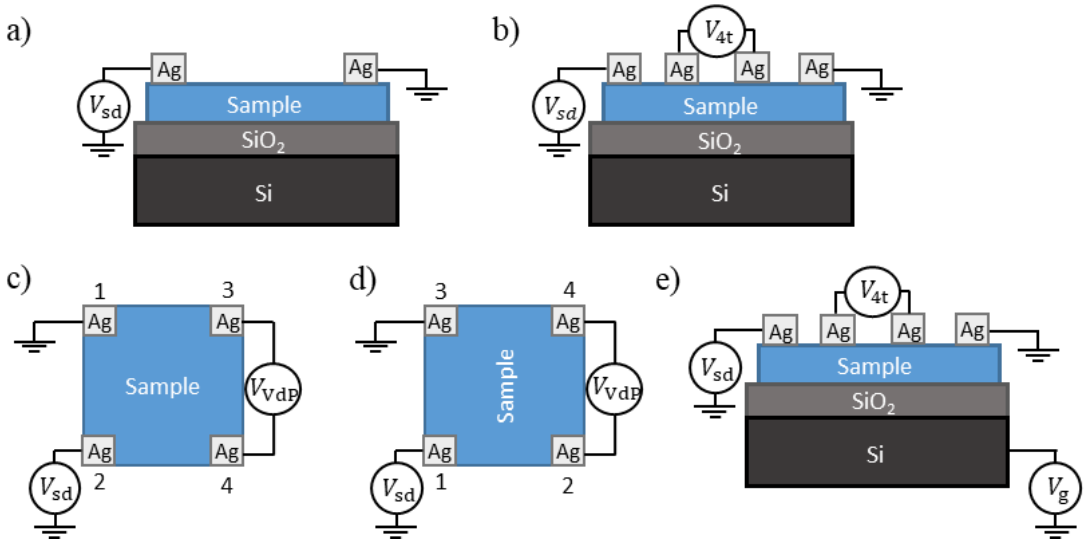


Figure 4.10. Schematics of electrical characterisation measurements performed in **a)** 2-terminal geometry, **b)** 4-terminal geometry, **c)** and **d)** Van der Pauw geometries (from above) for horizontal and vertical configurations, respectively, and **e)** gate dependent measurement with 4-terminal geometry.

For long and thin samples with low resistance (< 500 Ω), 4-terminal geometries were used to eliminate resistance contribution from the wires and contacts [295]. In these measurements, 4 electrical contacts were spread evenly across the length of the sample, each covering the width of the sample (**Figure 4.10b**). Using one Keithley 2401, a voltage (V_{sd}) was swept, and the current (I_{sd}) was measured between the source-drain (end) contacts. Meanwhile, using a Keithley 2000 multimeter, the voltage change ($V_{4\mathrm{t}}$) was recorded between the 4-terminal (central) contacts (**Figure 4.10b**). The 4-terminal resistance ($R_{4\mathrm{t}}$) was then calculated by plotting $V_{4\mathrm{t}}$ against I_{sd} and calculating the gradient. The sheet resistance R_{s} was then be calculated by:

$$R_{\mathrm{s}} = R_{4\mathrm{t}} \frac{w}{l_{4\mathrm{t}}}, \tag{10}$$

where $l_{4\mathrm{t}}$ is the distance between the two central contacts [295].

For wider samples (where $w \geq 0.5 \cdot l$), the Van der Pauw (VdP) method was used to calculate the sheet resistance [295]. Using a Keithley 2401, a voltage was swept (V_{sd}) and the current was measured between contacts 1 and 2 (I_{sd}). Meanwhile using a Keithley 2000 multimeter, the voltage was measured between the VDP contacts 3 and 4 (V_{VdP}) (**Figure 4.10c**). The vertical component of sheet resistance (R_{A}) could then be calculated by plotting V_{VDP} against I_{sd} and finding the gradient. To find the horizontal component of sheet resistance (R_{B}), this process was repeated in a horizontal configuration (sample rotated 90°) (**Figure 4.10d**) by applying V_{sd} and measuring I_{sd} between contacts 1 and 3, while measuring V_{VdP} between contacts 2 and 4. The sheet resistance can then be found by solving the following equation [295]:

$$e^{\left(\frac{-\pi R_{\mathrm{A}}}{R_{\mathrm{s}}}\right)} + e^{\left(\frac{-\pi R_{\mathrm{B}}}{R_{\mathrm{s}}}\right)} = 1 \qquad (11)$$

4.6.3 Electrical Measurements under Applied Gate Voltage

Gate voltage (V_{g}) dependent measurements were performed on samples printed on Si/SiO_2 substrates with SiO_2 dielectric constant ε = 3.6.The Si layer underneath was used as the gate electrode which was attached to the header with silver paste to form the gate contact (**Figure 4.10**e). Samples were mounted in a vacuum optical cryostat and gate voltage measurements were performed under vacuum. First, with one Keithey 2401, a constant V_{sd} was applied through the device while I_{sd} was measured continuously. Note that this continuous resistance measurement was performed in 2-terminal or 4-terminal geometries depending on the sample. With a second Keithley 2401, V_{g} was applied and slowly swept with sweep rate 0.1 V/s over a set range, which builds up an electric field across the dielectric. The resistance of the device, and thus

the resistivity, ρ_{sd}, and conductivity, σ_{sd}, was then calculated as a function of V_g. From these measurements, the field effect mobility, μ of SLG was approximated at the point of highest slope in the conductivity-gate voltage, $\sigma_{sd}(V_g)$ plot of the SLG, as was reported previously in [52], using the equation:

$$\mu = \frac{d}{\varepsilon\varepsilon_0}\frac{\sigma_{sd}}{V_g}, \tag{12}$$

where $\varepsilon_0$is the permittivity of free space, ε is the relative permittivity of the SiO_2 dielectric layer (3.9), and d is the SiO_2 dielectric thickness. Moreover, the charge carrier density n was calculated by:

$$n = n_0 + \frac{\varepsilon\varepsilon_0}{qd}V_g, \tag{13}$$

where q is the electron (or hole) charge and n_0 is the doping level at V_g = 0 V.

4.6.4 Photocurrent Measurements

Samples were mounted in a vacuum optical cryostat, equipped with a sapphire window so that the device could be illuminated by a light source (**Figure 4.11a**). Photocurrent measurements were performed in vacuum on samples in 2-terminal geometries. During photocurrent measurements, a constant V_g and V_{sd} were applied to the sample while I_{sd} was measured continuously. The sample was first measured in darkness for 2 minutes so that a dark current I_{dark} could be recorded. Then, an unfocused light source with wavelength, λ_{ex}, and a light spot larger than the device was used to illuminate the sample. The photoresponsivity R was calculated using:

$$R = \frac{I_{pc}}{P_{sample}}, \tag{14}$$

where the photocurrent I_{pc} is the maximum change in I_{sd} recorded after one minute of constant illumination and P_{sample} is the total light power incident on the sample. The total power of the laser was measured using a Thorlabs PM100D power meter and S120VC UV-extended (200−1100 nm) silicon photodiode, and the power density was calculated by dividing total power by spot size (measured with a ruler). $P_{sample}$was then calculated by multiplying the power density by sample area, since the sample was fully covered by the light spot. The power of the light sources was controlled using neutral density filters, which reduced laser power between 1 and 6 orders of magnitude. Time delays between the measurements were implemented to allow the photocurrent to return to its initial value, where $I_{sd} = I_{dark}$. The duration of these delays was dependent on the speed of the device, typically ~ 2 mins. To minimise relaxation time and to ensure minimal damage or bleaching to devices, measurements using low powers were conducted before measurements using high powers.

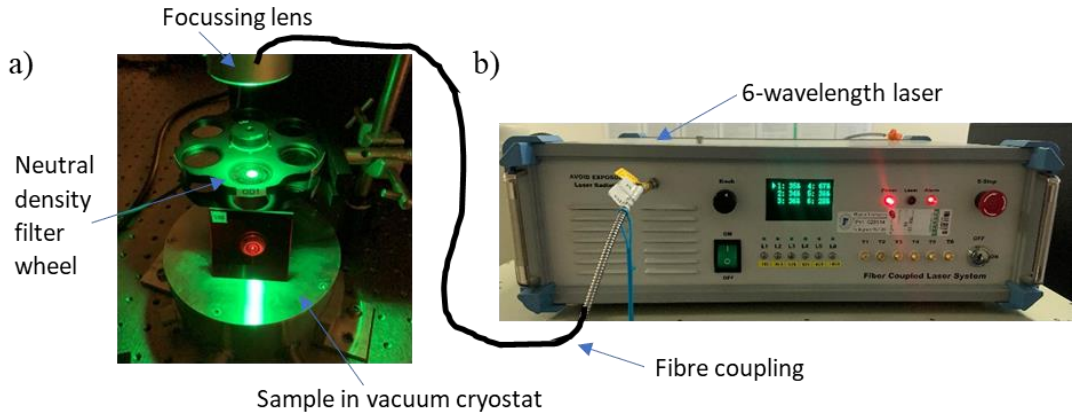


Figure 4.11. a) $CsPb(Br/I)_3$ sample on header mounted in cryostat with sapphire window for photocurrent measurements. The sample is being illuminated by λ_{ex} = 520 nm light and a 590 nm long-pass filter is used to show photoluminescence. **b)** 6λ fibre-coupled laser system with λ =405, 450, 532, 635, 808, and 1060 nm and power of < 30 mW.

Several light sources were employed for photocurrent measurements. Fixed wavelength excitations were provided by a 6-wavelength (6λ) fibre-coupled laser system (custom built system by Changchun New Industries Optoelectronics Tech. Co. Ltd) with wavelengths of 405, 450, 532, 635, 808, and 1060 nm which had full width at half maximum (FWHM) < 2 nm and power output < 30 mW per channel (**Figure 4.11b**). A deuterium lamp with a wavelength of 250 nm was also employed for UV measurements. A MicroHR monochromator (Horiba, MHRA-2X-FS, with 75 W xenon source) was also used for photocurrent measurements under tuneable wavelength (λ = 200 nm to 1000 nm).

4.6.5 Electrical Performance under Mechanical Bending

Mechanical bending testing was performed on samples printed on flexible substrates such as Kapton to test how mechanical bending affected a sample's electrical properties. The bending setup was made in-house and consisted of a stepper motor-based linear stage with 3D printed grips to mount the sample (**Figure 4.12**). The two ends of the sample were mounted between the end block and the moving carriage on the stage. The speed, curvature and number of bending cycles were controlled using a DRV8825 stepper motor. Electrical contacts were made at each end of the sample and a constant V_{sd} during bending while I_{sd} was measured continuously. $I(V)$ relationships were also measured on the sample at rest, at intervals between bending cycles.

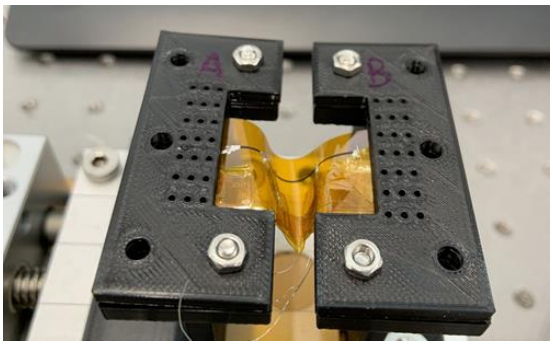


Figure 4.12. Printed iGr-$CsPbBr_3$ line on Kapton in mechanical bending setup, undergoing bending during electrical measurement.

5 FORMULATION AND CHARACTERISATION OF AM MATERIALS

Different low-D and polymeric materials were used in this project, including commercially available inks and new material formulations developed for inkjet deposition. This chapter describes the development and formulation of new inks, as well as the characterisation and optimisation of commercially available inks. Strategies for improving material performance through post-processing optimisations are also discussed, as well as studies to test material stability under different conditions.

The work included in this chapter on printed $CsPbBr_3$ and $CsPb(Br/I)_3$ (Br:I = 2:3) perovskite NCs is published in Austin et al., "Photosensitisation of inkjet printed graphene with stable all-inorganic perovskite nanocrystals", *Nanoscale, 2023, 15, 2134*. The work included in this chapter on PEDOT:PSS is published in Rivers et al., "Stable large area drop-on-demand deposition of a conductive polymer ink for 3D-printed electronics, enabled by bio-renewable co-solvents", *Addit. Manuf., 2023, 66, 103452.*

5.1 OPTIMISATION OF GRAPHENE INK AND DEVELOPMENT ON FLEXIBLE SUBSTRATES

The properties of inkjet printed graphene (iGr) using commercial graphene ink (Sigma Aldrich, product number: 793663) are well understood from previous studies [11], but to print high conductivity iGr films, very high thermal annealing temperatures (T_{anneal} = 250 °C, $t \geq 30$ mins) are required. This limits the applications of iGr in devices, as many materials and substrates cannot withstand these high temperatures, thus alternative post-deposition treatment strategies were explored.

For each annealing condition used, the resistance of 3 repeat samples were measured in 2-terminal geometries. First, thermal annealing at lower temperatures was explored. For 5 printed layer iGr films, annealing was conducted at T_{anneal} = 150 °C for t = 30 minutes and t = 2 hours, however, in both cases large sheet resistances R_s > 1 GΩ/sq were recorded, rendering them unsuitable for electrical applications. Longer annealing times of t = 18 hours at T_{anneal} = 150 °C were explored, and these samples displayed the far smaller sheet resistance R_s = 30 ± 20 kΩ/sq (**Figure 5.1**, blue line). While this resistance was about two orders of magnitude greater than that of iGr annealed at T_{anneal} = 250 °C (**Figure 5.1**, red line), it is ~ 10x smaller than that of iGr annealed 200 °C for 30 minutes [11]. This shows that conductive iGr layers can be achieved with decreased T_{anneal} using increased t. Further research is needed to fully understand the chemical changes that occur in iGr films following thermal annealing, such that annealing temperatures and times can be further optimised for specific applications.

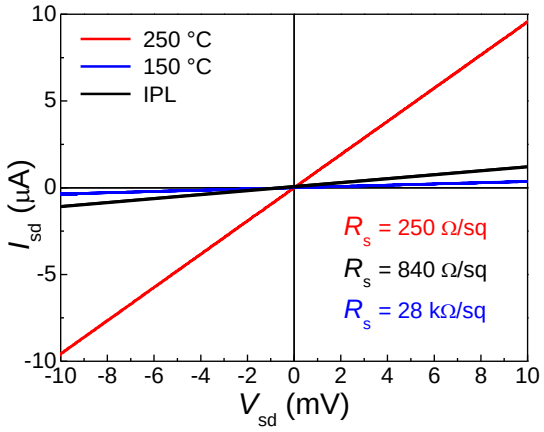


Figure 5.1. Representative $I(V)$ relationships of iGr films with 5 printed layers annealed using three different methods (thermal annealing at T_{anneal} = 250 °C for 30 mins, thermal annealing at T_{anneal} = 150 °C for 18 hours, and IPL annealing). All measured in 2-terminal geometry. Thermally annealed films were printed on Si/SiO_2 and IPL annealed film was printed on Kapton.

An alternative approach is photonic annealing. iGr films on Kapton were exposed to intense pulsed light (IPL), with a broad spectral range of λ = 550 - 900 nm with maximum intensity at 600 nm, pulse duration ~ 4 s, and flash power 5.4 J/cm^2 (**Chapter 4.4.2**). These samples displayed a sheet resistance of R_s = 700 ± 400 Ω/sq, comparable to that of iGr annealed at T_{anneal} = 250 °C (**Figure 5.1**, black line), but with larger variation between samples, possibly due to inhomogeneity in the IPL footprint. Initial studies suggest that the sheet resistance of IPL annealed iGr films is highly dependent on the substrate used, with much greater resistances (R_s > 10^5 Ω/sq) recorded for IPL annealed iGr films on glass and Si/SiO_2 substrates. It is likely that highly reflective substrates such as Si/SiO_2 and highly transparent substrates such as glass absorb less IPL than Kapton, resulting in less heating and thus poorer annealing of iGr films [296].

IPL annealing is a faster and less destructive post-processing step than thermal annealing and it was shown to be a promising method for post-processing of iGr. It also has the potential benefit of being performed in-situ during printing, however, further studies are needed to fully understand this process and ensure it is compatibility with different substrates.

5.2 Formulation of Perovskite Nanocrystals Inks

5.2.1 All-Inorganic $CsPbX_3$ NC Inks

The optical and morphological properties of all-inorganic $CsPbX_3$ (X = Cl, Br, I, or mixed) perovskite NCs were studied for light detection applications (**Chapter 7.2**). The NCs used are stable with respect to their optical properties for a period of at least 2 months (**Figure 5.2c**).The NCs were dispersed in hexane at a concentration of

5 mg/ml. The properties of $CsPbX_3$ NCs are highly dependent on their shape, size, and halogen composition.

All-inorganic $CsPbBr_3$ and $CsPb(Br/I)_3$ perovskite NCs capped with oleic acid and bromophenol ligands were used to formulate inks for inkjet printing. TEM imaging revealed that the $CsPbBr_3$ NCs had an average size of 11 ± 2 nm and were hexagonal in shape with high crystallinity (**Figure 5.2a,b**). A lattice spacing of 0.41 ± 0.02 nm was measured from TEM images, which corresponds to (110) plane of cubic $CsPbBr_3$ (**Figure 5.2a**) [297].

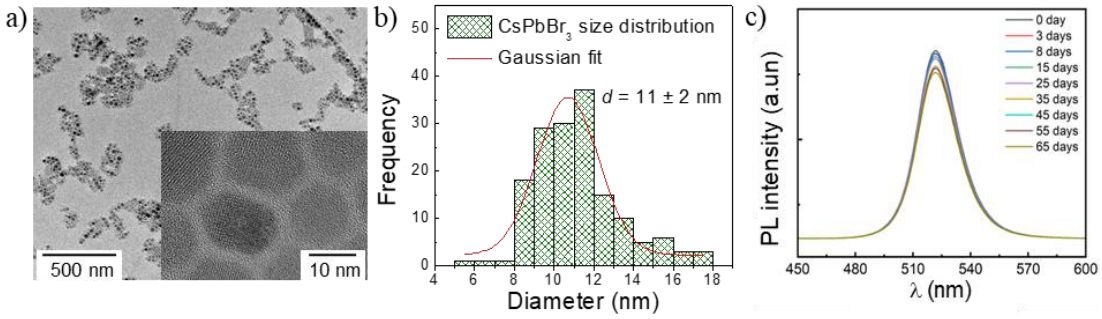


Figure 5.2. a) Representative TEM images of the $CsPbBr_3$ NCs (Imaged by Dr. Michael Fay) and **b)** size distribution of a profile of $CsPbBr_3$ NCs, with an average size of 11 ± 1 nm. **c)** PL spectra of $CsPbBr_3$ NCs recorded at different times over a period of two month (Provided by Dr. Chengxi. Zhang, Shanghai University).

To formulate the $CsPbX_3$ NCs inks for printing (**Figure 5.3a**), the NCs were added to a mixture of hexane, cyclohexanone, and terpineol (1 : 3 : 1 v/v) at a concentration of 5 mg/ml. The composition of the ink was optimised to achieve the viscosity of 1.53 mPa·s, surface tension of 37.8 mN/m, and density of 1.33 g/cm^3, giving an Ohnesorge number, Oh = 0.052 and an inverse Ohnesorge number, $Z = 1/Oh$ = 19. While this falls outside the optimal printing range ($1 < Z < 10$), consistent jetting was

achieved without satellite droplets. This is consistent with the literature, where jettable inks have been reported with Z values up to 35.5 [176].

To suppress the coffee ring effect, the high boiling point solvents terpineol and cyclohexanone, and the low boiling point solvent hexane are included together in the ink [40,298], and the substrate temperature was set to $T_{substrate}$ = 60 °C during printing for fast solvent evaporation. The inks were deposited in an inert N_2 atmosphere to avoid NC degradation during printing. A single droplet of NC ink printed onto Si/SiO_2 and on flexible Kapton formed spots with diameter of ~ 30 μm, thus to achieve uniform films, a 20 μm drop spacing was employed. The inks of $CsPbBr_3$ and $CsPb(Br/I)_3$ NCs were printed on flexible and rigid substrates (**Figure 5.3a**,**b**). After deposition, the $CsPbBr_3$ and $CsPb(Br/I)_3$ NC films had PL emissions centred at 515 nm and 625 nm with narrow FWHM of 17 and 30 nm, respectively (**Figure 5.3c**, dashed lines). The absorption edge of the $CsPb(Br/I)_3$ NCs was located at 625 nm, whereas the absorption edge of the $CsPbBr_3$ NCs was at 550 nm (**Figure 5.3c**, solid lines). Both inks demonstrated bright fluorescence under UV illumination (**Figure 5.3a,c**), and no change in the shape of their PL spectra was observed before and after deposition and drying.

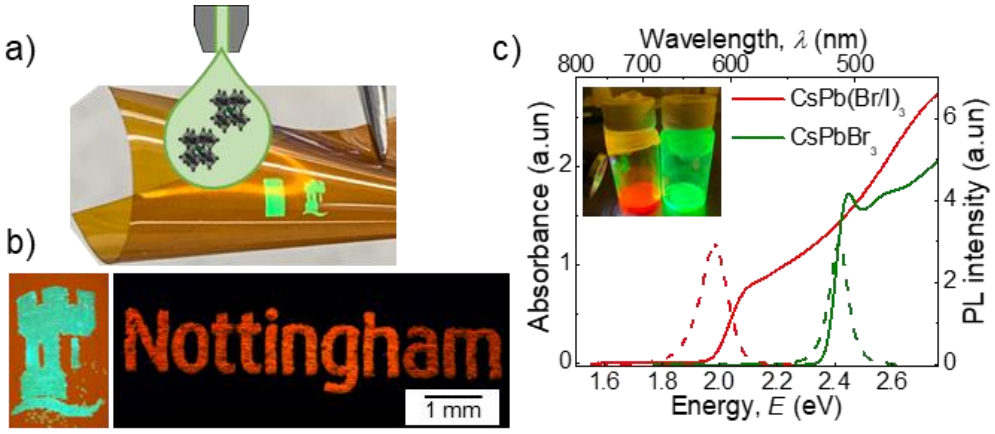


Figure 5.3. a) Diagram showing inkjet deposition of 5 mg/ml $CsPbX_3$ (X = Br or Br/I) perovskite NC ink formulation for inkjet printing (solvents (vol): 20% hexane, 60% cyclohexanone, 20% terpineol) with optical image of green pattern on Kapton undergoing bending with bright fluorescence under UV (λ_{ex} = 365 nm) illumination. **b)** Optical images of printed perovskite NC films, with green $CsPbBr_3$ on Kapton and red $CsPb(Br/I)_3$ (Br:I = 2:3) NCs on Si/SiO_2, both under UV illumination (λ_{ex} = 365 nm). **c)** Photoluminescence spectra (λ_{ex} = 405 nm) of printed films (dashed lines) and absorption spectra of inks (solid lines) for green $CsPbBr_3$ and red $CsPb(Br/I)_3$ NCs. Inset: optical image of $CsPb(Br/I)_3$ (red) and $CsPbBr_3$ (green) ink formulations for printing, illuminated under λ_{ex} = 365 nm UV light, with bright fluorescence.

PL mapping was used to assess the optical properties of $CsPbBr_3$ NC films with 1 and 2 printed layers, and 2 printed layers annealed at T_{anneal} = 100 °C, t = 30 mins under vacuum (**Figure 5.4a**). Note that uniform films were formed by inkjet deposition of one printed layer, due to reliable jetting and favourable ink wetting on the Si/SiO_2 substrate. A factor of 2 difference between the maximum and minimum PL intensity was recorded on PL maps of these samples (**Figure 5.4b**, right) which is attributed to surface roughness caused by the coffee ring effect, which was seen in optical microscopy images (**Figure 5.4b**, left). This could likely be reduced by changing the printing strategy such that printed swaths of subsequent layers are offset from the

previous layers, as was shown for PEDOT:PSS [26]. The non-uniformity in PL intensity of printed $CsPbBr_3$ films is reduced with increasing number of layers (**Figure 5.4c**). Importantly, thermal annealing, which is typically used as post deposition process (T_{anneal} = 100 °C), was shown to have a negligible effect on the PL uniformity (**Figure 5.4d**), or on the shape of the PL spectra (**Figure 5.4e**).

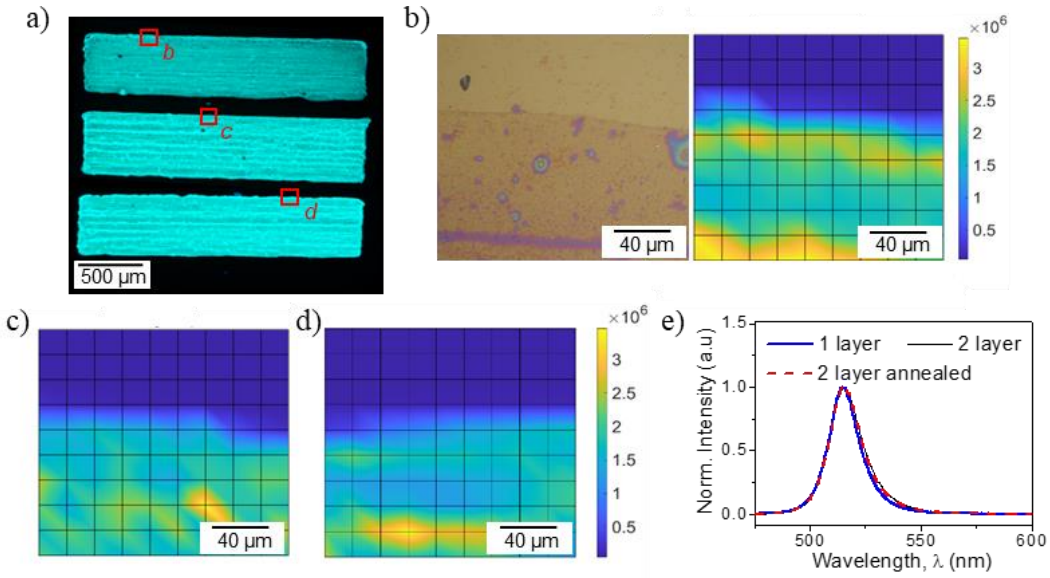


Figure 5.4. a) Representative optical images of $CsPbBr_3$ NC films under UV illumination (λ_{ex} = 365 nm). The top image shows 1 printed layer, middle image shows 2 printed layers and bottom image shows 2 printed layers annealed at T_{anneal} = 100 °C for t = 30 minutes. Representative maps of PL emission intensity (λ_{ex} = 405 nm) for **b)** 1 layer (with corresponding optical image shown on the left), **c)** 2 layers and **d)** 2 annealed layers of printed $CsPbBr_3$ NCs. **e)** Representative normalised PL spectra from each of the studied $CsPbBr_3$ films. PL measurements were performed with assistance from Dr. Tyler James.

AFM was used to determine the thickness at the edge of the perovskite NC film and access surface roughness. For five printed layers of $CsPbBr_3$ on Si/SiO_2 substrate, AFM images revealed a thickness of ~ 20 nm and a roughness of ~ 5 nm (**Figure 5.5a,b**). However, with AFM, the thickness of the printed film can only able measured

at its edge. The thickness of the $CsPbBr_3$ in the centre of printed swaths may be < 20 nm and roughness may be increased due to the coffee ring effect, as was indicated by PL mapping. Further studies of printed $CsPbX_3$ films should be carried out to access the morphology of films at the centre of printed swaths and further optimisation of the $CsPbX_3$ ink formulation could be carried out to improve uniformity of printed films.

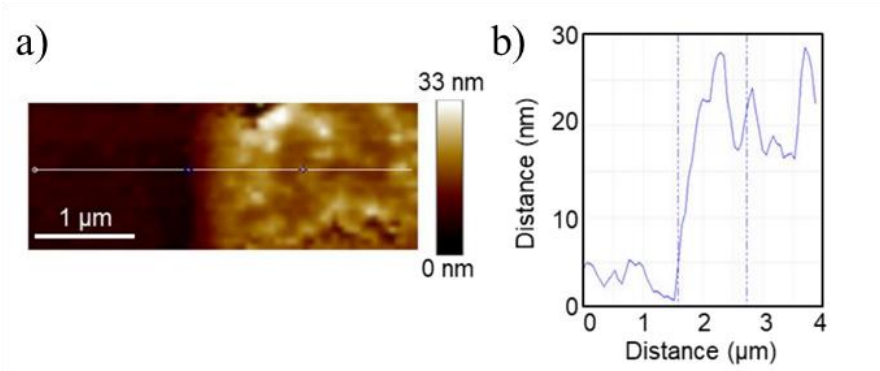


Figure 5.5. a) AFM image of the edge of 5 printed layers $CsPbBr_3$ film on Si/SiO_2 **b)** Height profile for the line indicated in the image (white line).

5.2.2 $CsPbX_3$-PVP Ink

Previous studies have shown that the addition of the polymer PVP to all-inorganic perovskite NC inks can improve environmental stability and ink rheology [102]. Addition of PVP may also affect the distribution of NCs within the printed films [186]. For these reasons, an ink was formulated that included both $CsPbX_3$ NCs and PVP ($CsPbX_3$-PVP). Studies were also performed to determine how the addition of PVP affects intermixing of NCs in printed heterostructures (**Chapter 6.3**).

$CsPbX_3$-PVP inks were formulated in the same way as the $CsPbBr_3$ and $CsPb(Br/I)_3$ inks but with the addition of 5 mg/ml of PVP. The addition of PVP increased the inks viscosity to 1.65 mPa·s and decreased surface tension 29.1 mN/m. This slightly improved ink printability as the inverse Ohnesorge number *Z* decreased to 16, closer

to the optimal printing range. The same printing parameters were used for the $CsPbX_3$ inks and the $CsPbX_3$-PVP inks. Visibly, printed $CsPbBr_3$-PVP films displayed the same bright green fluorescence under UV illumination as $CsPbBr_3$ films (**Figure 5.6a**).

PL spectra of the $CsPbBr_3$-PVP ink was comparable to the $CsPbBr_3$ ink used as a control (**Figure 5.6b**, solid green line) and displayed a PL peak position at λ = 515 nm and FWHM of 19 nm. The absorption spectrum of the $CsPbBr_3$-PVP ink was also comparable to the $CsPbBr_3$ ink in the visible range (**Figure 5.6b**, dashed green line), but the PVP greatly increased absorption at λ < 250 nm (**Figure 5.6c)**.

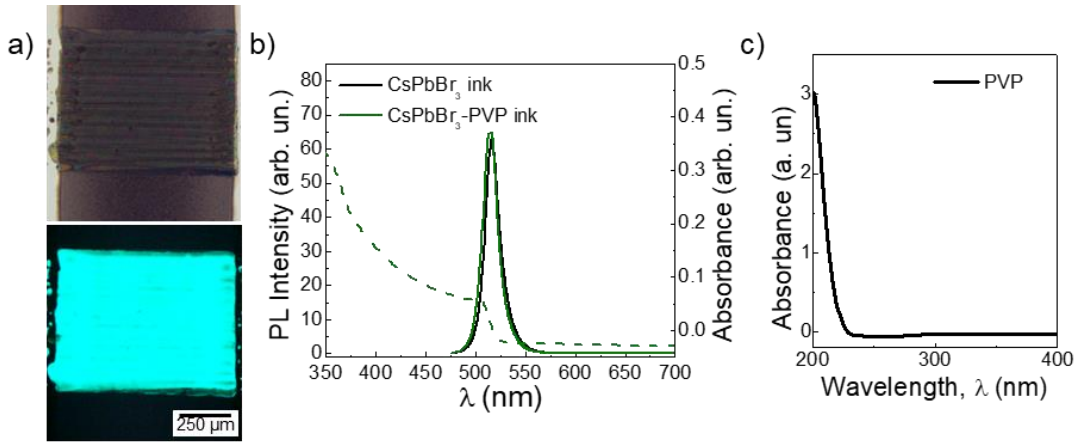


Figure 5.6. a) Optical images of 10 printed layer $CsPbBr_3$-PVP film on top of iGr line under white light (top) and λ_{ex} = 365 nm excitation (bottom) **b)** PL (solid) and absorption (dashed) spectra of $CsPbBr_3$ ink. PL spectra of $CsPbBr_3$ ink is also included for comparison **c)** Absorption spectra of PVP, measured in 1mg/ml cyclohexanone solution.

5.2.3 iGr-$CsPbX_3$ Hybrid Ink

Hybrid inks containing both iGr and perovskite NCs (iGr-$CsPbX_3$) were also formulated. The motivation behind this formulation was to include both the optically active material and the charge transport material in a single ink, so that photodetectors could be deposited in a single deposition step. It was also envisioned that the large

interfacial surface area created by mixing the two materials, may improve charge transport between them. iGr-$CsPbX_3$ inks were formulated for jetting by dispersing 5 mg/ml of $CsPbX_3$ NCs in a mixture of the iGr ink and hexane (2:1 v/v). The hybrid ink had a viscosity of 2.96 mPa·s, a surface tension of 27.4 mN/m, and density of 0.93 g/ml, giving $Z = 8$ which is within the optimal printing range.

Raman mapping was used to access printed iGr-$CsPbBr_3$ hybrid films, annealed at T_{anneal} = 150 °C, t = 30 mins. The peak intensity ratio I_D:I_G (peaks shown in **Figure 5.7a**) provides a quantitative descriptor of the number of structural defects in the graphene (the extent of deviation of the crystalline arrangement from a perfect hexagonally organized planar network of carbon atoms) [11]. The average I_D:I_G peak ratio was comparable to iGr and the observed small difference (**Figure 5.7b,c**) can be attributed to the different annealing temperature used [11].

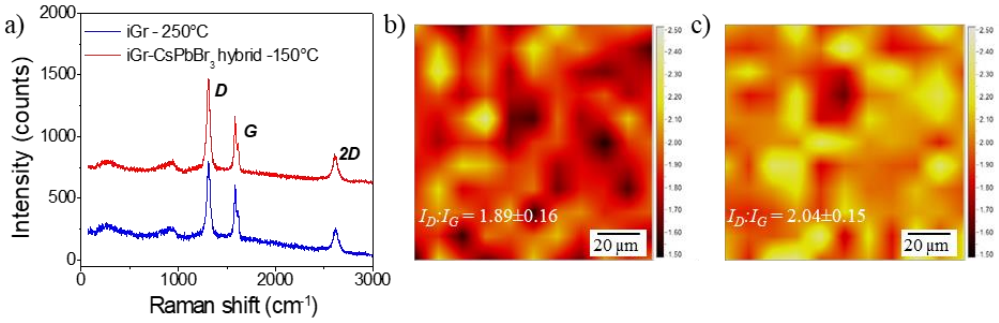


Figure 5.7. a) Representative Raman spectra of 5-printed layer iGr annealed at 250 °C for 30 mins and 5-printed layer iGr-$CsPbBr_3$ hybrid annealed at 150 °C for 30 mins. The D, G, and 2D peaks are labelled. Raman spectroscopic maps of the I_D:I_G peak ratio for **b)** iGr sample and **c)** iGr-$CsPbBr_3$ hybrid sample. Raman measurements were performed by Dr. Graham Rance.

Different annealing conditions were tested for printed iGr-$CsPbX_3$ hybrid films. For each annealing condition, 3 repeat samples were measured in 2-terminal geometries.

Printed films with 5 layers annealed at T_{anneal} = 250 °C for 30 mins displayed a sheet resistance R_s = 5 ± 3 x10^5 Ω/sq (**Figure 5.8**), however, they displayed no visible PL, indicating thermal degradation of perovskite NCs. Films annealed at T_{anneal} = 150 °C, t = 18 hours displayed a larger sheet resistance of R_s ~ 1 x10^7 Ω/sq for 5 printed layers, as was the case with the iGr films (**Figure 5.8b**), and the PL of the film remained visible after annealing (**Figure 5.8a**, inset). For both thermal annealing conditions, the iGr-$CsPbX_3$ films displayed significantly larger sheet resistance than iGr (**Figure 5.8b**), due to the presence of perovskite NCs, which can disrupt conductive graphene pathways and increase flake-to-flake junction resistance [11,299].

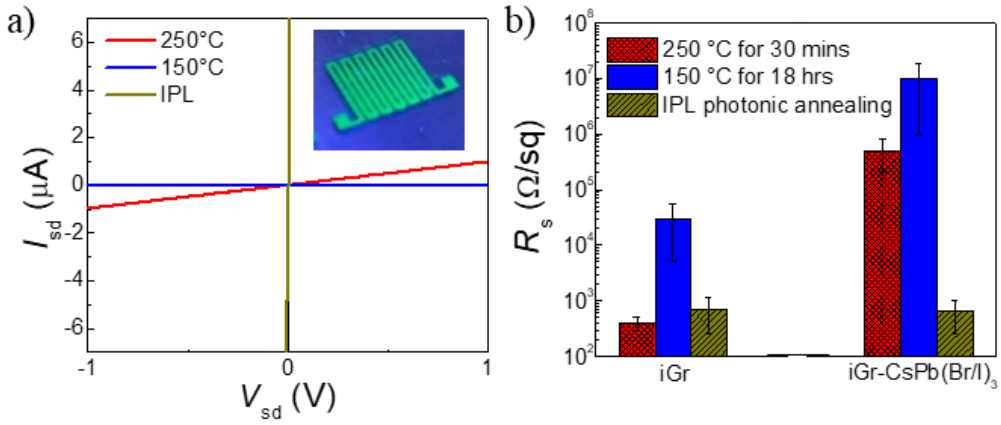


Figure 5.8. a) Characteristic $I(V)$ dependence of 5 printed layer iGr-$CsPb(Br/I)_3$ films annealed with 250 °C, 150 °C, and IPL photonic annealing. Inset: optical image of printed iGr-$CsPb(Br/I)_3$ hybrid film on glass annealed at 150 °C for 18 hours, with green fluorescence under λ_{ex} = 365 nm excitation. The pattern is ~ 1 cm in length. **b)** Comparison of the sheet resistances of 5 printed layer iGr and iGr-$CsPb(Br/I)_3$ films using different annealing conditions. Thermally annealed samples were printed on Si, IPL annealed samples were printed on Kapton. Error bars represent standard error from 3 repeat samples.

Photonic annealing using IPL was considered as an alternative annealing method for iGr-$CsPbX_3$ films, and achieved lower sheet resistance of 650 ± 400 Ω/sq for 5 printed

layers compared to thermal annealing (**Figure 5.8**). This result is in line with the effect of IPL annealing observed for iGr films (**Figure 5.8b**). Once again, no visible PL was observed for iGr-$CsPbX_3$ films annealed with IPL treatment, likely due to perovskite degradation under intense light exposure. The hybrid layers deposited onto flexible Kapton substrates (T_{anneal} = 150 °C, t = 18 hours) had stable electrical performance over at least 200 bending cycles, similar to the performance seen previously for iGr films [300], indicating that this material is suitable for flexible electronics application (**Figure 5.9**). By combining the optically active perovskite NCs and conductive graphene into a single ink, optoelectronic devices could be printed in a single deposition step. However, so far it has proved challenging to develop a printing and post-processing method that enables deposition of films which retain both the optical properties of the NCs and the electrical properties of iGr.

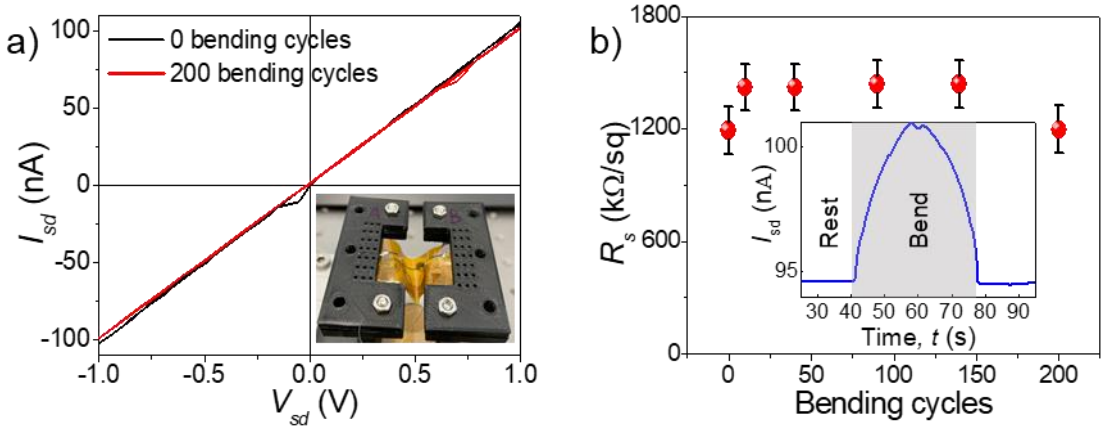


Figure 5.9. a) $I(V)$ dependence of 5-layer iGr-$CsPbBr_3$ hybrid line before and after undergoing 200 bending cycles with bending radius 0.5 cm. **b)** Sheet resistance of sample after different numbers of bending cycles, calculated from $I(V)$s at different intervals. Error bars were calculated from linear fitting of $I(V)$s and by the range of the resistance recorded in-situ (with constant V_{sd} = 1 V) using the 5 bending cycles before and after the $I(V)$ measurement was taken. Inset: current measured through the sample continuously during a single bending cycle (V_{sd} = 1 V).

The perovskite NC inks in this study were developed with the goal of producing thin and uniform inkjet printed films, on rigid and flexible substrates, for optoelectronic device applications, with stable optical performance following formulation and deposition. $CsPbX_3$ NC films with 5 printed layers displayed a thickness of ~ 20 nm with roughness of ~ 5 nm and maintained bright PL after printing and annealing at T_{anneal} = 100 °C for t = 30 mins. This was accompanied by a factor of 2 difference between regions of maximum and minimum PL intensity. The $CsPbX_3$ films developed here are an order of magnitude thinner than printed $CsPbBr_3$ films formulated previously for colour converter film applications [199]. Other works have demonstrated films with comparable thickness and uniformity [198], but the $CsPbX_3$ NC inks developed in this study have the advantage of being printable on both rigid and flexible substrates. Further morphological studies are required to fully access the $CsPbX_3$-PVP ink formulation, however it seems a promising formulation to improve environmental stability of printed films. Alternatively, the hybrid iGr-$CsPbX_3$ ink appears a promising for single step deposition of devices, but further studies are needed to develop a printing and post-processing method that retains both the optical properties of the NCs and the electrical properties of iGr.

5.3 GRAPHENE QUANTUM DOTS

Commercially available GQDs with sizes of < 5 nm were purchased from Sigma Aldrich (product number: 793663). AFM mapping of drop-cast GQDs (0.01 mg/ml in water) on glass revealed that the GQDs aggregate into clusters of ~ 50 nm in size (**Figure 5.10a**). The GQDs displayed blue fluorescence under λ_{ex} = 365 nm (**Figure 5.10b**, inset) and their PL spectra (measured in solution) displayed two peaks, a larger

primary peak at λ = 485 nm and a smaller one at λ = 610 nm (**Figure 5.10b**, solid line). The peak at λ = 485 nm is commonly attributed to GQD oxidation [301]. The absorption edge of the GQDs was observed at λ ~ 430 nm and absorption peaks were observed at λ = 350 nm and λ = 240 nm (**Figure 5.10b**, dashed line). The resistance of a GQD film was measured by depositing the GQDs via drop-casting (1 mg/ml in water) between pre-patterned Au contacts (20 µm gap) on Si/SiO_2 (inset of **Figure 5.10c**). The GQDs were observed to be highly insulating, with resistance of ~ 10^{10} Ω recorded in vacuum across the contacts on pristine Si/SiO_2 (300 nm of SiO_2) substrate, which was unchanged before and after the deposition of 1 to 5 drops of GQDs.

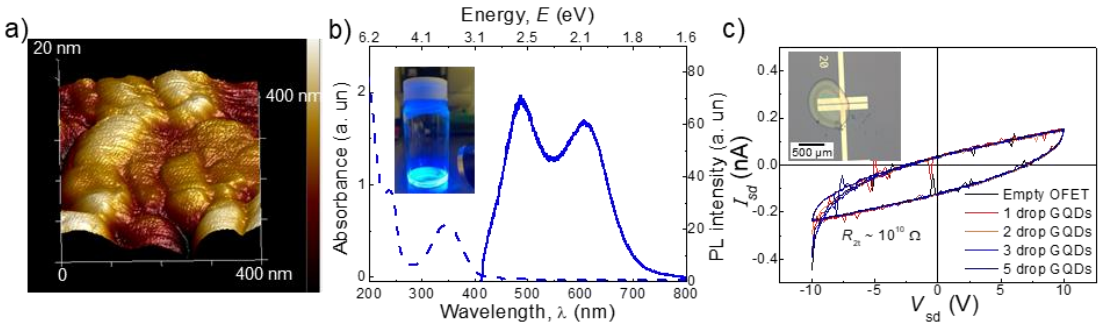


Figure 5.10. a) AFM map of drop-cast GQD film and **b)** absorption (dashed) and PL (solid) spectra, measured with λ_{ex} = 405 nm for GQDs ink. Inset: optical image of GQD ink with blue fluorescence under λ_{ex} = 365 nm. **c)** $I(V)$ relationships of 2-terminal OFET device with 20 µm space between contacts, before and after deposition of 1, 2, 3, 4, and 5 drops of GQD ink between the contacts via drop-casting. Inset: optical image of OFET following deposition with 1 drop of GQD ink.

GQD inks were formulated by mixing 1 mg/ml GQD solution in water (0.86 mL) with butanol (0.032 mL) and IPA (0.11 mL), which gave an ink with Z = 19; similar to the perovskite ink, and consistent jetting was achieved without any satellite droplets. Drop formation was stable, hence cleaning cycles were not employed at any stage during printing. After printing, GQD films were annealed at T_{anneal} = 100 °C for t = 30 mins

to remove solvents. While GQD ink jetting was consistent, de-wetting was observed on Si/SiO_2 substrates, leading to GQD films breaking up and forming many isolated islands of material. Based on optical microscopy, the best GQD films were formed on glass, however, they still displayed poor uniformity due to de-wetting (**Figure 5.11a**). Moreover, no visible photoluminescence was observed in the printed GQD films, likely due to reabsorption caused by GQD aggregation [125].

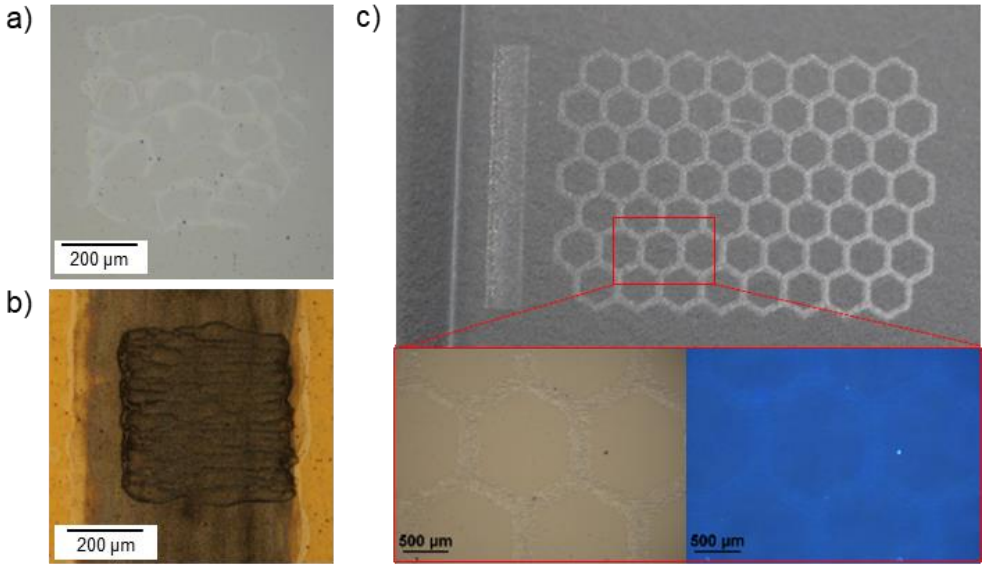


Figure 5.11. Optical images of **a)** 5 layer GQD film printed on glass, **b)** 5 layer GQD-PEG film printed on iGr, **c)** 5 layer GQD-PVP film printed on glass, printed in a honeycomb pattern. Inset: zoomed images of film under white light (left) and under λ_{ex} = 365 nm with blue fluorescence (right).

The polymers PEG and PVP were added to the GQD ink, formulating GQD-PEG and GQD-PVP inks to improve the wettability of GQD inks onto substrates such as Si/SiO_2, and also to improve PL of printed films by suspending the QDs in a polymeric matrix to reduce reabsorption. The GQD-PEG had a viscosity of 0.75 mPa·s, a surface tension of 71.2 mN/m, and density of 1.06 g/ml, leading to Z = 47. The GQD-PVP ink had a viscosity of 1.18 mPa·s, a surface tension of 32.6 mN/m, and a density of

1.06 g/ml, leading to $Z = 21$. In both inks Z was increased but consistent jetting was still achieved. The printed GQD-PEG ink still displayed poor wetting on glass and Si/SiO_2, but much more uniform films were formed on iGr (**Figure 5.11b**), which is potentially useful for photodetector applications (**Chapter 7.4**). The GQD-PVP ink displayed the best wetting (**Figure 5.11c**), and films could be printed on Si/SiO_2 substrate (**Figure 5.12d**), however, non-uniformity in the film was still evident and is likely caused by the inks high surface tension creating a capillary force that pulls the ink to the left during drying [302]. Unlike GQD films, both the GQD-PEG and GQD-PVP films displayed visible fluorescence under excitation with $\lambda_{ex} = 365$ nm (**Figure 5.11c**, inset), likely due to reduced GQD aggregation and reabsorption [125].

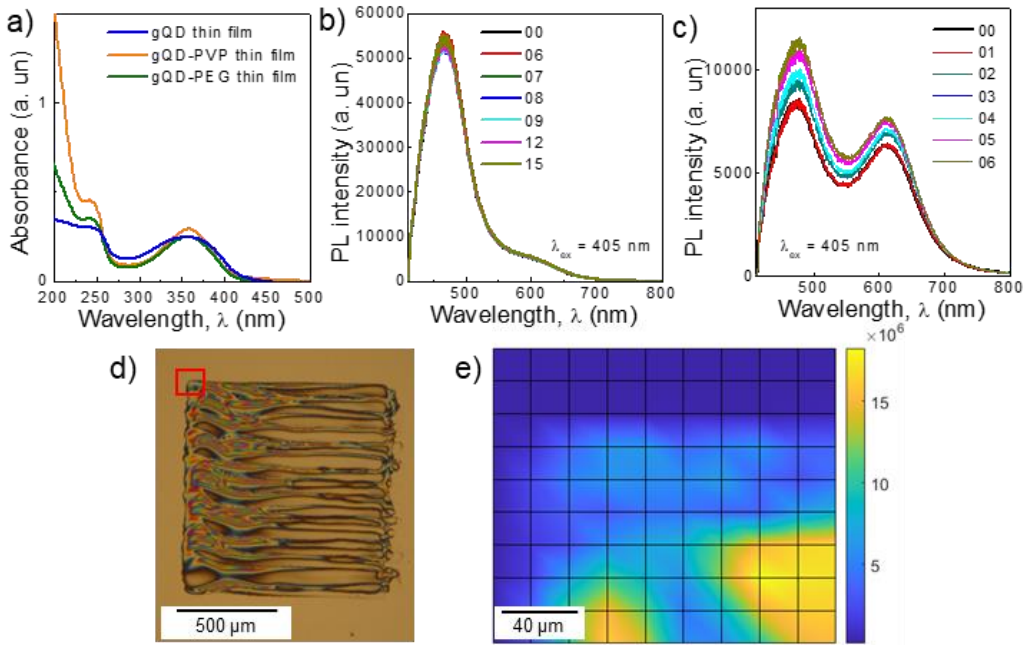


Figure 5.12. a) Optical absorbance of GQD, GQD-PEG, and GQD-PVP thin films deposited on quartz via drop-casting. **b)** PL spectra of GQD-PVP ink and **c)** PL spectra of printed GQD-PVP film (λ_{ex} = 405 nm). Successive PL spectra were taken multiple times in the same spot to access how the PL spectra changed after illumination. **d)** Optical image of 5 printed layer GQD-PVP film on Si/SiO_2. Red square indicates region over which PL mapping was conducted. **e)** PL intensity map of printed GQD-PVP film (λ_{ex} = 405 nm).

The absorption spectra of the GQD inks were not significantly changed after the addition of PEG or PVP. Only an increase in UV absorbance in GQD-PVP films at λ < 250 nm was observed (**Figure 5.12a**), in agreement with UV absorption spectrum of PVP [303]. PL spectra of the GQD-PVP ink (**Figure 5.12b**) and printed GQD-PVP films (**Figure 5.12c**) displayed large intensity peaks at λ = 480 and 470 nm, respectively. A smaller intensity peak at λ = 610 nm was still present for the printed GQD-PVP film (**Figure 5.12c**) but its intensity was reduced for the GQD-PVP ink (**Figure 5.12b**). This indicates that GQD oxidation largely occurs during printing. Also, since the peak at λ = 610 nm was observed in the GQD ink (**Figure 5.10b**), but

not in the GQD-PVP ink (**Figure 5.12b**), it was concluded that the PVP provided a degree of protection to the GQDs from oxidation. The PL intensity of the GQD-PVP ink remained constant upon successive PL measurements in the same spot (**Figure 5.12b**), however, the PL intensity of the GQD-PVP film increased with each successive measurement (**Figure 5.12c**). This may be caused by the optically induced Stark effect, which has previously been reported for bilayer GQDs [304], however, further studies are required to investigate this effect.

PL mapping of 5 printed layer GQD-PVP film on Si/SiO_2 substrate revealed significant non-uniformity of PL intensity with ~ 5× difference recorded across the mapped region (**Figure 5.12d,e**). This was attributed to non-uniformity in the printed layer, which was corroborated by AFM imaging (**Figure 5.13**). This revealed a film thickness of ~ 50 nm at the edge of the film (**Figure 5.13b**, red line) but also showed regions of material agglomeration with thickness of ~ 200 nm (**Figure 5.13b**, blue line). This may be due to the high surface tension of the GQD-PVP ink creating a capillary force that pulls the ink to the left during drying [302], thus further optimisation of the GQD inks should be studied to achieve greater uniformity.

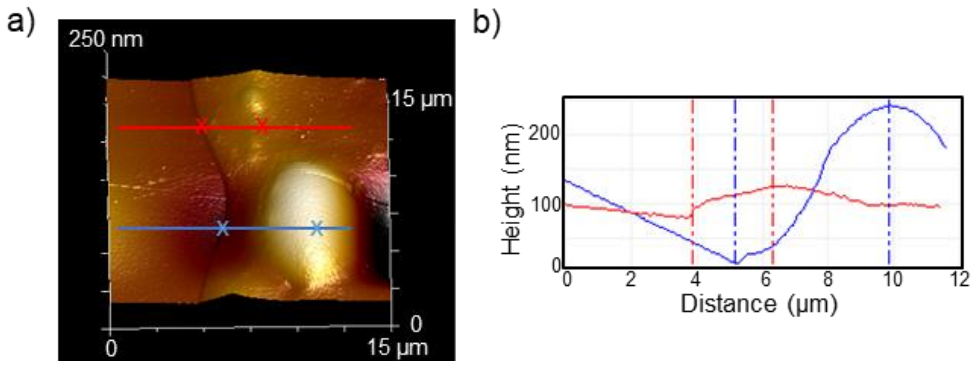


Figure 5.13. a) A representative 15 x 15 µm AFM map taken at the edge of the printed GQD-PVP film. **b)** Height profiles, measured across the red and blue lines marked on the AFM map.

Of the 3 different GQD inks formulated, the addition of PVP in the GQD-PVP ink improved wetting, PL intensity, and environmental stability and GQD-PVP films were printed on a variety of substrates. However, large non-uniformity was observed in the printed films and further optimisation is therefore required to reduce this for use in high performance optoelectronic devices. An increase in PL intensity following optical illumination was also observed, which may be caused by the optically induced Stark effect [304]. So far, very few works have demonstrated inkjet deposition of GQD [202,203]. In these examples, GQDs are deposited in a single non-polar solvent for chemical sensing applications and no characterisation of the GQD film morphology is shown. Therefore, this work has the significance of being the first water-based GQD ink formulation, and the morphological and optical characterisation performed on printed GQD films improves the understanding of printed GQDs, towards their integration into optoelectronic devices and with potential applications in bioelectronics.

5.4 PEDOT:PSS

PEDOT:PSS inks were developed by Dr. Rivers [26]. During printing of heterostructures and operation of devices, printed PEDOT:PSS layers will be exposed to different environments such as long-term exposure to ambient conditions, exposure to UV illumination when co-printed with photocured polymers (e.g. tripropylene glycol diacrylate (TPGDA) [305]), and exposure to IR or thermal annealing when co-printed with nanoparticle-based inks (e.g. AgNPs [186]and AuNPs [27]). Therefore, the stability of PEDOT:PSS inks with respect to their electrical properties in different environmental conditions was examined (**Figure 5.14**). Ink_{CG} denotes to the highly stable PEDOT:PSS ink formulated by Dr. Rivers [26] with the green renewable

solvents cyrene and glycerol carbonate that exhibits improved jetting stability and suppressed coffee ring formation during drying. Ink_{DMSO} denotes the DMSO-based control formulation which is similar to PEDOT:PSS inks formulated in previous works [207].

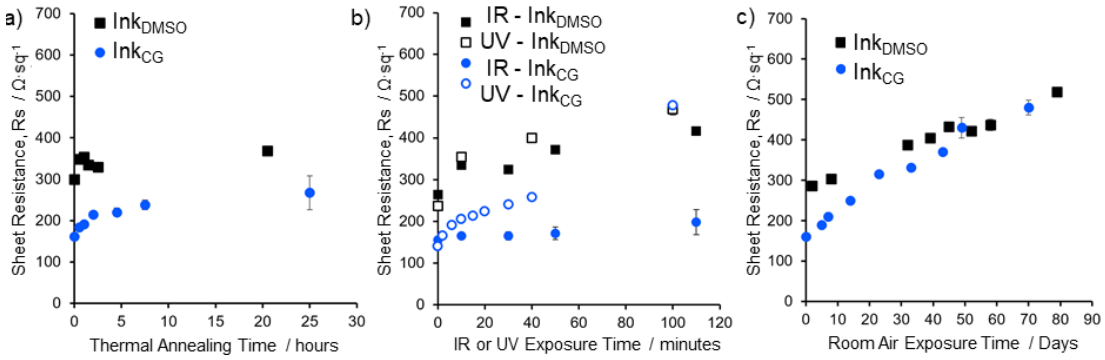


Figure 5.14. Sheet resistance of 4 layer printed films of PEDOT:PSS ink formulations Ink_{DMSO} and Ink_{CG} during exposure to **a)** thermal annealing (T_{anneal} = 140°C), **b)** irradiation by IR and UV, and **c)** room air exposure over time, respectively. Error bars are 0.95 confidence interval and 3 repeats.

PEDOT:PSS sheet resistance, *Rs*, was measured on printed squares (1.24 mm x 1.24 mm) in a Van der Pauw configuration (**Chapter 4.6.2**). Both Ink_{DMSO} and Ink_{CG} displayed a small change in sheet resistance after t = 2.5 hours of annealing at T_{anneal} = 140°C (**Figure 5.14a**), with Ink_{DMSO} demonstrating an increase from R_s = 299 Ω/sq to 329 Ω/sq and Ink_{CG} from R_s = 162 Ω/sq to 214 Ω/sq. Further increase in annealing time, however, (up to t = 24 hours) had no significant effect on R_s.

In contrast, during the first 2 hours of IR exposure (**Figure 5.14b**, filled data points), Ink_{CG} displayed no significant change, while an increase of R_s was observed for Ink_{DMSO}. For all tested IR exposure durations (t = 10 minute to t = 2 hours), the sheet resistance of Ink_{CG} remained lower than that of Ink_{DMSO}. This result indicates that the Ink_{CG} is more suitable for multi-material designs requiring deposition of nanoparticle

ink, where post-processing conditions would only have a small or negligible impact on its sheet resistance.

Both ink formulations demonstrated comparable stability under UV exposure (**Figure 5.14b**, hollow data points), where about 2× increase of sheet resistance of Ink_{CG} to 250 Ω/sq was observed after 40 minutes exposure (~ 890 $J \cdot cm^{-2}$). This UV exposure is comparable to that required for inkjet printing of over 1500 photocurable polymer layers using a Dimatix printer [306], and thus likely sufficient for inkjet deposition of 3D printed heterostructures and for deposition of electronic packaging layers. Long-term exposure to ambient conditions also affects the stability of electrical properties of both formulations (**Figure 5.14c**) with R_s increasing by a factor of 2 after 24 days storage. This instability is likely due to the presence of oxygen and can be improved by sealing the PEDOT:PSS with surface capping to prevent oxidation [307]. This was demonstrated by measuring the change in resistance, ΔR, normalised to initial resistance, R_0, for drop-cast Ink_{CG} specimens on glass, using cyanoacrylate glue (Loctite 1608412) as a protective capping layer (**Figure 5.15a**). The uncapped specimens degraded more rapidly than the capped ones (**Figure 5.15b**), confirming that oxygen and/or moisture affect the ink stability, likely contributing to the degradation of Ink_{CG} in air.

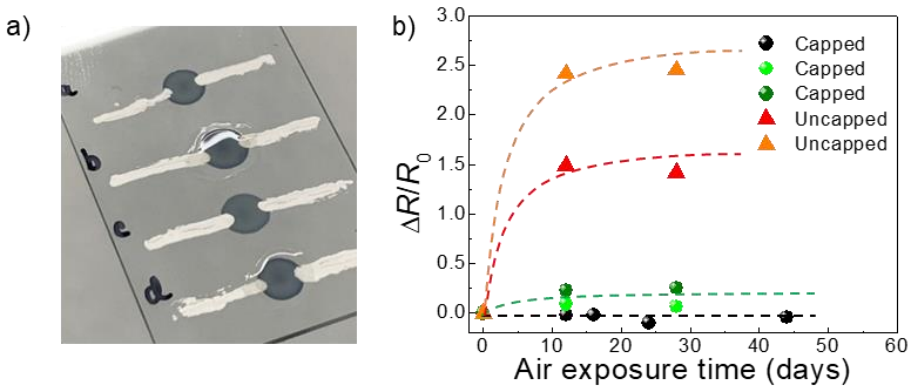


Figure 5.15. a) Optical photograph of drop-cast Ink_{CG} specimens on glass capped with cyanoacrylate glue (samples a and c) and uncapped (samples b and d). **b)** Relative resistance of capped and uncapped Ink_{CG} undergoing 2-month air exposure (dashed lines are a guide to the eye).

To explore its potential for flexible electronics, a line of Ink_{CG} (3 mm × 55 mm, 4 printed layers) was printed on a PEN substrate and subjected to bend testing (**Figure 5.16**), where only a 10% increase in R_s was observed after 2000 cycles, indicating that Ink_{CG} may be applicable to future flexible electronics applications.

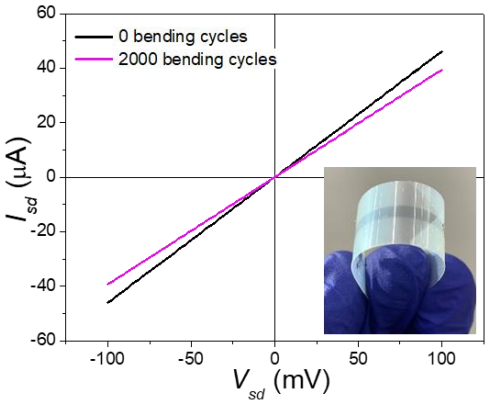


Figure 5.16. *I*(*V*) characteristics of 4-printed layer Ink_{CG} on PEN before and after undergoing 2000 bending cycles with a bending radius of 1.4 cm, measured in 2-terminal geometry. Inset: photograph of sample undergoing bending.

It was shown that the stability of the printed PEDOT:PSS using Ink_{CG} was improved or at least as good as the control Ink_{DMSO} formulation under all the conditions examined. The PEDOT:PSS films deposited with the Ink_{CG} formulation did not display a significant increase in resistance following 24 hours of thermal annealing at T_{anneal} =140°C, 2 hours of IR sintering, or 20 mins of UV exposure. Thus it was concluded that the PEDOT:PSS is suitable for use in heterostructure applications, where annealing conditions of the other materials are within these limits. It was also shown that the resistance of the Ink_{CG} PEDOT:PSS was highly increased after ~ 2 months exposure to ambient conditions. However, it was demonstrated that this could be greatly reduced by capping the surface with cyanoacrylate glue. Finally, the formulation was shown to be highly resistant to bending, showing its potential in flexible/wearable electronic devices.

5.5 POLY-TPD AND TPBI

As charge injection materials, poly-TPD and TPBI (with thicknesses of $\lesssim$ 50 nm) are commonly used in LED applications [158,163]. Therefore, poly-TPD and TPBI inks were formulated, with the goal of producing thin and uniform films via inkjet printing.

A poly-TPD ink was formulated as described in reference [210], by dispersing 1.5 mg/ml of poly-TPD in chlorobenzene (CB) and stirring at 40 °C for 2 hours. The ink had a viscosity of 0.61 mPa·s, a surface tension of 28.5 mN/m, and density of 1.28 g/ml, giving Z = 40. Despite large Z, consistent jetting was achieved without the formation of satellite droplets. Printing was performed with a custom waveform at room temperature with a drop spacing of 40 µm on Si/SiO_2 (**Figure 5.17a**) and on flexible PEN substrates.

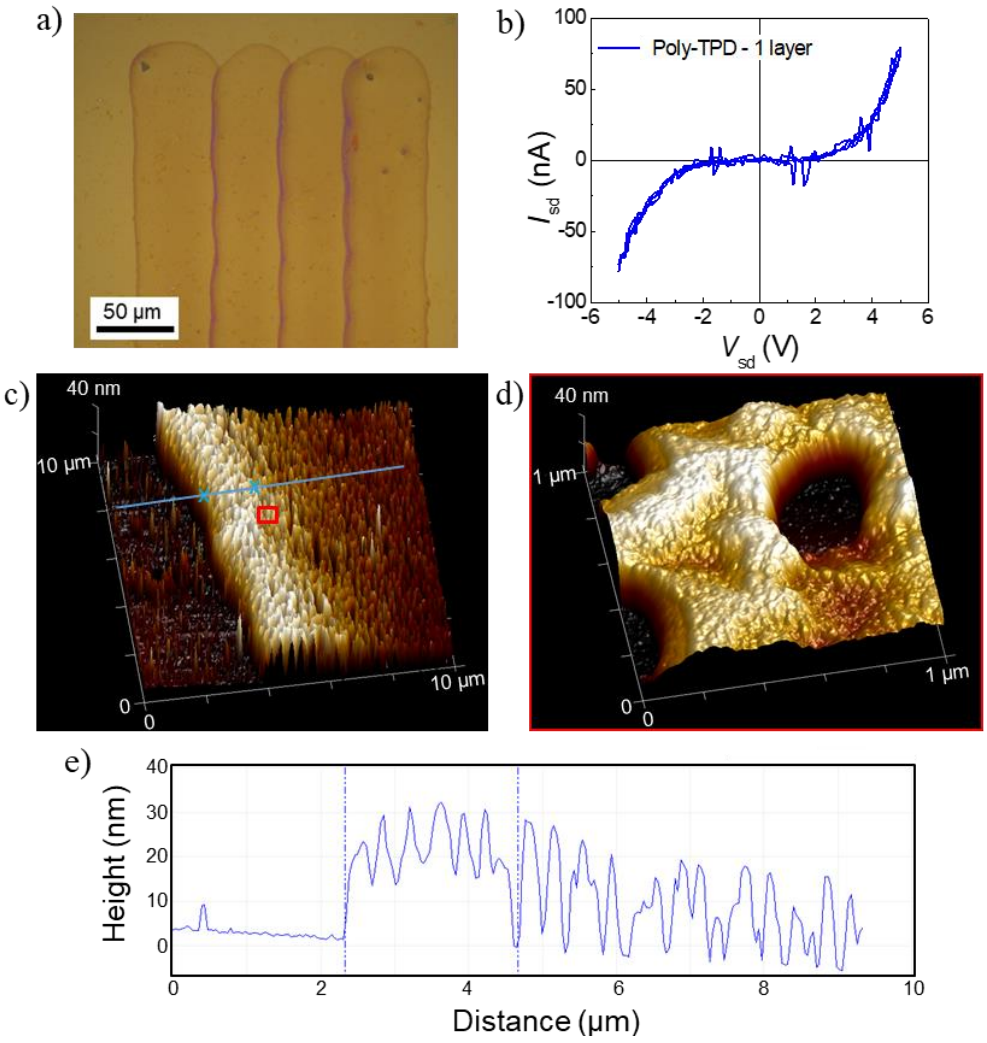


Figure 5.17. a) Optical image of a single layer printed poly-TPD film on Si/SiO_2 substrate. **b)** $I(V)$ relationship of film measured in 2-terminal configuration for 800 µm x 60 µm sample. AFM images of a single printed layer poly-TPD film on Si/SiO_2, **c)** shows a 10 x 10 µm map at the edge of the film and **d)** shows a 1 x 1 µm area map taken in the area marked by the red square. **e)** Height profile measured across the blue line marked on the AFM map.

The resistance of a single printed line of poly-TPD on Si/SiO_2 was measured in a 2-terminal geometry, and was shown to have non-Ohmic $I(V)$ dependence at $V_{sd} > 2$ V and displayed a sheet resistance of ~ 8 x 10^6 Ω/sq (**Figure 5.17b**) which is comparable to that reported previously for spin-coated poly-TPD films [308]. AFM imaging

showed that printed films have a thickness of ~ 20 nm, increasing to ~ 30 nm at the edge of the film due to the coffee ring effect (**Figure 5.17c-e**). This thickness is comparable to spin coated poly-TPD films used previously in LEDs [158,163]. The printed films are uniform over the area of several microns. However, some de-wetting is observed on the Si/SiO_2 substrate resulting in the formation of small pillars and valleys with areas of ~ 200 nm (**Figure 5.17d)**.

The TPBI ink was formulated by dispersing 4 mg/ml of TPBI in a mixture of hexane, n-butanol, and terpineol (1:3:1 v/v). The composition of the ink was optimised to achieve the viscosity of 2.62 mPa·s, surface tension of 26.4 mN/m, and density of 0.9 g/cm^3, giving Z = 8, which is within the range for optimal jetting. Printing was performed at $T_{substrate}$ = 40 °C to ensure rapid solvent evaporation and the mixture of high boiling point terpineol and low boiling point hexane was used in the ink to supress the coffee ring effect. Printed TPBI films with 2 printed layers on Si/SiO_2 (**Figure 5.18a**) displayed a sheet resistance of $R_s \sim 10^8$ Ω/sq (**Figure 5.18b**) and a thickness of ~ 20 nm (**Figure 5.18c,d**), comparable to TPBI films deposited via spin coating [167,173,309] for LED applications. However, the AFM map also revealed de-wetting, which creates large roughness in the film.

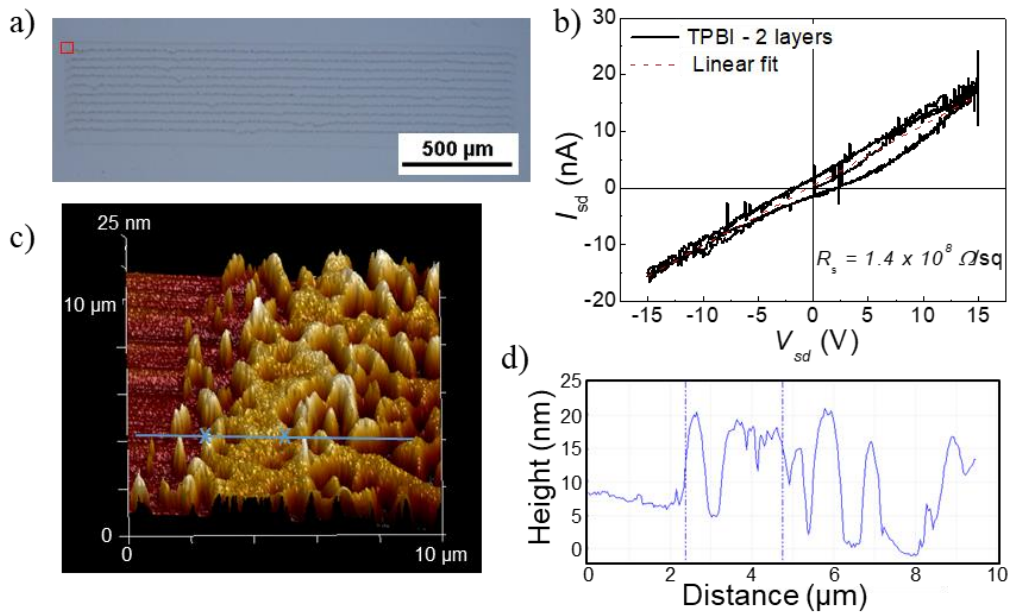


Figure 5.18 a) Optical image of 2 printed layer TPBI film on Si substrate. **b)** *I*(*V*) relationship of film measured in 2-terminal configuration for 0.26 mm x 0.25 mm sample **c)** 10 x 10 µm AFM map at the edge of the TPBI film. **d)** Height profile measured across the blue line marked on the AFM map.

The printed poly-TPD and TPBI films both display comparable thickness and sheet resistance to layers deposited previously via spin coating for charge injection applications in LEDs [308,309]. These results improve capability and understanding of printing charge injection layers for LEDs. However, both films display significant non-uniformity which may cause short-circuiting in vertical devices, thus further work is needed to fully optimise these inks for heterostructure applications.

5.6 SUMMARY

Commercial available and previously formulated inks were investigated for different applications. For the iGr ink, it was shown that higher conductivity can be achieved using lower T_{anneal} with longer *t*. It was also shown that photonic annealing using IPL

could achieve high conductivity films, allowing iGr to be printed on a wider range of substrates. For the PEDOT:PSS ink (Ink_{GC}) it was shown that printed films did not display a significant increase in resistance following 24 hours of thermal annealing at T_{anneal} =140°C, 2 hours of IR sintering, or 20 mins of UV exposure. Thus it was concluded that the PEDOT:PSS is suitable for use in heterostructure applications.

Inks were formulated for printing all-inorganic $CsPbX_3$ perovskite NCs, GQDs, poly-TPD and TPBI. The optical and electrical properties, and the morphologies of printed films were characterised to access their use for applications in optoelectronic heterostructure devices. Printed perovskite NC films had comparable morphology and optical properties to previous formulations [198], but with the advantage of being printable on both rigid and flexible substrates. The addition of PVP into the $CsPbX_3$ NC ink seems a promising method to improve environmental stability of printed films and the hybrid iGr-$CsPbX_3$ ink, with further post-processing optimisation, appears a promising method for single step deposition of devices.

For the first time, water-based ink formulations were developed for GQDs and it was found that the addition of PVP in the GQD ink improved wetting, PL intensity, and provided protection from oxidation. A poly-TPD ink, and for the first time, a TPBI ink were also formulated. For both materials, printed films displayed comparable thickness and sheet resistance to layers deposited previously via spin coating for charge injection applications in LEDs [308,309]. However, non-uniformity was observed in printed films for all these materials, thus further optimisation of ink formulation and deposition may be required for use in high performance optoelectronic devices.

For all the inks developed in this work, it was found that a good formulation strategy was to use a combination of low- and high-boiling point solvents to reduce the coffee ring effect. It was also generally found that use of a high substrate temperature was beneficial to quickly evaporate the solvents for improved film uniformity. Moreover, it was found that the inverse Ohnesorge number *Z*, was not the only indicator of ink printability. In theory, the optimal printing range is between 1 and 10, however, consistent jetting was achieved using inks with *Z* numbers up to 40, as was reported previously [176]. It was found that particle size and concentration generally had a larger effect on printability, as inks containing large graphene flakes tended to cause nozzle blockages and required frequent cleaning cycles. For inks of 0D nanomaterials, it was found that the addition of polymers (specifically PVP) was a promising method to improve ink wetting on various substrates, improve environmental stability, and prevent NC aggregation.

For 0D nanomaterials soluble in aqueous solvents, two common formulation strategies were established. The first employed a mixture of hexane, cyclohexanone, and terpineol and the second employed a mixture of water, butanol, and IPA. Since these studies, it has also been demonstrated that printing of lanthanide-doped upconverting NPs can be achieved using the first formulation, and printing of PbS QDs can be achieved using the second formulation. It is therefore proposed that for small (< 5 mg/ml) weight fraction of 0D nanomaterials, the solvent/additive mixture defines ink properties, thus these formulations are likely applicable to any 0D nanomaterial, so long as the solvent are compatible. Therefore, this work has the significance of developing ink formulations applicable to a wide range of materials, which greatly simplifies the process of ink formulation.

6 INKJET PRINTING HETEROSTRUCTURES

This chapter reports on a variety of investigations into inkjet printed heterostructures. First, an interesting wetting phenomenon is explored which occurs when printing heterostructures, which is exploited to print very precise patterns and heterostructure arrays. Then an investigation of printed heterostructures interfaces is shown using time-of-flight secondary ion mass spectroscopy (ToF-SIMs) and focussed ion beam scanning electron microscopy (FIB-SEM), with the goal of controlling printed heterostructure interfaces and the performance of vertical devices using different printing methods. Studies were also carried out to investigate how the morphology and electrical properties of printed layers are affected after inkjet deposition of other materials on top.

ToF-SIMS measurements were carried out by Dr. Gustavo Trindade and Dr. Yundong Zhou at the National Physics Laboratory. FIB-SEM and EDX were performed by Dr. Negar Gilani using equipment at the Nanoscale and Microscale Research Centre (nmRC).

6.1 INTRODUCTION

The heterostructures needed for solar cell and light emitting diode (LED) applications often require deposition of several layers (~ 5 to 10) on top of one another, with uniform thicknesses as small as ~ 50 nm [271]. The deposition of such thin and uniform films is challenging via inkjet printing and requires careful development of the formulation of inks and their integration with the deposition process. The wetting of inks must also be carefully controlled, since for many heterostructure geometries, a single layer must be printed across multiple different materials which can lead to

strange and non-uniform wetting phenomena. Most importantly, the deposition of heterostructures via inkjet printing can lead to intermixing between layers [11], due to redispersion, which has a significant effect on the ability to control the layer thickness and/or the quality of the interface, as well as on the electrical optical properties of the films [235]. Because of these challenges, fully inkjet printed heterostructures for LED and solar cell applications are rare and very challenging to manufacture [208,228].

Here, fully-inkjet printed heterostructures are studied to better understand and control their deposition with the goal of fabricating fully inkjet printed optoelectronic devices.

6.2 WETTING PHENOMENA OBSERVED ON PRINTED HETEROSTRUCTURES

Strange wetting phenomena were sometimes observed when overprinting one material with another to fabricate printed heterostructures. For example, poly-TPD lines were printed on a Si/SiO_2 substrate and annealed at 140 °C for 30 mins. A $CsPbBr_3$ film was then printed across these poly-TPD lines. After printing, $CsPbBr_3$ NC films were observed directly on top of the poly-TPD lines and also on the Si/SiO_2 substrate away from the poly-TPD lines (> 100 µm), but $CsPbBr_3$ films were not formed on the Si/SiO_2 directly next to the poly-TPD lines (**Figure 6.1**). In these regions (~ 100 µm wide) the $CsPbBr_3$ ink aggressively de-wets from the Si/SiO_2, leaving only very small islands of $CsPbBr_3$ NCs within these regions. It is assumed that the rest of the ink deposited in these regions is pulled to the side via capillary force [229,234,302].

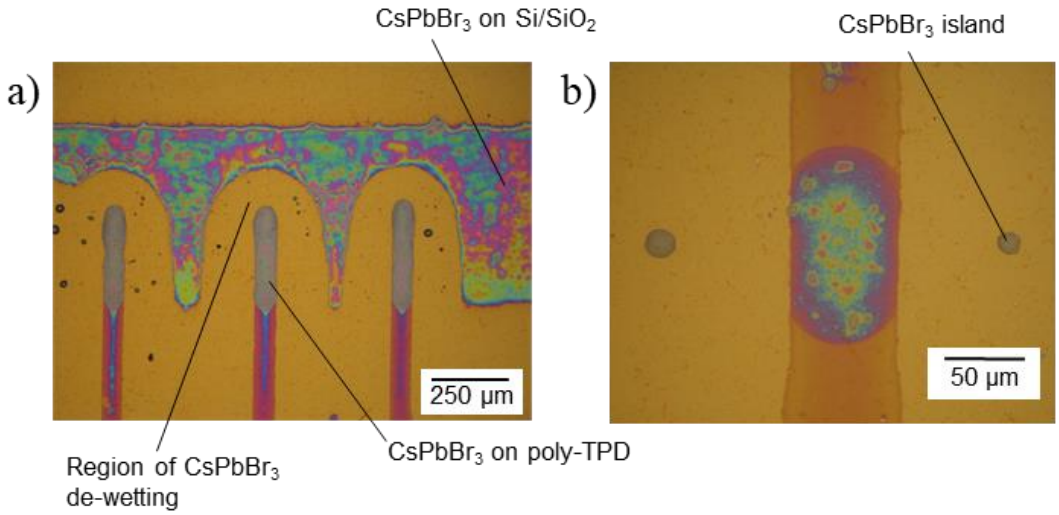


Figure 6.1. Optical images of poly-TPD lines printed on Si (vertical lines) with $CsPbBr_3$ films printed on top resulting in 'socially distant inks' effect. **a)** Shows a wide printed $CsPbBr_3$ bar across 3 poly-TPD lines and **b)** shows a single $CsPbBr_3$ line printed across a single poly-TPD line.

As well as $CsPbBr_3$/poly-TPD, this phenomenon was also observed for several other printed heterostructures on Si/SiO_2, including iGr/poly-TPD (**Figure 6.2a**), $CsPbBr_3$-PVP/iGr (**Figure 6.2b**), and PEDOT:PSS/iGr (**Figure 6.2c**). The effect could also be observed by removing the poly-TPD from the ink and just printing the chlorobenzene solvent followed by $CsPbBr_3$ (**Figure 6.2d**). By first masking the substrate with chlorobenzene, the effect was utilised to deposit very precise curved features (**Figure 6.2d**) which could not be achieved by conventional inkjet deposition techniques. The same effect was also observed using the solvent xylene instead of chlorobenzene.

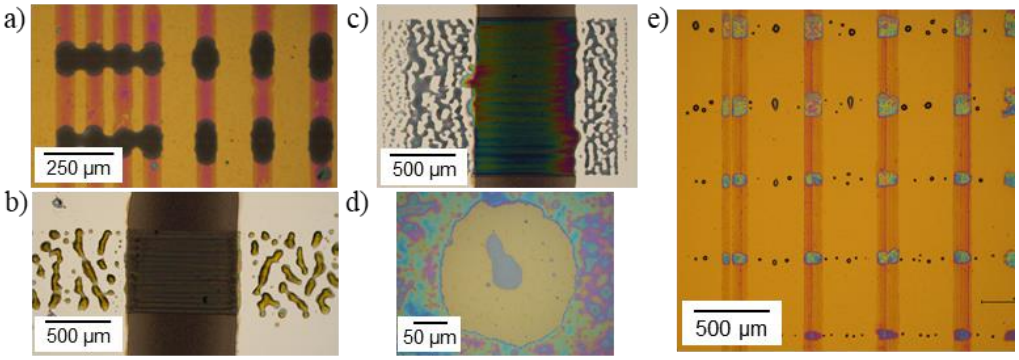


Figure 6.2. Optical images of a wetting phenomenon observed on Si/SiO_2 substrates in **a)** iGr/poly-TPD, **b)** $CsPbBr_3$-PVP/iGr, and **c)** PEDOT:PSS/iGr. **d)** A single printed drop of chlorobenzene printed on Si/SiO_2 and annealed at T_{anneal} = 140 °C for 30 mins overprinted with $CsPbBr_3$ NCs **e)** $CsPbBr_3$/poly-TPD heterostructure array on Si made via ink social distancing effect with varying sizes by changing number of printed lines in each.

This effect was not observed on other substrates such as PEN and Kapton. The effect was also inhibited on Si/SiO_2 when the poly-TPD layer was not annealed before printing the following layer. Analytically, the phenomenon can be explained by a change of the "de-wetting regions" on Si/SiO_2 from hydrophobic to hydrophilic [229,234], but the cause of this change in hydrophobicity is currently unknown and further studies are required. It is thought that the solvents in the first printed layer actually spread beyond the area where material is deposited and changes the wettability of these regions after annealing. With further control and understanding of this effect, it is envisioned that it could be used as a masking technique to print very precise features **(Figure 6.2d**) or alternatively as an efficient and accurate method to print arrays of devices, which was demonstrated with an array of $CsPbBr_3$/poly-TPD heterostructures with different size in **Figure 6.2e**.

6.3 PROBING CROSS-SECTIONAL HETEROSTRUCTURES

In this work, ToF-SIMS and FIB-SEM were used to vertically probe heterostructures deposited via inkjet printing to better understand the interfaces between the materials and thus better understand the performance of devices. ToF-SIMS can be used to give 3D distributions of a wide variety of different molecules that are present in heterostructures. FIB-SEM has poorer resolution, but can give information on the porosity of layers and is less prone to artefacts. FIB-SEM can also be used to calibrate the milling times in ToF-SIMS into real thicknesses. Therefore, combing these two techniques is a powerful method to probe printed heterostructures. Using this information, the aim is to gain some control over these interfaces in printed heterostructures by changing the inkjet deposition technique to better control device performance. Printed perovskite/graphene heterostructures have previously been used for photodetection applications [4,5] so $CsPbX_3$/iGr heterostructures were investigated to better understand and control the interface quality and device performance.

The sheet resistance of iGr (1 printed layer) increased by ~ 10% after inkjet deposition of $CsPb(Br/I)_3$ NCs on top from 10 kΩ/sq to 11 kΩ/sq (**Figure 6.3a**). Depth profiling using ToF-SIMS revealed the presence of perovskites throughout the iGr layer. Thus, it is proposed that intermixing between the perovskite and iGr layers was the cause of the observed increase of resistance (**Figure 6.3b**). For lateral photodetectors, intermixing of the iGr and $CsPb(Br/I)_3$ layers is not necessarily detrimental to device performance, however, vertical devices such as LEDs require highly uniform layers and interfaces to avoid short-circuiting and achieve high performances [310]. Therefore, investigations were carried out using different printing conditions, in an effort to improve the sharpness of interfaces of printed $CsPbBr_3$ NCs heterostructures.

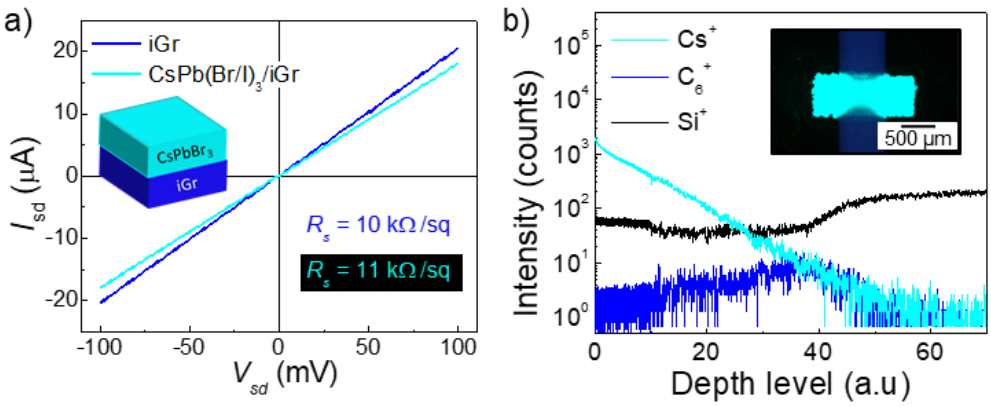


Figure 6.3. a) *I*(*V*) relationship of 1 layer of iGr before and after inkjet deposition of $CsPb(Br/I)_3$ (1 layer) on top (sample area is 30 µm x 60 µm), measured in 2-terminal geometry. Inset shows schematic diagram of heterostructure. **b)** Depth profiling of $CsPbBr_3$/iGr heterostructure with 10 printed layers of $CsPbBr_3$ and 10 printed layers of iGr on Si/SiO_2 substrate via ToF-SIMS in positive polarity mode. Inset: optical image of $CsPbBr_3$/iGr heterostructure on Si/SiO_2 with 10 layers of $CsPbBr_3$ and 3 layers of iGr under illumination (λ_{ex} = 365 nm).

Printed PEDOT:PSS ($Ink_{CG\text{-}Samba}$ formulation) (**Figure 6.4a-c**) and hBN (**Figure 6.4d**) interlayers between iGr and $CsPbBr_3$ were investigated to determine if the penetration of $CsPbBr_3$ NCs into iGr could be reduced. To produce these 3-layer heterostructures, a line of iGr was overprinted with a large square of PEDOT:PSS or hBN. A line of $CsPbBr_3$ NCs was then printed perpendicular to the iGr line on top of the interlayer square (**Figure 6.4b**). This method ensures the $CsPbBr_3$ and iGr lines do not make direct contact and forms a 3-layer heterostructure over the small area where the 3 materials intersect. The hBN interlayer had no significant effect on $CsPbBr_3$ intermixing as $CsPbBr_3$ NCs were still observed throughout the hBN and iGr layers (**Figure 6.4d**, cyan line). This may be caused by the presence of terpineol and cyclohexanone solvents in all 3 inks, which likely leads to redispersion of hBN and iGr during printing of the $CsPbBr_3$ layer. This is also indicated by the hBN/iGr

interface (**Figure 6.4d**, grey and dark blue lines) where intermixing is also observed due to their similar solvents. The PEDOT:PSS interlayer on the other hand did supress intermixing of $CsPbBr_3$ to a degree (**Figure 6.4a-c**). In the top layer of the sample, the $CsPbBr_3$ NC signal (**Figure 6.4c**, cyan line) is constant but peaks just above the PEDOT:PSS signal (**Figure 6.4c**, red line), indicating that $CsPbBr_3$ NCs accumulate on top of the PEDOT:PSS layer. The $CsPbBr_3$ signal then decreases throughout the PEDOT:PSS layer and totally disappears just as the iGr signal appears (**Figure 6.4c**, dark blue line). This indicates that the NCs are only present in the PEDOT:PSS layer and perhaps the very top of the iGr layer, but do not penetrate all the way through. Thus, the PEDOT:PSS interlayer reduced NC penetration depth into the iGr. Also, the PEDOT:PSS/iGr interface appeared sharper than the hBN/iGr interface, likely because the PEDOT:PSS ink is water-based and thus less compatible with the iGr, thus causing less material redispersion.

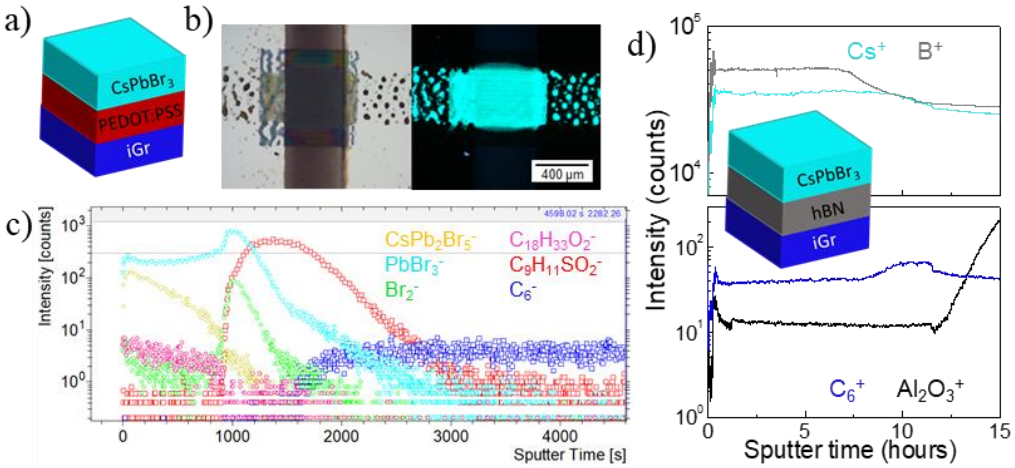


Figure 6.4. a) Schematic of fully printed $CsPbBr_3$/PEDOT:PSS/iGr heterostructure (10 layers of iGr and PEDOT:PSS ($Ink_{CG\text{-}Samba}$) and 100 layers of $CsPbBr_3$ printed on Si/SiO_2). **b)** Optical images of printed heterostructure under light and under λ_{ex} = 365 nm showing an iGr line (vertical) overprinted with a PEDOT:PSS square, overprinted again with a $CsPbBr_3$ line (horizontal). **c)** Depth profiling of heterostructure via ToF-SIMS in negative polarity mode. **d**) Depth profiling of fully printed $CsPbBr_3$/hBN/iGr heterostructure (each with 10 layers printed on Al_2O_3 sapphire substrate) via ToF-SIMS in positive polarity mode. Inset shows schematic of printed $CsPbBr_3$/hBN/iGr heterostructure.

To corroborate these ToF-SIMS results, a $CsPbBr_3$/PEDOT:PSS/iGr heterostructure printed on a Cu substrate was also investigated via FIB-SEM and energy dispersive X-ray (EDX) mapping (**Figure 6.5**). The top layer of $CsPbBr_3$ was very challenging to identify via FIB-SEM due to very small thickness. Only a thick film of at least 100 printed layers was identifiable, so 100 layer $CsPbBr_3$ was printed on top of 10 layer PEDOT:PSS and iGr. EDX maps revealed the formulation of a rough CuO layer on top of the Cu with a thickness of ~ 500 nm. After this, a trough in the O signal and a peak in the C signal were observed simultaneously, which is indicative of the iGr layer with a thickness of ~ 400 nm. FIB-SEM also revealed porosity in the iGr layer, which

may contribute to the intermixing seen previously in $CsPbBr_3$/iGr (**Figure 6.3b**) and $CsPbBr_3$/hBN/iGr (**Figure 6.4d**) heterostructures. The PEDOT:PSS layer is confirmed by increase in O and S signals, which show a PEDOT:PSS layer with thickness of ~ 400 nm which is present up to the surface of the structure. The $CsPbBr_3$ NCs are confirmed by the Br signal at the top of the device, which show a $CsPbBr_3$ NCs layer with thickness of ~ 150 nm. The $CsPbBr_3$ layer penetrates into the PEDOT:PSS layer but not into the iGr layer, as was observed with ToF-SIMS.

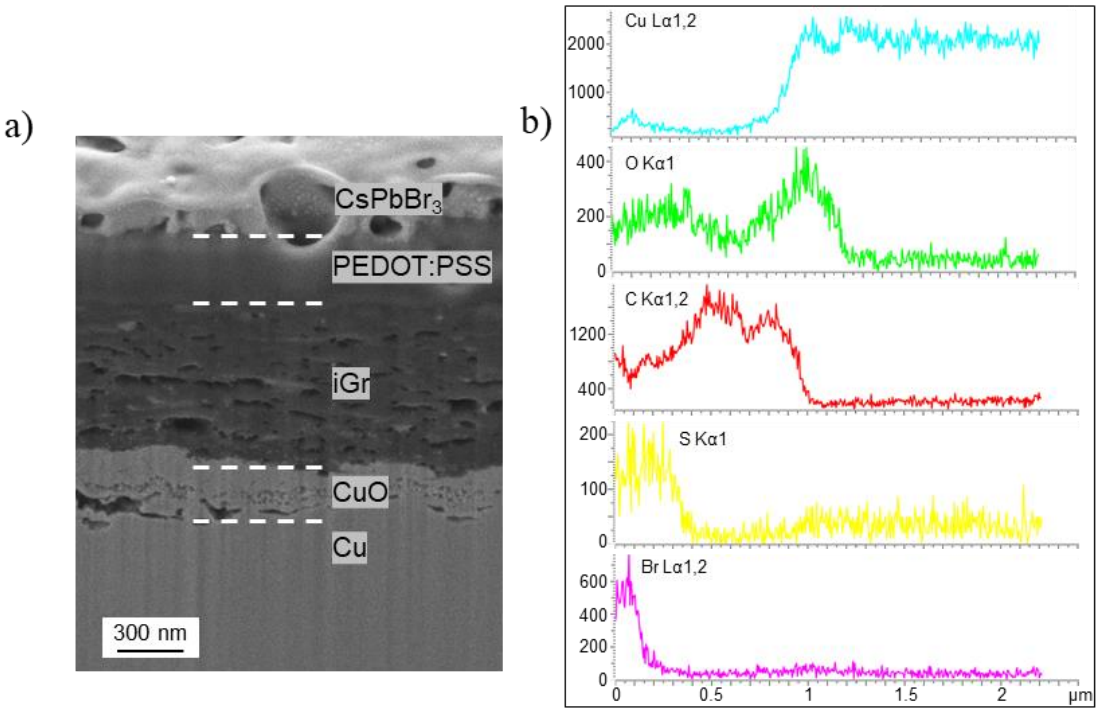


Figure 6.5. a) FIB-SEM cross-sectional image of $CsPbBr_3$ (100 layers), printed atop PEDOT:PSS ($Ink_{CG\text{-}Samba}$) and iGr (both 10 printed layers) on a copper substrate. **b)** EDX maps of different elements measured from the top surface down.

Different annealing conditions for $CsPbBr_3$ NCs printed on top of iGr were also shown to have a small effect on intermixing (**Figure 6.6a**). By increasing the annealing temperature from T_{anneal} = 60 °C to T_{anneal} = 100 °C, a small increase in the $CsPbBr_3$

penetration into the iGr was observed (**Figure 6.6a**, cyan lines). The increased annealing temperature also led to increased solvent evaporation, as indicated by a small reduction of organic $C_3H_5^+$ signal (**Figure 6.6a**, pink lines). The most successful method found to reduce intermixing of $CsPbBr_3$ NCs into iGr was by mixing the polymer PVP into the $CsPbBr_3$ ink ($CsPbBr_3$-PVP) (**Figure 6.6b**). While in previous experiments $CsPbBr_3$ NCs were detected deep within the iGr layer, the $CsPbBr_3$-PVP/iGr heterostructures displayed a sharp and short interface. This is corroborated by *I*(*V*) measurements which recorded only a 5% increase in iGr sheet resistance after deposition of $CsPbBr_3$-PVP on top due to intermixing (**Figure 6.6c**), a reduction from the 10% increase of iGr sheet resistance recorded previously by printing $CsPbBr_3$ on top (**Figure 6.3a**). Separation of PVP towards the top of inkjet printed layers was recorded previously in AgNP inks [186] and since the PVP forms a polymeric matrix around the $CsPbBr_3$, this can explain the reduction in intermixing observed.

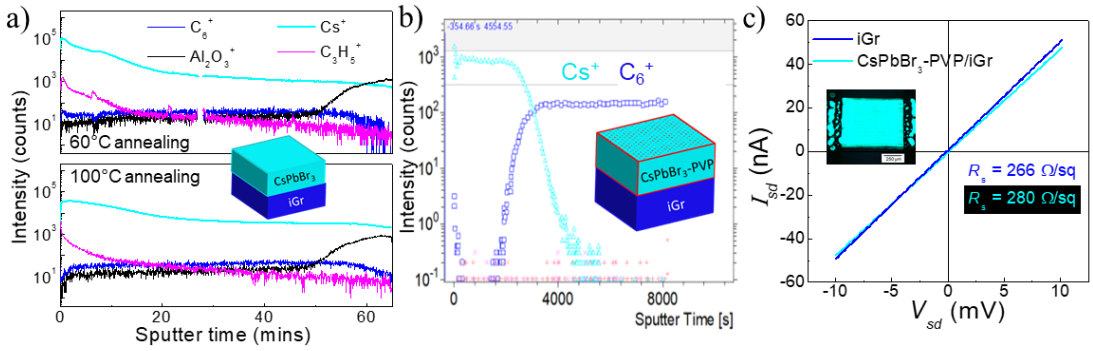


Figure 6.6. a) Depth profiles of $CsPbBr_3$/iGr heterostructures (10 layers of each material printed on Al_2O_3 sapphire substrate) after annealing $CsPbBr_3$ at (top) 60 °C for 30 mins and (bottom) 100 °C for 30 mins via ToF-SIMS in positive polarity mode **b)** Depth profiling $CsPbBr_3$-PVP/iGr heterostructures (10 layers of each material printed on Si/SiO_2 substrate) via ToF-SIMS in positive polarity mode. Insets of a and b show schematic diagrams of each heterostructure. **c)** *I*(*V*) relationships of 10 layer iGr before and after 10 layers of $CsPbBr_3$-PVP were printed on top), measured in 2-terminal geometry. Inset: optical image of device under λ_{ex} = 365 nm.

PEDOT:PSS/iGr heterostructures on Kapton were also investigated which are important for LED applications (**Chapter 7.5**). A line of PEDOT:PSS was printed onto a line of iGr perpendicularly (**Figure 6.7c**, inset). The sheet resistance of iGr increased by ~ 50% following PEDOT:PSS deposition (**Figure 6.7a**). As before, this is attributed to intermixing, as PEDOT:PSS (**Figure 6.7b**, top - red line) was detected deep within the iGr layer (**Figure 6.7b**, top - blue line) using ToF-SIMS. This intermixing was reduced and a sharper PEDOT:PSS/iGr interface was achieved by adjusting the Tween-80 surfactant content in the PEDOT:PSS ink formulation from 0.67 wt% (**Figure 6.7b**, top) to 0.30 wt% (**Figure 6.7b**, bottom). In both cases, the Tween-80 surfactant was seen to accumulate at the PEDOT:PSS/iGr interface (**Figure 6.7b**, pink lines) and reducing the Tween-80 content led to sharpening of the Tween-80 signal, indicating that the surfactant becomes more concentrated at the interface, which likely plays some role in the reduction of PEDOT:PSS/iGr intermixing.

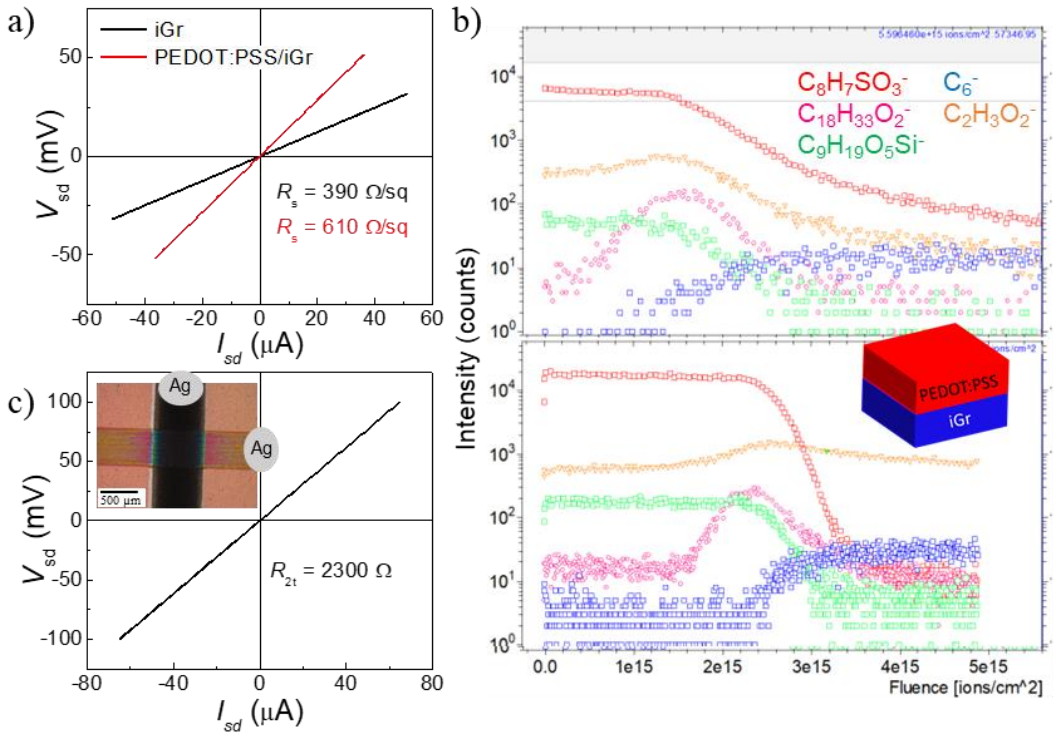


Figure 6.7. a) *I*(*V*) relationship of iGr on Kapton before (black) and after (red) inkjet deposition of PEDOT:PSS on top (6 layer PEDOT:PSS and 5 layer iGr on Kapton), measured in 2-terminal geometry. **b)** Depth profiles of PEDOT:PSS/iGr heterostructures (10 layers of each material printed on Kapton substrate) using $Ink_{CG\text{-}Samba}$ (top) and using a modified $Ink_{CG\text{-}Samba}$ with approximately half the surfactant content (0.3 wt% Tween-80) (bottom) via ToF-SIMS in negative polarity mode. **c)** *I*(*V*) relationship measured between iGr and PEDOT:PSS ($Ink_{CG\text{-}Samba}$), in 2-terminal geometry. Inset: optical image of 6 layer PEDOT:PSS (horizonal line) printed on top of 5 layer iGr on Kapton (vertical line), with graphics showing approximate positions of Ag contacts used for measured.

A resistance 2300 Ω was measured between the printed PEDOT:PSS ($Ink_{CG\text{-}Samba}$) and iGr lines (**Figure 6.7c**) with linear *I*(*V*) relationship, indicating Ohmic contact. Of this 2300 Ω measured, 1600 Ω is attributed to the iGr and PEDOT:PSS lines before they intersect. This was calculated by first measuring the sheet resistance of each material separately, then using the area between the Ag contacts and PEDOT:PSS/iGr overlap

area to calculate the resistance. Thus, only 700 Ω is attributed to the 700 x 500 µm PEDOT:PSS/iGr heterostructure (inset of **Figure 6.7c**), which is approximately the resistance expected from this area if it were just PEDOT:PSS. Hence, the resistance between the two materials can be considered ineffectual, which is essential for LED performance. The Tween-80 content in the PEDOT:PSS was not found to have a significant effect on the resistance between PEDOT:PSS and iGr.

To determine how the performance of PEDOT:PSS will change in printed heterostructure devices, the resistance of PEDOT:PSS was measured (2-terminal geometry) after printing different materials on top of it such as AgNPs, poly-TPD, $CsPbBr_3$ NCs, and iGr (**Figure 6.8a**). In all of these heterostructures, the sheet resistance of PEDOT:PSS after the deposition of the subsequent layers was comparable to that measured before, demonstrating the excellent potential for Ink_{CG} PEDOT:PSS in optoelectronic devices.

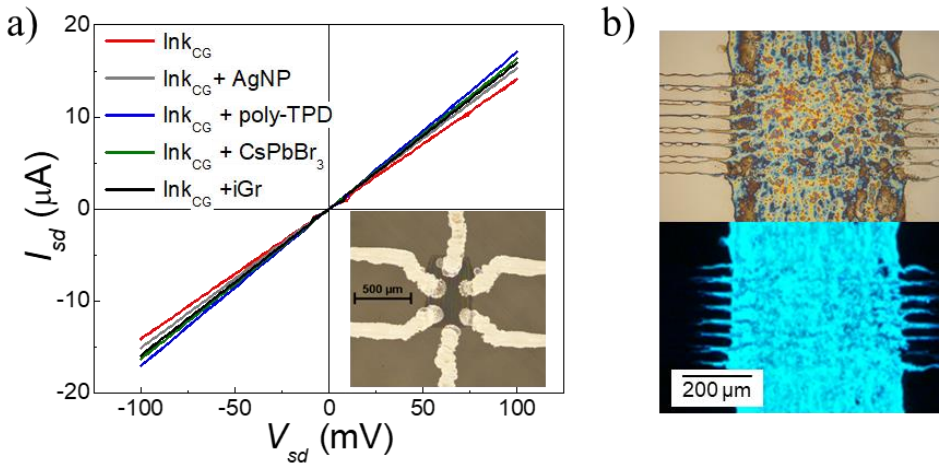


Figure 6.8. a) *I*(*V*) relationships (measured in 2-terminal geometries) for conductive lines of Ink_{CG} PEDOT:PSS (4 printed layers) on PEN, as printed, and over-printed with different inks in a heterostructure. Each was printed with a single layer and subsequently annealed at: T_{ann} = 150 °C, t = 30 mins for AgNP, T_{ann} = 140 °C, t = 30 mins for poly-TPD, T_{ann} = 60 °C, t = 30 mins for $CsPbBr_3$, T_{ann} = 150 °C t = 18 hours for iGr. Inset shows AgNPs overprinted on PEDOT:PSS in a hall bar geometry. **b)** Optical images of 5 printed layers of $CsPbBr_3$ (vertical) overprinted with 2 layers of printed TPBI (horizontal) on Si/SiO_2 under white light (top) and λ_{ex} = 365 nm illumination (bottom).

A TPBI electron injection layer is often printed on top of perovskite emissive layers in LEDs [106,172]. It is therefore important that the optical properties of the perovskites are maintained following TPBI deposition. TPBI/$CsPbBr_3$ heterostructures were printed on Si/SiO_2 and no visible change in $CsPbBr_3$ PL intensity was observed following TPBI deposition and annealing at T_{anneal} = 140 °C for t = 30 minutes (**Figure 6.8b**). However, a change in the morphology of the printed $CsPbBr_3$ film following TPBI deposition was observed, with some NCs even being moved along the printed TPBI swaths (**Figure 6.8b**), indicating that the NCs have been at least partially redispersed by the TPBI ink. With just optical images, it is unclear if the TPBI penetrates all the way through the perovskite layer, thus further cross-sectional

measurements are required to access the quality of the interface and determine if it is suitable for use in optoelectronic devices. Future studies should also explore TPBI/$CsPbBr_3$-PVP heterostructures in an effort decrease perovskite NC redispersion.

These studies of inkjet printed heterostructures have improved understanding of printed interfaces and have helped to inform printing strategies to achieve the uniform complex optoelectronic devices, such as LEDs.

6.4 SUMMARY

Inkjet printed heterostructures were investigated with the ultimate goal of fabricating, and controlling the interfaces within, fully printed complex vertical heterostructures with different materials. First, a wetting phenomenon was discovered that occurred when printing heterostructures. This was exploited to print very precise curved lines and arrays of devices. While this wetting phenomenon can be explained analytically, further studies are required to uncover and understand its origin.

Heterostructure interfaces were also explored using ToF-SIMS and FIB-SEM, and large penetration of perovskite NCs into iGr in printed perovskite/iGr heterostructures was identified. It was found that the use of a PEDOT:PSS interlayer or the addition of PVP into the perovskite NC ink were effective methods to inhibit NC penetration into iGr. It was also found that a reduction of surfactant content in PEDOT:PSS improved PEDOT:PSS/iGr interface quality. Moreover, the interfacial resistance between iGr and PEDOT:PSS was found to be negligible, which is essential for their use in vertical heterostructures. Finally, it was shown that the electrical performance of printed PEDOT:PSS was unchanged in a variety of heterostructures, and observed that $CsPbBr_3$ films maintained their optical properties, but were partially redispersed after

printing of TPBI on top. These studies help pave the way for the printing of more complex vertical heterostructures such as those needed for LEDs and other optoelectronic devices (**Chapter 7.5**).

7 PRINTED OPTOELECTRONIC DEVICES

This chapter reports on the fabrication and characterisation of photodetector devices based on single layer graphene (SLG) decorated with perovskite nanocrystals (NCs) and graphene quantum dots (GQD) photoactive materials via inkjet printing. The electronic properties of the SLG were characterised before and after material deposition via drop-casting and inkjet printing, and the performance of the photodetectors were characterised by measuring photoresponsivity and wavelength sensitivity range. This chapters also explores the fabrication of fully inkjet printed detectors that use inkjet printed graphene (iGr) instead of SLG, which are promising for application in flexible and wearable electronics. Finally, this chapter reports on significant progress towards the fabrication of a fully printed perovskite LED.

The work included in this chapter based on printed perovskite detectors is published in Austin et al., "Photosensitisation of inkjet printed graphene with stable all-inorganic perovskite nanocrystals", *Nanoscale, 2023, 15, 2134*.

7.1 INTRODUCTION

SLG is a highly attractive material for photodetection applications owing to its fast broadband spectral response [9], however, the responsivity of pure graphene photodetectors is limited to $R < 0.1$ A/W by the materials poor absorption cross-section, short lifetime of photogenerated carriers, and the absence of a photogain mechanism [311]. Functionalisation of planar SLG FETs with 0D materials was explored to drastically improve photosensitivity [4,8]. The deposition via drop-casting of QDs such as PbS onto SLG has achieved detectors with photoresponsivities up to $R \sim 10^9$ A/W [8] and more recently, all-inorganic $CsPbI_3$ perovskite NCs have achieved

$R \sim 10^6$ A/W [4]. The enhanced response of SLG is explained by trapped charges in the NCs with lifetimes of ~ 1 s. The charges accumulate on the NC layer and act as local photoexcited gates and generate more carriers in the SLG conductive channel [312]. For upscaled manufacturing and greater control over deposition, black phosphorus [255], HgTe [19], and PbS [18] were recently deposited onto SLG via inkjet printing and photoresponsivities up to $R \sim 10^4$ A/W were achieved. Printed devices generally display lower performance than drop-cast devices which is attributed to the change of the NC properties during printing [313] and the low mobility of iGr ($\mu < 100$ cm^2/V·s) [314] compared to SLG ($\mu > 1000$ cm^2/V·s) [4]. Fully printed detectors with $R \sim 1$ A/W, have also been demonstrated using perovskites ($CH_3NH_3PbCl_{X-3}I_3$) and iGr [5], but further work is required to better understand the performance of iGr detectors compared to SLG detectors and to develop the inkjet deposition of more stable perovskite materials such as $CsPbX_3$ perovskite NCs. There is also potential to extend the range of printed photodetectors with novel nanomaterials such as graphene quantum dots (GQD), which have not yet been incorporated into printed photodetector devices.

Fully-printed LEDs are also devices of interest; however, unlike photodetectors, LEDs tend to be much more challenging to print as they usually contain many more layers that must be very thin (~ 50 nm) and highly uniform [271]. Wetting phenomena and intermixing of layers can also lead to short circuiting of devices (**Chapter 6.3**). Because of these challenges, manufacturing of a fully printed perovskite LED remains challenging, and device efficiencies have been limited because printed LEDs have not yet incorporated hole and electron injection layers such as poly-TPD and TPBI [228].

7.2 PRINTED $CsPbBr_3$ AND $CsPb(Br/I)_3$ PEROVSKITE PHOTODETECTORS

To fabricate perovskite/graphene photodetectors via inkjet printing, the $CsPbBr_3$ and $CsPb(Br/I)_3$ NC inks and printing methods developed in **Chapter 5.2.1** were used. A single droplet of $CsPbBr_3$ was deposited onto SLG FETs by inkjet printing (**Figure 7.1a**) to fabricate a $CsPbBr_3$/SLG device (inset of **Figure 7.1b**). The perovskite NCs ink formulation had favourable wetting on the SLG, as many more $CsPbBr_3$ NCs were observed on the SLG compared the Si/SiO_2, although, the SLG device did not appear to be fully covered by the $CsPbBr_3$. After $CsPbBr_3$ deposition, a small increase in SLG resistance was measured (**Figure 7.1b**). The gate voltage (V_g) dependence on resistivity (ρ_{sd}) revealed that this was due to a small shift in the position of the Dirac point from +7 V to +6 V (**Figure 7.1c**), which indicates *n*-type doping of the SLG. Negligible hysteresis in $\rho_{sd}(V_g)$ was observed before or after perovskite NC deposition. *n*-type doping of SLG was previously observed on SLG functionalised with $CsPb(Br/Cl)_3$ NCs [315] and with $CsPbI_3$ NCs [4], due to the donor nature of $CsPbX_3$ NCs. However, in these cases, a much greater shift of > 10 V was observed along with much larger hysteresis. Moreover, only a small photoreponsivity was recorded for the $CsPbBr_3$/SLG device of R ~ 1 A/W (**Figure 7.1d**), which is ~ 10^5x smaller than previous drop-cast devices [4]. The low photoresponsivity and lack of hysteresis in $\rho_{sd}(V_g)$ indicates insufficient coverage of $CsPbBr_3$ NCs on top of SLG, thus the printing strategy was changed.

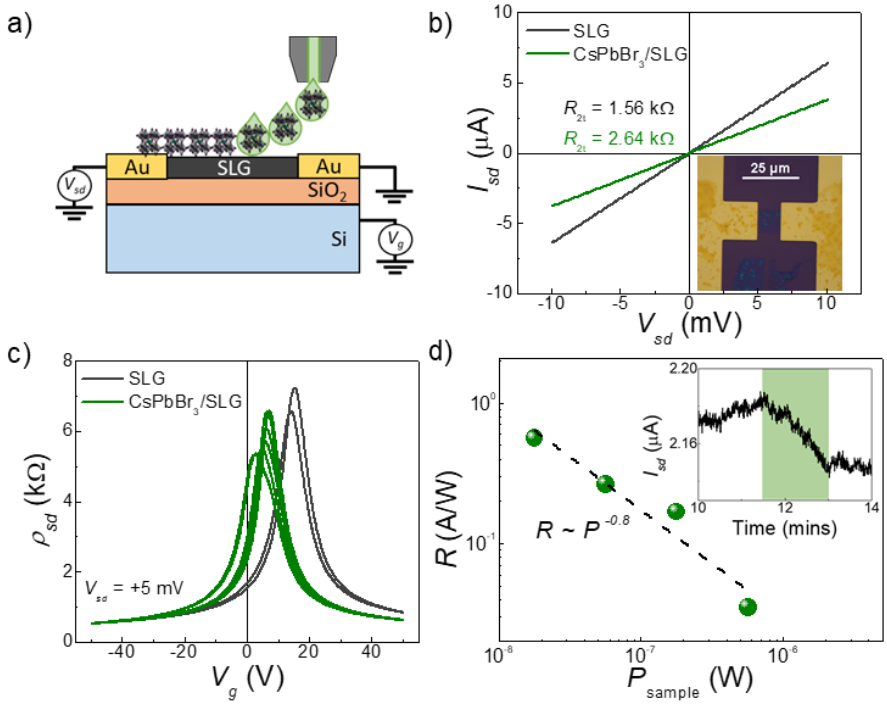


Figure 7.1. a) Schematic diagram depicting deposition of all-inorganic perovskite NCs via inkjet printing on a single layer graphene (SLG) FET device. **b)** *I*(*V*) relationship of SLG before (black) and after (green) a drop $CsPbBr_3$ was printed on top. Inset: optical image of $CsPbBr_3$/SLG device. **c)** Resistivity, ρ_{sd}, dependence on applied gate voltage V_g (V_{sd} = 5 mV, sweep rate = 0.1 V/s) for SLG before (black) and after (green) the $CsPbBr_3$ drop was printed on top. **d)** Photoresponsivity, *R*, of $CsPbBr_3$/SLG device as a function of illumination power on the sample, P_{sample}, after 1 minute under λ_{ex} = 520 nm exposure (V_{sd} = 10 mV, V_g = 0 V). Dashed line is a line of best fit. Inset: temporal response of $CsPbBr_3$/SLG device after illumination for 1 minute (λ_{ex} = 520 nm, V_{sd} = +5 mV, P = 1.8 kW/m^2), indicated by green shaded region.

Instead of printing a single drop of NCs, printed stripes with 2 layers, (~ 1 mm length, and 100 µm width) were instead used to cover the SLG FET devices (**Figure 7.2a**, top left). This approach made accurate deposition over the SLG much easier and resulted in greater and more uniform coverage of NCs on top of the SLG devices (**Figure 7.2a**, top right). $CsPbBr_3$ and $CsPb(Br/I)_3$ NC stripes were deposited onto SLG FETs by

inkjet printing to fabricate $CsPb(Br/I)_3$/SLG and $CsPbBr_3$/SLG devices. The gate voltage, V_g, dependence of SLG resistivity before and after deposition of $CsPb(Br/I)_3$ NCs revealed a large hysteresis when V_g was swept from -50 V to +50 V and then back to -50 V with a sweep rate of 0.1 V/sec (**Figure 7.2a**). This was accompanied by an average shift in the position of the Dirac point from +11 V towards 0 V, similar to that reported previously for drop-cast $CsPb(Br/Cl)_3$/SLG [315] and $CsPbI_3$/SLG [4] devices.

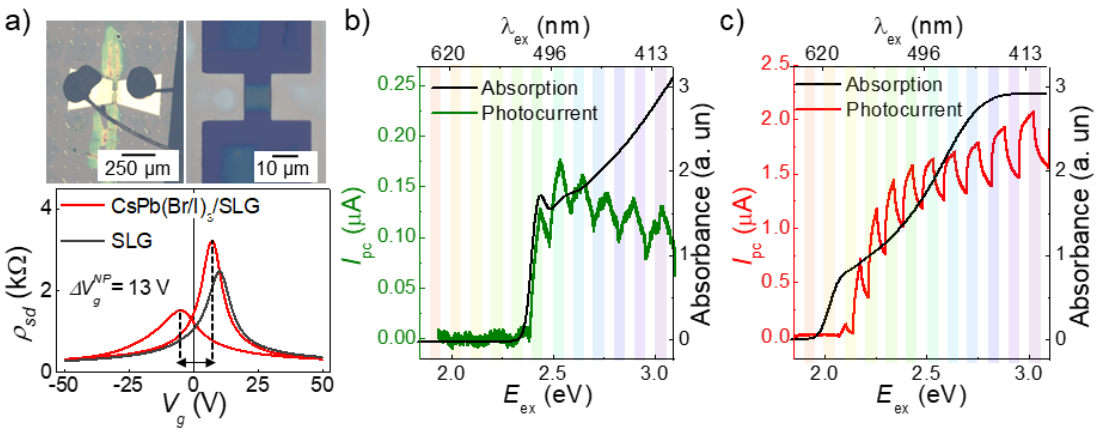


Figure 7.2. a) Optical images of $CsPbBr_3$ stripe (2 layers) printed over SLG FET (top) and dependence of SLG resistivity, ρ_{sd}, on applied gate voltage, V_g, before (black curve) and after (red curve) the inkjet printed deposition of $CsPb(Br/I)_3$ NCs (bottom). V_g is swept from -50 V to +50 V and then back to -50 V (V_{sd} = 5 mV, sweep rate = 0.1 V/s). Dependence of photocurrent, I_{pc}, on the energy of incident light for the **b)** $CsPbBr_3$/SLG device (P ~ 0.3 W/m^2, V_{sd} = 5 mV) and **c)** for the $CsPb(Br/I)_3$/SLG device (P ~ 0.03 W/m^2, V_{sd} = 10 mV) compared to their respective absorption spectra (black lines).

The electron and hole field-effect mobilities of the SLG device before NC deposition were calculated to be μ_e = 0.70 m^2/V·s and μ_h = 0.55 m^2/V·s, respectively. After deposition of $CsPb(Br/I)_3$ NCs, the mobilities decreased to μ_e = 0.53 m^2/V·s and μ_h = 0.40 m^2/V·s during forward voltage sweeps (-50 V to +50 V) and increased to μ_e =

0.73 $m^2/V \cdot s$ and μ_h = 0.64 $m^2/V \cdot s$ during backward voltage sweeps (+50 V to -50 V). Dependence of the field effect mobility on the direction of the V_g sweep can be explained using slow charge dynamics in the $CsPbX_3$/SLG devices [4].

The V_g position of the Dirac point of the $CsPbBr_3$/SLG device was also shifted to the left, consistent with *n*-type doping (**Figure 7.3**). However, due to gate leakage occurring at V_g = +45 V, only the forward V_g sweep could be measured, and hysteresis could not be observed. Despite this, a small increase in carrier mobilities was observed in the $CsPbBr_3$ device from μ_e = 0.33 $m^2/V \cdot s$ and μ_h = 0.53 $m^2/V \cdot s$ before NC deposition to μ_e = 0.38 $m^2/V \cdot s$ and μ_h = 0.36 $m^2/V \cdot s$ after NC deposition. The differences in gate voltage dependence between the devices decorated with $CsPb(Br/I)_3$ and $CsPb(Br)_3$ is likely due to the differences in the properties of the pristine graphene before deposition and difference in V_g sweep range . The onset of photoresponse was observed at an excitation wavelength, λ_{ex} = 600 nm for $CsPb(Br/I)_3$/SLG and λ_{ex} = 520 nm for $CsPbBr_3$/SLG, which is consistent with their respective absorption spectra (**Figure 7.2b,c**).

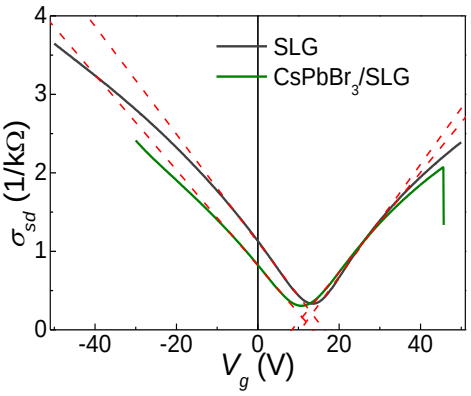


Figure 7.3. Dependence of SLG conductivity, σ_{sd}, on applied gate voltage, V_g, before (black curve) and after (green curve) the inkjet printed deposition of $CsPbBr_3$ NCs. For SLG, V_g was swept from -50 V to +50 V and then back to -50 V. For $CsPbBr_3$/SLG, V_g was swept from -30 V to +45 V where gate leakage was observed and thus the measurement was stopped (V_{sd} = 5 mV, sweep rate = 0.1 V/s). Red dashed lines are linear fits used to calculate field effect mobilities.

After illumination, the electrical properties of the devices recovered to their original value, but for large incident illumination powers ($P \gtrsim 0.1$ mW/m^2), the full recovery could take up to several hours (**Figure 7.4a**). For both devices, the relationship between incident light power, P, and the responsivity, R, follows $R \sim P^{-0.7}$ (**Figure 7.4b**), similar to the $R(P)$ previously reported for SLG decorated with $CsPbI_3$ NCs [4]. A much greater maximum photoresponse was observed for the $CsPb(Br/I)_3$ device ($R = 4 \times 10^6$ A/W) than for the $CsPbBr_3$ device ($R = 7 \times 10^3$ A/W). The difference in photoresponsivity of the photodetectors decorated with different perovskite NCs is due to the NC composition, which affects their absorption (**Figure 7.2b,c**) and energy level alignment with SLG for charge transfer (**Figure 7.4b**, inset). Since higher levels of absorptions at the used excitation energy (λ_{ex} = 405 nm) and longer lifetimes of photoexcited trapped charges are observed for mixed halide $CsPb(Br/I)_3$ NCs, these devices have higher photoresponsivity compared to the $CsPbBr_3$ NC decorated

devices. The devices demonstrated fast excitation and relaxation response times of τ_{rise} ~ 2 s and τ_{fall} ~ 6 s, respectively (**Figure 7.4c**).

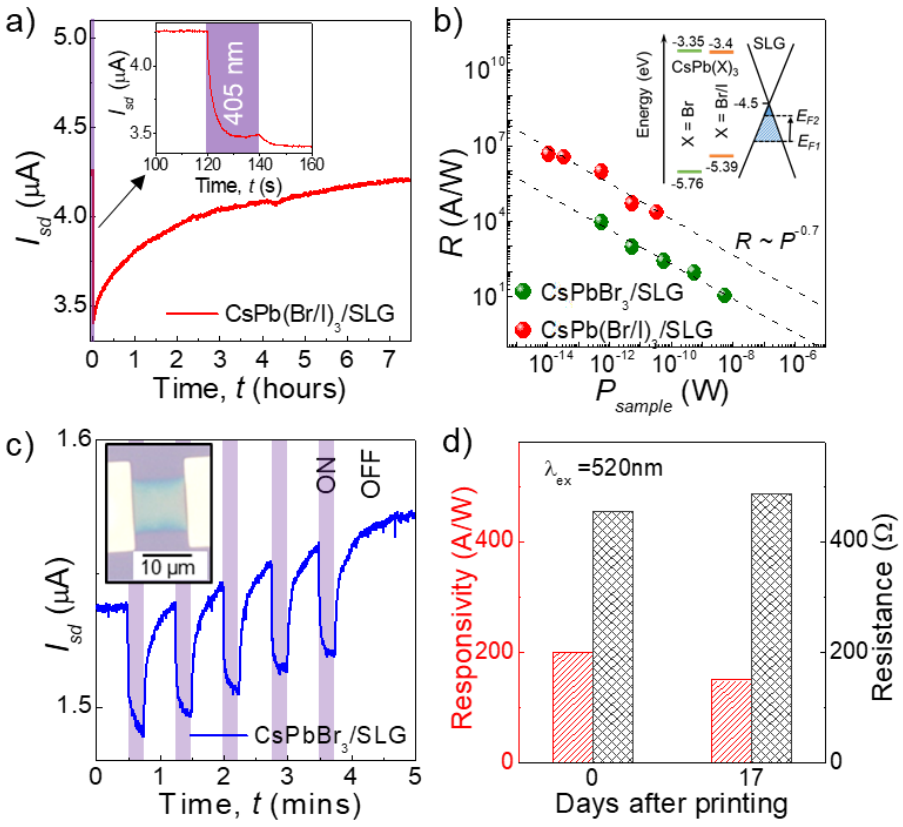


Figure 7.4. a) Temporal response of $CsPb(Br/I)_3$/SLG device to illumination for 20s (λ_{ex} = 405 nm, P = 0.56 W/m^2, V_{sd} = +2 mV). **b)** Photoresponsivity, R, of the $CsPb(Br/I)_3$/SLG and $CsPbBr_3$/SLG devices as a function of illumination power after 1 minute under λ_{ex} = 405 nm exposure (V_{sd} = 10 mV, V_g = 0 V). Inset: energy band diagram comparing $CsPbBr_3$ NCs, $CsPb(Br/I)_3$ NCs, and SLG. E_{F1} and E_{F2} denote the Fermi energy of the SLG device before (-4.6 eV) and after (-4.54 eV) $CsPb(Br/I)_3$ deposition, respectively. **c)** ON/OFF temporal response of $CsPbBr_3$/SLG device (λ_{ex} = 405 nm, P = 0.56 W/m^2, and V_{sd} = +2 mV) with excitation and relaxation time constants of τ_{rise} = 1.5 s and τ_{fall} = 5.6 s. Inset: optical image of $CsPbBr_3$/SLG device. **d)** Responsivity (red bars), measured with λ_{ex} = 520 nm and P = 5.6 mW/m^2, and resistance (black bars) of $CsPb(Br/I)_3$ /SLG device on the day of printing and after 17 days storage at ambient conditions.

The photoresponsivity achieved in these devices is significantly higher than that reported previously for printed perovskite detectors [5,12,15], which is attributed to the enhanced stability of the all inorganic perovskites used in this work and the optimised ink formulation. Perovskite NCs can be susceptible to environmental degradation, however, the devices fabricated here maintained stable performances for up to two weeks, with only a small decrease of photoresponsivity and increase in resistance observed following storage in ambient conditions (**Figure 7.4d**). The higher responsivity observed in the inkjet printed perovskite detectors fabricated in this work, compared to other works [5,12,15], is attributed to improved NC stability, which is enabled by efficient surface passivation (and low surface defect density). An additional significant benefit of the enhanced stability of the perovskite NCs used here, is their ability to withstand the inkjet deposition and post deposition processes and provide stable performance in the device.

SLG devices were also functionalised with the $CsPbBr_3$-PVP ink formulated in **Chapter 5.2.2**, in an effort to further improve device stability (inset of **Figure 7.5a**). Once again favourable wetting was observed on the SLG. Before $CsPbBr_3$-PVP deposition, the SLG $\rho_{sd}(V_g)$ dependence revealed little hysteresis and the Dirac point was located at V_g = +4 V (**Figure 7.5a**, black lines). The hole and electron mobilities were calculated to be μ_e = 0.47 $m^2/V{\cdot}s$ and μ_h = 0.44 $m^2/V{\cdot}s$. Following inkjet deposition of $CsPbBr_3$-PVP ink on top of SLG, increased hysteresis was observed (**Figure 7.5a**, red lines) and the position of the Dirac point shifted to V_g = -22 V and V_g = -13 V during forward (-50 V to +50 V) and backwards (+50 V to -50 V) V_g sweeps, respectively. Moreover, a decrease in mobilities was measured for both forward (μ_e = 0.29 $m^2/V{\cdot}s$ and μ_h = 0.29 $m^2/V{\cdot}s$) and backward sweeps (μ_e = 0.25 $m^2/V{\cdot}s$ and μ_h = 0.32 $m^2/V{\cdot}s$). The effect of $CsPbBr_3$-PVP ink on the electrical

properties of the SLG is very similar to the $CsPbBr_3$ and $CsPb(Br/I)_3$ inks measured previously. Thus, addition of PVP does not appear to have a large effect on the electrical properties of SLG.

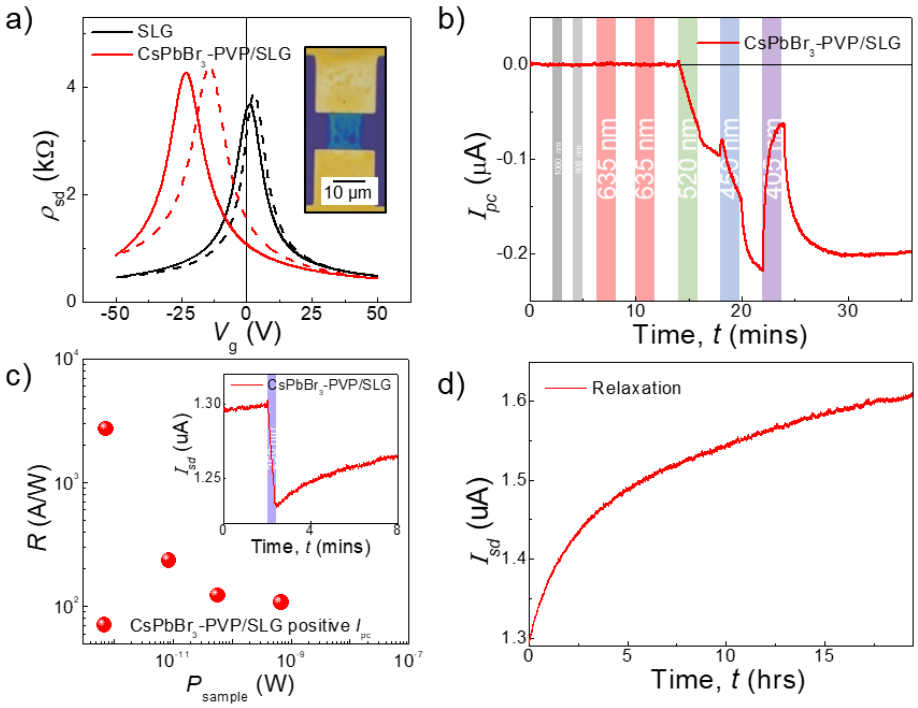


Figure 7.5. a) Dependence of SLG resistivity, ρ_{sd}, on applied gate voltage, V_g, before (black curve) and after (red curve) the inkjet printed deposition of $CsPbBr_3$-PVP ink. V_g is swept from -50 V to +50 V (solid lines) and then back to -50 V (dashed lines) (V_{sd} = 2 mV, sweep rate = 0.1 V/s). **b)** Temporal response of the photocurrent, I_{pc} of $CsPbBr_3$-PVP/SLG device following illumination with λ_{ex} = 1080, 808, 635, 520, 450, and 405 nm (V_{sd} = 2 mV, P = 68 W/m^2). **c)** Responsivity of the device measured using only the positive photocurrent as a function of power (V_{sd} = 2 mV, λ_{ex} = 405 nm). Inset: temporal response following illumination with λ_{ex} = 250nm (V_{sd} = 2 mV, P = 20 W/m^2). **d)** Temporal response of $CsPbBr_3$-PVP/SLG device after illumination with λ_{ex} = 520nm (V_{sd} = 2 mV, P = 1.8 kW/m^2).

The onset of photoreponse of the $CsPbBr_3$-PVP/SLG device was recorded at λ_{ex} = 520 nm (**Figure 7.5b**), the same as the $CsPbBr_3$/SLG device measured previously.

However, more complex photocurrent behaviour was observed in the $CsPbBr_3$-PVP/SLG device (**Figure 7.5b**). At λ_{ex} = 520 nm, a small positive photocurrent was observed at the start of illumination, followed by a larger negative photocurrent which becomes the dominant effect after a few seconds. At λ_{ex} = 450 nm, a similar effect is observed but the positive photocurrent has increased amplitude. At λ_{ex} = 405 nm, the positive photocurrent becomes the dominant effect throughout illumination and the negative photocurrent can no longer be observed, with a maximum photoresponsivity of $R = 3 \times 10^3$ A/W (**Figure 7.5c**). This is ~ 10x smaller than the responsivity recorded for the $CsPbBr_3$/SLG, which is attributed to the inhibition of the positive photocurrent by the negative photocurrent. Also, a non-logarithmic relationship between R and P was observed, which is likely also caused by the presence of two competing photocurrents with different power dependencies. Interestingly, at λ_{ex} = 250 nm (inset of **Figure 7.5c**), the negative photoresponse reappears and becomes the dominant effect.

The complex photocurrents observed in this device imply that more than one photoinduced charge trapping mechanism is occurring. The positive photocurrent had response times of τ_{rise} ~ 10 s and τ_{fall} ~ 30 s, which is similar to previous $CsPbX_3$/SLG devices. The negative photocurrent on the other hand appears linear, so is likely much slower, and has very long relaxation times of τ_{fall} > 6 hours (**Figure 7.5d**). Therefore, the fast positive photocurrent is likely caused by charge carriers created in the NCs transferred directly to SLG, the same effect that creates photocurrents in $CsPbX_3$/SLG devices. The exact cause of the negative photocurrent is unknown. The absorption edge of PVP was measured at λ = 250 nm (**Chapter 5.2.2**, **Figure 5.6c**), so at λ_{ex} = 250 nm, charge carriers may be created in the PVP and cause the negative photocurrent. However, it is unlikely that photoexcited charges are created in the PVP at λ_{ex} = 520

or 450 nm which the PVP cannot absorb. Instead at these wavelengths, charge carriers created in the $CsPbBr_3$ may be transferred and trapped in the PVP. Further experiments are required to fully understand the performance observed in $CsPbX_3$-PVP/SLG devices and uncover the source of the negative photocurrent. Due to this complex photocurrent behaviour, $CsPbX_3$-PVP/SLG detectors have inferior performance to $CsPbX_3$/SLG detectors, thus the $CsPbX_3$-PVP ink was not explored further for light detection applications. The $CsPbX_3$-PVP ink developed in **Chapter 5.2.2** should instead be investigated for light emission applications (**Chapter 7.5**).

7.3 FULLY PRINTED $CsPbBr_3$ AND $CsPb(Br/I)_3$ PEROVSKITE PHOTODETECTORS

The next step towards fully printed photodetectors was to replace SLG with iGr. First, a single droplet of iGr was printed onto a Si/SiO_2 FET between two pre-patterned gold contacts, and then, $CsPb(Br/I)_3$ NCs were deposited by drop-casting on top of the device to functionalise the iGr (**Figure 7.6a**). The conductivity, σ_{sd}, of this $CsPb(Br/I)_3$/iGr device as a function of gate voltage, V_g, showed a shift in the Dirac point from about +60 V before $CsPb(Br/I)_3$ NC deposition to about +50 V after (**Figure 7.6b**), indicating *n*-type doping, as previously observed in the $CsPbX_3$/SLG devices (**Figure 7.2a**). The hole mobility (μ_h = 3 $cm^2/V{\cdot}s$) was unchanged after $CsPb(Br/I)_3$ NC deposition but the conductivity of the device was decreased over all V_g values measured. Low mobility and thus large uncertainty in the Dirac point position, and significant hysteresis already present in the pristine iGr device (blue curve in **Figure 7.6b**) resulted in insignificant increase of hysteresis in $\sigma_{sd}(V_g)$ for the $CsPb(Br/I)_3$/iGr device.

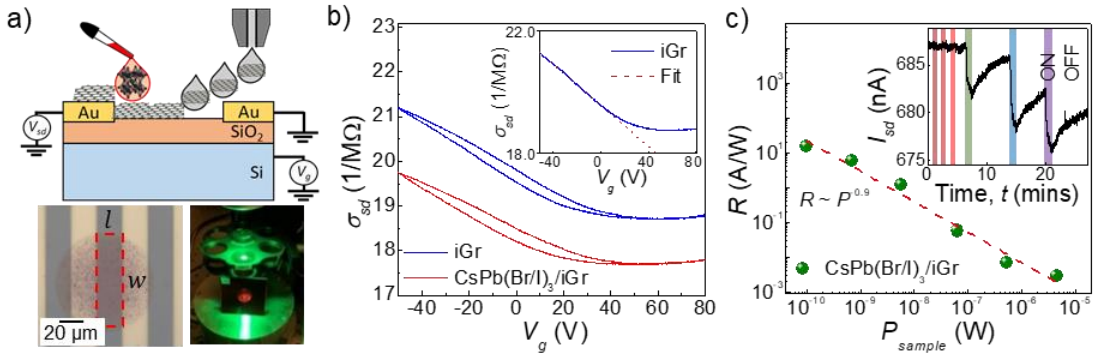


Figure 7.6. a) Schematic showing inkjet deposition of iGr and drop-cast $CsPb(Br/I)_3$ to fabricate $CsPb(Br/I)_3$/iGr photodetector (top). Optical image of iGr droplet printed on empty gold OFET device (left) and photograph of device after $CsPb(Br/I)_3$ NCs were drop-cast on top, displaying red fluorescence (λ_{ex} = 520 nm) (right). **b)** Conductivity of iGr before (blue curve) and after (red curve) drop-cast deposition of $CsPb(Br/I)_3$ NCs (V_{sd} = 10 mV). Inset: gate voltage dependence of iGr conductivity (V_{sd} = 10 mV) and linear fit for field effect model mobility calculation, giving a hole mobility, μ_h, of 3 cm^2/Vs. **c)** Photoresponsivity, R, of $CsPb(Br/I)_3$/iGr photodetector as a function of the power on the sample (λ_{ex} = 520 nm, V_{sd} = 10 mV). Inset: temporal response of device under light illumination (V_{sd} = 10 mV, V_g = 0 V, P = 566 W/m^2) at different wavelengths: 1060, 808, 635, 520, 450, and 405 nm, respectively.

The photoresponsivity threshold of the $CsPb(Br/I)_3$/iGr device is observed at ~ 600 nm (**Figure 7.6c**, inset), similar to the responsivity threshold observed in the $CsPb(Br/I)_3$/SLG device. The relationship between responsivity and incident power for the $CsPb(Br/I)_3$/iGr device followed $R \sim P^{-0.9}$ dependence, similar to the $R \sim P^{-0.7}$ dependence observed in the SLG device. $CsPb(Br/I)_3$/iGr displayed a maximum responsivity of 10^1 A/W, ~ 1000× smaller than the SLG device, and a response time constant of τ_{rise} = 6 s (**Figure 7.6c**, inset), which is similar to the SLG device. Note, high photoresponsivity in $CsPbX_3$/graphene photodetectors is proportional to the ratio between perovskite NC charge trapping time, τ_{trap}, and electron transport time, τ_e ~

$1/\mu$, i.e. the time it takes an electron to pass through the device, $R \sim \tau_{trap}/\tau_e$ [8]. iGr devices demonstrate field effect mobility, $\mu_{FE} \approx 3$ cm^2/V·s and SLG FETs show $\mu_{FE} \approx$ 6000 cm^2/V·s. Thus, the responsivity of iGr devices should be at least 3 orders of magnitude lower than the responsivity of SLG devices decorated with the same perovskite NCs.

A fully inkjet printed $CsPb(Br/I)_3$/iGr heterostructure devices (**Figure 7.7a,b**) was successfully fabricated with a pair of Au contact pads printed using AuNP ink [27] onto Si/SiO_2 with a gap of ~ 30 μm. A single printed line of iGr was deposited across the gold-electrodes and functionalised with inkjet deposited $CsPb(Br/I)_3$ NCs (2 printed layers). The $CsPb(Br/I)_3$/iGr device displayed a responsivity of 20 A/W (**Figure 7.7c**), which is comparable to the drop-cast $CsPb(Br/I)_3$/iGr device (**Figure 7.6c**). The photoresponsivity threshold of λ_{ex} = 520 nm and response time of τ_{rise} = 10 s recorded for the printed $CsPb(Br/I)_3$/iGr device (**Figure 7.7c**, inset), was also comparable to the previous $CsPb(Br/I)_3$ devices.

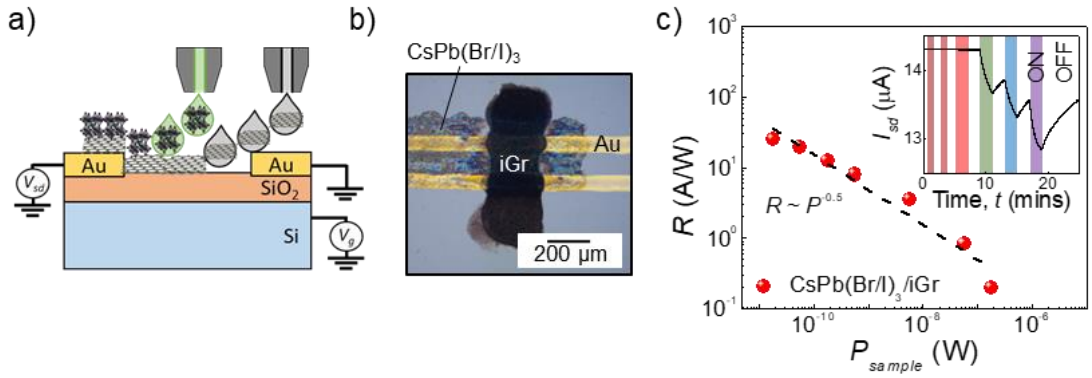


Figure 7.7. a) Schematic of inkjet deposition of perovskite NCs on top of iGr to fabricate fully printed detector. **b)** Optical image of printed $CsPb(Br/I)_3$/iGr device on Si/SiO_2 (10 layer $CsPb(Br/I)_3$, 3 layer iGr) with printed Au NP contact pads. **c)** Photoresponsivity, *R*, versus power for fully printed $CsPb(Br/I)_3$/iGr heterostructure (1 layer $CsPbBr_3$ and 1 layer iGr) device with printed AuNP electrodes (1 printed layer) (λ_{ex} = 520 nm illumination, V_{sd} = 100 mV, V_g = 0 V) . Inset: temporal response of $CsPb(Br/I)_3$/iGr heterostructure device under light illumination (V_{sd} = 100 mV, V_g = 0 V, P = 56.6 W/m^2) at different wavelengths of λ_{ex} = 1060, 808, 635, 520, 450, and 405 nm, respectively.

This fully printed $CsPb(Br/I)_3$/iGr device had 10× greater photoresponsivity than previous fully printed perovskite/graphene detectors [5], which is once again attributed to the enhanced stability of all inorganic perovskites used in this work and the optimised ink formulation. Now that the performance of these devices has been demonstrated on Si/SiO_2 substrates, further work is required to study how their performance changes on flexible substrates and under deformation for wearable/flexible photodetection applications.

Pristine undecorated iGr films may also demonstrate a measurable photoresponse without surface decoration, stronger than the one measured for SLG [311]. iGr films with 5 printed layers were deposited on flexible Kapton, and displayed a positive photocurrent under illumination with λ_{ex} = 520 nm (**Figure 7.8a**), with fast response

time constants of τ_{rise} = 1.5 s and τ_{fall} = 1.0 s, and a maximum photoresponsivity of R ~ 10^{-4} A/W (**Figure 7.8c**). A fast positive photocurrent was also observed at λ_{ex} = 1060, 808, and 635 nm, however, at λ_{ex} = 450 and 405 nm, the fast positive photocurrent was followed by a slower negative photocurrent (**Figure 7.8b**). Both the positive and negative photocurrents displayed photoresponsivities up to R ~ 10^{-4} A/W (**Figure 7.8c**).

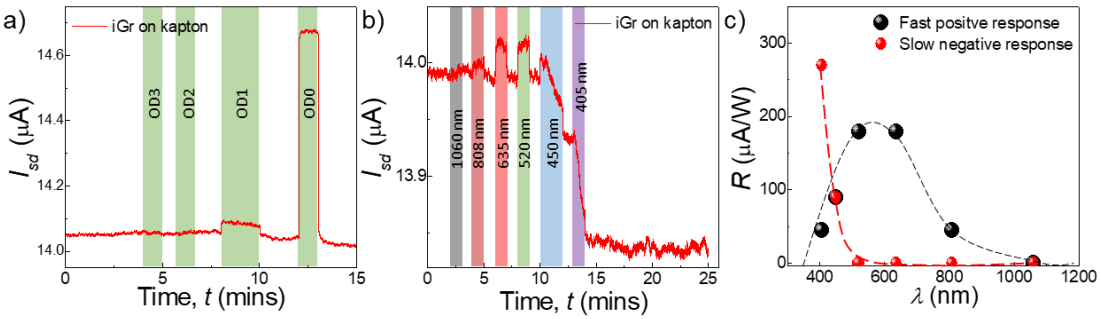


Figure 7.8. a) ON/OFF temporal response of iGr device printed on Kapton (5 layers) under illumination with increasing power from P = 12.7 W/m^2 (OD3) to 12.7 kW/m^2 (OD0) (V_{sd} = +3 mV, λ_{ex} = 520 nm). **b)** ON/OFF temporal response of device at different wavelengths (V_{sd} = +3 mV, P = 1.27 kW/m^2). **c)** R vs excitation wavelength for both the positive and negative photocurrents observed in the sample (dashed lines are a guide to the eye).

Similar photoresponses were measured for iGr films printed on Kapton and on Si/SiO_2, so it is unlikely that the substrate plays a role in generating the photocurrent. The source of the photocurrents measured in the iGr is unknown and requires further investigations. It is possible that some residuals of the EC additive in the ink may remain after annealing [316] and could be responsible for the photoresponse. In the $CsPbX_3$/iGr devices, the photocurrents induced by iGr are negligible compared to the large photocurrents induced by the $CsPbX_3$ NCs, so the iGr photoresponse does not impact the performance of these devices.

Formulation of a hybrid ink containing both iGr and $CsPbX_3$ NCs (iGr-$CsPbX_3$) (shown in **Chapter 5.2.3**), was also explored as another potential method to achieve fully printed devices in a single deposition step. No photoresponse was observed for iGr-$CsPb(Br/I)_3$ films annealed at 150 °C, likely due to their very high resistance (R_s ~ 10^7 Ω/sq). iGr-$CsPb(Br/I)_3$ films annealed at 250 °C were photoresponsive, although, no visible PL was observed for these films and the photoresponse was not fully reversible (**Figure 7.9a**). These iGr-$CsPb(Br/I)_3$ hybrid films printed on Si/SiO_2 displayed an onset of photoresponse at ~ 520 nm (**Figure 7.9a**) similar to the previous $CsPb(Br/I)_3$ devices, a maximum responsivity of 10^{-3} A/W, and the relationship between responsivity and incident power followed $R \sim P^{-0.5}$ (**Figure 7.9b**). Further studies of iGr-$CsPbX_3$ annealing conditions are required to improve photoresponsivity and ensure photoresponse is fully recoverable.

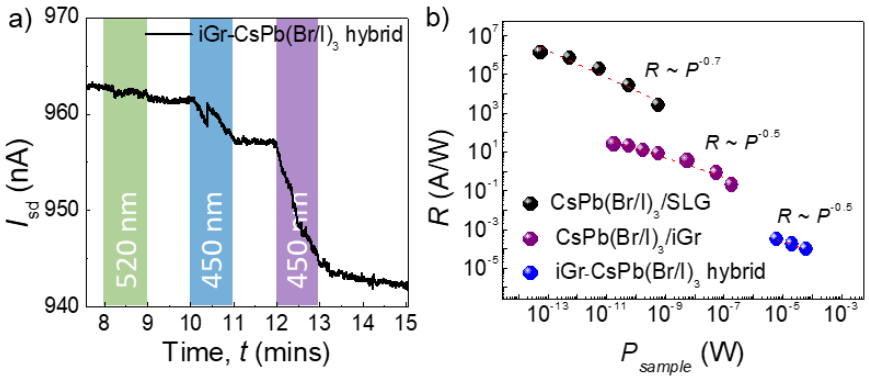


Figure 7.9. a) Temporal response of iGr-$CsPb(Br/I)_3$ hyrbid film (5 printed layers on Si/SiO_2) annealed at 250 °C under light illumination with λ_{ex} = 520, 450, and 405 nm (P = 0.18 W/cm^2 and V_{sd} = 1 V). **b)** Photoresponsivity, R, of the iGr-$CsPb(Br/I)_3$ hybrid device as a function of illumination power after 1 minute under λ_{ex} = 405 nm exposure (V_{sd} = 1 V, V_g = 0 V) compared to that of the printed $CsPb(Br/I)_3$/SLG device and fully printed $CsPb(Br/I)_3$/iGr heterostructure shown previously.

iGr-CsPb(Br/I)$_3$ films on Kapton, sintered using the IPL photonic annealing method were also investigated. Once again no visible PL was observed in the films after annealing. Similar to the iGr on Kapton measured previously (**Figure 7.8b**), these samples displayed a photoreponse at all wavelengths measured from λ_{ex} = 1060 nm to λ_{ex} = 405 nm, with the greatest response measured at λ_{ex} = 520 nm (**Figure 7.10a,b**). However, unlike the iGr measured previously, a fast negative photocurrent was observed at low bias voltages (V_{sd} < 10 mV), with 'spikes' in the photocurrent at the start and end of illumination (**Figure 7.10a**). This was a self-powered (photovoltaic) effect, occurring even at zero bias voltage (V_{sd} = 0 V). At higher bias voltages (V_{sd} > 100 mV), only a fast positive photocurrent was observed (**Figure 7.10b**), similar to that seen previously in iGr, and the responsivity of the device increased with increasing bias voltage (**Figure 7.10c**). At a bias voltage of 1 V with excitation of λ_{ex} = 520 nm, the device displayed a maximum responsivity of ~ 1 A/W, and the relationship between responsivity and incident power followed $R \sim P^{-0.5}$ (**Figure 7.10d**).

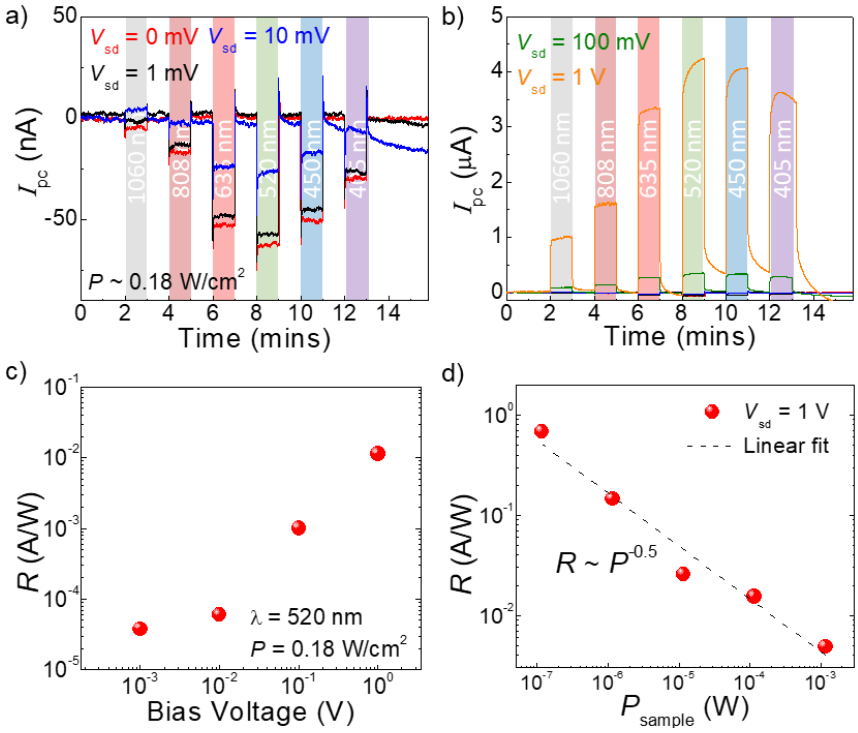


Figure 7.10. Temporal response of 5 layer iGr-CsPb(Br/I)$_3$ hybrid on Kapton, annealed using IPL, showing excitation with λ_{ex} = 1080, 808, 520, 450, and 405 nm with **a)** V_{sd} = 0, 1, and 10 mV and **b)** V_{sd} = 100 mV and 1 V. **c)** Photoresponsivity, R of hybrid device vs applied bias voltage, V_{sd} (λ_{ex} = 520 nm, P = 0.18 W/cm). **d)** Photoresponsivity, R of hybrid device vs power (λ_{ex} = 520 nm, V_{sd} = 1 V).

The responsivity of the iGr-CsPb(Br/I)$_3$ hybrid devices are much lower than that of the CsPb(Br/I)$_3$/iGr heterostructure, therefore, the CsPb(Br/I)$_3$/iGr heterostructure seems a more promising method to achieve fully-printed photodetectors. Further studies should be carried out to ensure the performance of CsPb(Br/I)$_3$/iGr heterostructures is consistent on flexible and rigid substrates. On the other hand, the iGr-CsPb(Br/I)$_3$ hybrid enabled simpler manufacturing and was used to create a self-powered detector. However, the mechanism behind photodetection in the IPL annealed iGr-CsPb(Br/I)$_3$ is not understood. The device was responsive at wavelengths much greater than the perovskite NCs band gap, so it is unlikely that the NCs played a significant role in

photodetection. Instead, some interaction between the iGr, Kapton, and IPL annealing method may be responsible for the photoresponse, however, further studies are required to fully understand these devices and improve their performance.

7.4 GQD PHOTODETECTORS

To explore graphene detectors functionalised with alternative nanonaterials and expand the spectral sensitivity of printed detectors into the UV range, GQD inks were formulated (as described in **Chapter 5.3**) and deposited on SLG. Before GQD ink deposition, the SLG $\sigma_{sd}(V_g)$ dependence revealed little hysteresis and the Dirac point was located at V_g = +55 V (**Figure 7.5a**, black lines). The hole and electron mobilities were calculated to be μ_e = 2100 cm^2/V·s and μ_h = 3500 cm^2/V·s. A drop of GQD ink was deposited onto SLG (**Figure 7.11a**) via drop-casting, which led to an increase in hysteresis and a large n-type shift in the Dirac point of the SLG to -5 V and 0 V during forward and backward V_g sweeps, respectively (**Figure 7.11b**, blue line**)**. After GQD deposition, the electron mobility of SLG was increased to μ_e = 3500 cm^2/V·s during forward V_g sweep and μ_e = 4200 cm^2/ V·s during backwards V_g sweep, whereas the hole mobility was decreased to μ_h = 2300 cm^2/V·s during forward V_g sweep and μ_h = 2000 cm^2/V·s during backwards V_g sweep. Subsequent addition of a drop of GQD-PEG ink onto the same device, GQD-PEG/GQD/SLG (**Figure 7.11a**), resulted in a further small increase of hysteresis and the Dirac point shifted to 0 V during forward V_g sweep and +18 V during backwards V_g sweep (**Figure 7.11b**, orange line). Following GQD-PEG deposition, the hole mobility was increased to μ_h = 4100 cm^2/V·s during forward V_g sweep and μ_h = 3400 cm^2/V·s during backwards V_g sweep, and the electron mobility was decreased to μ_e = 3000 cm^2/V·s during forward V_g sweep and increased to μ_e = 4900 cm^2/V·s during backwards V_g sweep.

During smaller V_g sweeps of ± 20 V instead of ± 50 V, no hysteresis was observed (**Figure 7.11c**). During these smaller V_g sweeps, the Dirac point of the GQD/SLG and GQD-PEG/GQD/SLG devices were located at +1 V and +9 V, respectively (**Figure 7.11c**). The emergence of hysteresis in $\sigma_{sd}(V_g)$ at V_g sweep ranges somewhere in the region between ± 20 V and ± 50 V, shows that there is an activation energy that must be overcome in order for charges to accumulate in the GQDs.

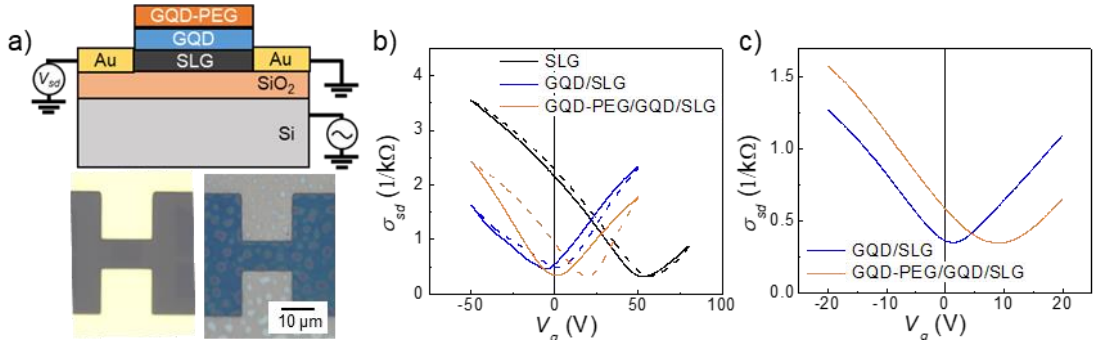


Figure 7.11. a) Schematic showing GQD-PEG/GQD/SLG device configuration with GQD and GQD-PEG deposited onto SLG OFET via drop-casting (top). Optical images of SLG OFET before (left), after drop-cast deposition of GQD and GQD-PEG (right). **b)** Dependence of SLG conductivity, σ_{sd}, on applied gate voltage, V_g, before and after drop-cast deposition of GQDs and GQDs-PEG. V_g is swept from -50 V to +50 V (+90 V for SLG) (solid lines) and then back to -50 V (dashed lines) (V_{sd} = 2 mV, sweep rate = 0.17 V/s). **c)** $\sigma_{sd}(V_g)$ dependence of GQDs/SLG and GQDs-PEG/GQD/SLG devices when V_g is swept from -20 V to +20 V (solid lines) and then back to -20 V (dashed lines) (V_{sd} = 2 mV, sweep rate = 0.17 V/s).

$\sigma_{sd}(V_g)$ dependence for GQD-PEG/GQD/SLG device was changed by reducing V_g sweep speed to 0.013 V/s (**Figure 7.12a)**. For the forward V_g sweep, Dirac point remained at ~ 0 V but the dependence had broadened, indicating a decrease of hole and electron mobility from μ_e = 3000 cm^2/V·s and μ_h = 4100 cm^2/V·s to μ_e =

1700 $cm^2/V{\cdot}s$ and μ_h = 1800 $cm^2/V{\cdot}s$. For the backward V_g sweep, the hole and electron mobilites were comparable at both V_g sweep rates, but at reduced V_g sweep rate the position of the Dirac point was shifted from 18 V to 30 V. The changes in $\sigma_{sd}(V_g)$ dependence with decreasing sweep speed is indicative of slow charge dynamics. Charge dynamics were further explored by AC electrical measurements (**Figure 7.12b)**. The capacitance of the SLG device was constant at C ~ 16 pF for all frequencies measured. However, after deposition of GQD and GQD-PEG, the capacitance increased with decreasing frequency (**Figure 7.12b)**. Hence, it is theorised that charges are only able to accumulate in the GQD at low frequencies due to slow charge dynamics.

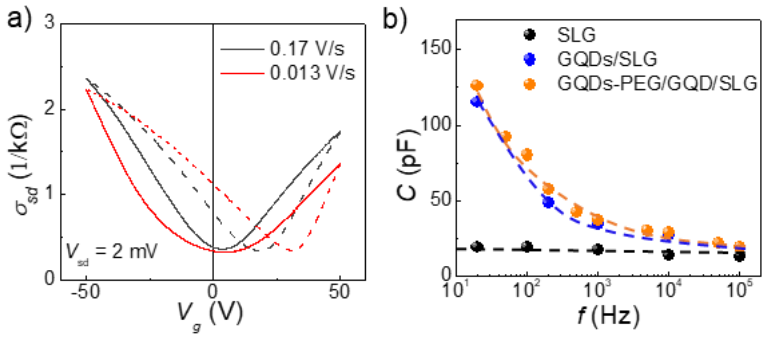


Figure 7.12. a). $\sigma_{sd}(V_g)$ dependence of GQDs-PEG/GQD/SLG when V_g is swept from -50 V to +50 V (solid lines) and then back to -50 V (dashed lines) with a sweep rate of 0.17 V/s (grey curves) and 0.013 V/s (red curve) (V_{sd} = 2 mV). **b)** Capacitance of SLG, GQD/SLG, and GQD-PEG/GQD/SLG devices as a function of frequency, measured between the gate and the source-drain contacts (dashed lines are a guide to the eye).

The photoresponse of these devices was also measured, to extend the spectral sensitivity of printed photodetectors into the UV range. The photoresponse onset of the GQD/SLG devices was recorded at λ_{ex} = 450 nm (**Figure 7.13a**) corresponding to the output of GQD absorption (**Figure 5.12a)**. A large photoreponse (maximum R ~

10^3 A/W) under exposure to UV light was measured, with time constant of τ_{rise} = 50 s and long relaxation periods after illumination due to slow charge dynamics (**Figure 7.13b**). Under excitation the $I_{sd}(V_g)$ dependence of GQD/SLG devices shifted towards the n-type by ~ 10 V (**Figure 7.13c**). During forward V_g sweep the value of I_{sd} at Dirac point decreased by 80 nA. By subtracting the $I_{sd}(V_g)$ measured under λ_{ex} = 405 nm illumination from the $I_{sd}(V_g)$ measured in the dark, a plot of photocurrent, I_{pc} as a function of V_g was produced (**Figure 7.13d**). This shows that I_{pc}, increases close to the Dirac point: at V_g = -4 V during forward V_g sweeps and at V_g = +14 V during backwards V_g sweep.

The photoreponsivity, *R*, was measured at V_g = 0 V, which is close to the value of maximum I_{pc}. A maximum photoresponsivity of R = 170 A/W was measured for the GQD/SLG device and a slightly larger R = 530 A/W was measured for the GQD-PEG/GQD/SLG device (**Figure 7.13e**), which is attributed to PEG capping the surface of the GQDs, protecting them from oxidation. Both devices had a similar $R(P)$ relationship of $R \sim P^{-0.9}$. GQDs and GQD-PVP were also deposited onto SLG via inkjet printing, GQD-PVP/GQD/SLG, to produce the first printed GQD photodetector, which displayed maximum R = 28 A/W and had an $R(P)$ relationship of $R \sim P^{-0.6}$ (**Figure 7.13e**).

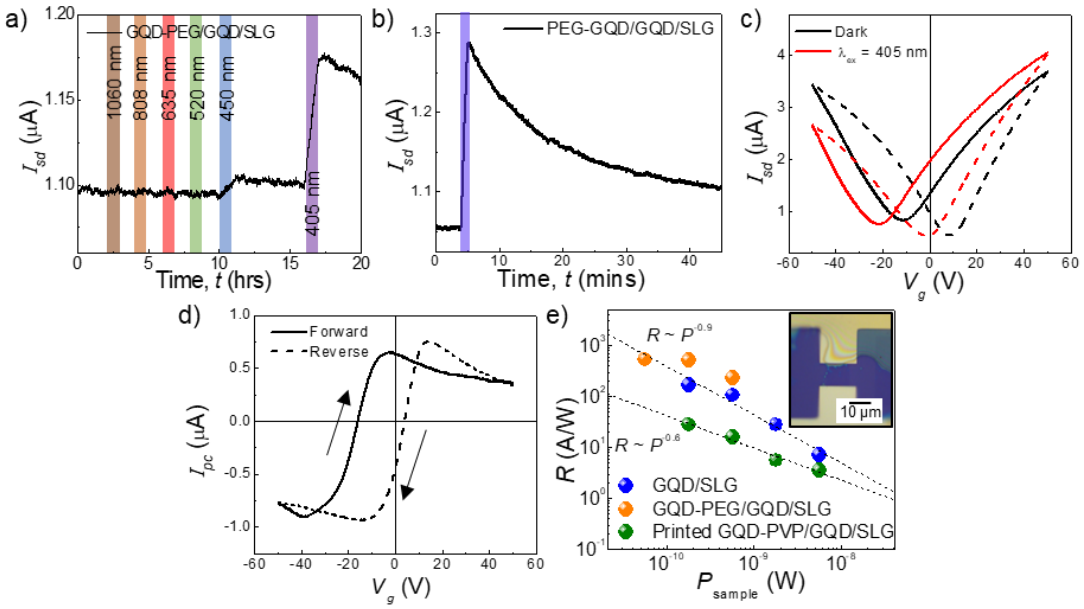


Figure 7.13. a) Temporal response of GQD-PEG/GQD/SLG device after illumination with λ_{ex} = 1060, 808, 635, 520, and 405 nm light (V_{sd} = 2 mV, V_g = 0 V, P = 5600 W/m^2). **b)** Temporal response of GQD-PEG/GQD/SLG device after illumination with λ_{ex} = 250 nm (V_{sd} = 2 mV, V_g = 0 V, P = 18 W/m^2). **c)** Dependence of GQD/SLG source-drain current, I_{sd}, on applied gate voltage, V_g, in the dark (black lines), and under λ_{ex} = 405 nm excitation (purple lines). V_g is swept from -50 V to +50 V (solid lines) and then back to -50 V (dashed lines) with a sweep rate of 0.17 V/s (V_{sd} = 2 mV, P = 56 W/m^2). **d)** Photocurrent, I_{pc} as a function of V_g calculated by subtracting I_{sd} during λ_{ex} = 405 nm excitation from dark I_{sd}. **e)** Photoresponsivity, R as a function of incident power on the sample for the drop-cast devices: GQD/SLG, GQD-PEG/GQD/SLG and for the printed device GQD-PVP/GQD/SLG (V_{sd} = 2 mV, V_g = 0 V, λ_{ex} = 405 nm). Dashed lines indicate lines of best fit. Inset: optical image of inkjet printed GQD-PVP/GQD/SLG device.

A printed GQD/SLG photodetector has not been fabricated previously so there is no direct comparison for the devices fabricated in this work. A vertical detector with GQD layer deposited by spin coating and sandwiched between two graphene sheets in a vertical configuration [317] achieved much faster responses (nanoseconds) than the

lateral devices fabricated in this work due to smaller channel length (45 nm) [317]. However, the printed GQD detectors fabricated in this work demonstrate ~ 100x greater responsivity. This increase in responsivity is likely due to lateral geometry and different GQD composition.

Due to the hydrophobic nature of graphene, uniform coverage of the SLG with GQDs was very challenging with water-based inks, via drop-casting or by inkjet printing. Inkjet printing with very small volumes led to small amounts of GQDs on top of the SLG which likely hampered device performance (**Figure 7.13e** - inset). Drop-casting on the other hand often achieved greater coverage due to larger volume of ink (**Figure 7.11a**), however, this often led to unresponsive devices, as incident light was completely absorbed by the thick GQD layer far above the SLG. For more consistent performance on SLG, a GQD ink based on different solvents should be explored with better wettability on SLG.

The water-based GQD inks developed in this work should instead be explored for applications on iGr and on flexible substrates, where ink wetting is more favourable (bottom row of **Figure 7.14**). Printing 10 layers of GQD or GQD-PVP ink onto a 10 layer iGr line on flexible Kapton substrate resulted in an increase in iGr resistance, R_{2t} by ~ 60% (**Figure 7.14a,c**). A similar increase in iGr resistance by ~ 120 % was seen after deposition of GQD-PEG ink (**Figure 7.14b**). This is likely caused by intermixing of the insulating GQDs into the iGr layer, which is discussed further in **Chapter 6.3**. Overall, this approach appears a promising route to achieve flexible fully printed detectors sensitive in the UV range, however, further studies are required to investigate photoresponse of these devices.

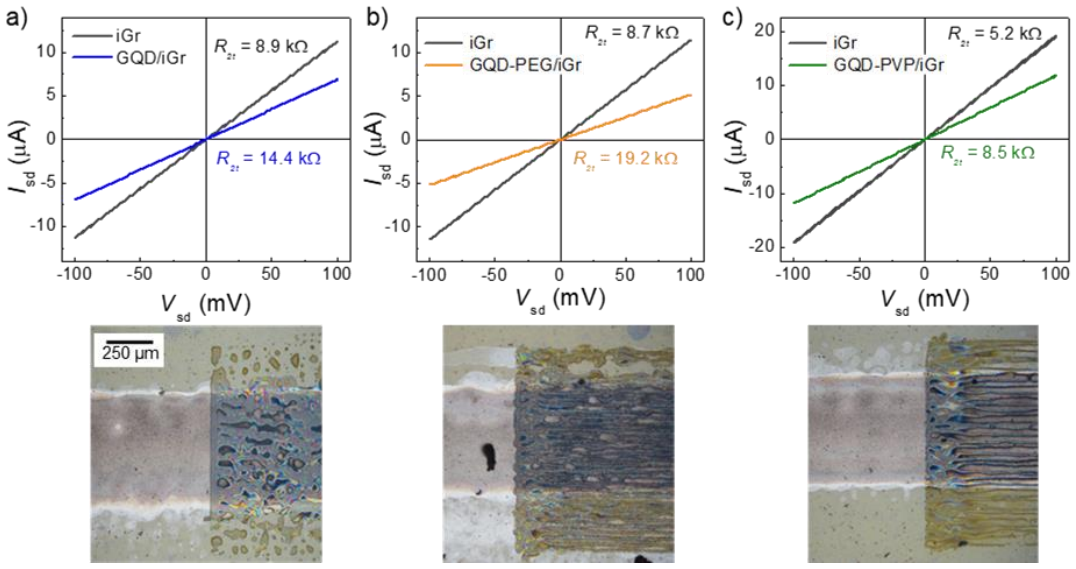


Figure 7.14. *I*(*V*) relationship of 10 layer inkjet printed graphene on Kapton before and after inkjet deposition of 10 layers of **a)** GQDs, **b)** GQD-PEG, and **c)** GQD-PVP, with optical images of the heterostructures below.

GQDs seem a promising material in graphene-based photodetectors and may help to expand the sensitivity range of printed photodetectors. In this work, the first printed GQD photodetector was demonstrated, displaying high performances with up to 100× greater responsivity than previous GQD/graphene devices produced via spin-coating [317]. The charge dynamics in GQD/SLG devices were also investigated to increase understanding of their performances. Future work should investigate new ink formulations with improved wetting onto SLG to improve the performance of printed GQD/SLG devices and further investigations are required to investigate the performance of fully printed detectors.

7.5 FULLY-PRINTED PEROVSKITE LED

In this work, an all inkjet printed perovskite LED was fabricated with an iGr bottom electrode, PEDOT:PSS hole transport layer, poly-TPD hole injection layer, $CsPbBr_3$

perovskite NCs emissive layer, TPBI electron injection layer, and AuNP top electrode (**Figure 7.15a,b**). LEDs with similar structures have been demonstrated in previous works, owing to the favourable band alignment of graphene, PEDOT:PSS, poly-TPD, $CsPbBr_3$, and TPBI, with spin-coated or thermally evaporated layers [106,318], but not with all layers deposited by inkjet printing. AuNP are less commonly used in such devices due to the large energy barrier between the AuNP and the conduction band of TPBI. Despite this, AuNPs were deemed the best material for the top electrode as more common choices such as Al/LiF require deposition by thermal evaporation, and AgNPs deposited via inkjet printing tend to short-circuit devices due to the presence of highly mobile Ag ions generated in the presence of heat or electric fields [27,319].

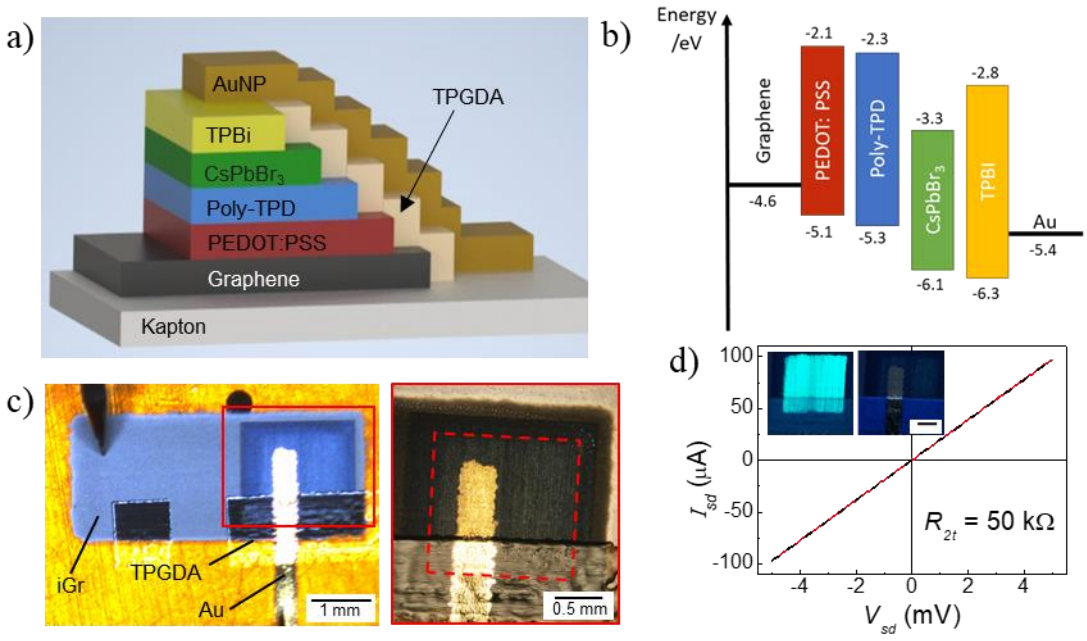


Figure 7.15. a) Schematic diagram and **b)** energy band diagram of fully-inkjet printed LED. The band edge energies for each material were taken from references [98,160,320–322]. **c)** Optical images of fully printed LED with Au electrode, TPGDA, and iGr labelled. The dashed red-line indicated the active area of the LED which contains all layers from Au to iGr. **d)** *I*(*V*) relationship of LED, measured between Au and iGr electrodes. Inset: optical images of LED active area under λ_{ex} = 365 nm illumination before (left) and after (right) deposition of top AuNP layer (scale bar = 500 μm).

In the design of this device, the architecture was chosen such that graphene was the bottom layer (as opposed to AuNP) since it required the highest annealing temperature of T_{anneal} = 250 °C. The addition of a dielectric layer of TPGDA was also chosen to be printed across one side of the device underneath the AuNP layer to enable more practical wiring of the device and prevent short-circuiting (**Figure 7.15a**). The device was printed in a pyramid structure, with each layer having ~ 200 μm smaller width and length than the last to prevent short circuiting. The device was printed on a flexible Kapton substrate with 5 printed layers of iGr, 4 layers of PEDOT:PSS, 1 layer of poly-TPD, 5 layers of $CsPbBr_3$, 2 layers of TPBI, 3 layers of TPGDA, and 3 layers of AuNP

(**Figure 7.15c**). These thicknesses were chosen to reflect those used in previous LED devices [106,318], while ensuring enough layers were printed to form uniform films.

No emission was visible from the LED under applied voltage between Au and iGr electrodes. Two reasons for this were identified. First, the *I*(*V*) relationship was linear and displayed much lower resistance than expected (**Figure 7.15d**). This indicates that a *p*-*n* junction was not formed, possibly due to short-circuit between the Au and iGr electrodes due to the low resistance recorded. This leakage of AuNPs may be directly through all layers the LED, but is more likely through the TPGDA layer, which looked particularly rough at the edges of the LED due to poor wetting across 6 different materials (**Figure 7.15c**), possibly owing to the wetting phenomenon described in **Chapter 6.2**. Secondly, the PL of the $CsPbBr_3$ perovskite NCs was greatly reduced after deposition and annealing of AuNPs (150 °C for 45 mins) due to thermal degradation of the NCs (**Figure 7.15d**, inset). Note that PL was still observed after printing and thermal annealing of all previous layers. Usually, a shorter annealing time of ~ 30 mins is sufficient for 1 printed layer of AuNP. However, 3 layers were required to produce a continuous film across the rough and tall TPGDA layer, thus 45 minutes were required. Therefore, it appears that both issues are caused by the TPGDA and Au layers, so a different approach was taken.

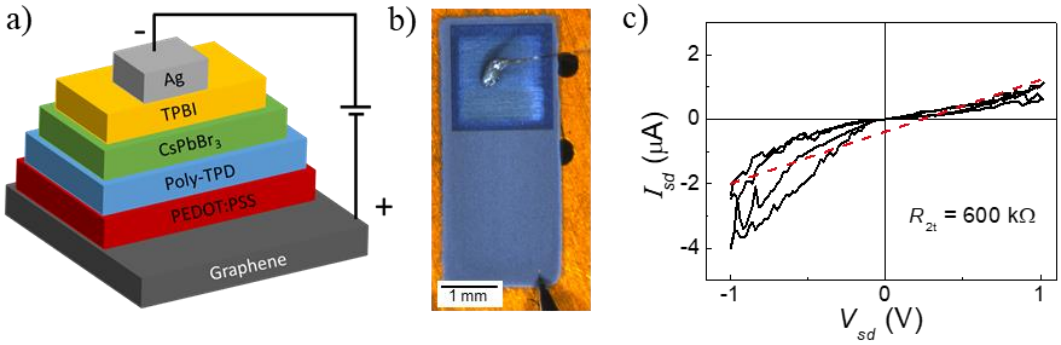


Figure 7.16. a) Schematic diagram and **b)** optical image of fully inkjet printed LED with mechanical Ag top contact instead of printed Au and TPBI. **c)** *I*(*V*) relationship of LED (black line) with linear fit (red dashed line).

Another LED was fabricated in the same way up to the TPBI layer but using a mechanical Ag top contact instead of the printed TPGDA and AuNPs to avoid short-circuiting the device and thermally degrading the NCs (**Figure 7.16a,b**). Again, no light emission was recorded from the LED under applied voltage. However, the resistance recorded for this device was much greater than before and the *I*(*V*) relationship of the device was non-linear, possibly indicating the formation of *p*-*n* junction (**Figure 7.16a,b**). This shows that at least some layers of the device (including the hole and electron injection layer poly-TPD and TPBI) are present. Possible causes for the lack of emission include: the perovskite layer has penetrated into the layers underneath leaving no emission material between the injection layers. If this is the case, using the $CsPbBr_3$-PVP ink will reduce intermixing of $CsPbBr_3$ (as shown in **Chapter 6.3**) and may enable the device to function. It is also possible that light emission is occurring, but only directly under the Ag contact where is difficult to detect. The use of a transparent contact such as ITO may enable visible emission.

While the ultimate goal of producing a working fully printed LED was unsuccessful, some promising signs were shown, which indicate that a printed LED using this

approach is possible. Going forward, the interfaces within the LED will be investigated and alternative device designs will be explored with a transparent top electrodes to bring this printed LED to light.

7.6 SUMMARY

Printing strategies were developed for perovskite NC inks as photosensitive layers in graphene-based photodetectors, including fully printed devices, and their performance was explored. $CsPbX_3$ NCs were first printed onto SLG and complex charge dynamics were uncovered in these devices, comparable to those seen previously in drop-cast devices [4,315]. These $CsPbX_3$/SLG devices achieved a photoresponsivity of $R > 10^3$ A/W for both red and green emitting perovskite NC inks. It was also demonstrated that SLG can be replaced by iGr in sensing applications. A lower responsivity $R > 10^1$ A/W was measured for the perovskite inks used to decorate iGr, and this was explained by lower charge mobility in printed graphene networks compared to SLG. Further work is required to improve iGr properties and printed $CsPbX_3$ stability to develop fully printed flexible and wearable detectors. Addition of polymer additives to the $CsPbX_3$ ink was also studied to improve NC stability, but complex photocurrents were observed which hindered photodetector device performances. Also, strange photocurrent behaviour was observed in printed iGr films and photovoltaic behaviour was observed in printed iGr-$CsPbX_3$ hybrid films, both of which merit further studies. The experiments and analysis of device performances provide a future strategy for development of nanomaterials for fully additively manufactured optoelectronics.

The first printed GQD photodetector was fabricated, with up to 100× greater responsivity than previous GQD/graphene devices produced via spin-coating [317]. Progress was also made towards understanding the complex charge dynamics in GQD/SLG devices. Slow charge dynamics and *n*-type doping of the SLG were observed following GQD deposition and device illumination, and high photoresponsivity in the UV-Vis range up to $R \sim 10^3$ A/W was measured for drop-cast GQD ink on SLG. However, a lower photoresponsivity of $R \sim 10^1$ A/W was observed for printed GQDs on SLG which is attributed to poor wetting of the GQD inks on SLG. Further work should be carried out to formulate GQD inks with hydrophobic solvents for applications on SLG. The water-based GQD inks developed in this work should instead be explored for applications on iGr and on flexible substrates, where ink wetting is more favourable. The results reported here provide opportunities for precise and upscalable surface functionalisation, by semiconducting NCs and QDs, of graphene-based devices produced using convectional Si-technologies as well as additive manufacturing methods, for potential applications in sensing and flexible/wearable optoelectronics.

Finally, a fully printed LED was fabricated, however, issues with the design and top layers of TPGDA and AuNP led to a failed device. By altering the device design, the formation of a *p*-*n* junction was shown, which is promising sign that a printed LED using this approach is possible. Overall, this work lays the foundations to achieve a fully printed perovskite LED and increases understanding of heterostructures deposited by inkjet printing for optoelectronic devices.

8 CONCLUSIONS

The primary aim of this PhD project was met and a number of functional material inks were developed for inkjet deposition and their applicability in exemplar optoelectronic devices was demonstrated. The key findings that are considered the most important and prospective for future studies are summarised below:

(**i**) Inks were formulated and inkjet deposition was developed for all-inorganic $CsPbX_3$ perovskites NCs and GQDs, increasing the availability of optically active materials for additive manufacturing technologies. Printed $CsPbX_3$ perovskite NC films displayed high uniformity, with thickness of ~ 20 nm, and maintained their bright fluorescence and optical properties after ink formulation and inkjet deposition onto Si/SiO_2 and flexible Kapton. The addition of PVP to this formulation appears a promising method to improve stability. Moreover, a hybrid ink containing both $CsPbX_3$ and iGr was formulated and is a promising solution for simplified manufacturing of optoelectronic devices, however, further optimisation of the post-processing protocol is required.

(**ii**) For the first time, water-based GQD inks were formulated and developed for inkjet printing to expand the spectral sensitivity of printed devices to the UV range. The addition of PEG and PVP in these inks was shown to improve the optical properties of printed films, provide the GQD with protection from oxidation, and improve substrate wettability on Si/SiO_2. Printed films with ~ 50 nm thickness were demonstrated and were shown to be highly electrically insulating and maintained their photoluminescence. Since these studies, the perovskite and GQD ink formulations have been used to print lanthanide-doped upconverting nanoparticles and PbS QDs, respectively. Thus, this work has the significance of developing and demonstrating ink formulations applicable to a wide range of 0D materials, which greatly simplifies the process of ink formulation.

(**iii**) Inks were formulated and inkjet deposition was developed for the polymers poly-TPD and TPBI, increasing the availability of charge transport materials for additive manufacturing technologies. For both polymers, printed films were demonstrated with comparable electrical properties and thicknesses (< 30 nm) to those previously deposited via spin coating. Previously developed PEDOT:PSS inks were also studied, and displayed good stability with respect to their electrical properties in ambient conditions, under UV and IR illumination, under T_{anneal} = 150 °C, under bending, and after inkjet deposition of a wide range of different materials on top of it. These studies demonstrate the excellent potential for the printed PEDOT:PSS ink in flexible heterostructure devices.

(**iv**) Different post-processing conditions for iGr were investigated to improve its compatibility with different substrates and other printed materials, and showed that lower thermal annealing temperatures of T_{anneal} = 150 °C over longer periods, displayed a sheet resistance R_s = 30 kΩ/sq, which is an improvement on previous studies using higher annealing temperatures for shorter time periods [11]. This approach was used to print iGr in heterostructures, such as PEDOT:PSS/iGr, and onto a variety of flexible substrates. Photonic annealing of iGr was also explored as a fast in-situ annealing solution, which achieved printed iGr films with R_s = 700 Ω/sq, comparable to the usual thermal annealing conditions of T_{anneal} = 250 °C. Finally, a photoresponse was measured for iGr films, which merits future studies.

(**v**) Fully inkjet printed heterostructures were fabricated, and a wetting phenomenon which occurred on Si/SiO_2 when printing certain materials on top of others was investigated. It was shown that this phenomenon could be used to print very precise curved lines and arrays of devices, and while this phenomenon can be explained analytically, further studies are required to uncover and understand its origin.

(**vi**) Printed heterostructures were probed using ToF-SIMS and FIB-SEM and it was found that large intermixing occurred between materials such as perovskite NCs and iGr, which is detrimental to performance of heterostructures for LED applications. The printing strategies were optimised to reduce intermixing as to achieve more uniform interfaces in printed heterostructures. The most successful methods to reduce intermixing were by the introduction of PVP to the perovskite NC ink, or alternatively, by adding a PEDOT:PSS interlayer between the perovskite and iGr layers. Reduction of the surfactant content in the PEDOT:PSS ink was also shown to improve interface quality between PEDOT:PSS and iGr. Thus, the combination of ToF-SIMS and FIB-SEM appears a promising method to probe the interfaces of printed heterostructures and inform the printing strategy to achieve improved device performance.

(**vii**) The developed 0D ink formulations were explored as photosensitive layers in graphene-based photodetectors, including fully printed devices. Complex charge dynamics were investigated in these devices, and photodetectors using printed perovskite NCs achieved the highest photoresponsivity in the UV-Vis range (R ~ 10^6 A/W on SLG and R ~ 10 A/W on iGr) reported to date for similar inkjet fabricated devices. Printed GQD photodetectors were also demonstrated for the first time here, with photoresponsivity up to R ~ 10^3 A/W in the UV-Vis range. The results reported here provide opportunities for surface functionalisation of devices produced using convectional Si-technologies as well as potential applications in flexible/wearable optoelectronics.

(**viii**) A fully printed heterostructure needed for a perovskite LED was manufactured, comprising of 6 different materials, including the hole and electron injection layers poly-TPD and TPBI. Using a mechanical Ag top electrode, a non-linear $I(V)$ relationship was measured through the LED which is attributed to the formation of a

p-n junction due to the successful deposition of poly-TPD and TPBI layers. However, no emission was recorded from the LED, possibly due to intermixing of perovskites into previous layers or due to emission only occurring beneath the Ag contact. While the ultimate goal of producing a working fully printed LED was unsuccessful, some promising signs are shown, which indicate that a printed LED using this approach is possible.

In summary, the studies presented in this thesis have expanded the availability of low-dimensional and polymeric materials for additive manufacturing technologies and have demonstrated the potential of graphene-based UV-Vis photodetectors and LEDs fabricated by inkjet printing. Printed perovskite/graphene detectors displayed high photoresponsivity and tuneable spectral response and graphene quantum dots are a promising material to expand their spectral range deeper into the UV range. The fully inkjet printed detectors demonstrated in this work have potential applications in next generation wearable/flexible electronics. With the deeper understanding of printed heterostructures that were gained in this work, more complex multilayer devices such as LED and fully printed circuits could be printed in the future.

9 OUTLOOK AND FUTURE WORK

For future work, further optimisation of the inks formulated in this thesis is recommended, to further improve the uniformity of printed layers. For poly-TPD and TPBI inks, the addition of additives such as Triton X-100 (Tx) and Tween-80 should be investigated, along with different surface treatments, such as ozone treatment, to reduce drop angle on the substrate. For the perovskite NC inks, the morphology of printed $CsPbX_3$-PVP films should be investigated, to access how the PVP affects printed film uniformity. Increasing substrate temperatures to > 60 °C during printing of perovskite NCs is another method that should be explored to improve film uniformity.

Formulation of a GQD ink should also be explored using solvents with more favourable wetting on SLG (e.g. the perovskite NC ink formulation developed in this work), to improve uniformity of GQD/SLG photodetectors. The water-based GQD ink presented here should instead be investigated for fully printed iGr-based detectors, where wetting is more favourable. Deposition of more 0D nanomaterials should be explored using the inks formulated in this thesis, to enable the printing of detectors sensitive over a wider spectral range. Since these studies, both PbS QDs and UCNPs have been printed using the formulations developed in this work.

Further studies should also be conducted on printed iGr and iGr-$CsPbX_3$ films. Photonic annealing of iGr should be explored on different substrates to access its viability, and the annealing conditions of iGr-$CsPbX_3$ should be optimised to preserve both the electrical and optical properties of the film. To achieve this, the addition of different iGr ink formulations should be used in the hybrid ink. Other graphene inks do not contain EC, and thus do not necessarily require such harsh annealing temperatures to function. Alternatively, different 0D materials with greater thermal

stability, such as lanthanide-doped upconverting NPs could be added to the hybrid ink instead of perovskite NCs, to enable single step deposition of detectors. The photoresponse observed in iGr films should also be studied further. The response should be investigated using iGr films printed on different substrates and annealed using different conditions to uncover its origin. FIB-SEM and ToF-SIMS could also be used to investigate how the morphology/porosity of iGr changes under different annealing conditions. Finally, in-situ annealing of iGr should be investigated by measuring the morphology and electrical performance of printed films that have been annealed after deposition of each individual layer, rather than after all layers have been printed. This may prove an effective method to reduce porosity in iGr and improve its performance.

The source of the two opposing photocurrents observed in $CsPbX_3$-PVP/SLG devices should be investigated further. To achieve this, the photoresponse measurements should be repeated at a variety of different temperatures. Thus, if the two effects have different activation energies, the two photoresponses could be observed and measured independently. Moreover, for all the fully printed detectors demonstrated in this thesis, further investigations should be carried out to access how their performances changes on flexible or stretchable substrates, and the effect of bending/stretching on photoreponse should be examined, to demonstrate their potential in wearable electronics.

Finally, further efforts are needed to understand the source of the wetting phenomenon observed when printing heterostructures, and to fabricate the fully printed LED. SIMS should be performed on the de-wetting regions before and after printing and annealing of the first layer, to access how the wettability of these regions change. For the LED, the use of a $CsPbX_3$-PVP emissive layer should be investigated to prevent intermixing.

Annealing of all layers should be conducted in vacuum to prevent oxidation, and further device architectures should be explored to prevent short-circuiting and enable printing of the AuNP top electrode.

REFERENCES

[1] S.M. Sze and K.K. Ng, “Physics of Semiconductor Devices: Third Edition”, (2006).

[2] R. Zhao, Z. Gu, P. Li, Y. Zhang, and Y. Song, *Adv. Mater. Technol.*, **7**, 2101124 (2022).

[3] M. Peng, Z. Wen, and X. Sun, *Adv. Funct. Mater.*, **33**, 2211548 (2023).

[4] N.D. Cottam, C. Zhang, L. Turyanska, L. Eaves, Z. Kudrynskyi, E.E. Vdovin, A. Patane, and O. Makarovsky, *ACS Appl. Electron. Mater.*, **2**, 147–154 (2020).

[5] A.M. Alamri, S. Leung, M. Vaseem, A. Shamim, and J.H. He, *IEEE Trans. Electron Devices*, **66**, 2657–2661 (2019).

[6] J. Shamsi, A.S. Urban, M. Imran, L. De Trizio, and L. Manna, *Chem. Rev.*, **119**, 3296–3348 (2019).

[7] Q. Zhang and Y. Yin, *ACS Cent. Sci.*, **4**, 668–679 (2018).

[8] L. Turyanska, O. Makarovsky, S.A. Svatek, P.H. Beton, C.J. Mellor, A. Patanè, L. Eaves, N.R. Thomas, M.W. Fay, A.J. Marsden, and N.R. Wilson, *Adv. Electron. Mater.*, **1**, 1500062 (2015).

[9] C.H. Liu, Y.C. Chang, T.B. Norris, and Z. Zhong, *Nat. Nanotechnol.*, **9**, 273–278 (2014).

[10] K. Cho, T. Lee, and S. Chung, *Nanoscale Horizons*, **7**, 1161–1176 (2022).

[11] F. Wang, J.H. Gosling, G.F. Trindade, G.A. Rance, O. Makarovsky, N.D. Cottam, Z. Kudrynskyi, A.G. Balanov, M.T. Greenaway, R.D. Wildman, R. Hague, C. Tuck, T.M. Fromhold, and L. Turyanska, *Adv. Funct. Mater.*, **31**, 2007478 (2021).

[12] Z. Gu, Y. Wang, S. Wang, T. Zhang, R. Zhao, X. Hu, Z. Huang, M. Su, Q. Xu, L. Li, Y. Zhang, and Y. Song, *Nano Res.*, **15**, 1547–1553 (2022).

[13] Q. Wang, G. Zhang, H. Zhang, Y. Duan, Z. Yin, and Y.A. Huang, *Adv. Funct. Mater.*, **31**, 2100857 (2021).

[14] V.R.F. Schröder, F. Hermerschmidt, S. Helper, C. Rehermann, G. Ligorio, H. Nässtrom, E.L. Unger, and E.J.W. List-Kratochvil, *Adv. Eng. Mater.*, **24**, 2101111 (2022).

[15] Y. Liu, F. Li, C. Perumal Veeramalai, W. Chen, T. Guo, C. Wu, and T.W. Kim, *ACS Appl. Mater. Interfaces*, **9**, 11662–11668 (2017).

[16] M. Min, R.F. Hossain, N. Adhikari, and A.B. Kaul, *ACS Appl. Mater. Interfaces*, **12**, 10809–10819 (2020).

[17] H. Lee, W. Harden-Chaters, S.D. Han, S. Zhan, B. Li, S.Y. Bang, H.W. Choi, S. Lee, B. Hou, L.G. Occhipinti, and J.M. Kim, *ACS Appl. Nano Mater.*, **3**, 4454–4464 (2020).

[18] M.J. Grotevent, C.U. Hail, S. Yakunin, D.N. Dirin, K. Thodkar, G. Borin Barin, P. Guyot-Sionnest, M. Calame, D. Poulikakos, M. V. Kovalenko, and I. Shorubalko, *Adv. Opt. Mater.*, **7**, 1900019 (2019).

[19] M.J. Grotevent, C.U. Hail, S. Yakunin, D. Bachmann, M. Calame, D. Poulikakos, M. V. Kovalenko, and I. Shorubalko, *Adv. Sci.*, **8**, 2003360 (2021).

[20] S. Singamneni, Y. LV, A. Hewitt, R. Chalk, W. Thomas, and D. Jordison, *J. Aeronaut. Aerosp. Eng.*, **08**, 215 (2019).

[21] R. Lastra, A. Pereira, M. Díaz-Cacho, J. Acevedo, and A. Collazo, *Appl. Sci.*, **12**, 10564 (2022).

[22] M. Touri, F. Kabirian, M. Saadati, S. Ramakrishna, and M. Mozafari, *Adv. Eng. Mater.*, **21**, 1800511 (2019).

[23] C. Weller, R. Kleer, and F.T. Piller, *Int. J. Prod. Econ.*, **164**, 43–56 (2015).

[24] J. O'Donnell, M. Kim, and H.S. Yoon, *J. Manuf. Sci. Eng. Trans. ASME*, **139**, 010801 (2017).

[25] G. Liu, X. Zhang, X. Chen, Y. He, L. Cheng, M. Huo, J. Yin, F. Hao, S. Chen, P. Wang, S. Yi, L. Wan, Z. Mao, Z. Chen, X. Wang, Z. Cao, and J. Lu, *Mater. Sci. Eng. R Reports*, **145**, 100596 (2021).

[26] G. Rivers, J.S. Austin, Y. He, A. Thompson, N. Gilani, N. Roberts, P. Zhao,

C.J. Tuck, R.J.M. Hague, R.D. Wildman, and L. Turyanska, *Addit. Manuf.*, **66**, 103452 (2023).

[27] J. Im, G.F. Trindade, T.T. Quach, A. Sohaib, F. Wang, J. Austin, L. Turyanska, C.J. Roberts, R. Wildman, R. Hague, and C. Tuck, *ACS Appl. Nano Mater.*, **5**, 6708–6716 (2022).

[28] I. Recalde, A.F. Gualdrón-Reyes, C. Echeverría-Arrondo, A. Villanueva-Antolí, J. Simancas, J. Rodriguez-Pereira, M. Zanatta, I. Mora-Seró, and V. Sans, *Adv. Funct. Mater.*, **33**, 2210802 (2023).

[29] O. Kassem, L. Pimpolari, C. Dun, D.K. Polyushkin, M. Zarattini, E. Dimaggio, L. Chen, G. Basso, F. Parenti, J.J. Urban, T. Mueller, G. Fiori, and C. Casiraghi, *Nanoscale*, **15**, 5689–5695 (2023).

[30] N. Saengchairat, T. Tran, and C.K. Chua, *Virtual Phys. Prototyp.*, **12**, 31–46 (2017).

[31] P.F. Moonen, I. Yakimets, and J. Huskens, *Adv. Mater.*, **24**, 5526–5541 (2012).

[32] M.A.M. Leenen, V. Arning, H. Thiem, J. Steiger, and R. Anselmann, *Phys. Status Solidi Appl. Mater. Sci.*, **206**, 588–597 (2009).

[33] S. Khan, L. Lorenzelli, and R.S. Dahiya, *IEEE Sens. J.*, **15**, 3164–3185 (2015).

[34] M. Singh, H.M. Haverinen, P. Dhagat, and G.E. Jabbour, *Adv. Mater.*, **22**, 673–685 (2010).

[35] H.P. Le, *J. Imaging Sci. Technol.*, **42**, 49–62 (1998).

[36] F. Mathies, E.J.W. List-Kratochvil, and E.L. Unger, *Energy Technol.*, **8**, 1900991 (2020).

[37] H. Kipphan, "Handbook of print media: technologies and production methods", (2002).

[38] D. Lohse, *Annu. Rev. Fluid Mech.*, **54**, 349–382 (2021).

[39] B. Derby, *J. Eur. Ceram. Soc.*, **31**, 2543–2550 (2011).

[40] A. Gao, J. Yan, Z. Wang, P. Liu, D. Wu, X. Tang, F. Fang, S. Ding, X. Li, J. Sun, M. Cao, L. Wang, L. Li, K. Wang, and X.W. Sun, *Nanoscale*, **12**, 2569–2577 (2020).

[41] D. Soltman and V. Subramanian, *Langmuir*, **24**, 2224–2231 (2008).

[42] G. Cai, P. Darmawan, M. Cui, J. Chen, X. Wang, A.L.S. Eh, S. Magdassi, and P.S. Lee, *Nanoscale*, **8**, 348–357 (2016).

[43] Y. Liu, N.O. Weiss, X.X. Duan, H.C. Cheng, Y. Huang, and X.X. Duan, *Nat. Rev. Mater.*, **1**, 1–17 (2016).

[44] K.S. Novoselov, A.K. Geim, S. V. Morozov, D. Jiang, Y. Zhang, S. V. Dubonos, I. V. Grigorieva, and A.A. Firsov, *Science*, **306**, 666–669 (2004).

[45] S.C. Ray, "Applications of Graphene and Graphene-Oxide based Nanomaterials", (2015).

[46] A.K. Geim and K.S. Novoselov, *Nat. Mater.*, **6**, 183–191 (2007).

[47] J.C. Meyer, A.K. Geim, M.I. Katsnelson, K.S. Novoselov, T.J. Booth, and S. Roth, *Nature*, **446**, 60–63 (2007).

[48] A.H. Castro Neto, F. Guinea, N.M.R. Peres, K.S. Novoselov, and A.K. Geim, *Rev. Mod. Phys.*, **81**, 109–162 (2009).

[49] H. Zhou, W.J. Yu, L. Liu, R. Cheng, Y. Chen, X. Huang, Y. Liu, Y. Wang, Y. Huang, and X. Duan, *Nat. Commun.*, **4**, 1–8 (2013).

[50] B. Chen, H. Huang, X. Ma, L. Huang, Z. Zhang, and L.M. Peng, *Nanoscale*, **6**, 15255–15261 (2014).

[51] J. Marcelo and J. Lopes, MBE growth of graphene, in: Mol. Beam Ep. Mater. Appl. Electron. Optoelectron., (2019).

[52] S. V. Morozov, K.S. Novoselov, M.I. Katsnelson, F. Schedin, D.C. Elias, J.A. Jaszczak, and A.K. Geim, *Phys. Rev. Lett.*, **100**, 016602 (2008).

[53] A.G. Kelly, T. Hallam, C. Backes, A. Harvey, A.S. Esmaeily, I. Godwin, J. Coelho, V. Nicolosi, J. Lauth, A. Kulkarni, S. Kinge, L.D.A. Siebbeles, G.S. Duesberg, and J.N. Coleman, *Science*, **356**, 69–73 (2017).

[54] Z. Li, R.J. Young, C. Backes, W. Zhao, X. Zhang, A.A. Zhukov, E. Tillotson, A.P. Conlan, F. Ding, S.J. Haigh, K.S. Novoselov, and J.N. Coleman, *ACS Nano*, **14**, 10976–10985 (2020).

[55] E. Jabari, F. Ahmed, F. Liravi, E.B. Secor, L. Lin, and E. Toyserkani, *2D Mater.*, **6**, 042004 (2019).

[56] S. Haar, M. Bruna, J.X. Lian, F. Tomarchio, Y. Olivier, R. Mazzaro, V. Morandi, J. Moran, A.C. Ferrari, D. Beljonne, A. Ciesielski, and P. Samorì, *J. Phys. Chem. Lett.*, **7**, 2714–2721 (2016).

[57] M. Döbbelin, A. Ciesielski, S. Haar, S. Osella, M. Bruna, A. Minoia, L. Grisanti, T. Mosciatti, F. Richard, E.A. Prasetyanto, L. De Cola, V. Palermo, R. Mazzaro, V. Morandi, R. Lazzaroni, A.C. Ferrari, D. Beljonne, and P. Samorì, *Nat. Commun.*, **7**, 11090 (2016).

[58] S. Priyadarsini, S. Mohanty, S. Mukherjee, S. Basu, and M. Mishra, *J. Nanostructure Chem.*, **8**, 123–137 (2018).

[59] P. He and B. Derby, *2D Mater.*, **4**, 021021 (2017).

[60] J.D. Caldwell, I. Aharonovich, G. Cassabois, J.H. Edgar, B. Gil, and D.N. Basov, *Nat. Rev. Mater.*, **4**, 552–567 (2019).

[61] G.W. Mudd, M.R. Molas, X. Chen, V. Zólyomi, K. Nogajewski, Z.R. Kudrynskyi, Z.D. Kovalyuk, G. Yusa, O. Makarovsky, L. Eaves, M. Potemski, V.I. Fal'Ko, and A. Patanè, *Sci. Rep.*, **6**, 1–10 (2016).

[62] S.H. Mir, V.K. Yadav, J.K. Singh, and J.K. Singh, *ACS Omega*, **5**, 14203–14211 (2020).

[63] T. Carey, S. Cacovich, G. Divitini, J. Ren, A. Mansouri, J.M. Kim, C. Wang, C. Ducati, R. Sordan, and F. Torrisi, *Nat. Commun.*, **8**, 1202 (2017).

[64] S. Ahmed and J. Yi, *Nano-Micro Lett.*, **9**, 1–23 (2017).

[65] W. Tang, C. Liu, L. Wang, X. Chen, M. Luo, W. Guo, S.W. Wang, and W. Lu, *Appl. Phys. Lett.*, **111**, 153502 (2017).

[66] C. Wang, F. Yang, and Y. Gao, *Nanoscale Adv.*, **2**, 4323–4340 (2020).

[67] R. Khursheed, K. Dua, S. Vishwas, M. Gulati, N.K. Jha, G.M. Aldhafeeri,

F.G. Alanazi, B.H. Goh, G. Gupta, K.R. Paudel, P.M. Hansbro, D.K. Chellappan, and S.K. Singh, *Biomed. Pharmacother.*, **150**, 112951 (2022).

[68] H.W. Tan, J. An, C.K. Chua, and T. Tran, *Adv. Electron. Mater.*, **5**, (2019).

[69] V. Mody, R. Siwale, A. Singh, and H. Mody, *J. Pharm. Bioallied Sci.*, **2**, 282 (2010).

[70] S. Hamacher, B. Bachmann, B. Wolfrum, and A. Yakushenko, Development of a gold nanoparticle conductive ink with a relatively low sintering temperature, in: Adv. Mater. - TechConnect Briefs 2017, (2017), pp. 141–144.

[71] A. Cetin and M. Ilk Capar, *J. Phys. Chem. B*, **126**, 5534–5543 (2022).

[72] M. Vetten and M. Gulumian, *Toxicol. Appl. Pharmacol.*, **363**, 131–141 (2019).

[73] L. Nayak, S. Mohanty, S.K. Nayak, and A. Ramadoss, *J. Mater. Chem. C*, **7**, 8771–8795 (2019).

[74] G.C. Jensen, C.E. Krause, G.A. Sotzing, and J.F. Rusling, *Phys. Chem. Chem. Phys.*, **13**, 4888–4894 (2011).

[75] G. Zhu, L. Pan, H. Sun, X. Liu, T. Lv, T. Lu, J. Yang, and Z. Sun, *ChemPhysChem*, **13**, 769–773 (2012).

[76] A. Määttänen, P. Ihalainen, P. Pulkkinen, S. Wang, H. Tenhu, and J. Peltonen, *ACS Appl. Mater. Interfaces*, **4**, 955–964 (2012).

[77] A.F. Al-Hossainy, A.A.I. Abd-Elmageed, and A.T.A. Ibrahim, *Arab. J. Chem.*, **12**, 2853–2863 (2019).

[78] G.M.A. Gad and M.A. Hegazy, *Mater. Res. Express*, **6**, 085024 (2019).

[79] M. Abulikemu, E.H. Da'as, H. Haverinen, D. Cha, M.A. Malik, and G.E. Jabbour, *Angew. Chemie*, **126**, 430–433 (2014).

[80] M.B. Gawande, A. Goswami, F.X. Felpin, T. Asefa, X. Huang, R. Silva, X. Zou, R. Zboril, and R.S. Varma, *Chem. Rev.*, **116**, 3722–3811 (2016).

[81] X.F. Zhang, Z.G. Liu, W. Shen, and S. Gurunathan, *Int. J. Mol. Sci.*, **17**, 1534 (2016).

[82] I.J. Fernandes, A.F. Aroche, A. Schuck, P. Lamberty, C.R. Peter, W. Hasenkamp, and T.L.A.C. Rocha, *Sci. Rep.*, **10**, 8878 (2020).

[83] S. Magdassi, M. Grouchko, and A. Kamyshny, *Materials (Basel).*, **3**, 4626–4638 (2010).

[84] E.G. Barbagiovanni, D.J. Lockwood, P.J. Simpson, and L. V. Goncharova, *Appl. Phys. Rev.*, **1**, (2014).

[85] A.P. Alivisatos, *Science*, **271**, 933–937 (1996).

[86] V.A. Singh, V. Ranjan, and M. Kapoor, *Bull. Mater. Sci.*, **22**, 563–569 (1999).

[87] L. Brus, *J. Phys. Chem.*, **90**, 2555–2560 (1986).

[88] J.M. Pietryga, Y.S. Park, J. Lim, A.F. Fidler, W.K. Bae, S. Brovelli, and V.I. Klimov, *Chem. Rev.*, **116**, 10513–10622 (2016).

[89] A.P. Litvin, I. V. Martynenko, F. Purcell-Milton, A. V. Baranov, A. V. Fedorov, and Y.K. Gun'Ko, *J. Mater. Chem. A*, **5**, 13252–13275 (2017).

[90] L. Protesescu, S. Yakunin, M.I. Bodnarchuk, F. Krieg, R. Caputo, C.H. Hendon, R.X. Yang, A. Walsh, and M. V. Kovalenko, *Nano Lett.*, **15**, 3692–3696 (2015).

[91] Y. Yu, J. Xia, and Y. Liang, *AIP Adv.*, **12**, 055307 (2022).

[92] E.B. Kim, M.S. Akhtar, H.S. Shin, S. Ameen, and M.K. Nazeeruddin, *J. Photochem. Photobiol. C Photochem. Rev.*, **48**, (2021).

[93] J. Huang, Y.H. Wu, Z.G. Zhu, W.Y. Shih, and W.H. Shih, *Chem. Phys. Lett.*, **702**, 21–25 (2018).

[94] Z.Y. Zhang, H.Y. Wang, Y.X. Zhang, Y.W. Hao, C. Sun, Y. Zhang, B.R. Gao, Q.D. Chen, and H.B. Sun, *Sci. Rep.*, **6**, (2016).

[95] K.H. Wang, L.C. Li, M. Shellaiah, and K.W. Sun, *Sci. Rep.*, **7**, 13643 (2017).

[96] C. Zhang, L. Turyanska, H. Cao, L. Zhao, M.W. Fay, R. Temperton, J. O'Shea, N.R. Thomas, K. Wang, W. Luan, and A. Patanè, *Nanoscale*, **11**, 13450–13457 (2019).

[97] C.H. Tien, L.C. Chen, K.Y. Lee, Z.L. Tseng, Y.S. Dong, and Z.J. Lin,

Energies, **12**, 3507 (2019).

[98] A.K. Guria, S.K. Dutta, S. Das Adhikari, and N. Pradhan, *ACS Energy Lett.*, **2**, 1014–1021 (2017).

[99] S. Thomas and A. Thankappan, "Perovskite photovoltaics: Basic to advanced concepts and implementation", Elsevier, (2018).

[100] M. Cahay and Electrochemical Society., "Quantum confinement VI : nanostructured materials and devices : proceedings of the international symposium", Electrochemical Society, (2001).

[101] Q. Zhang, H. Nan, Y. Zhou, Y. Gu, M. Tai, Y. Wei, F. Hao, J. Li, D. Oron, and H. Lin, *J. Mater. Chem. C*, **7**, 6795–6804 (2019).

[102] Y. Liu, F. Li, L. Qiu, K. Yang, Q. Li, X. Zheng, H. Hu, T. Guo, C. Wu, and T.W. Kim, *ACS Nano*, **13**, acsnano.8b08582 (2019).

[103] S. Karabel Ocal, N.B. Kiremitler, A.F. Yazici, N. Celik, E. Mutlugun, and M.S. Onses, *ACS Appl. Nano Mater.*, **5**, 6201–6212 (2022).

[104] L.J. Ruan, B. Tang, and Y. Ma, *J. Phys. Chem. C*, **123**, 11959–11967 (2019).

[105] Y. He, Y.J. Yoon, Y.W. Harn, G. V. Biesold-McGee, S. Liang, C.H. Lin, V. V. Tsukruk, N. Thadhani, Z. Kang, and Z. Lin, *Sci. Adv.*, **5**, 4424 (2019).

[106] C. Zhang, S. Wang, X. Li, M. Yuan, L. Turyanska, and X. Yang, *Adv. Funct. Mater.*, **30**, 1910582 (2020).

[107] C. Otero-Martínez, N. Fiuza-Maneiro, and L. Polavarapu, *ACS Appl. Mater. Interfaces*, **14**, 34291–34302 (2022).

[108] S. Zou, Y. Liu, J. Li, C. Liu, R. Feng, F. Jiang, Y. Li, J. Song, H. Zeng, M. Hong, and X. Chen, *J. Am. Chem. Soc.*, **139**, 11443–11450 (2017).

[109] F. Liu, C. Ding, Y. Zhang, T.S. Ripolles, T. Kamisaka, T. Toyoda, S. Hayase, T. Minemoto, K. Yoshino, S. Dai, M. Yanagida, H. Noguchi, and Q. Shen, *J. Am. Chem. Soc.*, **139**, 16708–16719 (2017).

[110] R. Sharma, A. Sharma, S. Agarwal, and M.S. Dhaka, *Sol. Energy*, **244**, 516–535 (2022).

[111] S. Gupta, T. Smith, A. Banaszak, and J. Boeckl, *Nanomaterials*, **7**, 301 (2017).

[112] C. Zhao, X. Song, Y. Liu, Y. Fu, L. Ye, N. Wang, F. Wang, L. Li, M. Mohammadniaei, M. Zhang, Q. Zhang, and J. Liu, *J. Nanobiotechnology*, **18**, 142 (2020).

[113] S. Shafraniuk, "Graphene: Fundamentals, devices and applications", (2015).

[114] J. Shen, Y. Zhu, X. Yang, J. Zong, J. Zhang, and C. Li, *New J. Chem.*, **36**, 97–101 (2012).

[115] P. Tian, L. Tang, K.S. Teng, and S.P. Lau, *Mater. Today Chem.*, **10**, 221–258 (2018).

[116] S. Reagen, Y. Wu, X. Liu, R. Shahni, J. Bogenschuetz, X. Wu, Q.R. Chu, N. Oncel, J. Zhang, X. Hou, C. Combs, A. Vasquez, and J.X. Zhao, *ACS Appl. Mater. Interfaces*, **13**, 43952–43962 (2021).

[117] S. Gu, C. Te Hsieh, C.Y. Yuan, Y.A. Gandomi, J.K. Chang, C.C. Fu, J.W. Yang, and R.S. Juang, *J. Lumin.*, **217**, 116774 (2020).

[118] Y. Liu and D.Y. Kim, *Chem. Commun.*, **51**, 4176–4179 (2015).

[119] Z. Gan, S. Xiong, X. Wu, T. Xu, X. Zhu, X. Gan, J. Guo, J. Shen, L. Sun, and P.K. Chu, *Adv. Opt. Mater.*, **1**, 926–932 (2013).

[120] Z. Gan, H. Xu, and Y. Hao, *Nanoscale*, **8**, 7794–7807 (2016).

[121] X. Guo, C.F. Wang, Z.Y. Yu, L. Chen, and S. Chen, *Chem. Commun.*, **48**, 2692–2694 (2012).

[122] Y. Dong, H. Pang, H. Bin Yang, C. Guo, J. Shao, Y. Chi, C.M. Li, and T. Yu, *Angew. Chemie - Int. Ed.*, **52**, 7800–7804 (2013).

[123] D. Pan, J. Zhang, Z. Li, and M. Wu, *Adv. Mater.*, **22**, 734–738 (2010).

[124] S. Yang, J. Sun, X. Li, W. Zhou, Z. Wang, P. He, G. Ding, X. Xie, Z. Kang, and M. Jiang, *J. Mater. Chem. A*, **2**, 8660–8667 (2014).

[125] Z. Gan, H. Xu, and Y. Fu, *J. Phys. Chem. C*, **120**, 29432–29438 (2016).

[126] A. Kovalchuk, K. Huang, C. Xiang, A.A. Martí, and J.M. Tour, *ACS Appl. Mater. Interfaces*, **7**, 26063–26068 (2015).

[127] N. Gobi, D. Vijayakumar, O. Keles, and F. Erogbogbo, *ACS Omega*, **2**, 4356–4362 (2017).

[128] M. Aghajamali, M.A. Vieira, R. Firouzi-Haji, K. Cui, J.Y. Cho, A.J. Bergren, H. Hassanzadeh, and A. Meldrum, *Nanoscale Adv.*, **4**, 4080–4093 (2022).

[129] M. Li, T. Chen, J.J. Gooding, and J. Liu, *ACS Sensors*, **4**, 1732–1748 (2019).

[130] J. Kang and L.W. Wang, *J. Phys. Chem. Lett.*, **8**, 489–493 (2017).

[131] M. Bacon, S.J. Bradley, and T. Nann, *Part. Part. Syst. Charact.*, **31**, 415–428 (2014).

[132] S. Chung, R.A. Revia, and M. Zhang, *Adv. Mater.*, **33**, 1904362 (2021).

[133] M. Angelopoulos, *IBM J. Res. Dev.*, **45**, 57–75 (2001).

[134] B. Weng, R. Shepherd, J. Chen, and G.G. Wallace, *J. Mater. Chem.*, **21**, 1918–1924 (2011).

[135] Z. Stempien, T. Rybicki, E. Rybicki, M. Kozanecki, and M.I. Szynkowska, *Synth. Met.*, **202**, 49–62 (2015).

[136] T. Rödlmeier, T. Marszalek, M. Held, S. Beck, C. Müller, R. Eckstein, A.J. Morfa, R. Lovrincic, A. Pucci, U. Lemmer, J. Zaumseil, W. Pisula, and G. Hernandez-Sosa, *Chem. Mater.*, **29**, 10150–10158 (2017).

[137] M. Baklar, P.H. Wöbkenberg, D. Sparrowe, M. Gonalves, I. McCulloch, M. Heeney, T. Anthopoulos, and N. Stingelin, *J. Mater. Chem.*, **20**, 1927–1931 (2010).

[138] T. Kim, S. Park, J. Seo, C.W. Lee, and J.M. Kim, *Org. Electron.*, **74**, 77–81 (2019).

[139] X. Fan, W. Nie, H. Tsai, N. Wang, H. Huang, Y. Cheng, R. Wen, L. Ma, F. Yan, and Y. Xia, *Adv. Sci.*, **6**, (2019).

[140] M.N. Gueye, A. Carella, J. Faure-Vincent, R. Demadrille, and J.-P. Simonato, *Prog. Mater. Sci.*, **108**, 100616 (2020).

[141] Y. Yang, H. Deng, and Q. Fu, *Mater. Chem. Front.*, **4**, 3130–3152 (2020).

[142] H.W. Chen and C. Li, *Chinese J. Polym. Sci. (English Ed.*, **38**, 435–448

(2020).

[143] C. Yeon, G. Kim, J.W. Lim, and S.J. Yun, *RSC Adv.*, **7**, 5888–5897 (2017).

[144] L. V. Lingstedt, M. Ghittorelli, H. Lu, D.A. Koutsouras, T. Marszalek, F. Torricelli, N.I. Crăciun, P. Gkoupidenis, and P.W.M. Blom, *Adv. Electron. Mater.*, **5**, 1800804 (2019).

[145] A. Singh, S. Mandal, V. Singh, A. Garg, and M. Katiyar, Inkjet printed PEDOT:PSS for organic devices, in: 16th Int. Work. Phys. Semicond. Devices, (2012).

[146] R. Bail, J.Y. Hong, and B.D. Chin, *RSC Adv.*, **8**, 11191–11197 (2018).

[147] N. Graddage, T.Y. Chu, H. Ding, C. Py, A. Dadvand, and Y. Tao, *Org. Electron.*, **29**, 114–119 (2016).

[148] S. Wang, C. Yang, X. Li, H. Jia, S. Liu, X. Liu, T. Minari, and Q. Sun, *J. Mater. Chem. C*, **10**, 6196–6221 (2022).

[149] Y. He, F. Zhang, E. Saleh, J. Vaithilingam, N. Aboulkhair, B. Begines, C.J. Tuck, R.J.M. Hague, I.A. Ashcroft, and R.D. Wildman, *Addit. Manuf.*, **16**, 153–161 (2017).

[150] W. Su, B.S. Cook, Y. Fang, and M.M. Tentzeris, *Sci. Rep.*, **6**, 35111 (2016).

[151] F. Zhang, C. Tuck, R. Hague, Y. He, E. Saleh, Y. Li, C. Sturgess, and R. Wildman, *J. Appl. Polym. Sci.*, **133**, n/a-n/a (2016).

[152] K. Suematsu, M. Arimura, N. Uchiyama, S. Saita, and T. Makino, *Compos. Part B Eng.*, **104**, 80–86 (2016).

[153] M. Mikolajek, T. Reinheimer, N. Bohn, C. Kohler, M.J. Hoffmann, and J.R. Binder, *Sci. Rep.*, **9**, (2019).

[154] V.I. Arkhipov, E. V. Emelianova, Y.H. Tak, and H. Bässler, *J. Appl. Phys.*, **84**, 848–856 (1998).

[155] N. Chopra, J. Lee, Y. Zheng, S.H. Eom, J. Xue, and F. So, *Appl. Phys. Lett.*, **93**, 143307 (2008).

[156] R. Saha, D.A. Lyashenko, and A.A. Zakhidov, *Phys. Status Solidi Appl.*

Mater. Sci., **219**, 2100872 (2022).

[157] M.A. Khan, W. Xu, Khizar-ul-Haq, Y. Bai, X.Y. Jiang, Z.L. Zhang, and W.Q. Zhu, *Semicond. Sci. Technol.*, **23**, 055014 (2008).

[158] L. Lan, B. Liu, H. Tao, J. Zou, C. Jiang, M. Xu, L. Wang, J. Peng, and Y. Cao, *J. Mater. Chem. C*, **7**, 5755–5763 (2019).

[159] S. Yoon, S. Sohn, J. Kwon, J.A. Park, and S. Jung, *Thin Solid Films*, **607**, 55–58 (2016).

[160] Q. Shan, J. Song, Y. Zou, J. Li, L. Xu, J. Xue, Y. Dong, B. Han, J. Chen, and H. Zeng, *Small*, **13**, 1701770 (2017).

[161] X. Dai, Z. Zhang, Y. Jin, Y. Niu, H. Cao, X. Liang, L. Chen, J. Wang, and X. Peng, *Nature*, **515**, 96–99 (2014).

[162] A. Giuri, S. Masi, A. Listorti, G. Gigli, S. Colella, C. Esposito Corcione, and A. Rizzo, *Nano Energy*, **54**, 400–408 (2018).

[163] P. Yang, L. Zhang, D.J. Kang, R. Strahl, and T. Kraus, *Adv. Opt. Mater.*, **8**, 1901429 (2020).

[164] T. Watanabe, K. Nakamura, S. Kawami, Y. Fukuda, T. Tsuji, T. Wakimoto, and S. Miyaguchi, *Org. Light. Mater. Devices IV*, **4105**, 175 (2001).

[165] J. Kalinowski, M. Cocchi, D. Virgili, P. Di Marco, and V. Fattori, *Chem. Phys. Lett.*, **380**, 710–715 (2003).

[166] D. Troadec, G. Veriot, and A. Moliton, Blue light emitting diodes with bathocuproine layer, in: Synth. Met., (2002), pp. 165–168.

[167] A. Chittawanij and K. Locharoenrat, *Adv. Condens. Matter Phys.*, **2017**, (2017).

[168] J. Calimano, F. Li, J. Florián, D.M. Piñero-Cruz, T.R. Fielitz, R.J. Holmes, and J.W. Ciszek, *J. Phys. Chem. C*, **124**, 23716–23723 (2020).

[169] Y. Tao, C. Yang, and J. Qin, *Chem. Soc. Rev.*, **40**, 2943–2970 (2011).

[170] J. Yu, N. Wang, Y. Zang, and Y. Jiang, *Sol. Energy Mater. Sol. Cells*, **95**, 664–668 (2011).

[171] J.G. Jang and H.K. Shin, *Thin Solid Films*, **517**, 4122–4126 (2009).

[172] P. Chen, Z. Xiong, X. Wu, M. Shao, X. Ma, Z.H. Xiong, and C. Gao, *J. Phys. Chem. Lett.*, **8**, 1810–1818 (2017).

[173] Z. Xiao, Y. Wu, L. He, X. Yang, Y. Lian, G. Li, and X. Yang, *RSC Adv.*, **9**, 29037–29043 (2019).

[174] F. Torrisi, T. Hasan, W. Wu, Z. Sun, A. Lombardo, T.S. Kulmala, G.W. Hsieh, S. Jung, F. Bonaccorso, P.J. Paul, D. Chu, and A.C. Ferrari, *ACS Nano*, **6**, 2992–3006 (2012).

[175] H. Guo, R. Lv, and S. Bai, *Nano Mater. Sci.*, **1**, 101–115 (2019).

[176] D. McManus, S. Vranic, F. Withers, V. Sanchez-Romaguera, M. Macucci, H. Yang, R. Sorrentino, K. Parvez, S.K. Son, G. Iannaccone, K. Kostarelos, G. Fiori, and C. Casiraghi, *Nat. Nanotechnol.*, **12**, 343–350 (2017).

[177] S. Majee, W. Zhao, A. Sugunan, T. Gillgren, J.A. Larsson, R. Brooke, N. Nordgren, Z. Zhang, S. Zhang, D. Nilsson, and A. Ahniyaz, *Adv. Mater. Interfaces*, **9**, 2101884 (2022).

[178] T. Carey, A. Alhourani, R. Tian, S. Seyedin, A. Arbab, J. Maughan, L. Šiller, D. Horvath, A. Kelly, H. Kaur, E. Caffrey, J.M. Kim, H.R. Hagland, and J.N. Coleman, *Npj 2D Mater. Appl.*, **6**, 1–11 (2022).

[179] A.C.M. de Moraes, W.J. Hyun, J.T. Seo, J.R. Downing, J. Lim, and M.C. Hersam, *Adv. Funct. Mater.*, **29**, 1902245 (2019).

[180] R. Martínez-Flores, E.J. Canto-Aguilar, G. Rodríguez-Gattorno, G. Oskam, D. Meneses-Rodríguez, and M.A. Ruiz-Gómez, *J. Electrochem. Soc.*, **166**, 3279–3285 (2019).

[181] T. Mahmoudi, Y. Wang, and Y.B. Hahn, *Nano Energy*, **47**, 51–65 (2018).

[182] R.F. Hossain and A.B. Kaul, *J. Vac. Sci. Technol. B*, **38**, 042206 (2020).

[183] Y. Jeong, J. Shin, Y. Hong, M. Wu, S. Hong, K.C. Kwon, S. Choi, T. Lee, H.W. Jang, and J.H. Lee, *Solid. State. Electron.*, **153**, 27–32 (2019).

[184] T. Carey, A. Arbab, L. Anzi, H. Bristow, F. Hui, S. Bohm, G. Wyatt-Moon, A. Flewitt, A. Wadsworth, N. Gasparini, J.M. Kim, M. Lanza, I. McCulloch, R.

Sordan, and F. Torrisi, *Adv. Electron. Mater.*, **7**, 2100112 (2021).

[185] J. Niittynen, R. Abbel, M. Mäntysalo, J. Perelaer, U.S. Schubert, and D. Lupo, *Thin Solid Films*, **556**, 452–459 (2014).

[186] G.F. Trindade, F. Wang, J. Im, Y. He, A. Balogh, D. Scurr, I. Gilmore, M. Tiddia, E. Saleh, D. Pervan, L. Turyanska, C.J. Tuck, R. Wildman, R. Hague, and C.J. Roberts, *Commun. Mater.*, **2**, 47 (2021).

[187] T. Du, C. Tang, B. Xing, Y. Lu, F. Huang, and C. Zuo, *J. Electron. Mater.*, **48**, 231–237 (2019).

[188] A. Albrecht, A. Rivadeneyra, A. Abdellah, P. Lugli, and J.F. Salmerón, *J. Mater. Chem. C*, **4**, 3546–3554 (2016).

[189] M. Grouchko, A. Kamyshny, and S. Magdassi, *J. Mater. Chem.*, **19**, 3057–3062 (2009).

[190] S. Jeong, K. Woo, D. Kim, S. Lim, J.S. Kim, H. Shin, Y. Xia, and J. Moon, *Adv. Funct. Mater.*, **18**, 679–686 (2008).

[191] S. Mekhmouken, N. Battaglini, G. Mattana, A. Maurin, S. Zrig, B. Piro, D. Capitao, and V. Noel, *Electrochem. Commun.*, **123**, (2021).

[192] E. Sowade, M. Polomoshnov, A. Willert, and R.R. Baumann, *Adv. Eng. Mater.*, **21**, 1900568 (2019).

[193] G. Kara, S. Bolat, K. Sharma, M.J. Grotevent, D.N. Dirin, D. Bachmann, R. Furrer, L.F. Boesel, Y.E. Romanyuk, R.M. Rossi, M. V. Kovalenko, M. Calame, and I. Shorubalko, *Adv. Mater. Technol.*, **8**, (2023).

[194] Y. Dong, Y. Zou, J. Song, J. Li, B. Han, Q. Shan, L. Xu, J. Xue, and H. Zeng, *Nanoscale*, **9**, 8580–8585 (2017).

[195] X. Pi, L. Zhang, and D. Yang, *J. Phys. Chem. C*, **116**, 21240–21243 (2012).

[196] H.M. Haverinen, R.A. Myllylä, G.E. Jabbour, and G.E. Jabbour, *IEEE/OSA J. Disp. Technol.*, **6**, 87–89 (2010).

[197] Z. Li, P. Li, G. Chen, Y. Cheng, X. Pi, X. Yu, D. Yang, L. Han, Y. Zhang, and Y. Song, *ACS Appl. Mater. Interfaces*, **12**, 39082–39091 (2020).

[198] L. Shi, L. Meng, F. Jiang, Y. Ge, F. Li, X. gang Wu, and H. Zhong, *Adv. Funct. Mater.*, **29**, 1903648 (2019).

[199] C. Kang, Z. Zhou, J.E. Halpert, and A.K. Srivastava, *Nanoscale*, **14**, 8060–8068 (2022).

[200] C. Liang, P. Li, H. Gu, Y. Zhang, F. Li, Y. Song, G. Shao, N. Mathews, and G. Xing, *Sol. RRL*, **2**, 1700217 (2018).

[201] J. Liu, B. Shabbir, C. Wang, T. Wan, Q. Ou, P. Yu, A. Tadich, X. Jiao, D. Chu, D. Qi, D. Li, R. Kan, Y. Huang, Y. Dong, J. Jasieniak, Y. Zhang, and Q. Bao, *Adv. Mater.*, **31**, 1901644 (2019).

[202] Y. Jeong, S. Hong, G. Jung, W. Shin, J. Park, D. Kim, Y.S. Choi, J.H. Bae, B.H. Hong, and J.H. Lee, *Sensors Actuators, B Chem.*, **343**, 130134 (2021).

[203] T. Van Tam, S.H. Hur, J.S. Chung, and W.M. Choi, *Sensors Actuators, B Chem.*, **329**, 129250 (2021).

[204] Z. Stempien, M. Khalid, M. Kozanecki, P. Filipczak, A. Wrzesińska, E. Korzeniewska, and E. Sąsiadek, *Materials (Basel).*, **14**, 3577 (2021).

[205] Y. Xu, I. Hennig, D. Freyberg, A. James Strudwick, M. Georg Schwab, T. Weitz, and K. Chih-Pei Cha, *J. Power Sources*, **248**, 483–488 (2014).

[206] E. Bihar, T. Roberts, M. Saadaoui, T. Hervé, J.B. De Graaf, and G.G. Malliaras, *Adv. Healthc. Mater.*, **6**, 1601167 (2017).

[207] N. TU and S.W. Ricky LEE, Inkjet Printing PEDOT:PSS without Coffee Ring Effect for QLED Applicaitons, in: 2019 20th Int. Conf. Electron. Packag. Technol., IEEE, (2019), pp. 1–4.

[208] E. Bihar, D. Corzo, T.C. Hidalgo, D. Rosas-Villalva, K.N. Salama, S. Inal, and D. Baran, *Adv. Mater. Technol.*, **5**, 2000226 (2020).

[209] T.M. Eggenhuisen, Y. Galagan, A.F.K.V. Biezemans, T.M.W.L. Slaats, W.P. Voorthuijzen, S. Kommeren, S. Shanmugam, J.P. Teunissen, A. Hadipour, W.J.H. Verhees, S.C. Veenstra, M.J.J. Coenen, J. Gilot, R. Andriessen, and W.A. Groen, *J. Mater. Chem. A*, **3**, 7255–7262 (2015).

[210] A. Giuri, E. Saleh, A. Listorti, S. Colella, A. Rizzo, C. Tuck, and C. Esposito

Corcione, *Nanomaterials*, **9**, 582 (2019).

[211] H. Gorter, M.J.J. Coenen, M.W.L. Slaats, M. Ren, W. Lu, C.J. Kuijpers, and W.A. Groen, *Thin Solid Films*, **532**, 11–15 (2013).

[212] C. Schmitz, M. Thelakkat, and H.W. Schmidt, *Adv. Mater.*, **11**, 821–826 (1999).

[213] D. Kruangam, M. Deguchi, T. Toyama, H. Okamoto, and Y. Hamakawa, *IEEE Trans. Electron Devices*, **35**, 957–965 (1988).

[214] R.D. Boehm, P.R. Miller, J. Daniels, S. Stafslien, and R.J. Narayan, *Mater. Today*, **17**, 247–252 (2014).

[215] A. Scholz, L. Zimmermann, U. Gengenbach, L. Koker, Z. Chen, H. Hahn, A. Sikora, M.B. Tahoori, and J. Aghassi-Hagmann, *Nat. Commun.*, **11**, 5543 (2020).

[216] Z. Zheng, N. Kim, W.S. Wong, and J.T.W. Yeow, *Sensors Actuators, B Chem.*, **327**, 128920 (2021).

[217] M.D. Dankoco, G.Y. Tesfay, E. Benevent, and M. Bendahan, *Mater. Sci. Eng. B Solid-State Mater. Adv. Technol.*, **205**, 1–5 (2016).

[218] M. Liu, Y. Zhao, Y. Shao, Q. Zhang, and C. Liu, 3D Printed Force Sensor with Inkjet Printed Piezoresistive Based Strain Gauge, in: IEEE SENSORS, IEEE, (2018), pp. 1–4.

[219] V. Dua, S.P. Surwade, S. Ammu, S.R. Agnihotra, S. Jain, K.E. Roberts, S. Park, R.S. Ruoff, and S.K. Manohar, *Angew. Chemie*, **122**, 2200–2203 (2010).

[220] G. Li, Z. Meng, J. Qian, C.L. Ho, S.P. Lau, W.Y. Wong, and F. Yan, *Mater. Today Energy*, **12**, 155–160 (2019).

[221] K.H. Choi, J.T. Yoo, C.K. Lee, and S.Y. Lee, *Energy Environ. Sci.*, **9**, 2812–2821 (2016).

[222] R. Worsley, L. Pimpolari, D. McManus, N. Ge, R. Ionescu, J.A. Wittkopf, A. Alieva, G. Basso, M. MacUcci, G. Iannaccone, K.S. Novoselov, H. Holder, G. Fiori, and C. Casiraghi, *ACS Nano*, **13**, 54–60 (2019).

[223] H.-C. Wang, Y. Hong, Z. Chen, C. Lao, Y. Lu, Z. Yang, Y. Zhu, and X. Liu,

Nanoscale Res. Lett., **15**, 176 (2020).

[224] J. Li, S. Yuan, G. Tang, G. Li, D. Liu, J. Li, X. Hu, Y. Liu, J. Li, Z. Yang, S.F. Liu, Z. Liu, F. Gao, and F. Yan, *ACS Appl. Mater. Interfaces*, **9**, 42779–42787 (2017).

[225] F. Hermerschmidt, F. Mathies, V.R.F. Schröder, C. Rehermann, N.Z. Morales, E.L. Unger, and E.J.W. List-Kratochvil, *Mater. Horizons*, **7**, 1773–1781 (2020).

[226] Y. Liu, F. Li, Z. Xu, C. Zheng, T. Guo, X. Xie, L. Qian, D. Fu, and X. Yan, *ACS Appl. Mater. Interfaces*, **9**, 25506–25512 (2017).

[227] F. Mathies, T. Abzieher, A. Hochstuhl, K. Glaser, A. Colsmann, U.W. Paetzold, G. Hernandez-Sosa, U. Lemmer, and A. Quintilla, *J. Mater. Chem. A*, **4**, 19207–19213 (2016).

[228] J. Zhao, L.W. Lo, H. Wan, P. Mao, Z. Yu, and C. Wang, *Adv. Mater.*, **33**, 2102095 (2021).

[229] H.P. Jansen, K. Sotthewes, J. van Swigchem, H.J.W. Zandvliet, and E.S. Kooij, *Phys. Rev. E*, **88**, 013008 (2013).

[230] Z. Du, Y. Liu, X. Xing, T. Lin, L. Liu, T. Chu, L. Wang, D. Zhang, and Z. Cui, *J. Phys. D. Appl. Phys.*, **53**, 355105 (2020).

[231] J.S. Kim, M. Granström, R.H. Friend, N. Johansson, W.R. Salaneck, R. Daik, W.J. Feast, and F. Cacialli, *J. Appl. Phys.*, **84**, 6859–6870 (1998).

[232] P.M. Grubb, H. Subbaraman, S. Park, D. Akinwande, and R.T. Chen, *Sci. Rep.*, **7**, 1202 (2017).

[233] K. Sztymela, M. Bienia, F. Rossignol, S. Mailley, S. Ziesche, J. Varghese, and M. Cerbelaud, *Heliyon*, **8**, (2022).

[234] H. Patrick Jansen, K. Sotthewes, H.J.W. Zandvliet, and E.S. Kooij, *Appl. Surf. Sci.*, **361**, 122–132 (2016).

[235] S. Prakash, M. Sims, I. Wyrsta, I.D. Parker, D. Kondakov, and W. Gao, *Dig. Tech. Pap. - SID Int. Symp.*, **44**, 678–681 (2013).

[236] S. Ho, S. Liu, Y. Chen, and F. So, *J. Photonics Energy*, **5**, 057611 (2015).

[237] C.A. Zuniga, S. Barlow, and S.R. Marder, *Chem. Mater.*, **23**, 658–681 (2011).

[238] Y.-H. Niu, M.S. Liu, J.-W. Ka, and A.K.Y. Jen, *Appl. Phys. Lett.*, **88**, 093505 (2006).

[239] B. Ma, B.J. Kim, D.A. Paulsen, S.J. Pastine, and J.M.J. Fréchet, *Adv. Funct. Mater.*, **19**, 1024–1031 (2009).

[240] Y. Fang, X. Wu, S. Lan, J. Zhong, D. Sun, H. Chen, and T. Guo, *ACS Appl. Mater. Interfaces*, **10**, 30587–30595 (2018).

[241] T. Zhang, E. Asher, and J. Yang, *Adv. Mater. Technol.*, **3**, 1700346 (2018).

[242] J. Kimionis, M. Isakov, B.S. Koh, A. Georgiadis, and M.M. Tentzeris, *IEEE Trans. Microw. Theory Tech.*, **63**, 4521–4532 (2015).

[243] P. Xiao, Y. Zhou, L. Gan, Z. Pan, J. Chen, D. Luo, R. Yao, J. Chen, H. Liang, and H. Ning, *Micromachines*, **11**, (2020).

[244] M. Kennert and J. Wolf, Inkjet in the PCB -Production, in: Inkjet Print. Ind., (2022), pp. 1255–1268.

[245] J. Im, Y. Liu, Q. Hu, G.F. Trindade, C. Parmenter, M. Fay, Y. He, D.J. Irvine, C. Tuck, R.D. Wildman, R. Hague, and L. Turyanska, *Adv. Funct. Mater.*, **33**, 2211920 (2023).

[246] L.T. Le, M.H. Ervin, H. Qiu, B.E. Fuchs, and W.Y. Lee, *Electrochem. Commun.*, **13**, 355–358 (2011).

[247] Q. Fatima, A.A. Haidry, Z. Yao, Y. He, Z. Li, L. Sun, and L. Xie, *Nanoscale Adv.*, **1**, 1319–1330 (2019).

[248] H.L. Kao, C.L. Cho, L.C. Chang, C.B. Chen, W.H. Chung, and Y.C. Tsai, *Coatings*, **10**, 792 (2020).

[249] T.K. Kang, *Coatings*, **11**, 1–8 (2021).

[250] J.B. Andrews, J.A. Cardenas, C.J. Lim, S.G. Noyce, J. Mullett, and A.D. Franklin, *IEEE Sens. J.*, **18**, 7875–7880 (2018).

[251] T. Yamada, Y. Hayamizu, Y. Yamamoto, Y. Yomogida, A. Izadi-Najafabadi, D.N. Futaba, and K. Hata, *Nat. Nanotechnol.*, **6**, 296–301 (2011).

[252] G. Pace, A. Grimoldi, D. Natali, M. Sampietro, J.E. Coughlin, G.C. Bazan, and M. Caironi, *Adv. Mater.*, **26**, 6773–6777 (2014).

[253] S. Saggar, S. Sanderson, D. Gedefaw, X. Pan, B. Philippa, M.R. Andersson, S. Lo, and E.B. Namdas, *Adv. Funct. Mater.*, **31**, 2010661 (2021).

[254] J. Liu, M. Gao, J. Kim, Z. Zhou, D.S. Chung, H. Yin, and L. Ye, *Mater. Today*, **51**, 475–503 (2021).

[255] G. Hu, T. Albrow-Owen, X. Jin, A. Ali, Y. Hu, R.C.T. Howe, K. Shehzad, Z. Yang, X. Zhu, R.I. Woodward, T.-C. Wu, H. Jussila, J.-B. Wu, P. Peng, P.-H. Tan, Z. Sun, E.J.R. Kelleher, M. Zhang, Y. Xu, et al., *Nat. Commun.*, **8**, 278 (2017).

[256] H.C. Wang, Y. Hong, Z. Chen, C. Lao, Y. Lu, Z. Yang, Y. Zhu, and X. Liu, *Nanoscale Res. Lett.*, **15**, (2020).

[257] R. Sliz, M. Lejay, J.Z. Fan, M.J. Choi, S. Kinge, S. Hoogland, T. Fabritius, F.P. Garciá De Arquer, and E.H. Sargent, *ACS Nano*, **13**, (2019).

[258] J. Liu, B. Shabbir, C. Wang, T. Wan, Q. Ou, P. Yu, A. Tadich, X. Jiao, D. Chu, D. Qi, D. Li, R. Kan, Y. Huang, Y. Dong, J. Jasieniak, Y. Zhang, and Q. Bao, *Adv. Mater.*, **31**, (2019).

[259] S.D. Stranks, G.E. Eperon, G. Grancini, C. Menelaou, M.J.P. Alcocer, T. Leijtens, L.M. Herz, A. Petrozza, and H.J. Snaith, *Science*, **342**, 341–344 (2013).

[260] Y. Wang and R. Long, *J. Phys. Chem. Lett.*, **10**, 4354–4361 (2019).

[261] H. Wang and D.H. Kim, *Chem. Soc. Rev.*, **46**, 5204–5236 (2017).

[262] D. Liu, C. Yang, and R.R. Lunt, *Joule*, **2**, 1827–1837 (2018).

[263] C.H. Kang, I. Dursun, G. Liu, L. Sinatra, X. Sun, M. Kong, J. Pan, P. Maity, E.-N. Ooi, T.K. Ng, O.F. Mohammed, O.M. Bakr, and B.S. Ooi, *Light Sci. Appl.*, **8**, 94 (2019).

[264] S.J. Ho, H.C. Hsu, C.W. Yeh, and H.S. Chen, *ACS Appl. Mater. Interfaces*, **12**, 33346–33351 (2020).

[265] L. Zhou, L. Yang, M. Yu, Y. Jiang, C.F. Liu, W.Y. Lai, and W. Huang, *ACS*

Appl. Mater. Interfaces, **9**, 40533–40540 (2017).

[266] H. Tang, S. Jia, S. Ding, P. Liu, J. Ma, X. Xiao, X. Qu, H. Liu, H. Yang, B. Xu, W. Chen, G. Li, Z. Pikramenou, C. Anthony, K. Wang, and X.W. Sun, *ACS Appl. Electron. Mater.*, **3**, 3005–3014 (2021).

[267] S.G.R. Bade, J. Li, X. Shan, Y. Ling, Y. Tian, T. Dilbeck, T. Besara, T. Geske, H. Gao, B. Ma, K. Hanson, T. Siegrist, C. Xu, and Z. Yu, *ACS Nano*, **10**, 1795–1801 (2016).

[268] J.G. Sánchez, V.S. Balderrama, S.I. Garduño, E. Osorio, A. Viterisi, M. Estrada, J. Ferré-Borrull, J. Pallarès, and L.F. Marsal, *RSC Adv.*, **8**, 13094–13102 (2018).

[269] S.H. Eom, H. Park, S.H. Mujawar, S.C. Yoon, S.S. Kim, S.I. Na, S.J. Kang, D. Khim, D.Y. Kim, and S.H. Lee, *Org. Electron.*, **11**, 1516–1522 (2010).

[270] S. Il Ahn, W.K. Kim, S.H. Ryu, K.J. Kim, S.E. Lee, S.H. Kim, J.C. Park, and K.C. Choi, *Org. Electron.*, **13**, 980–984 (2012).

[271] M. Rai, L.H. Wong, and L. Etgar, *J. Phys. Chem. Lett.*, **11**, 8189–8194 (2020).

[272] G. Vescio, G. Mathiazhagan, S. González-Torres, J. Sanchez-Diaz, A. Villaueva-Antolí, R.S. Sánchez, A.F. Gualdrón–Reyes, M. Oszajca, F. Linardi, A. Hauser, F.A. Vinocour-Pacheco, W. Żuraw, S. Öz, S. Hernández, I. Mora-Seró, A. Cirera, and B. Garrido, *Adv. Eng. Mater.*, **25**, 2300927 (2023).

[273] J. Jeong, J.H. Park, C.H. Jang, M.H. Song, and H.Y. Woo, *Adv. Mater.*, **32**, 2002176 (2020).

[274] F. Mathies, H. Eggers, B.S. Richards, G. Hernandez-Sosa, U. Lemmer, and U.W. Paetzold, *ACS Appl. Energy Mater.*, **1**, 1834–1839 (2018).

[275] M.A. Green, Y. Hishikawa, W. Warta, E.D. Dunlop, D.H. Levi, J. Hohl-Ebinger, and A.W.H. Ho-Baillie, *Prog. Photovoltaics Res. Appl.*, **25**, 668–676 (2017).

[276] G.H. McKinley and M. Renardy, *Phys. Fluids*, **23**, 127101 (2011).

[277] X. Qiu, X. Gong, X. Zhang, and W. Zheng, *Coatings*, **12**, 1893 (2022).

[278] Y. Son, C. Kim, D.H. Yang, and D.J. Ahn, *Langmuir*, **24**, 2900–2907 (2008).

[279] H. Mescher, F. Schackmar, H. Eggers, T. Abzieher, M. Zuber, E. Hamann, T. Baumbach, B.S. Richards, G. Hernandez-Sosa, U.W. Paetzold, and U. Lemmer, *ACS Appl. Mater. Interfaces*, **12**, 15774–15784 (2020).

[280] J.S. Austin, N.D. Cottam, C. Zhang, F. Wang, J.H. Gosling, O. Nelson-Dummet, T.S.S. James, P.H. Beton, G.F. Trindade, Y. Zhou, C.J. Tuck, R. Hague, O. Makarovsky, and L. Turyanska, *Nanoscale*, **15**, 2134–2142 (2022).

[281] B. Cook, M. Gong, D. Ewing, M. Casper, A. Stramel, A. Elliot, and J. Wu, *ACS Appl. Nano Mater.*, **2**, 3246–3252 (2019).

[282] S. Pezzini, V. Mišeikis, S. Pace, F. Rossella, K. Watanabe, T. Taniguchi, and C. Coletti, *2D Mater.*, **7**, 041003 (2020).

[283] H.A. Barnes, *Powder Technol.*, **86**, 313 (1996).

[284] H. Ibach, "Physics of surfaces and interfaces", (2006).

[285] T.G. community, GNU Image Manipulation Program website, http://smk.kemdikbud.go.id/konten/992/gimp-gnu-image-manipulation-program .

[286] F. Bassani, G.L. Liedl, and P. Wyder, "Encyclopedia of condensed matter physics", (2005).

[287] M. De Graef, "Introduction to Conventional Transmission Electron Microscopy", Cambridge University Press, (2003).

[288] ImageJ, https://imagej.nih.gov/ij/index.html .

[289] V.D. Hodoroaba, Energy-dispersive X-ray spectroscopy (EDS), in: Charact. Nanoparticles Meas. Process. Nanoparticles, (2019), pp. 397–417.

[290] F.J. Giessibl, *Rev. Mod. Phys.*, **75**, 949–983 (2003).

[291] NISE Network, Scientific Image - Atomic Force Microscope Illustration, https://www.nisenet.org/catalog/scientific-image-atomic-force-microscope-illustration .

[292] E. Smith and G. Dent, "Modern raman spectroscopy: A practical approach",

(2019).

[293] T. Aoki, Photoluminescence Spectroscopy, in: Charact. Mater., Wiley, (2012), pp. 1–12.

[294] M. Picollo, M. Aceto, and T. Vitorino, *Phys. Sci. Rev.*, **4**, (2019).

[295] D.K. Schroder, "Semiconductor Material and Device Characterization: Third Edition", (2005).

[296] E.B. Secor, T.Z. Gao, M.H. Dos Santos, S.G. Wallace, K.W. Putz, and M.C. Hersam, *ACS Appl. Mater. Interfaces*, **9**, 29418–29423 (2017).

[297] Y. Su, Q. Zeng, X. Chen, W. Ye, L. She, X. Gao, Z. Ren, and X. Li, *J. Mater. Chem. C*, **7**, 7548–7553 (2019).

[298] X. Yu, R. Xing, Z. Peng, Y. Lin, Z. Du, J. Ding, L. Wang, and Y. Han, *Chinese Chem. Lett.*, **30**, 135–138 (2019).

[299] S. Barwich, J. Medeiros de Araújo, A. Rafferty, C. Gomes da Rocha, M.S. Ferreira, and J.N. Coleman, *Carbon N. Y.*, **171**, 306–319 (2021).

[300] T. Pandhi, C. Cornwell, K. Fujimoto, P. Barnes, J. Cox, H. Xiong, P.H. Davis, H. Subbaraman, J.E. Koehne, and D. Estrada, *RSC Adv.*, **10**, 38205–38219 (2020).

[301] S. Jeong, R.L. Pinals, B. Dharmadhikari, H. Song, A. Kalluri, D. Debnath, Q. Wu, M.H. Ham, P. Patra, and M.P. Landry, *Sci. Rep.*, **10**, 7074 (2020).

[302] W.K. Hsiao, G.D. Martin, and I.M. Hutchings, *Langmuir*, **30**, 12447–12455 (2014).

[303] G. Oster and E.H. Immergut, *J. Am. Chem. Soc.*, **76**, 1393–1396 (1954).

[304] X. Wang, Y. Cui, L. Zhang, and M. Yang, *Nano Res.*, **14**, 3935–3941 (2021).

[305] E. Saleh, F. Zhang, Y. He, J. Vaithilingam, J.L. Fernandez, R. Wildman, I. Ashcroft, R. Hague, P. Dickens, and C. Tuck, *Adv. Mater. Technol.*, **2**, 1700134 (2017).

[306] P. Zhao, Y. He, G.F. Trindade, M. Baumers, D.J. Irvine, R.J.M. Hague, I.A. Ashcroft, and R.D. Wildman, *Mater. Des.*, **208**, 109889 (2021).

[307] J.C. Yu, J.A. Hong, E.D. Jung, D. Bin Kim, S.-M. Baek, S. Lee, S. Cho, S.S. Park, K.J. Choi, and M.H. Song, *Sci. Rep.*, **8**, 1070 (2018).

[308] H. Wang, X. Gong, D. Zhao, Y.B. Zhao, S. Wang, J. Zhang, L. Kong, B. Wei, R. Quintero-Bermudez, O. Voznyy, Y. Shang, Z. Ning, Y. Yan, E.H. Sargent, and X. Yang, *Joule*, **4**, 1977–1987 (2020).

[309] Y. Wang, B. Li, C. Jiang, Y. Fang, P. Bai, and Y. Wang, *J. Phys. Chem. C*, **125**, 16753–16758 (2021).

[310] S. Shao and M.A. Loi, *Adv. Mater. Interfaces*, **7**, 1901469 (2020).

[311] Y. Wang, Y. Zhang, Y. Lu, W. Xu, H. Mu, C. Chen, H. Qiao, J. Song, S. Li, B. Sun, Y.B. Cheng, and Q. Bao, *Adv. Opt. Mater.*, **3**, 1389–1396 (2015).

[312] G. Konstantatos, M. Badioli, L. Gaudreau, J. Osmond, M. Bernechea, F.P.G. De Arquer, F. Gatti, and F.H.L. Koppens, *Nat. Nanotechnol.*, **7**, 363–368 (2012).

[313] A. Karavioti, D.A. Chalkias, G. Katsagounos, A. Mourtzikou, A.N. Kalarakis, and E. Stathatos, *Electronics*, **10**, 1904 (2021).

[314] G. Calabrese, L. Pimpolari, S. Conti, F. Mavier, S. Majee, R. Worsley, Z. Wang, F. Pieri, G. Basso, G. Pennelli, K. Parvez, D. Brooks, M. Macucci, G. Iannaccone, K.S. Novoselov, C. Casiraghi, and G. Fiori, *Nanoscale*, **12**, 6708–6716 (2020).

[315] N.D. Cottam, J.S. Austin, C. Zhang, A. Patanè, W. Escoffier, M. Goiran, M. Pierre, C. Coletti, V. Mišeikis, L. Turyanska, and O. Makarovsky, *Adv. Electron. Mater.*, **9**, 2200995 (2023).

[316] S. Santra, G. Hu, R.C.T. Howe, A. De Luca, S.Z. Ali, F. Udrea, J.W. Gardner, S.K. Ray, P.K. Guha, and T. Hasan, *Sci. Rep.*, **5**, 17374 (2015).

[317] C.O. Kim, S.W. Hwang, S. Kim, D.H. Shin, S.S. Kang, J.M. Kim, C.W. Jang, J.H. Kim, K.W. Lee, S.H. Choi, and E. Hwang, *Sci. Rep.*, **4**, 1–6 (2014).

[318] Q. Zhang, H. Yu, Z. Liu, Y. Lu, D. Ye, J. Qian, Y. Wu, W. Gu, B. Ma, L. Zhang, Y. Duan, L. Liu, K. Cao, S. Chen, and W. Huang, *RSC Adv.*, **9**, 20931–20940 (2019).

[319] P. Jepiti, S. Yoon, and J. Kim, *ACS Appl. Nano Mater.*, **5**, 2569–2577 (2022).

[320] L. Liu, D. Ye, R. Dong, D. Chen, S. Li, K. Cao, G. Cheng, S. Chen, and W. Huang, *ACS Appl. Energy Mater.*, **3**, 4068–4077 (2020).

[321] W. Cao, P. Liu, W. Chen, W. Wang, B. Xu, D. Wu, J. Hao, W. Cao, F. Fang, Y. Li, Y. Zeng, R. Pan, S. Chen, X.W. Sun, and K. Wang, *Chem. Mater.*, **29**, 5168–5173 (2017).

[322] F.L.M. Sam, C.A. Mills, L.J. Rozanski, and S.R.P. Silva, *Laser Photonics Rev.*, **8**, 172–179 (2014).